Localised Dosing and Nanodetection Using a Novel Scanning Ion Conductance Microscope and Its Application to Alzheimer's Disease

Wei-Hsin Chen

Wolfson College, Cambridge

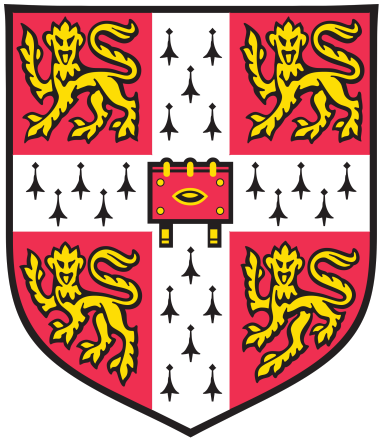

Thesis submitted in fulfilment of the requirements for the degree of

Doctor of Philosophy at the University of Cambridge

September, 2017

Deposit & Copying of Dissertation Declaration

UNIVERSITY OF CAMBRIDGE

Board of Graduate Studies

Please note that you will also need to bind a copy of this Declaration into your final, hardbound copy of thesis - this has to be the very first page of the hardbound thesis.

1 Surname (Family Name)	Forenames(s)	Title

2 Title of Dissertation as approved by the Degree Committee

In accordance with the University Regulations in *Statutes and Ordinances* for the PhD, MSc and MLitt Degrees, I agree to deposit one print copy of my dissertation entitled above and one print copy of the summary with the Secretary of the Board of Graduate Studies who shall deposit the dissertation and summary in the University Library under the following terms and conditions:

1. Dissertation Author Declaration

I am the author of this dissertation and hereby give the University the right to make my dissertation available in print form as described in 2. below.

My dissertation is my original work and a product of my own research endeavours and includes nothing which is the outcome of work done in collaboration with others except as declared in the Preface and specified in the text. I hereby assert my moral right to be identified as the author of the dissertation.

The deposit and dissemination of my dissertation by the University does not constitute a breach of any other agreement, publishing or otherwise, including any confidentiality or publication restriction provisions in sponsorship or collaboration agreements governing my research or work at the University or elsewhere.

2. Access to Dissertation

I understand that one print copy of my dissertation will be deposited in the University Library for archival and preservation purposes, and that, unless upon my application restricted access to my dissertation for a specified period of time has been granted by the Board of Graduate Studies prior to this deposit, the dissertation will be made available by the University Library for consultation by readers in accordance with University Library Regulations and copies of my dissertation may be provided to readers in accordance with applicable legislation.

3 Signature	Date

Corresponding Regulation

Before being admitted to a degree, a student shall deposit with the Secretary of the Board one copy of his or her hard-bound dissertation and one copy of the summary (bearing student's name and thesis title), both the dissertation and the summary in a form approved by the Board. The Secretary shall deposit the copy of the dissertation together with the copy of the summary in the University Library where, subject to restricted access to the dissertation for a specified period of time having been granted by the Board of Graduate Studies, they shall be made available for consultation by readers in accordance with University Library Regulations and copies of the dissertation provided to readers in accordance with applicable legislation.

Localised Dosing and Nanodetection Using a Novel Scanning Ion Conductance Microscope and Its Application to Alzheimer's Disease

Wei-Hsin Chen, Wolfson College, Cambridge

Thesis submitted in fulfilment of the requirements for the degree of

Doctor of Philosophy at the University of Cambridge. September, 2017

Abstract

Scanning ion conductance microscopy (SICM) is a technique for non-contact topographic imaging. In this thesis, a biophysical investigation into Alzheimer's Disease (AD) was carried, with toxic oligomers dosed locally and quantitatively on to single astrocytes using SICM and simultaneously monitoring the response of the target cell.

Examination of the effectiveness of antibodies that bind to Abeta or α-synuclein (Asyn) peptides depends on the measurement of oligomer-induced abnormal calcium homeostasis in single astrocytes. The method was shown to work at physiological concentrations of oligomers. A series of experiments measuring the reduction in calcium influx in mixtures of antibodies and cerebrospinal fluid (CSF) of AD patients suggested that the binding to co-oligomers composed of Abeta and Asyn may be crucial in the treatment of AD. Furthermore, it may be beneficial to test antibodies before the clinical trial using this assay.

The mechanism of this entry of calcium is hypothesised to be the result of the formation of oligomer-induced transient pores in the cell membrane. To verify this hypothesis, a new SICM instrument was built with two nanopipettes; one for dosing and one for detection of the adenosine triphosphate (ATP) release from these pores. A variety of different ATP sensors were made. The best had a sensitivity of $10\,\mu$M and works as a hexokinase-cofunctioned electrolyte-gated organic field-effect-transistor. However no statistically significant results for ATP release have been obtained in the experiments performed to date.

Overall this thesis describes new biophysical methods to study the effect of protein aggregates on live cells and the effectiveness of potential therapies, such as antibodies and nanobodies, to reduce these aggregate induced effects. It can be applied to synthetic aggregates of Abeta or the aggregates present in human CSF.

"An indispensable hypothesis, even though still far from being a guarantee of success, is however the pursuit of a specific aim, whose lighted beacon, even by initial failures, is not betrayed."

Max K. E. L. Planck (1858-1947)

Acknowledgements

Foremost, I would like to express my gratitude to my supportive and patient supervisor, Professor David Klenerman, for accepting me into his research group to pursue my PhD degree, which is aimed at defeating neurodegenerative diseases using biophysical investigations. I still remember vividly when, before submitting my official PhD application, I took the long journey from Oxford to Cambridge for a lab tour on a sunny day. After the tour and a few interesting scientific conversations with the group members, Dave suggested four research topics that I could choose from, noting that investigation using SICM was "two times harder than the others." In fact, I had already almost made the decision to go for this topic before the visit, being highly attracted by studying biological mechanisms using SICM on a single-cell level, and this difficulty could not stop me from taking on this project.

It turned out that his description was no exaggeration. Performing experiments at a single-cell level using SICM was indeed in no way straightforward, and measurements sometimes suffered greatly from intermittent electrical noise. At the same time, the complexity of the manufacturing processes for nanoscale ATP biosensors fabricated on the tips of capillary probes increased the difficulty significantly. Fortunately, Dave's continuous support and the inspirational talks in the previous three years have always been encouraging and kept me going forward.

For her great help with experimental details, special thanks go to Dr Anna Drews. Her expertise in biology and her thorough support with data acquisition and analysis have allowed this interdisciplinary project to go smoothly; I could not have finished my thesis without her generous help. My appreciation goes to Dr Alexander Zhukov, an expert in electronics, who helped to diagnose and solve many of the technical problems of our homemade SICMs,

including the electronics and coding in various computer languages. He has been my role model as a scientist, with outstanding skill sets in engineering. I would like to say thank you to our collaborators at Imperial College London, including Professor Yuri Korchev, Dr Paolo Actis, Dr Yanchun Zhang and Dr Ainara L?pez C?rdoba, who all have world-leading expertise in SICM and its applications, for supporting my research during the period of my PhD course. Additionally, I would like to thank our collaborators at the University of Bristol, Professor Kei Cho, Dr Daniel Whitcomb, Dr Jee Hyun Yi and Dr Dong Hyun Kim, for guiding me in performing patch-clamp measurements on neurons in every detail.

Under the immense stress that can come from a PhD, along with the serious and sudden knocks that life may bring, I may not always have been able to deal with the burdens very well, and have sometimes vented my feelings on people around me who were not to blame. Therefore, special thanks go to my girlfriend, Dr Yen-Chun Lin, not only for her important spiritual support and company, no matter where I was, but also for her patience and tolerance when she might have expected me to show more consideration. Additionally, I would like to thank my parents, Mrs Hsi-Ming Chao and Mr Tang-Sheng Chen, and my uncle, Mr Hsi-Hua Chao, for their everlasting love throughout my life. Thank you for always being supportive and wonderful! Also, I would like to thank all the members of the Klenerman and Lee group, who have infused my time at the office with joy and laughter. I especially thank Chieh (Jason) Sang for arranging an impressive post-viva party for me in the Department of Chemistry. Last but not least, my appreciation goes to the Cambridge Commonwealth, European and International Trust and the Ministry of Education, Taiwan for their financial support via the Taiwan-Cambridge Scholarship, and Wolfson College, Cambridge for its Sport Awards and travel funds.

Contents

Publications

A. Drews, S. De, P. Flagmeier, D. C. Wirthensohn, W.-H. Chen, D. R. Whiten, M. Rodrigues, C. Vincke, S. Muyldermans, R. W. Paterson, C. F. Slattery, N. C. Fox, J. M. Schott, H. Zetterberg, C. M. Dobson, S. Gandhi and D. Klenerman. Inhibiting the Calcium Influx Induced by human CSF. *Cell Reports*, **21(11)**:3310-3316, 2017.

W.-H. Chen, S. De, A. Drews, C. Vincke, S. Gandhi, D. Klenerman. Co-aggregates of beta amyloid and asynuclein cause calcium influx in the Alzheimer's patient CSF. *Manuscript in preparation.*

Chapter 1

Introduction

The aim of the projects described in this thesis are to utilise the techniques of nanodosing and single-cell detection provided by upgraded scanning ion conductance microscopy (SICM) to address the basic biology in Alzheimer's Disease (AD) induced by oligomeric misfolded peptides of amyloid beta (Abeta). Therefore, in this chapter, basic theory and development of SICM, and the corresponding applications in biological and other fields, including investigations using hybrid SICM techniques and a processed nanopipette without performing scanning, will be introduced in details.

1.1 Single-molecule imaging

In a biological system, cellular functions operate on a hierarchical level, from a peptide to an organ. To investigate their specific individual tasks, it is crucial to examine quantitatively and spatially the chemical and reaction pathways in heterogeneous subpopulations. On a single-cell level, transmission of signals across the cell membrane is achieved by protein receptors in the cell membrane that bind ligands, resulting in ion channels opening or conformational changes. For most cells it is not known how these receptors are organised over the cell surface, and this is important since it is unlikely that the distribution is random and will be related to how receptor signalling gives rise to the overall cellular response to any stimulus. Far-field microscopy has significantly improved our understanding of life on a microscale level, where waves, including light and electrons, are used as the illumination

source for the sample, and then reflected or scattered signals are collected for imaging. However, the resolution of far-field microscopy is constrained by the diffraction limit decided by the wavelength of the illumination source, which is ∼200 nm for light. Although transmission electron microscopy (TEM) and scanning electron microscopy (SEM) use electrons as their illumination source to achieve a much better resolution than light (∼ $\mathring{A}$), they usually present problems when it comes to biological samples; for example, dehydration and additional staining or coating may damage the sample, the sample may be too thick for the electrons to penetrate, and the contrast of a biological sample is usually low.

On the other hand, emerging biophysical methods circumventing the diffraction limit of light are appealing. Fluorescence-based single-molecule methodologies can unambiguously reveal microscopic details in a specimen which may have been averaged out in traditional ensemble measurements [1, 2]. For example, they are able to image individual molecules labelled by fluorescent dyes, acquiring static or dynamic distributions of their interactive behaviours between other species. Nevertheless, topographic information on the cell related to fluorescent measurements is not obtained at the same time.

1.2 Scanning probe microscopy

Scanning probe microscopy (SPM) is a technique complementary to single-molecule fluorescence spectroscopy. The general principle of SPM is that the signal coming from the surface interaction with the probe is used for feedback control of a vertically-aligned piezoelectric actuator, and consequently the collected z-axis data is de-convoluted to map out the distributed surface height of the sample in a predefined area. Of these techniques, scanning tunnelling microscopy (STM) is the first instrument classified as SPM to give rise to atomic-level lateral resolution, and it involves a quantum tunnelling current between a metal probe and the conducting sample surface while a bias voltage is applied. This is used to determine the probe-sample separation and for further reconstruction of the topography of the sample [3]. The disadvantage of STM for biological samples is that, like SEM, an addi-

tional procedure of coating is also necessary to make the surface conductive, which means the biological sample is not in its natural state any more. Besides, the limitation for the z-axis scanning range of ∼200 nm is relatively unsuitable for cells of a normal micron height. Another technique in the SPM regime, atomic force microscopy (AFM), measures the force between the sample surface and a soft cantilever with a tip as the probe, when they are in atomic proximity to each other [4]. The deflection of the cantilever is recorded by the movement of a laser spot illuminated on it. AFM can achieve even subatomic spatial resolution; nevertheless, the raster scanning of ATM may interfere with the original cell conditions and may result in damage to the soft samples. The force applied by AFM cannot be ignored even it is measured in non-contact mode [5].

1.3 Scanning ion conductance microscopy

Therefore, new biophysical methods must be used on nonconductive biological samples for research of medically relevant-problems to reveal fundamental biology that has not been thoroughly understood. The critical feature of SICM, which was originally developed by Hansma *et al.* [6] in 1989, is that it provides real non-perturbing detection to probe the topography of live cells. In SICM, as shown in Figure 1.1, a nanopipette with a nanoscale aperture and a dish containing the sample are both filled with the same appropriate electrolyte, which is similar to a physiological rig for the conducting patch–clamp technique. In addition, a pair of Ag/AgCl electrodes is individually immersed in the nanopipette and the bath electrolyte. When the tip of the nanopipette is dipped in the bath solution, ions in the electrolyte constantly flow through the nanopipette aperture and scanning settings, which is driven by a suitable bias voltage applied between the electrodes. The ion current will be hindered by an object appearing in proximity to the tip. Therefore, the variation of ion current in the z-axis can be used as a feedback signal for control of the vertical distance between the tip and the sample surface, realising a constant tip-substrate separation during the scanning. The topography of the sample can be reconstructed using information on the z-axis positions of the tip, which is similar to the working principle of other SPMs. The

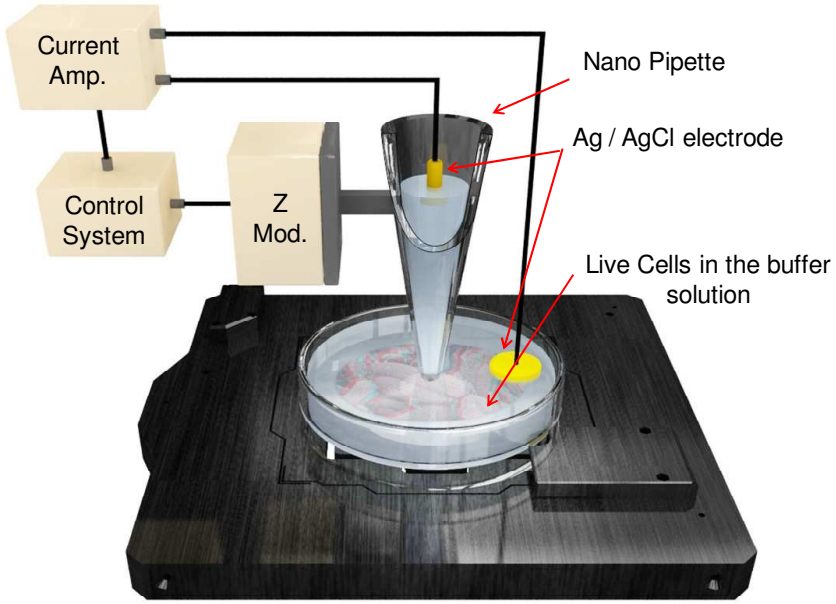

Figure 1.1: Schematic illustration of a simplified setup for scanning ion conductance microscopy (SICM). A buffer solution-loaded nanopipette is immersed in a Petri dish containing live cells and the same buffer solution. One of a pair of Ag/AgCl electrodes is immersed in this nanopipette and the other in the dish, with suitable bias voltage applied between the two in order to generate the ion current that flows through the aperture of the nanopipette. This ion current is amplified and utilised as a feedback signal for an automated control system. Therefore, the z-axis piezoelectric actuator holding the nanopipette is able to maintain a constant height at the tip from the substrate underneath to avoid physical contact. Excerpted from [10].

lateral resolution is basically determined by the nanopipette aperture and scanning settings, defined by images of two adjacent objects that can be resolved. The best lateral resolution reported was 3–6 nm using a tip inner diameter (r_i) of 12.5 nm [7]. However, the lateral resolution of SICM is debatable, since experimental and simulation results suggested 0.5 r_i and 2–3 r_i [8, 9], respectively.

The ion current is modelled by an equivalent circuit of multiple resistors in series with a bias voltage (V). Among them, the resistor related to the size of the nanopipette aperture, and therefore defining lateral resolution, is determined in advance by the laser-pulling process; whilst the resistor related to the tip–substrate distance (R(z)) is variable when the nanopipette moves along the z-axis. An approach curve following the relationship $I=V/(R_c+R(z))$ is exhibited, when the nanopipette immersed in the bath solution moves

vertically towards the substrate, where R_c is the constant resistance contributed by all other factors other than the nanopipette height, e.g. nanopipette aperture and electrolyte. This curve includes a steady-state component, in that the ion current stays almost constant when the nanopipette is far away from the bottom of the dish, and a nanopipette height-dependent component when in proximity to the substrate. Therefore, the distance-dependent resistor, R(z), is critical, as a certain amount of normalised current decrease (usually $\leq$5%) in the feedback signal is defined as a stop point in the constant-height scanning mode.

It is crucial to utilise a suitable scanning mode in order to gain a sufficiently high time resolution for studying dynamics. Raster scanning on a constant z-axis is extremely fast for topography, but only works for a fairly flat sample because the sensing distance of the nanopipette is short. For a relatively convoluted sample, scanning modes modulating the nanopipette height to stay at a constant tip–substrate distance are necessary to avoid collisions. The piezoelectric actuator controlling the z-position of the nanopipette applied by direct current (DC) as well as alternating current (AC) [11, 12] has a lower probability of causing tip-sample interference than when modulated only by DC [6] in raster scanning. AC mode (DC plus AC component ($\leq$KHz)) generates oscillation at the tip, so a steeper signal representing the AC response appears when the tip–substrate distance is comparable to r_i, making it significantly more sensitive to topographic changing than DC mode. Although trying to maximise the distance between the tip and the sample might decrease the chance of causing physical contact, SICM sensitivity at a hemispherical proximity around the tip, is nevertheless reduced [13]. For a sample with complex features, the non-continuous hopping mode [14] (also termed a standing approach (STA) [15] or backstep [16] by different research groups) is often adopted, which withdraws the nanopipette to a safe distance and moves it to the next scanning spot to avoid any tip-sample physical contact. It is the most secure way to perform SICM, but this algorithm massively decreases the scanning speed. An alternative way to increase the scanning efficiency is to lower the spatial resolution, only adding detection pixels at predefined subareas with high roughness. A trade-off between spatial and time resolutions is usually inevitable, unless a brand new concept for scanning is developed. Fast SICM (FSICM) combines the scanning methods described above [17]. Firstly, a rough

Table 1.1: Comparison between various farfield and scannin-probe microscopies, in which TEM, SEM, AFM, STM and SICM stand for transmission electron microscopy, scanning electron microscopy, atomic force microscopy, scanning tunnelling microscopy and scanning ion conductance microscopy, respectively.

Microscopy	Vertical resolution	Sample preparation	Measurement environment
TEM	Å	Dehydration	Dry
SEM	10 nm	Coating to be conductive	Dry
AFM	Å	Immobilisation only	Dry/wet
STM	10 pm	Coating to be conductive	Dry
SICM	10 nm	Immobilisation only	Wet

prescan along a straight line is performed using hopping mode, and then iterative refinement is incorporated into the fast scanning regime. Subsequently, the nanopipette is retracted and the accurate first line is used as a reference for the next parallel scanning. This procedure is repeated until the entire image is complete. The scanning rate is nearly 60 times that of hopping mode. In addition, it is possible to modulate not only physical oscillation of the tip position, but also bias voltage (in hundreds of kHz) to induce a change in amplitude and phase in the ion current in order to generate a feedback signal, which is sensitive to the tip-sample distance, for a phase-sensitive detector. This method, termed bias modulated SICM (BM-SICM), eliminates net ion current flow so as to reduce the effects of polarisation of electrodes and electroosmotic flow inside the nanopipette.

The most powerful feature of SICM is that it is not only capable of two-dimensional topographical imaging, but it can also combine various functional mapping at the same time, correlating cell structure with its cellular functions. In addition to its mapping ability, the nanopipette itself can also be modified for various applications. The summary of the characteristics of various high-resolution microscopies are listed in Table 1.1. Among these techniques, AFM and SICM are more appropriate for biological applications, because both of them can conduct the topographic measurements in buffer solution; however, the disadvantages of AFM will be discussed in the next section.

1.4 Comparison between AFM and SICM for biological samples

AFM has been widely applied to biological samples due to the fact that it is label-free and has sub-atomic resolution. However, live cells are delicate and easily distorted by external mechanical interference, leading to the disturbance of biochemical reactions and potentially switching on mechanosensitive ion channels. This unignorable force might even cause irreversible damage to the cell. Rheinlaender and coworkers have made a direct comparison of topographic mapping of fixed fibroblast cells with AFM and SICM using the contact, tapping and non-contact modes [18]. Apparently, the contact mode induces mapping artefacts due to its physical contact between the tip at the cantilever and the sample surface, as well as lower height profiles. This phenomenon is improved under tapping mode, as demonstrated in Figure 1.2, which shows loosely-attached branches of the cell. The topography imaging using SICM in AC mode demonstrated that the morphology of cellular extensions was not deformed by repeated scanning and by the direction of scannings; on the other hand AFM in tapping mode induced an observable difference in imaging in the same area compared with SICM, in which many components of the cell structure were damaged, and some of the features were not reproducible in repeated scanning. Due to the high aspect ratio of the SICM tip, the complete morphology of the cell was maintained in scanning using hopping mode. However, even though AFM was operated in non-contact mode, the imaging was made convoluted by the pedestal of the tip, i.e. the cell border was physically pressed by the tip and therefore exhibited artificial features. Therefore, SICM was proved to be more appropriate for live cell imaging than AFM in terms of generating the least disturbance with soft biological samples.

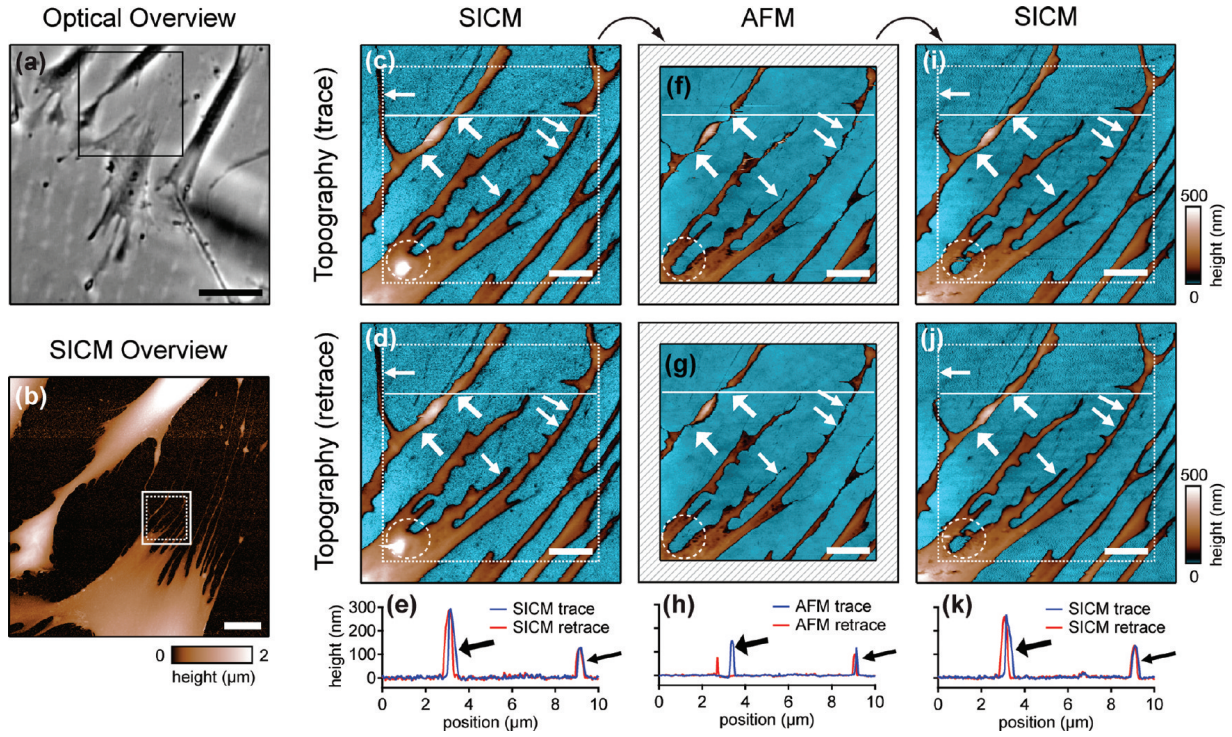

Figure 1.2: (a) An image of the target cell under optical illumination. (b) An image of local topographic scanning using SICM of the cell demonstrated in (a). (c)–(k) Comparison of subcellular features using repeated raster scanning in reverse directions with SICM and atomic force microscopy (AFM). Note that arrows in the images indicate structural features of the sample. Excerpted from [18].

1.5 SICM scanning mode and resolution

The intrinsic properties of SICM, including non-contact detection and the fact that it is performed in a buffer solution, make it an appropriate biophysical tool for the investigation of live cells. The ability to generate reproducible imaging of a fixed object at the bottom of a dish immersed in the electrolyte is one of the most important prerequisites for time-course comparison of cell morphology. Happel and coworkers evaluated the reproducibility of periodic scans of a single cell fixed at the bottom of some glass using line-scan mode. Although the biggest error of standard deviation (700 nm) always occurred at the cell boundary, the standard deviation was 50 nm at the centre of the cell, demonstrating it was highly suitable for a relatively flat sample region [19]. On the other hand, Korchev and coworkers examined the reproducibility of volumetric cell measurement, defined as $\Sigma z(x,y) \times dx \times dy$, using raster scans with a resolution of 2.5×10^{-20} litres and a margin of error of less than 0.2% [20]. After

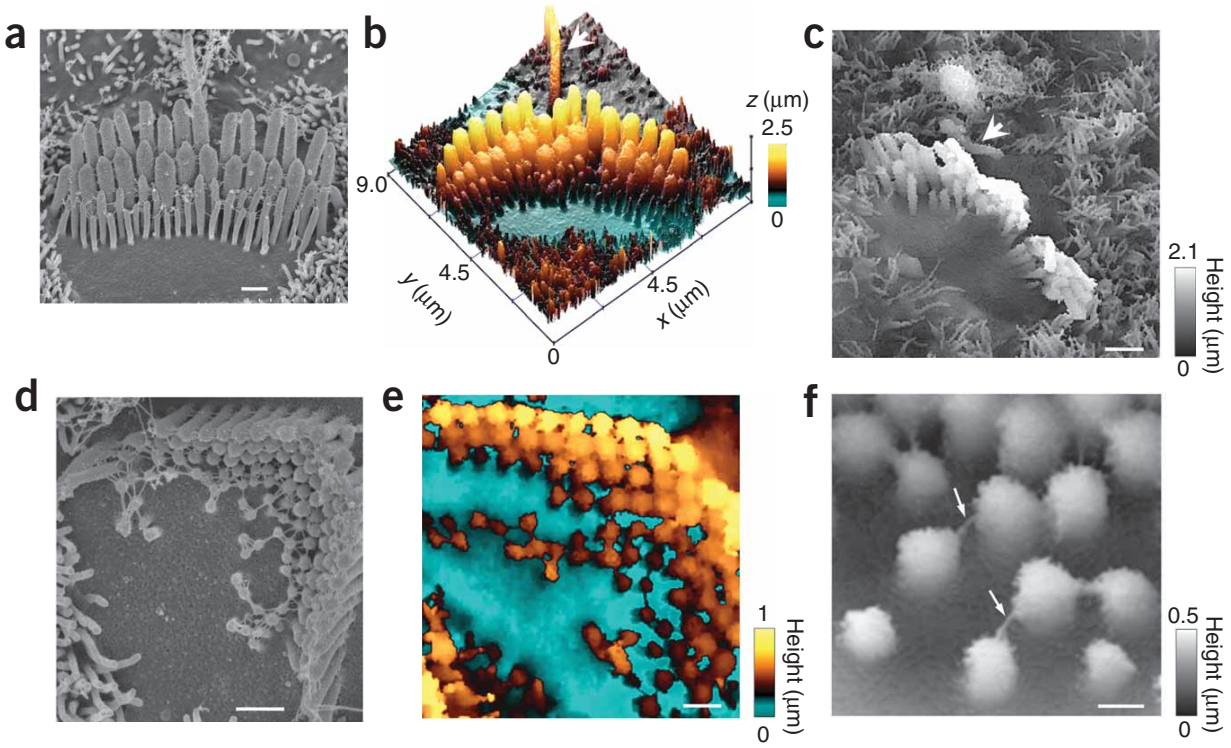

Figure 1.3: Topographic imaging of convoluted structures of stereocilia of inner and outer auditory hair cells. (a,d) Images obtained using scanning electron microscopy (SEM) with scale bars of 500 nm. (b, c, e, f) Images obtained using hopping–mode SICM, with arrows indicating (c) a kinocilium and (f) filaments interlinking stereocilia. Scale bars are 1 μm in (c), 500 nm in (e) and 200 nm in (f). Excerpted from [14].

the development of hopping mode in SICM, topographic imaging of a fairly complex morphology of cells became even more reliable than using DC and AC modes, as shown in Figure 1.3, although a certain amount of time resolution is sacrificed [14, 15]. Recently, Shevchuk and coworkers have managed to make the SICM setup angular-aligned, which can allow a simpler integration of SICM with a physiological patch–clamp system without further modification of the microscope, meaning that optical instruments with a better illumination, e.g. phase contrast, than a traditional SICM rig is possible [21]. The photo of their rig is shown in Figure 1.4.

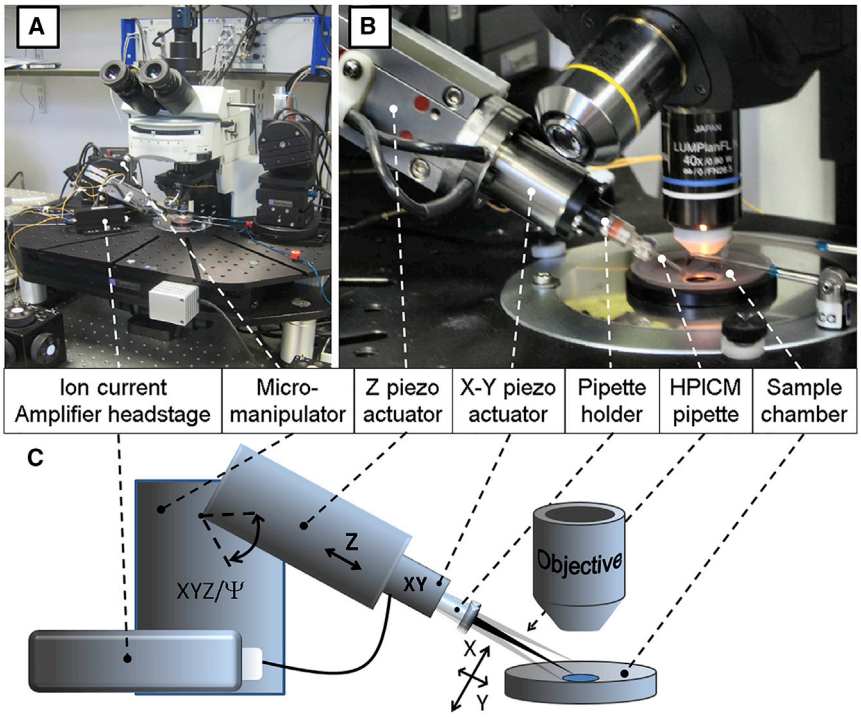

Figure 1.4: (A,B) Photographs of angular-aligned SICM installed on a microscope and (C) its schematic illustration, with an additional freedom of angular movement in the nanopipette, Ψ, compared with conventional SICM. Excerpted from [21].

1.6 Topographic investigations using SICM

1.6.1 Steady-state SICM in physiological conditions

Biochemical properties of live cells or the functions of an organ can usually be determined by topographic parameters, e.g. volume, and can be linked with morphological features in physiological conditions. Thus, SICM is a powerful and reliable tool for characterising the topography of samples without generating physical interference with their intrinsic biological behaviours, which is beneficial for solving different biological questions that have not yet been answered. Usually imaging at a high resolution, of below 100 nm takes roughly 30 minutes. In the early development of SICM, some studies focused on technical upgrading of the technique itself, and provided evidence that it was capable of being applied to various model cells. With the maturation of the technique, and more research groups being able to create an SICM setup, various techniques, such as fluorescent imaging of stained cells and physiological

patch–clamp techniques, have sometimes been applied separately to the sample in order to address different aspects of biological phenomena in a complementary way.

Novak and coworkers have successfully visualised the extremely complex topography of protruding stereocilia of auditory hair cells at a high aspect ratio [14], which is shown in Figure 1.3, as well as cell lines of MCF-7 (breast cancer), HeLa (cervical cancer), CHO (epithelial cell), myotubes in mouse myoblast cells (C2C12) and axons of a neuroblastic cell (PC12) [15] using a hopping-mode SICM. Differentiation and transdifferentiation in cancer cells usually decreases the effectiveness of therapies that are designed only to target a single specific subpopulation; therefore, Liu and coworkers have also used hopping-mode SICM to conduct pathology studies of all of three phenotypes in a live neuroblastoma SK-N-SH cell line. In their results, cell volume, cell height and surface roughness determined by microvilli morphology could be used to distinguish the difference between N-type, S-type and I-type subgroups [22]. A mature ventricular cardiomyocyte, i.e. a cardiac muscle cell, has grooved structures (Z-grooves) on its surface, and T-tubular invaginations under the sarcolemma, which couples the functioning of L-type calcium channels to the calcium release at sarcoplasmic reticulum. Gorelik and coworkers used SICM to obtain surface morphology to define a novel Z-groove index to characterise detubulation quantitatively, i.e. by flattening the Z-groove structures at the surface [23]. Lyon *et al*. further examine the healthy and failing hearts of humans and rats using SICM to confirm the profound alterations of T-tubule organisation, as shown in Figure 1.5. The loss of T-tubule openings and Z-grooves, which interfered with calcium signalling, represented one of the phenotypic changes in the failing human cardiomyocyte [24]. Topographic study could include both the biological samples and the surrounding environment if necessary. Behaviours of live cells are influenced by an extracellular matrix; topographic structures of underlying scaffolds comparable to the cell size could therefore interact with cell biochemical characteristics. Sun and coworkers took advantage of SICM results to investigate the morphological features of fibroblasts and cortical astrocytes on artificial poly-dimethylsiloxane (PDMS) membranes with periodic pores (100–350 μm in diameter) [25].

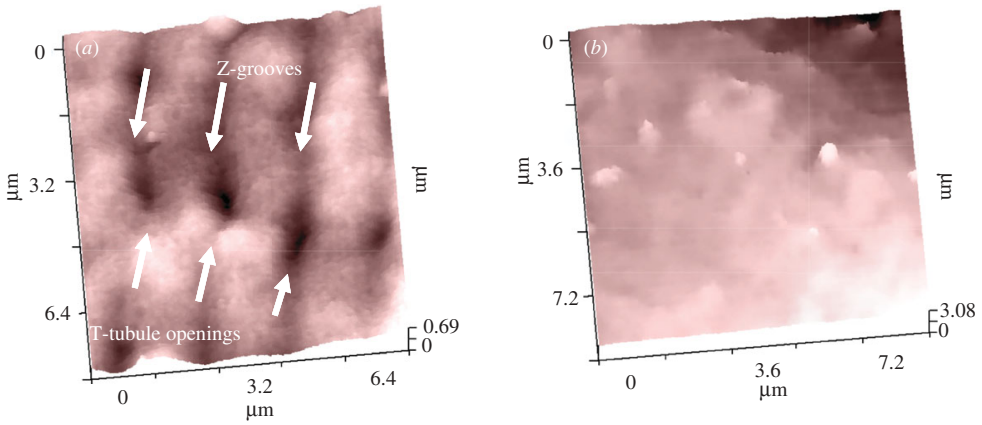

Figure 1.5: Topographic SICM scanning of cardiomyocytes in (a) healthy and (b) failing heart of humans. Arrows indicate subcellular features of Z-grooves and T-tubule openings on the healthy cell. Excerpted from [26].

1.6.2 Dynamic investigation of the whole or regions of cells

In addition to steady-state investigation, the methodology of SICM imaging has also been widely adopted for recording time-course behaviours of samples in recent studies. Dynamics of the whole cell or subcellular structure can be therefore resolved. Generally, degradation of the scanning resolution to an acceptable degree may be allowed if necessary to gain sufficiently high scanning speed for performing time-lapse imaging. By using SICM imaging over time, it was first observed by Korchev and coworkers that the microvillus structure (actin bundles) in the cell line (A6) of renal tubular cells protruded through its apical membrane during differentiation; ventricular myocytes showed the regulation of their volumes under external osmotic stress, which is a phenomenon that involved, like reperfusion and ischemia in the functioning of the heart; the T47D cell line of neoplastic breast cancer also demonstrated FGF2-induced protruding of microvillus structures, increasing membrane roughness significantly [20]. Similar regulation of volume according to changes in extracellular osmolarity to that discussed in [20] was also seen in hippocampal cells using a fast scan ($30\,\mu \times 30\,\mu$ in 2 min) [19, 27]. In addition, an A6 monolayer was observed to keep its permeability integrity by forming protective balloon-like structures at cell junctions when treated with hypertonic stress [28]. Live cells loosely fixed at the bottom of the glass dish tend to move or develop their growth cone with slightly limited freedom. Happel *et al.* observed natural movements

of oligodendrocytes from pig white matter loosely fixed on poly-L-lysine substrate as time passed [19, 29], and mature and immature oligodendrocytes had a migration velocity of 4.29 μm/h and 0.86 μm/h, respectively [27].

Evidence of the correlation between biological functions and cell morphology was shown in work by Gorelik and coworkers, who found morphological changes in microvilli on live epithelial cells (A6) in different life cycles in physiological conditions, in which a height-dependent formation that was stable but shorter with height-irrelevant retraction of microvilli took roughly 12 min in total to occur [30]. As shown in Figure 1.6, long time-scale (hrs) observation revealed the stretching and shrinking of A6 cells accompanied by the formation and deformation of the microvillus structure, respectively [30]. Other detailed subcellular structures of individual protein complexes on an acrosome-reacted boar spermatozoon were resolved and this made it possible to observe of the very fast diffusion of complexes that were not anchored to the cytoskeleton [31]. The inner diameter of this SICM nanopipette was approximately 12.5 nm and achieved a resolution of 3–6 nm with the help of two-dimensional fast Fourier transform (FFT), which is the highest SICM resolution at present [31].

1.6.3 Time-course imaging with extracellular stimulation

In addition to physiological conditions, it would be interesting to investigate the cell morphology in a steady or dynamic state when there exists physical (e.g. mechanical and electrical) or pharmaceutical stimulation. SICM was utilised for characterising volumetric parameters of soma and extensions of oligodendrocyte progenitor cells treated by inflammatory cytokine, which affected cell survival and differentiation, but corticosteroid was capable of reversing those morphological effects applied by cytokine [32]. Similarly when they were treated with a chemical stimulation, PC12 cells develope morphologically after three, six, or nine days during neuronal differentiation to be more nerve-like after being treated with nerve growth factor [33]. More studies using SICM with simultaneous chemical dosing in a bath solution or with a local application are introduced below. A pair of temporary exocytosis-induced surface dips on an adrenal chromaffin cell formed after stimulation of a high concentration

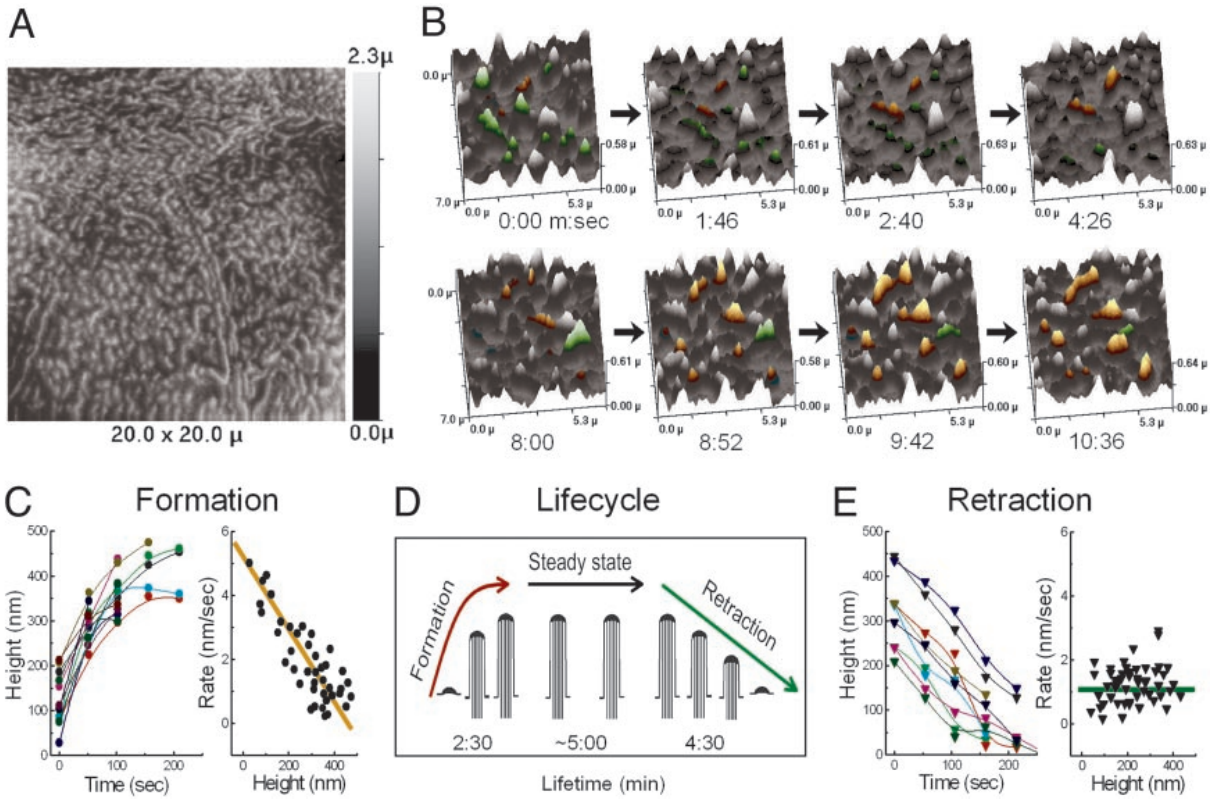

Figure 1.6: (A) Topographic imaging of microvilli in an A6 epithelial cell. (B) Time-course movements of individual microvilli in an observation window for 10 minutes. (C) Dynamics of the microvilli formation, with growth rates dependent on their heights. (D) Schematic diagram of the three-stage lifecycle of microvilli, including formation, steady state and retraction, over approximately 12 minutes in total. (E) Dynamics of the microvilli retraction, with retraction rates independent of their heights. Excerpted from [30].

of K^+ solution was imaged using SICM over a time-scale of minutes, and an increase of surface area (roughly 67%) after dips appeared was also estimated [34]. Time-course recordings using SICM revealed membrane damage of living human alveolar epithelial cells (A549) after they were exposed to 100 μg/mL of toxic zinc oxide nanoparticles [35] and 50–100 nm of amine-modified polystyrene latex nanoparticles [35] [36]. SICM also made it possible to study the morphological changes due to stimulated P2X4-like receptors mediating Na^+ channel activity caused by the addition of 2-methylthio-ATP to the basolateral side of A6 cells [37].

Cells that respond not only to pharmaceutical stimuli, but also to their biological functions are also significantly influenced by extracellular mechanical force. Ibrahim and cowork-

ers found that appropriate mechanical uploading could recover surface structures of Z-groove and T-tubule openings and improve Ca^{2+}-induced Ca^{2+} release (CICR), which is involved in the mechanism of contraction and relaxation of a cardiomyocyte [38]. In contrast, prolonged mechanical unloading, prolonged culture or osmotic shock with formamide in a healthy rat heart was likely to cause malfunctioning of the CICR interaction between the t-tubule and sarcoplasmic reticulum, which is also attributed to the disruption of surface morphology [23, 39]. Potter and coworkers have reported that porcine aortic endothelial cells (PAEC) isolated from descending thoracic aortas were aligned with the direction of artificially-applied pulsatile shear stress [40]. With the help of SICM, it was also found that at the edge of the dish wall (with directional and higher shear stress), cells showed phenotypic elongated morphology as endothelium at atheroprotected regions; whilst cells at the centre (with non-directional and low shear stress) exhibited morphology such as is exhibited by those at atheroprone regions, where aterosclerosis is inclined to happen [40, 41].

1.7 Hybrid system with SICM and other techniques

Topographic investigations of live cells using SICM are currently of great interest; however, information on morphology only is sometimes not enough to resolve complex biological mechanisms. Thus, researchers have put effort into combining other mature techniques that have been broadly used in biological experiments with SICM, e.g. the physiological patch–clamp technique, fluorescent imaging and electrochemical analysis, in order to obtain spatially functional mapping. In the following subsections, various important hybrid systems with SICM will be introduced.

1.7.1 SICM–patch-clamp hybrid technique

The Patch–clamp technique is an important electrophysiological tool that takes advantage of the glass pipette, which can resolve single-channel conductance with a high temporal resolution by the opening of one or more sets of ionic channels distributed on an individual cell

membrane. It was developed by Sakmann and Neher in the late 1970s [42], and is mainly used for the investigation on the networks of excitable cells, for example, neurons and cardiomyocyte cells. Before measurement, a tight contact (patch) between the pipette tip and the cell membrane should be formed (a gigaohm seal) by the application of suction from the back of the pipette, so only intracellular ions can flow through the aperture. The ion current responding to the applied stimulation through the electrically-isolated patch is at the level of tens to hundreds of picoamperes and can be recorded by a specialised electronic amplifier. This recording configuration is termed cell-attached recording. If another means of strong suction is applied to rupture the membrane patch, leading to a continuous connection between the pipette's inner surface and the cell cytoplasm, it is called whole-cell recording. This is frequently used to study electrical signals from the entire cell. The other two operation modes are inside-out and outside-out recordings, which are utilised to examine the characteristics of single-channel currents in different intracellular and extracellular chemical environments, respectively.

However, the disadvantage of the patch–clamp technique is that it lacks the ability to determine where the patch really is located in subcellular structures, if the probing region is smaller than the optical resolution of the microscopic objectives. Therefore, the combination of SICM and patch–clamp analysis provides precise positioning of the recorded channels. Korchev and coworkers were the first to adopt a pair of nanopipettes, with one applying whole-cell voltage clamping to a single cell to monitor its response to whole activated ion channels, and the other conducting simultaneous localised nanodosing at each component of the cell using SICM, as shown in Figure 1.7. When appropriate solution compositions in the bath solution and in the nanopipette were chosen, their results exhibited successful mapping of ATP-regulated K^+ channels in cardiomyocytes, which were located in the Z-grooves of the sarcolemma and tended to cluster together in several small groups [43].

Alternatively, in the technique using a single nanopipette, the same nanopipette is first utilised for SICM to obtain high-resolution imaging of cell topography, with digital information from the image saved during the scan and providing the later-stage nanopipette

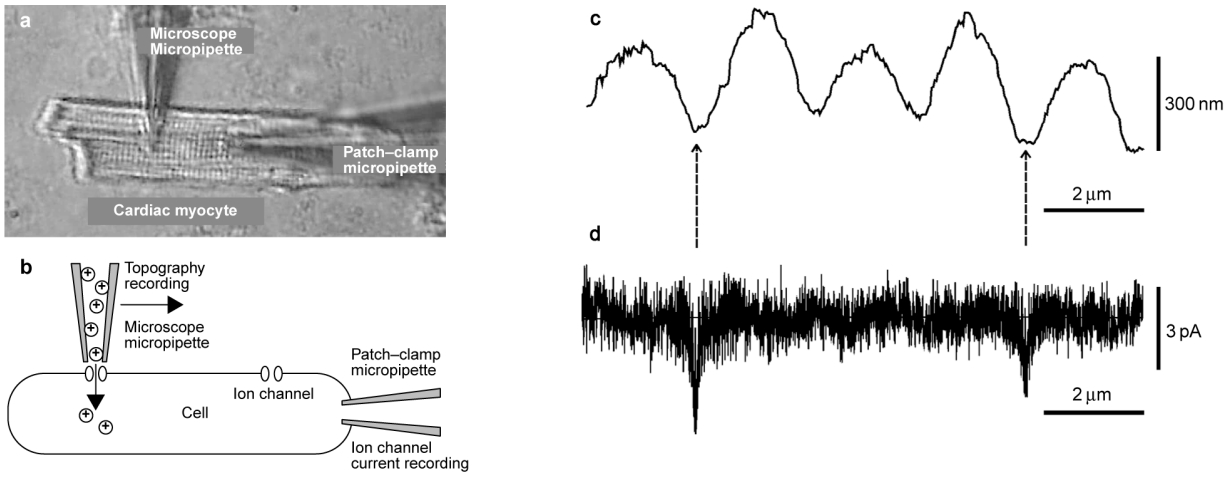

Figure 1.7: (a) Microscopic observation of a patched cardiac myocyte with an SICM nanopipette situated right above it. (b) Schematic illustration of (a) explains how this two-pipette patchclamp technique determines the surface distribution of a specific kind of ion channel. (c) Topographic features of sarcolemma and (d) corresponding integrated current recording of K_{ATP} channels. Arrows indicate subcellular locations of individual K_{ATP} channels on sarcolemma of cardiac myocytes. Excerpted from [43].

positioning for cell patching (cell-attached mode) with nanoscale precision. Gu and coworkers first used this technique to study precisely the single-channel response on Z-grooves, T-tubule openings and scallop crests on cardiomyocyte sarcolemma, revealing the spatial distribution of three different Cl^- channels in either Z-grooves or T-tubule openings, whilst a voltage-gated L-type Ca^{2+} channel in the T-tubule region controlled action potential propagation through sarcomeres [44]. Gorelik *et al.* have further demonstrated that this method is capable of conducting ion channel recordings in a small cell and subcellular structure, such as in sea urchin spermatozoa and neurite junctions on superior cervical ganglion neurons [45]. Based on the technique termed the scanning patch–clamp or smart patch–clamp method performed in the cell-attached mode, the functional distribution of voltage-dependent sodium channels and tetrodotoxin-sensitive channels [46], maxi-anion channels [47] and protein kinase A-dependent Cl^- channels [48] were determined on ventricular cardiomyocytes. However, a nanopipette with a small aperture diameter of roughly 100 MΩ used to obtain high-resolution imaging is merely suitable for single-channel recordings using the patch–clamp method. To overcome this limitation, Novak and coworkers developed a method to widen the nanopipette tip reliably to less than 50 MΩ. As shown in Figure 1.8, the experimental

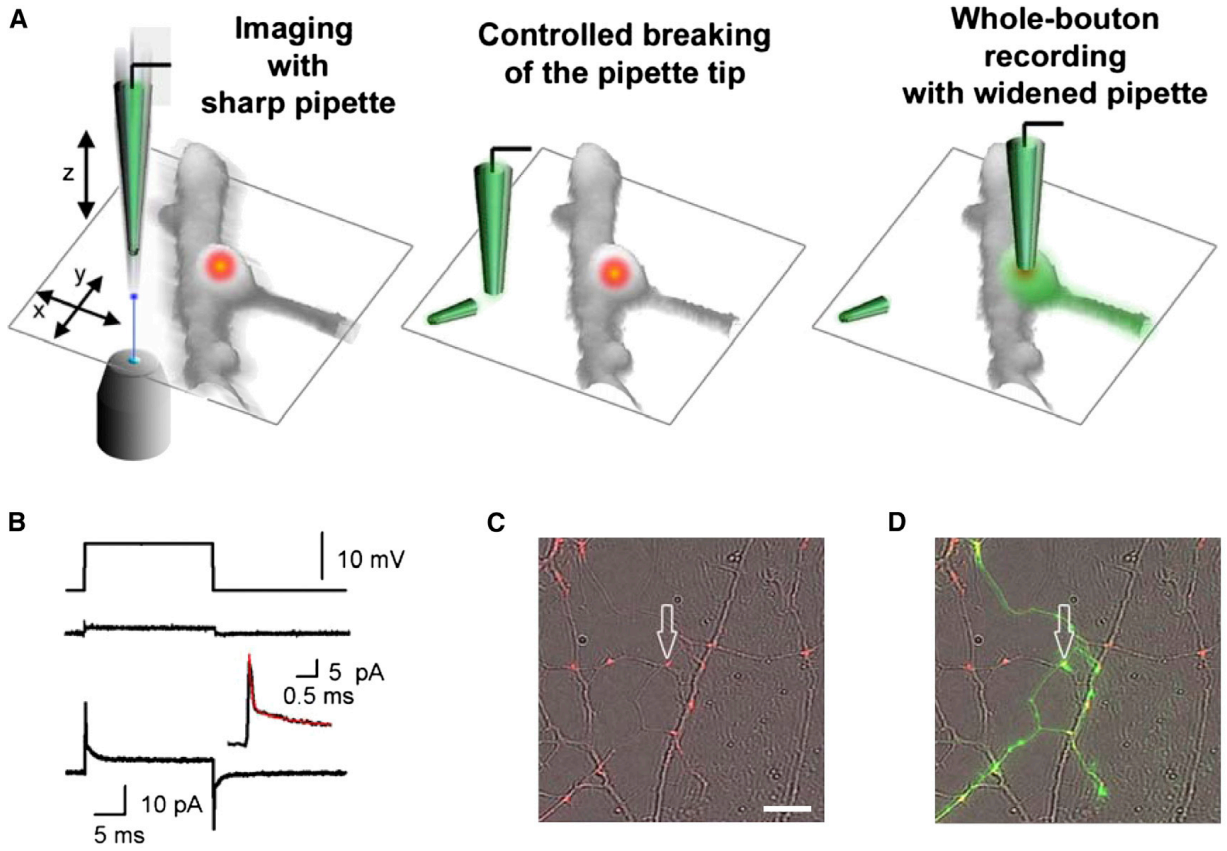

Figure 1.8: (A) Schematic illustration describes procedures of smart-clamp technique to perform a subcellular whole-cell recording. (B) Characteristic voltage-clamp traces before and after the realisation of the whole-cell stage. (C) Overlay of the fluorescent image of FM1-43-labelled boutons and the corresponding bright-filled image, with a scale bar of 10 μm, and (D) the same overlaid images after the rupture of the cell membrane using a widened nanopipette loaded with Alexa Fluor 488. Excerpted from [49].

protocol is as follows: (1) surface topography with a nanoscale resolution is first obtained by SICM with a sharp nanopipette tip; (2) the nanopipette is widened using an automated system with the same setup; (3) the predefined three-dimensional coordinates used in SICM are used for the whole-cell analysis. K^+, Na^+, Cl^- and Ca^{2+} channels at presynaptic terminals in cultured hippocampal neurons were determined, and four operation modes of traditional patch–clamp method were successfully demonstrated [49].

1.7.2 SICM–fluorescence hybrid technique

Fluorescence microscopy is a mature method to observe time-resolved behaviours of dye-labelled whole cells or subcellular structures, which are laser-excited and can be simply acquired on a conventional microscopy without further modification. Various forms of high-resolution imaging overcoming the differential limit have been developed, including scanning near-field optical microscopy (SNOM) [50], laser scanning confocal microscopy (LSCM) [51] and super-resolution image reconstruction [52]. Some of these most advanced optical methods are also combined with SICM to obtain a complementary functional image.

SICM–FRET method

The sensor, Epac2-camps, is designed to detect the optical signal of cyclic adenosine monophosphate (cAMP)-induced Förster resonance energy transfer (FRET). Epac2-camps is composed of a pair of a yellow fluorescent protein (YFP) and a cyan fluorescent protein (CFP), and its conformation, i.e. the distance between YFP and CFP, will change when a cAMP molecule is combined with it. Viacheslav and coworkers have used this FRET microscopy coupled with SICM to determine the distribution of β_1- and β_2-adrenergic receptors (βARs) on cardiomyocytes, which are correlated with heterotrimeric guanine nucleotide-binding proteins to produce cytosolic second messenger cAMP. They found that in failing hearts of rats, (β_2ARs) were relocated from T-tubules to crests in sarcomeres and caused diffusive cAMP distribution [53].

SICM–SSCM method

Scanning surface confocal microscopy (SSCM) is the combination of LSCM and SICM [54, 55]. LSCM is an imaging technique which can effectively increase spatial resolution using a monochromatic laser light source, with small apertures arranged carefully to filter out unfocused reflecting light. SSCM inherits the merits of LSCM—high optical resolution and high signal-to-noise ratio. As shown in Figure 1.9, the confocal volume is always set just

below the tip of the nanopipette by a computer-controlled platform to obtain a topography-correlated distribution of fluorescently-labelled species. In addition, the laser is designed to be only turned on right after information on ion current and nanopipette positions has been collected at a probing point using hopping mode, so the photobleaching of fluorophores can be minimised. Using this technique with a resolution capable of imaging individual fluorescent particles on the cell surface, interactions between the cell plasma membrane and extracellular molecules can be visualised. Gorelik and coworkers utilised SSCM to recorded the initial stages of endocytic pathways of fluorescently-labelled virus-like particles (VLPs) being absorbed into live monkey COS 7 cells through a plasma membrane [56, 57], and an alternative closure mechanism of clathrin-coated endocytic pits that had not previously been reported [58]. Clarke and coworkers also used SSCM images to accertain the ratio of VLPs among all of the virus preparation particles used in the Poisson model so that neutralization curves of the Herpes simplex virus could be successfully fitted [59]. Shevchuk and coworkers also used LSCM (with performing scanning) so that the cell height of contracting cardiac myocyte and the local calcium concentration just below the plasma membrane could be simultaneously recorded [11].

SICM–SNOM method

SNOM is another alternative method to realise high-resolution optical imaging. It involves evanescent electromagnetic waves being focused through an aperture and interacting with a nanoscale region, termed near-field optics; therefore, it circumvents the diffraction limit of light to achieve high-resolution imaging. SICM provides an appropriate platform to incorporate SNOM, as long as the light source can be guided stably through the aperture of the nanopipette tip. Korchev and coworkers were the first to introduce SNOM into an SICM setup, using a 532 nm laser guided from the back of a nanopipette coated with 100–150 nm of aluminium via a multimode optical fibre, and transmission light was finally collected by a photomultiplier tube. They demonstrated near-field imaging of cardiomyocyte sarcomeres to have alternating bright and dark stripes due to the periodic structures of Z-lines and

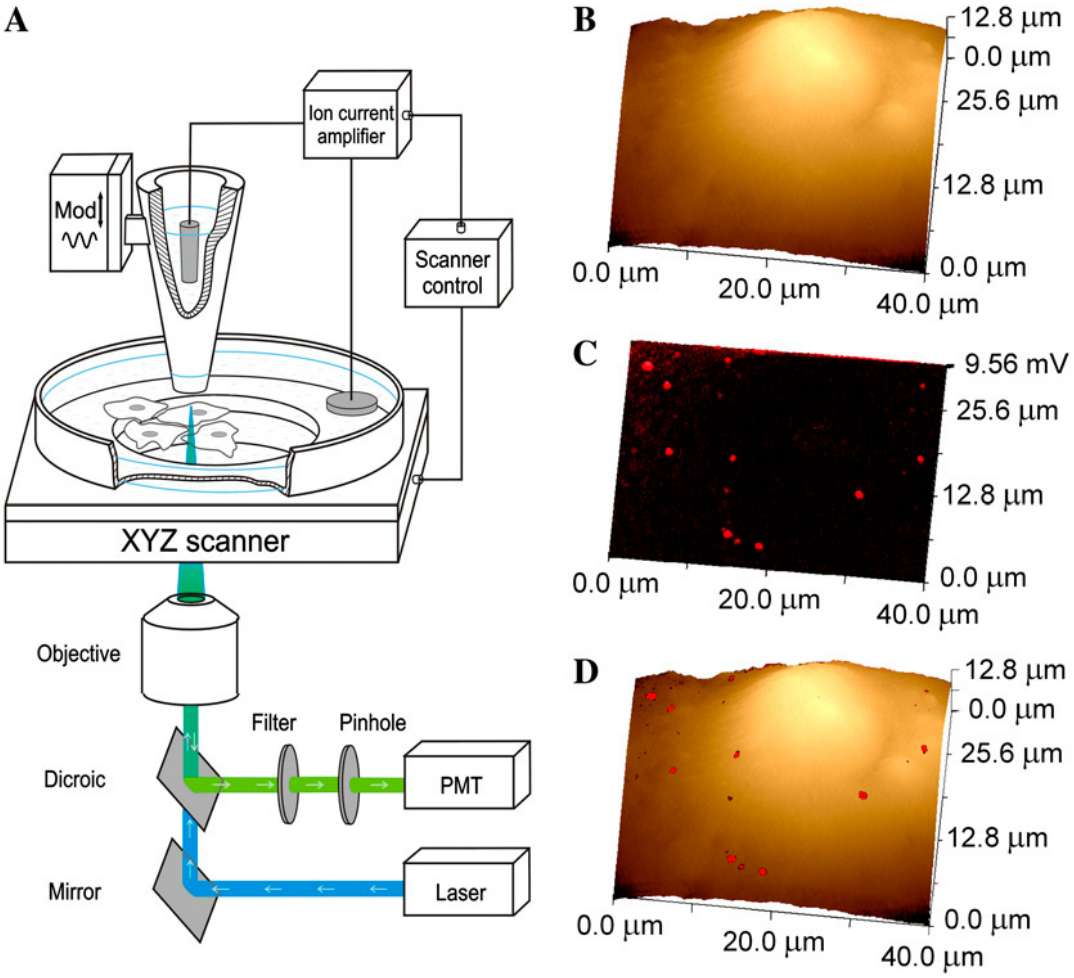

Figure 1.9: (A) Schematic illustration of scanning surface confocal microscopy (SSCM), in which the confocal volume of a laser focused underneath via an objective is located under the tip of a nanopipette in order to record simultaneously a topographic profile of the sample and its surface distribution of intracellularly-labelled fluorescent dyes. (B) Topographic imaging of a COS7 cell. (C) Corresponding surface distribution of Cy5-labelled virus-like particles (VLPs) obtained at the same time as (B). (D) An overlay image of (B) and (C). Excerpted from [57].

Z-grooves [11, 60]. Rothery and coworkers established a novel light source using the fluorescent interaction of an activated calcium indicator (fluo-3) on an uncoated nanopipette tip, which improved the transmission efficiency of light and could therefore increase the scanning resolution [61].

SICM–TERS method

It is also worth noting that tip-enhanced Raman scattering (TERS) is an alternative method for near-field optics that does not use complex nanostructures as the substrate, like nanoparticle-on-mirror (NPoM). It would be interesting to conduct scanning TERS via an aluminium-coated nanopipette in biological applications, which ought to have the same configuration as SICM/SNOM. Its resolution could potentially be as high as tens of nm. To the best of my knowledge, there have been no papers about SICM/TERS reported.

1.7.3 SICM–SECM hybrid technique

SECM method

Scanning electrochemical microscopy (SECM) is a technique to detect electrochemical processes based on a similar concept to SICM. A ultramicroelectrode (UME), a counterpart to the nanopipette in SICM, is used in SECM to approach to a specimen in order to detect the electrochemical response on the substrate surface with the cofunctioning of redox mediative species, where Faradaic current through the UME is formed via a redox mediator between the tip and the substrate. Therefore, the kinetics of electron and mass transfers at various kinds of interfaces in an electrochemical cell can be quantitatively recorded. A typical UME utilises platinum or carbon as the material for a conductive wire, which is sealed by an insulating sheath and is then polished to expose its disc-shaped cross section. If the size of the tip cross section is on a nanoscale, the relationship between the UME current and potential will demonstrate a diffusion-controlled sigmoidal curve.

The UME approach response curve when an inert insulating or a conductive substrate electrode is involved exhibits different feedback modes, because redox species are depleted near an insulator (negative mode) and can be regenerated close to the conductor (positive mode). Therefore, information about rate constant of a specific redox reaction at a local area on the substrate electrode and height of UME is obtained, where potentiostat, i.e. voltage clamping, and cyclic voltammograms (CV) are usually conducted. Note that the height of

the tip should be maintained at less than 10 times of the diameter of UME for performing feedback-mode electrochemistry [62]. For applications in biological samples, which are intrinsically insulating, the substrate generation/tip collection mode is often utilised. Concentration and flux of targeted redox chemical species generated from a biological sample fixed on a glass dish bottom may be mapped using SECM. In contrast, the mechanism of tip generation/substrate collection mode is exactly reversed, with redox species generated at the tip and collected by an insulating or conductive substrate electrode with a distance of approximately the diffusion layer from the tip [62]. In addition, surface interrogation mode can quantitatively analyse adsorbed species generated at a biased substrate electrode by recording their transient Faradaic current in an electrochemical cell [63]. On a biological sample fixed on an insulating substrate, the Faradaic current formed by the mediator flux at the tip will be hindered with the approach to the substrate, so it can be used as a feedback signal for the SECM imaging system, where the control of the vertical scanning direction by a piezoelectric actuator is designed following the same concept as in SICM. The spatial resolution and sensitivity of SECM are decided by the tip diameter and the distance between the tip and substrate.

SICM–SECM single-barrel method

The integration of SICM and SECM has also been developed to collect simultaneously the topography and redox activity of the target surface. SICM can provide a convenient and robust way to keep the tip at a constant height from a convoluted substrate. In addition, it may more easily be introduced together with SECM than other methods for height-regulation, e.g. shear-force mode [64] and AFM [65]. In principle two types of processed nanopipettes have been adopted in conduction SICM–SECM imaging. One of these replaces the traditional UME with a modified single-barrel nanopipette with concentric coating layers of a nanoring electrode and an insulating film at the tip [66–69]. Demonstrations of functional mapping correlated with topographic information were carried out on fixed enzyme spots (horse radish peroxidase (HRP) and glucose oxidase (GOD)) and single live A6 cells, superior

cervical ganglion (SCG) cells and cardiomyocytes [66]. Sequential degradation of artificial membrane Nafion 212 by Fenton's reaction was also studied with this single-barrel type of SICM/SECM probe [69]. Morris and coworkers established a similar SICM/SECM probe but with only one half of the nanopipette coated with gold layers to detect redox reactions. It is worth noting that this method has the advantage that a maximum forty probes can be fabricated at one time [70]. They also managed to deposit a polyaniline (PANI) film on the gold layer using cyclic voltammetry to turn the original probe into a pH sensor for pH 2.5–12 [71]. However, its fabrication process is rather complex, including atomic layer deposition [67], sputtering followed by electrophoretic deposition [66], thermal deposition [70, 71] or vacuum evaporation followed by electrophoretic deposition [68]. Before measurement, this modified tip may experience focused ion beam milling in order to ensure appropriate exposure of the detection parts.

On the other hand, Takahashi and coworkers used a carbon-deposited single-barrel nanopipette to trace topography biased at –500 mV, as shown in Figure 1.10(a), when the redox mediator flux is hindered at the insulating substrate (negative feedback mode), and then to measure Faradaic current at each setpoint of the hopping mode by switching the bias voltage to be positive. This method was verified by imaging epidermal growth factor receptors on A431 cells and by time-course monitoring of neurotransmitters released from rat hippocampal neurons after whole cell stimulation of K^+ [72].

SICM–SECM double-barrel method

Alternatively, a simple method of depositing pyrolytic graphite as a conductive electrode in one of the channels in a double-barrel nanopipette was established by Takahashi and coworkers, as shown in Figure 1.10(b) [73]. To simplify the fabrication method, an easier way to combine SICM and SECM is to use a double-barrel nanopipette allowing carbon to be deposited in one of the barrels by the pyrolytic decomposition of butane. Thus, SICM and SECM imaging are carried out in the separate barrels. A successful high-resolution topographic imaging was obtained using this double-barrel SICM/SECM probe, and K^+ was

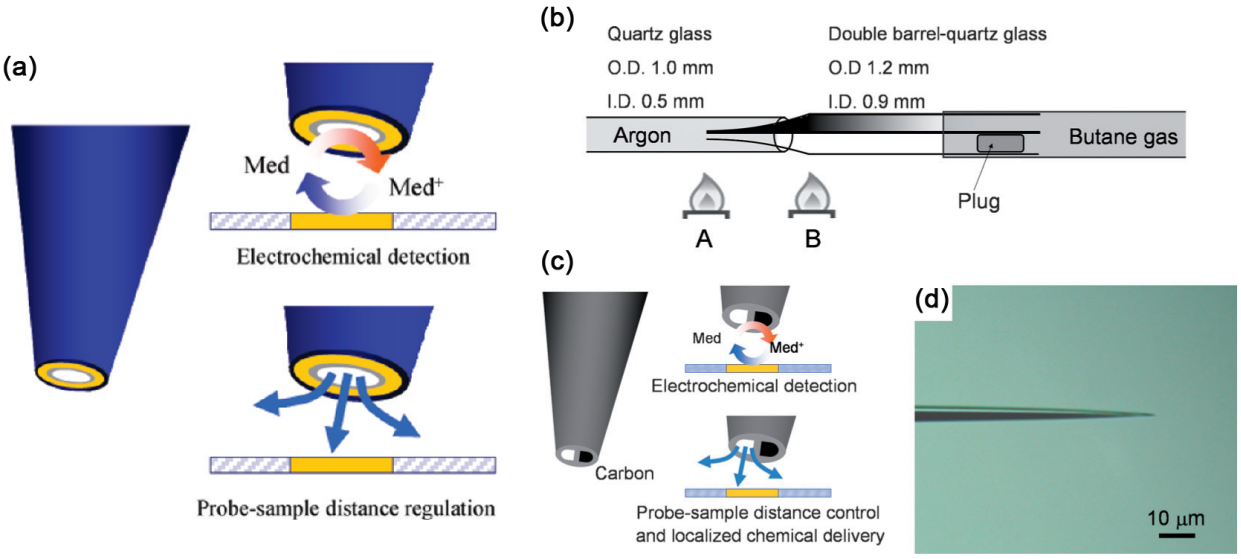

Figure 1.10: (a) A nanopipette with concentric coating layers on the tip to create a nanoring-shaped electrode (yellow) and an external insulating envelope (blue) in order to conduct electrochemical mapping of the sample correlated with its topographic information at the same time. (b) Schematic illustration of a relatively simple method to produce a pyrolytically-coated graphite channel in a double-barrel nanopipette. (c) An alternative method to perform simultaneous topographic and electrochemical mapping of the substrate. (d) A photograph demonstrates this double-barrel SICM–SECM probe. Excerpted from [66, 73].

locally delivered via the SICM channel onto a PC12 cell; at the same time the neurotransmitter released from the cell was detected by the SECM electrode at the other channel [73]. The sensitivity of the carbon-filled channel in a SICM/SECM probe can be greatly improved by additional platinum modification [74–76]. O'Connell and coworkers used the same double-barrel SICM/SECM probe with and without the addition of a platinised SECM carbon probe to mapping electrochemically the catalytic activity on Pt and gold nanostructures, respectively [75]. Thus, oxygen consumption on Pt nanoparticles [75] and hydrogen peroxide generated on Au nanoparticles were separately observed on a single nanoparticle level [76]. Nadappuram and coworkers used a similar strategy to electrodeposit hydrous iridium oxide on the carbon electrode of an SICM/SECM probe to gain pH sensitivity (pH 2–10). The pH mapping experiment was demonstrated on a calcite microcrystal, whose dissolution in water increases the surrounding pH [77]. With the same configuration of double-barrel nanopipette, the SICM channel can be used to deliver a redox mediator in order to map the concentration and flux of this molecule and the uptake rate of the live cell underneath the

probe [78].

Some other modifications of the double-barrel SICM/SECM probe for novel applications are listed below. McKelvey and coworkers pyrolytically deposit carbon in both channels of a double-barrel nanopipette to generate a probe conducting generation/collection mode between two carbon-filled openings separated by the septum [79]. Zhou and coworkers used a double-barrel nanopipette termed a potentiometric SICM (P–SICM), with one channel responsible for SICM topographic scanning and a second one for potential measurement, to characterise the potential difference across an artificial membrane with poles [80] and measure paracellular transport conductance on canine epithelial kidney cells [81, 82].

SECCM method

Single- or double-barrel SICM/SECM probes provide useful information correlating to topography and electrocatalytic reactions simultaneously. Although a miniaturised probe tip may significantly increase the spatial resolution of SECM, this is intrinsically limited by the large volume of liquid bath solution around the sample and the probe, because the diffusion mechanism of reacted redox mediators detected by the probe tip may not be influenced by surrounding areas outside the detection site underneath the probe tip.

Scanning electrochemical cell microscopy (SECCM), was developed by the research group of Professor Patrick R. Unwin [83–85], and it allows SECM to be deployed on a substrate in a dry environment, i.e. without the need for a bath solution containing redox mediators. Instead, as shown in Figure 1.11, the filling electrolyte in both of the channels in a double-barrel nanopipette already contains the desired redox mediator, and at the tip of the double-barrel nanopipette, a liquid meniscus with a precise size is established naturally due to surface tension, with the ion current formed under the voltage application across the Ag/AgCl electrodes in two barrels. The magnitude of the ion current is affected by the shape of the meniscus when in contact with the substrate, which can be used as a feedback signal to maintain the probe tip at constant height ($\sim$150 nm) in order to realise functional mapping; this system containing a pair of electrodes (one of them as the quasi-reference electrode) and

a confined volume of electrolyte touching the conductive or semiconductive sample surface (as the working electrode) is treated as a tiny electrochemical cell. The advantage of this technique is that the interfacial electrochemistry of a dry sample surface may be investigated, which minimises any negative influences from the electrolyte on the sample surface.

SECCM has recently been developed that can be performed with a single- [86, 87] or a quad-barrel probe, in addition to double-barrel methods, and these have been adopted for characterising (semi)conductive nanomaterials [88]. In a quad-barrel probe, a pair of opposing channels is filled with pyrolytic carbon, and the other two with suitable electrolyte. This probe can be used on insulating, semiconductive and conductive substrates with ∼100% collection rate for reactive redox species [88]. The position of SECCM probes is modulated with an AC signal to generate an AC component in the ion current, which is highly sensitive to any variation in the meniscus shape; therefore, the meniscus can maintain an equal volume during the scanning, when fluctuation of the AC component is taken as the feedback signal for controlling the probe height. In addition to raster scanning mode, a spiral scanning pattern was applied to achieve an ultrafast frame rate: 1000 pixels μm^{-2} every 4 s, as shown in Figure 1.11 [89, 90].

1.8 Other applications for a nanopipette

1.8.1 Mechanical stimulation via a nanopipette

An SICM nanopipette can be used to apply local mechanical stress on a targeted cell via a solution jet. It is a tool that can investigate how live cells respond to mechanical stimulus from their environment and how they convert the stress into intracellular signals. Thus, compliance of endothelial cells from different parts of the aorta after the treatment of various patterns of shear stress was characterised with a nanopipette applying 30–40 kPa [41]. Sánchez and coworkers also used a nanopipette to apply non-contact mechanical stimulation onto roughly 0.385 μm^2 of a dendrite of human and rat dorsal root ganglia sensory neurons.

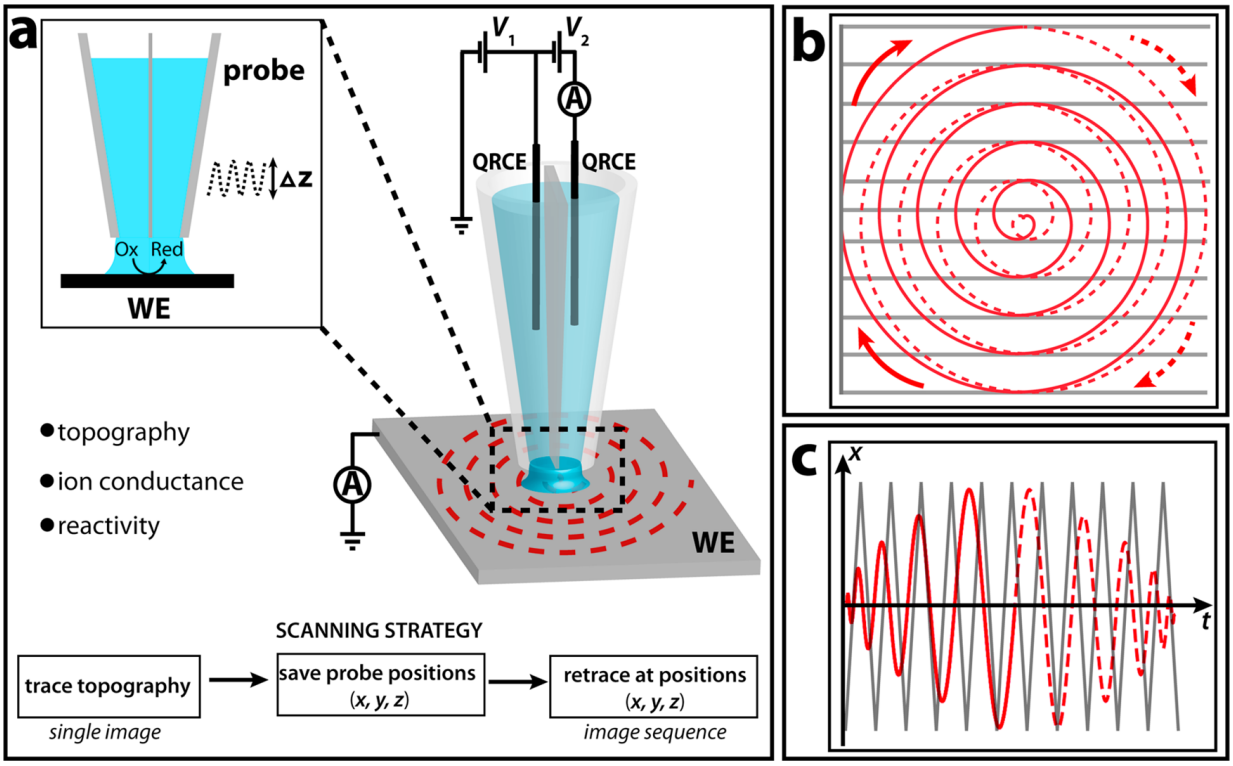

Figure 1.11: (a) Schematic illustration of scanning electrochemical cell microscopy (SECCM), which is capable of conducting dry scanning, i.e. without a liquid bath solution, on a conductive substrate referred to as a working electrode. This technique is able to obtain information on topography and redox reactivity on the substrate simultaneously. (b) The fast scanning method with a spiral pattern. Solid and dashed lines indicate trace and retrace trajectories, respectively. (c) X-axis positions of the tip during spiral-mode fast scanning. Excerpted from [89].

At the same time whole-cell recording using the physiological patch–clamp technique or Ca^{2+} imaging was conducted on the sample to monitor how these activated mechanosensitive ion channels influenced biochemical signalling in the whole cell; therefore the topographic distribution of mechanosensitive ion channels was investigated [91]. In addition, hydrostatic mechanical pressure (0.1–150 kPa) applied through the nanopipette tip can be adjusted to be positive or negative via tubing and a syringe, and it was quantitatively calibrated by applying force from an AFM cantilever that caused it to be bent [92, 93]. Recently, Miragoli and coworkers applied mechanical stimulation via a nanopipette on a sarcolemma to investigate calcium propagation in healthy and arrhythmogenic hearts [94]. Such a method was extended to perform stiffness mapping at a sub-100 nm resolution using pure colloidal pressure [95] between the nanopipette tip and substrate, revealing structures underlying the plasma

membrane that cannot be seen, e.g. the cytoskeleton, using conventional topographic imaging [96]. Pellegrino and coworkers also utilised this weak mechanical interaction between the current at the tip of the nanopipette at decrease criterion $\geq$5% to perturb the development direction of growth cones on neurons, although this guiding mechanism, which is probably related to the hydrostatic force has not been fully understood [97, 98].

1.8.2 Localised trapping, dosing and deposition of molecules

Localised trapping and dosing of molecules

Due to the tapered shape of a nanopipette, a high electric field ($10^6\,\mathrm{Vm}^{-1}$) can be generated and localised at the tip [99]. Thus, local nanodosing can be achieved by suitable pressure and/or voltage application to the electrode inserted in the nanopipette and to that in the bath in order to adjust the non-equilibrium forces on charged species induced by electroosmotic, electrophoretic and dielectrophoresis flows [100]. Depending on the different amounts of charges carried on various particles, they can be trapped at the interior of the tip or delivered through its opening.

For instance, the delivery of DNA and antibodies can be finely controlled by each voltage pulse via a nanopipette, and still keep their original functionality [101, 102] and trapped during the negative half cycle of an AC signal with frequency lower than 1 Hz [103]. The amount of DNA being delivered, which can be controlled by surface modification, the tapered angle and the value of bias voltage, was estimated by single-molecule detection. This delivery technique was extended for local dosing of water-soluble reagents, e.g. sodium and hydroxide ions [104], TRPV1 agonist capsaicin at a single sensory neuron [105] or fluorescent dye, Atto 647-WGA, onto a spermatozoa to study the dynamics of Atto 647-WGA molecules deposited at various acrosomal regions [106]. Also, roughly 100 attolitres of enzyme can be trapped at the tip without surface modification to act on targeted substrate molecules; therefore, it becomes a nanoreactor as long as its enzymatic production can be quantitatively analysed. For example, alkaline phosphatase was constrained at the pipette tip and catalyse fluorescein

diphosphate in the pipette, whilst the fluorescence of its product, fluorescein, was collected and detected by an avalanche photodiode [107]. The number of dosed molecules being driven out of the nanopipette by the application of voltage and pressure can be approximated by hydrodynamic modelling and physical simulation [108]. This method was utilised by Drews and coworkers to evaluate the toxicity of oligomers of amyloid beta, which is probably the cause of Alzheimer's Disease, to neuronal cells and test the effectiveness of antibodies to block abnormal calcium homeostasis induced by oligomers of amyloid beta right at the initial stage [109].

A novel method enables delivery even at attolitre level, which is a precision that could not be achieved using previous systems in which voltage and/or pressure are applied to drive molecules out of the nanopipette. Laforge and coworkers introduced an interface between the tip aperture and the bath electrolyte, i.e. organic phase was loaded in the nanopipette. Fine adjustment of applied voltage in the nanopipette modified the surface tension, and therefore the liquid/liquid interface can be shifted to eject the loaded molecules or collect molecules in the bath solution [110]. Actis *et al* used this electrowetting concept to penetrate the tip of the nanopipette filled with organic phase into the cell membranes of human fibroblasts and collect mitochondrial DNA for next-stage DNA sequencing [111]. As the SICM–patch–clamp hybrid technique uses the same nanopipette for topographic mapping and detection, Nashimoto and coworkers first used a similar approach to obtain a high resolution surface scanning of a breast cancer cell (cell line MCF-7) using the SICM channel, and then a small amount of cytosol (500–1000 fL) was collected after puncturing into the cell at a specific position using the other organic-phase channel for quantitative analysis of mRNA at a later-stage [112].

Molecular deposition

By using programmed nanopipette movement for localised dosing, a reagent loaded in a single- or double-barrel nanopipette can be deposited to produce complex patterns on the substrate, taking advantage of the mechanism of electrowetting to drive molecules out of the

nanopipette in a precise way. In a double-barrel nanopipette system, one or two kinds of molecules, and therefore, potentially, a combination of two colours, can be delivered to form designed point patterning [113, 114] or even to draw complicated paintings composed of multiple points[115]. Furthermore, line pattering is possible under refined electro-oxidative control using various materials, for instance, PANI on a gold surface [116], dopamine on a highly orientated pyrolytic graphite (HOPG) [117], and N-hydroxyethyl acrylamide (poly(HEAA)) films on a gold surface functionalised with bis-[2-(2-bromoisobutyryloxy)ethyl] disulfide [118]. Ultimately, using a similar strategy with additional monitoring of the z-axis deposition, successful 3-dimensional printing was also reported, with copper deposited on a gold or platinum substrate electrode, which is a breakthrough for bottom-up nanotechnology [119, 120].

1.8.3 Local detection using a tip-modified biosensor

Artificial ion-channel biosensor

The tip of a nanopipette can be modified by attaching a layer of artificially-made membrane with embedded receptors for detecting specific ions. Bright and coworkers were the first to study the properties of a suspended lipid membrane, or black lipid membranes, BLMs, formed across the opening aperture at a silanised nanopipette by dimethylchlorosilane (PFDCS) [121], and then single or multiple protein channel α-hemolysin (α-HL), which is remarkably stable and has an inner diameter allowing a single-stranded nucleic acid to pass through, were incorporated at the BLMs [122]. Based on a similar concept, Macazo and coworkers also utilised (α-HL)-incorporated BLMs at a nanopipette tip that was not chemically-treated beforehand to detect β-cyclodextrin (βCD) diffused from a glass micropore substrate below the tip [123]. Note that α-HL is not a ligand-gated protein channel, so it would be useful if a channel responding only to a specific ligand were used for nanopore biosensing.

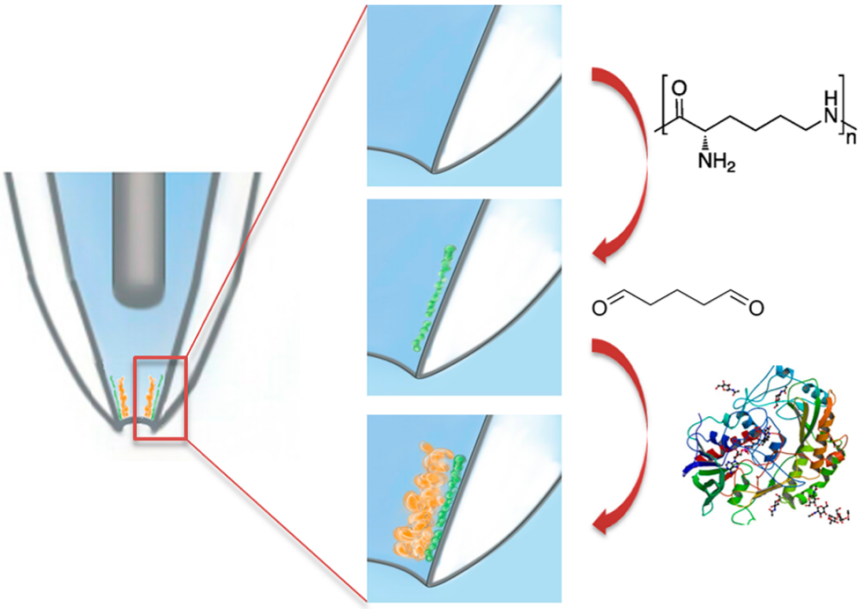

Figure 1.12: Schematic illustration of the surface-modified tip of a nanopipette performing glucose sensing, with PLL, glutaraldehyde and glucose oxidase fixed on the interior of the tip in stages. Excerpted from [130].

Chemically-functionalised biosensor

The inner wall surface of the nanopipette tip can be modified to respond either electrostatically or ligand-receptor-interactively to targeted species in the bath solution, so the flux of ions is influenced by this local treatment to exhibit rectified characteristics of ion current. For a proof of concept, demonstrations of electrostatic rectification were made by coating poly-L-lysine (PLL) [124, 125] or polyacrylic acid (PAA) at the interior of the tip; and rectified current behaviour was also observed by Biotin–Streptavidin and antigen–antibody recognitions at the internal part of the tip [125]. The same research group has extended the investigation of such current rectification, termed signal transduction by ion nanogating (STING) via the inner side of a nanopipette coated with CaM1 or silanised CaM2 for sensing Ca^{2+} [126], aptamer for Thrombin [127], Chitosan and PAA multilayers for Cu^{2+} [128], IgG linked to Sulfo-SMCC for HT-2 mycotoxin [129], and glucose oxidase for glucose in live cells [130] (Figure 1.12). Note that some of the functional units were established on layers of PLL and/or PAA on the inner wall of the tip.

Ion-current rectification

Current rectification is also observed when an untreated nanopipette tip is at a submicron distance from a locally-charged (positive or negative) substrate; therefore, ion transport is significantly influenced, which is termed ion current rectification (ICR) [131, 132]. Cations and anions in the surrounding subenvironment are, respectively, repelled and attracted when the tip is in close proximity to a negatively-charged substrate. Perry and coworkers successfully utilised the same concept to realise a mapping of surface charge by characterising the double layer on live cells [133]. This implies conventional topographic imaging actually convolute with the distribution of surface charge. Thus, bias-modulated (BM) SICM that applies zero net bias can solve this issue, and the surface charge can be analysed by shifting the phase of the applied voltage signal in the nanopipette [134].

1.9 Thesis outline

This thesis focus on applications based on SICM that are relevant to the investigation of Alzheimer's Disease (AD), in which neuronal cells exhibit abnormal behaviours in the presence of toxic oligomeric beta-amyloid. The technique in SICM is used in order to perform localised dosing of synthetic or naturally-secreted oligomers at a fixed height above single cells; the real-time response of the target cell is analysed by recording either the time-resolved fluorescence emitted from a laser-excited ion indicator that is pre-loaded in cells, or the transduced electronic signal of a novel biosensing system over time. The structure of the thesis is organised as follows:

Chapter 2 will introduce fundamental knowledge on the conventional setup for SICM, in terms of its electronic characteristics and mechanical designs. SICM relies on the feedback of the ion current; therefore, the reduction of vibrational and electrical noise that will result in the instability of the system is critical. The parameters for fabricating a nanopipette with a suitable aperture using a laser puller, which is referred to as the probe in SICM, are discussed. In addition, various components, including the electrodes, the nanopipette

holder, the piezoelectric actuator and the nanopositioner are also introduced individually. Finally, a schematic diagram demonstrates how all the electrical components are connected, and communicated with, to establish an automated system, making hopping mode possible, which adopts a sample roughness-dependent algorithm.

Various modelling methods for describing the ion current and the inner electric field are reviewed in Chapter 3, including analytical modelling that is based on an equivalent circuit, and numerical modelling using the finite element analysis. On the other hand, the hydrostatic and hydrodynamic mechanisms in a nanopipette are complicated due to its tapered-shape near the tip under the application of a bias voltage between the electrodes, with electrophoresis, electroosmosis and dielectrophoresis all simultaneously involved in the transportation of charged carriers. For a locally quantitative dosing of molecules of interest on single cells, it is helpful to approximate the spatial distribution of the concentration of the dosed molecules when they leave the tip of the nanopipette. Furthermore, in order to describe a hydrodynamic flow, Laplace, Navier–Stokes and Nernst–Planck equations need to be coupled together in a computer simulation; the boundary conditions for these equations are introduced. If a carbon electrode replaces the nanopipette, SECM can be conducted. In this case, an analytical model for the Faradaic current on this electrode, which can estimate its radius, is described.

The original experimental results and corresponding discussions are contained in three chapters in this thesis. The examination of the effectiveness of antibodies/nanobodies, which are designed specifically against AD or Parkinson's Disease (PD), using the SICM platform combined with fluorescence detection of individual cells over time is in Chapter 4. Imbalanced calcium homeostasis, i.e. an increase in calcium influx in astrocytes, is observed in the presence of synthetic Abeta42 oligomers of physiological concentrations (∼pM), which is presumably a subtle pathological sign of the early stage of AD. Subsequently, the effectiveness of various antibodies/nanobodies to cerebrospinal fluid (CSF) from AD patients are determined by whether the reduction of calcium influx with a statistical significance is observed.

Mechanism of entry for calcium induced by oligomers in the bath solution has not been fully understood. One of the hypotheses of this phenomenon is that temporary membrane interference is formed, when oligomers attempt to pass through the cell membrane. If transient pores exist, the release of cytosolic ATP is likely to be detected by an ATP sensor located next to the dosing spot of oligomers on an astrocyte. Therefore, the establishment of the new SICM setup, which can accommodate an angular-aligned micromanipulator for holding an ATP sensor, in order to prove this hypothesis is introduced in Chapter 5. The mechanical modular frame and every component used in the setup are explained, as well as the optical table that can provide active vibration isolation, the LED light source and the camera.

In Chapter 6, the manufacturing process for a novel ATP sensing system based on a double-barrel nanopipette and the corresponding measurements of live cells are discussed. At first, the two vacant channels of a double-barrel nanopipette must be filled with pyrolytic graphite to become a pair of adjoined carbon nanoelectrodes. The size of these nanoelectrodes is characterised using cyclic voltammetry in a solution containing the redox mediator FcMeOH. After this, polypyrrole (Ppy) is deposited electrochemically to bridge these two nanoelectrodes, forming an electrolyte-gated organic field-effect transistor (EGOFET), in order to amplify the drain-to-source current that is significantly influenced by the amount of protons, i.e. the pH, in the surrounding environment. In the next stage, hexokinases are maintained near the Ppy layer in order to convert an EGOFET to an ATP sensor, in which protons are generated locally when phosphorylation of the substrate catalysed by hexokinase with the involvement of ATP is carried out. Three approaches to constrain hexokinases around the Ppy layer are examined and following corresponding measurements of the ATP leakage from astrocytes for the first time are discussed.

Finally, Chapter 7 provides a summary of the work in this thesis, together with the outlook for future experiments that are based on the methodology of localised dosing and fluorescence detection, this newly-developed setup, and the novel concept of the ATP sensor presented here.

Chapter 2

Experimental Methods

2.1 Fundamentals of SICM

SICM is a form of scanning probe microscopy that can perform real non-contact probing of a target substrate. A nanopipette fabricated from a cylindrical glass capillary using a nanopipette-pulling machine is utilised as the probe, which can have a submicron tapered tip opening. The nanopipette has to be filled with buffer solution containing the necessary salts with its tip immersed in the same solution or a modified buffer bath reservoir, where the targeted object is situated, to perform the measurement, as shown in Figure 2.1. Two Ag/AgCl coated wires playing the role of quasi-reference counter electrodes (QRCEs) are placed separately in the nanopipette and in the bath. On one of the QRCEs an appropriate voltage bias is applied, while the other is electronically grounded. Thus, the charge carriers in the buffer solution drift from one QRCE to the other in the direction of the electric field generated between the two QRCEs through the aperture of the nanopipette. The supporting electrolyte usually contains chloride ions, for example potassium chloride (KCl), so that the applied potential of the QRCEs can be characterised by the concentration of chloride ions in the bath solution, according to the half reactions of Ag and AgCl described in the Nernst equation. The principle of SICM is based on the measurement of overall resistance including an intrinsic component in the nanopipette, R_p, and a resistance as a function of the distance

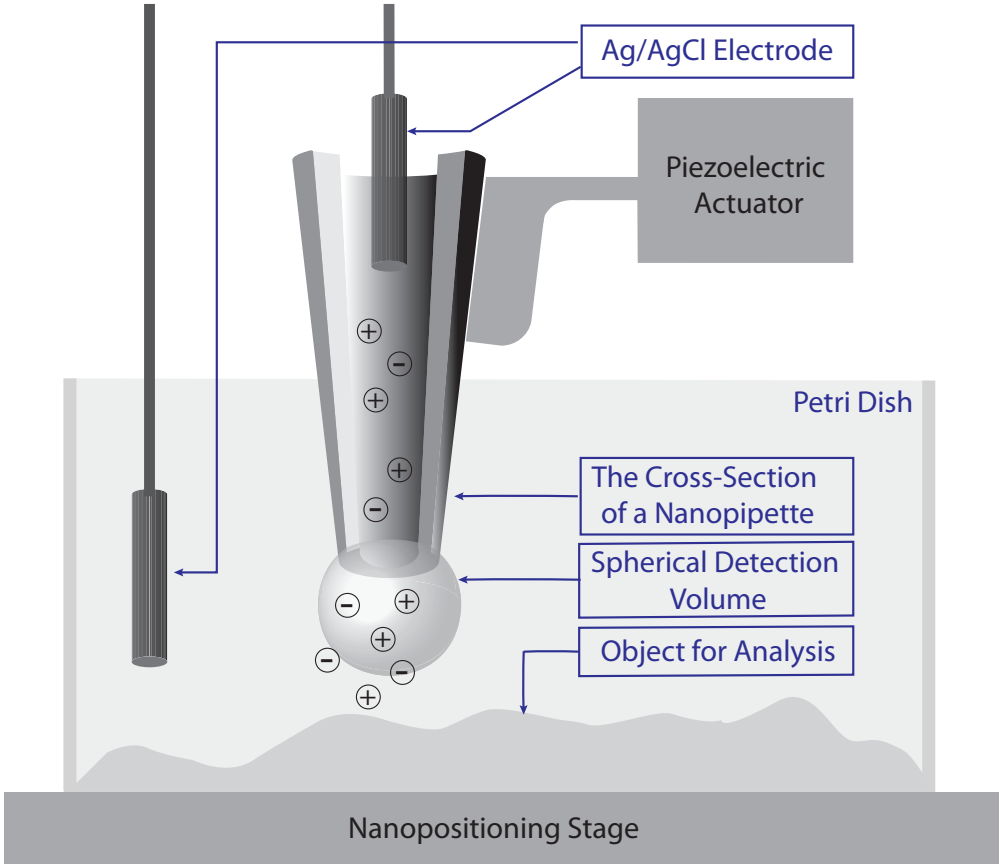

Figure 2.1: The cross-section of a nanopipette used in SICM is illustrated, where bias application between a pair of Ag/AgCl electrodes immersed in the electrolyte solution in the nanopipette and the Petri dish leads the ions to drift through the nanopipette aperture. This ion flow will be partially hindered if an object appears within a spherical volume of roughly the radius of the inner tip opening, resulting in ion current reduction. This correlation between ion current and distance from the subject is used for SICM scanning, which is conducted by a vertically-aligned piezoelectric actuator to hold the nanopipette and a horizontal nanopositioner on which the Petri dish may move.

between the nanopipette and the sample surface, R_h. When the nanopipette is in proximity to a substrate within a spherical detection region of its diameter, the ion current will be hindered partially. This height-dependence of the ion current is amplified and sent back as a feedback signal to the automated control system built using a vertically-aligned piezoelectric actuator to avoid contact between the nanopipette tip and the object. It is the ionic property around the object environment being monitored without interfering with the object itself that is especially beneficial for the probing of a soft or even a floating biological sample to realise a contactless scanning measurement. Furthermore, the size of the tip opening decides not

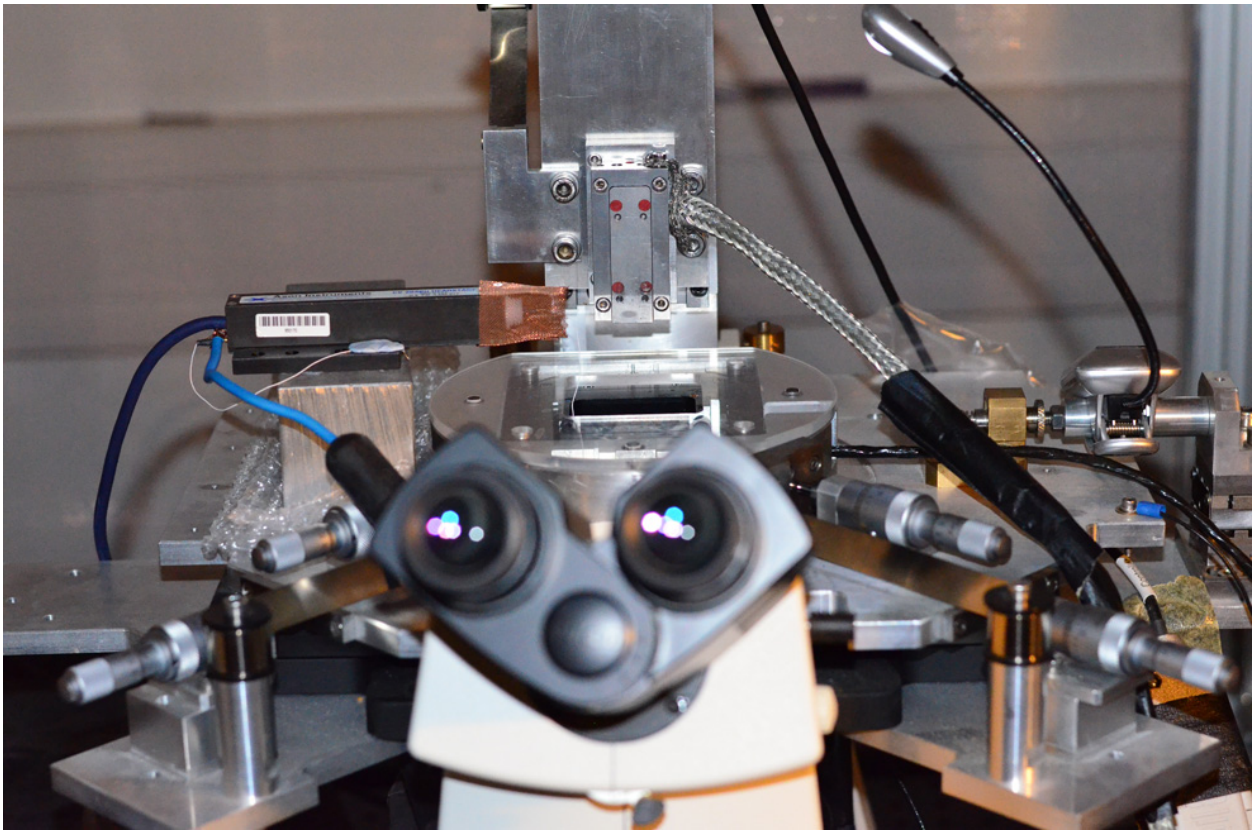

Figure 2.2: The homemade SICM setup is installed on an inverted microscope, in which coarse movements of the stage and the nanopipette can be carried out manually, followed by fine adjustments by piezo actuators, in order to achieve the alignment between the nanopipette and the target cell.

only the scanning resolution of the topographic image but also the aperture resistance for the ion current to flow through. In general, if the tip of the nanopipette is at an inner-radius from the sample surface, the ion current is reduced to around 99 % of its original value. Notably the inverse of the resistance is mathematically defined as the conductance, and for this reason this probing concept is referred to as scanning ion conductance microscopy. Our homemade SICM is shown in Figure 2.2. More details about this setup will be discussed in the following sections.

2.2 Reduction of vibrational and electrical noises

Our laboratory is located in the basement of the Department of Chemistry, which may eliminate a certain level of ground vibration from street traffic, but foot traffic from the upper floor, air flow from an air conditioner, and equipment coupled directly to the experiment setup could lead to serious interference with the measurements. After identifying the source and type of the vibrations, it is necessary to introduce a suitable vibration isolation system on which the SICM may be arranged. Thus, this homemade SICM instrument based on an inverted microscope (Eclipse T1, Nikon) equipped with a microscopic objective (Plan Apo VC Water immersion 60×, MRD07601, Nikon) is placed on a passive vibration isolation workstation (Minus K Technology, MK26, with BM-1 bench top vibration isolation platform). It is designed with stiff springs and high internal structural frequencies to achieve an ultra-low natural frequency (1/2 Hz or less vertical and horizontal), in order to reduce greatly both periodic and random unwanted noises, usually ranging from 4-100 Hz [135]. Therefore, this passive vibration isolation workstation acts as a low pass filter. In addition, the x- and y-axis piezo actuators on the SICM setup for the horizontal stage motion are physically separated from the motor and z-axis piezo actuator for vertical pipette movement, in order to decouple the acoustic vibrations resulting from topographic scanning.

On the other hand, electrical noise and electromagnetic interference (EMI) introduced from neighbouring electrical devices, which can lead to a false reading of the ion current or further nanopipette damage, can be effectively reduced by shielding the setup with a homemade uncoated aluminium Faraday cage. Electrons on the surface of the neutral Faraday cage will be redistributed in the presence of an external electric field, and the whole conductor will then reach a new polarised state of equilibrium. According to Gauss's Law, no electric field lines will remain in the Faraday cage. Thus, in theory the stability of the SICM setup should be improved. However, the front side of the Faraday cage is usually left open for the user's convenience, so the noise coming from the front cannot usually be screened out completely; furthermore, this noise and interference do not only appear outside the Faraday cage but can also exist in the setup itself. For these reasons, additional careful

grounding, i.e. avoiding creating ground loops for each metal component in the setup, is essential. Furthermore, coaxial metal sheaths encasing wires provide isolation of electrical crosstalk between cables.

2.3 Fabrication of nanopipette

A reproducible size and shape for the tip opening of a nanopipette is critical for SICM and its extensive applications. Here, a cylindrical glass capillary of various lengths (e.g. 7.5 or 10 cm) is adopted to produce a nanopipette using a laser-based patch–clamp pipette puller (P–2000, Sutter Instrument), shown in Figure 2.3. Note that the patch–clamp technique is an established physiological method for using a micropipette to investigate single or multiple ion channels on the membrane of individual cells, and the idea of SICM originates from it. A glass capillary of either aluminosilicate, borosilicate or quartz is used as the material for nanopipette processing, according to the requirements of the aperture size. Usually aluminosilicate and quartz glass have the lowest and highest melting points; whilst the properties of borosilicate glass fall between the two. At first, when a pair of puller bars is moved manually to the middle of the puller, the capillary must be symmetrically fixed by clamping knobs onto the V-shaped grooves of the puller bars, which are connected to cables delivering the pulling force of linear actuator solenoids. As depicted in Figure 2.4, a 20 W Class IV CO_2 laser beam is shone onto a reflective scanning mirror and then guided to the middle of the capillary [136]. The divergent laser will be collected by a concave reflective retro mirror to illuminate the other side of the capillary, with the aim of generating uniform heat on the tubing. When the middle of the glass capillary reaches the melting point, the centre part of the tubing will become soft and begin to be extended by the pulling force at the two ends. At a certain point the capillary will be separated and create a pair of two identical nanopipettes with an opening tip of the required size and tapered length. Finally, the clamping knobs are untightened and the successfully-made pair of nanopipettes is carefully transferred into a suitable container, which is often a Petri dish of 90 mm diameter with a long piece of Blu-Tack attached to the middle of its underside.

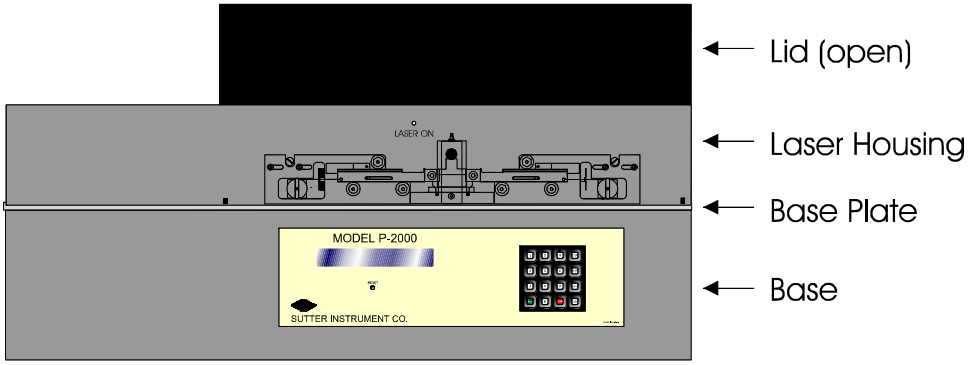

Figure 2.3: The schematic appearance of a P-2000 laser puller purchased from Sutter Instrument. A 20W Class IV CO_2 laser is located in the laser housing, and the pulling assembly, which can be covered by a lid is fixed on the base plate. The pulling operation is finely controlled by integrated circuits and electronic components in the base via a touch-tone user panel on the front of the base. Figure excerpted from [136].

The laser puller itself is a programmable device for outputting nanopipettes with controllable parameters, including the size of the aperture, the length of the taper tip and other features for various applications. A cycle consisting of five parameters in the manufacturing process allows users to make adjustments using the keypad on the front panel. These are explained as follows:

(1) Heat: the output power of the laser, which will be projected onto the middle part of the tubing in order to melt a certain type of glass capillary;

(2) Filament: limits of the tilt angles of the scanning mirror operated on a stepper motor, which defines the area illuminated by the laser beam during the process;

(3) Velocity: the moving speed of the pulling bars when the middle of the tubing is melted to become viscid before the final hard pull is conducted;

(4) Delay: the period of time before the initialisation of the hard pull after the laser is turned off;

(5) Pull: the force of the hard pull from the solenoid actuators.

The pulling program performing laser treatment can be made more complicated, i.e. multiple sets of these five parameters are permitted. For example, two lines (sets) of pulling com-

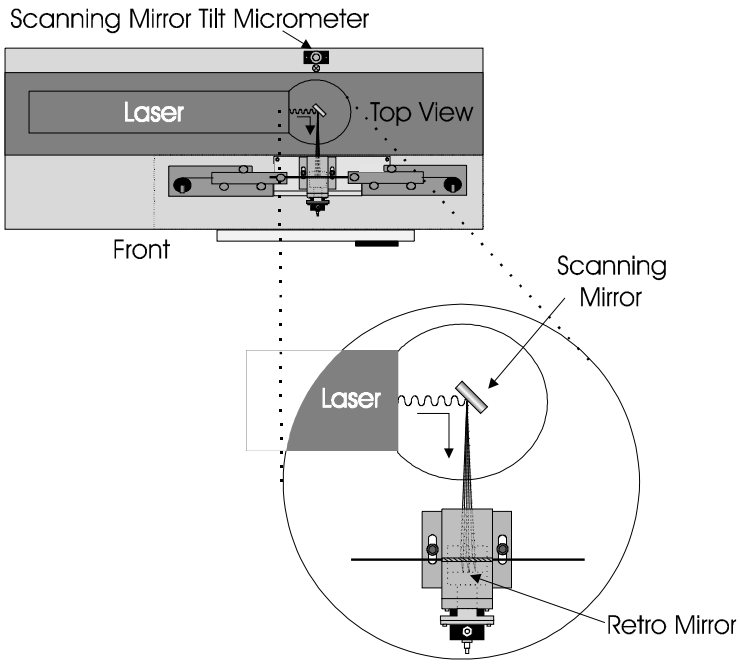

Figure 2.4: Top view of the P-2000 laser puller. When pulling is performed, the laser firstly illuminates the scanning mirror and is then reflected by the retro mirror in order to heat up the centre of the capillary fixed between the puller bars homogeneously in the pulling assembly. Consequently the capillary is first pulled apart when its centre is softened due to melting, and it then generates a pair of identical nanopipettes with targeted tip opening. Figure excerpted from [136].

mands enable the middle of the tubing to be narrowed firstly and then to be pulled apart, generating a pair of nanopipettes with a small aperture, which is probably achieved more easily than with a single line of command. Despite its multifunctionality, in real experiments it has never been intuitive to obtain the desired characteristics for a nanopipette. Disadvantages of this model P–2000 laser puller include that (1) no corresponding physical values are related to the parameters, (2) no embedded sensors are installed to monitor how the fabrication is going and (3) the parameters in the pulling command are not mutually independent. Thus, these parameters are usually acquired empirically after a trial and error process (the time needed depends on the user's knowledge and experience) and they vary machine by machine. The glass capillaries of an outer diameter of 1 mm and an inner diameter of 0.58 mm, 0.68 mm and 0.50 mm for borosilicate, aluminosilicate and quartz, respectively, are suggested to produce optimised nanopipette opening tips using the parameters shown in Table 2.1 [137, 138]. As described above, in these two-line pulling programs, the parameters of the first line allow the

Table 2.1: List of capillary materials and corresponding optimised diameters when converted into nanopipette tips, and the pulling programs containing five parameters: Heat, Filament, Velocity, Delay and Pull used for P-2000 laser puller [138]. Note that in the 2-line programs, the first row carries out the preliminary thinning of the capillary wall and the second row the next-stage separation.

Capillary Material/ Tip Diameter (r_i)	Sutter P–2000 Laser Puller Optimal Pulling Program
Borosilicate/ $r_i \approx 75\,nm$	Heat:350, Filament:3, Velocity:30, Delay:220, Pull:none Heat:390, Filament:2, Velocity:40, Delay:180, Pull:255
Aluminosilicate/ $r_i \approx 50\,nm$	Heat:380, Filament:5, Velocity:30, Delay:200, Pull:none Heat:420, Filament:3, Velocity:27, Delay:145, Pull:250
Quartz/$r_i \approx 25\,nm$	Heat:700, Filament:4, Velocity:60, Delay:145, Pull:175

laser to conduct the preliminary modification of the capillary thickness, followed by subsequent finer control. However, these parameters may need to be adjusted with time. Thus, in our case of using borosilicate capillaries, modified 2-line parameters for generating sub 100 nm nanopipette opening were utilised: Heat:400, Filament:3, Velocity:30, Delay:220, Pull:none and Heat:450, Filament:2, Velocity:20, Delay:180, Pull:255. The size of the opening nanopipette tip can be estimated indirectly by the readout of the amplified ion current, which avoids spending time on complicated imaging procedures before each measurement.

2.4 Nanopipette holder and quasi–reference counter electrodes

The nanopipette needs to be fixed vertically on the piezoelectric actuator using a holder with a straight body (ESW-F10P, Warner Instruments), as shown in Figure 2.5, which is designed for a glass tubing of 1.0 mm outer diameter. The barrel of the holder is made of polycarbonate to reduce mechanical noise, and the nanopipette can be assembled inside the pipette seat through a silicone washer, which is compressed by a screwed Teflon cap [139]. A silver chloride coated silver wire (Ag/AgCl) going through the barrel is able to reach the taper of the nanopipette, and its other end is coiled and compressed onto a silicon seal by a metal part, which allows the wire to be connected to the headstage of a current amplifier.

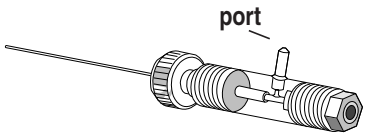

Figure 2.5: Schematic illustration of a nanopipette holder used in SICM. The nanopipette is inserted into the pipette seat with the Ag/AgCl electrode going through to its tip from the left of the figure. Positive or negative air pressure can be applied through the port. Figure excerpted from [139].

Note that a port is jointed at the barrel to apply pressure to the electrolyte loaded in the nanopipette by a plastic syringe with a hose.

The silver wire is coated with a silver chloride layer using electrolysis (9 V) in 3 M NaCl for 10 minutes. It may be observed that the metal wire will turn grey when the process is completed. An Ag/AgCl wire inserted straight through the nanopipette and the other immersed in the bath electrolyte are used as QRCEs; i.e. the Ag/AgCl wires are capable of playing the roles of both counter and reference electrodes when the current density flowing through them is small enough. Ag/AgCl QRCE is an ideally non-polarisable electrode, which means Faradaic current is allowed to flow freely between the electrode surface and the neighbouring electrolyte, so the thickness of the electrical double layer is minimised and there is almost zero overpotential across the electrode. The potential difference between the two identical electrode/electrolyte interfaces is therefore kept constant in the open circuit. The half-cell redox reaction is shown as follows:

$$\mathrm{AgCl_{(s)}} + \mathrm{e^-} \Leftrightarrow \mathrm{Ag_{(s)}} + \mathrm{Cl^-} \tag{2.1}$$

Thus, the potential E for the QRCE can be characterised by the Nernst equation:

$$E = E^0 + \frac{RT}{nF} \ln \frac{1}{a_{\mathrm{Cl^-}}}, \tag{2.2}$$

where E^0 is the standard potential (0.222 V versus standard hydrogen electrode (SHE) at 25 °C [140]), R is the universal gas constant ($8.314\,JK^{-1}mol^{-1}$), T is the temperature in degrees Kelvins, n is the number of moles of electrons transferred in the reaction, F is the Faraday constant ($9.649\times10^4\,Cmol^{-1}$), and a_{Cl^-} is the chemical activity for chloride ions. KCl is usually chosen as the inert supporting electrolyte, which fulfils the conditions of the ionic strength in the solution being so high that the effect of the electric field on charged carriers can be neglected. Therefore, the mass transport near the electrodes, which is supposed to include charge migration and diffusion, can be simplified to only the contribution of ion diffusion. Note that a saturated KCl electrolyte will make E of Ag/AgCl 0.197 V at 25 °C [141]. To emphasise, current is conducted by the movement of electrons and ions in a metal electrode and in the electrolyte, respectively.

2.5 Piezoelectric actuator and nanopositioning stage

The movement of the nanopipette along the z-axis is performed using a coarse control by a translation stage (M-111.2DG, PI), on which further fine adjustment is carried out with a piezoelectric linear actuator (P-753.2CD, PI), as shown in Figure 2.6. The holder of the nanopipette is immobilised on this piezoelectric actuator. The horizontal piezoelectric nanopositioning stage (P-733.3CL, PI), which involves controlling the x- and y-axes, as shown in Figure 2.7, is isolated from the z-axis stage, which avoids coupling of vibrational noise generated from the movement of the horizontal stage being delivered to the vertical actuator during topographic scanning. The technology for precise positioning on a nanoscale takes advantage of the physical properties of piezoelectric ceramic materials, e.g. lead zirconate titanate (PZT), and the fact that asymmetric ferroelectric expansion of a polar axis takes place under the Curie temperature, when a strong electric field ($\sim 10^5$ KV/mm) is applied [142]. This phenomenon is also referred to as the inverse piezoelectric effect, in which electrical energy is transformed into mechanical energy.

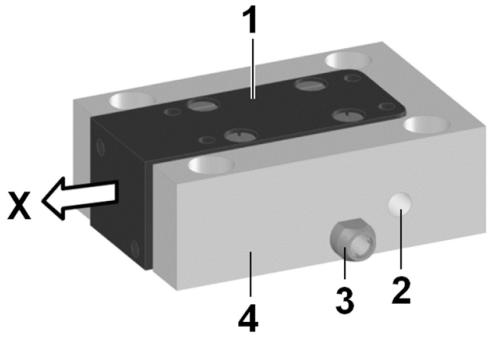

Figure 2.6: The piezoelectric actuator used in SICM: 1 is the moving platform; 2 is the protective earth connection; 3 is the cable outlet; 4 is the base metal bulk; X denotes the moving axis of the platform with a maximum closed-loop travel of 25 microns. The nanopipette holder is firmly fixed on the top of the platform via a linker, and the nanopipette tip therefore also points in direction X. The actuator is placed vertically on the SICM setup. Figure excerpted from [143].

2.6 Other electronic devices in SICM

The instrument configuration and data processing for SICM scanning is explained in Figure 2.8. An SICM control system must be established using a combination of a processing unit, analogue-to-digital converters (ADCs) and digital-to-analogue converters (DACs). In the real world, any kind of signal exists in a continuous form, which means its physical values (e.g. temperature) change with time continuously. However, a computer can only manage digitised data, so all of the analogue signals acquired by input devices have to go through ADCs to be sampled, quantised and encoded to become time-discrete and then stored in a computer memory. On the other hand, output devices may need these digital data to be converted back to analogue signals via DACs and processed by reconstruction filtering and amplification. In our setup, a USB/PCI board (SBC6711, Innovative Integration) containing digital signal processing (DSP) (TMS320, Texas Instruments) and a field-programmable gate array (FPGA) (Spartan-3, Xilinx) is adopted. FPGA has an array of logic blocks which allows the user to program and design freely to execute simple to complex functions (e.g. from a logic gate even to a microprocessor). In our case, the FPGA is a platform interconnecting the DACs, ADCs and DSP. Therefore, our SICM control system is able to digitise the amplified signal of the raw ion current flowing through a pair of QRCEs, with

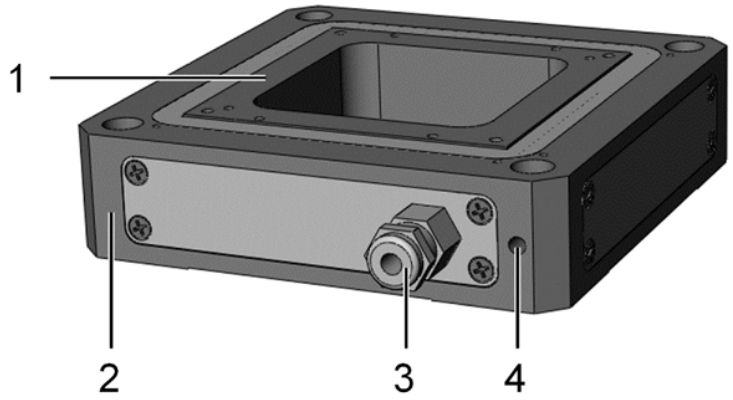

Figure 2.7: The nanopositioner used in SICM: 1 denotes the moving platform with a rectangular cavity; 2 the base bulk; 3 the cable outlet; 4 the protective earth connection. The stage is arranged horizontally with a maximum closed-loop travel of 30 μm $\times$ 30 μm, and with the Petri dish placed in the cavity via an adaptor. Figure excerpted from [144].

parameters being adjusted via a graphical user interface written using Delphi integrated development environment (IDE), and analogical feedback positioning of piezoactuators is then performed. It is worth mentioning that the SBC6711 board we used (DSP+ADCs+DACs) has been discontinued by the company; however, any similar arrangement with input/output (I/O) plus CPU may fulfil the task of automated controlling. For example, a combination of FPGA (RC-240, Mentor Graphics)+ADCs+DACs, digitizer (digidata 1550B, Molecular Devices)+any kind of CPU, IO INTERFACES (OpenIOLabs), or LabVIEW FPGA Module (PXI-7854, National Instruments) could all accomplish the scanning task.

A modular piezo controller (E-500.00, PI), which contains power amplifiers (LVPZT-AMPLIFIER) and sensor/servo controllers, is adopted to control and monitor the motion of the piezoelectric actuator and stage. The position of the stage is monitored without contact with individual pairs of capacitive sensors installed in the actuator and the stage [145]. Between the surface plates (one referred to as the "probe" and the other as the "target") on those pairs of capacitive sensors, a homogeneous electric field is applied [144]. There is a change in capacitance according to the distance between the two plates to be measured. These signals regarding the stage position are inputted to the sensor/servo controller for the next stage of processing by the DSP and the computer. Note that a sensor monitor on the controller can optionally provide the output of instantaneous signals acquired by the sensors.

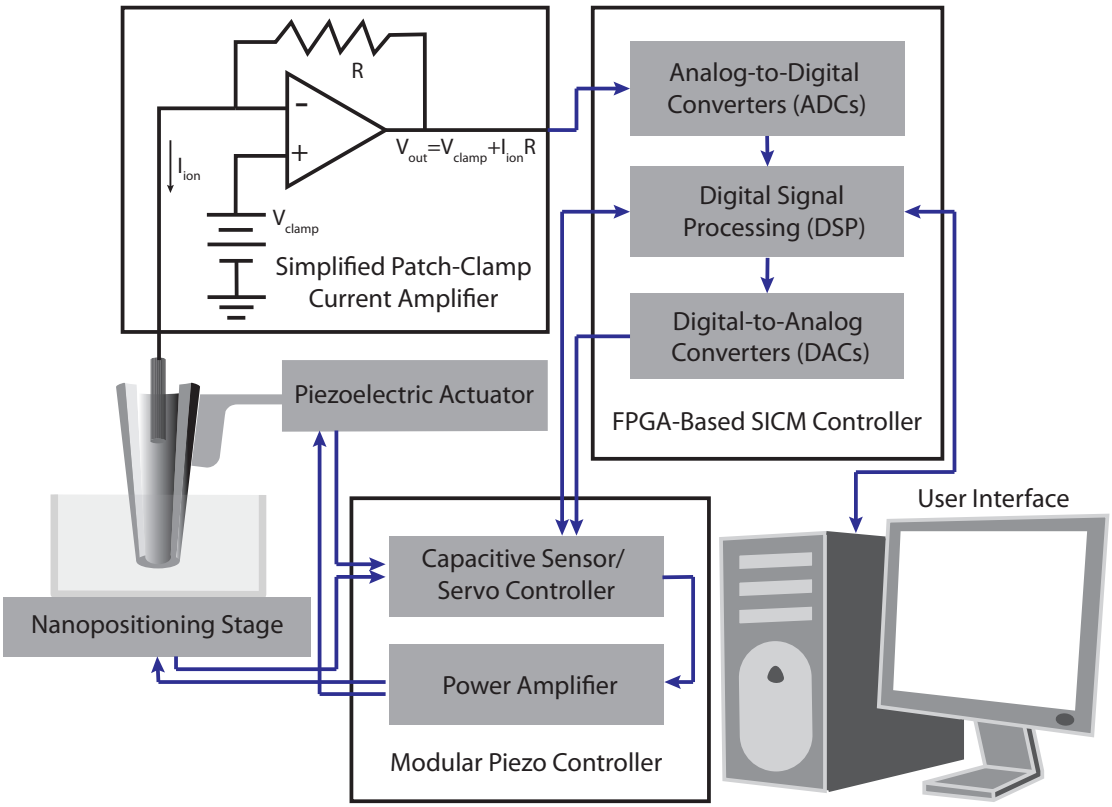

Figure 2.8: The configuration of the SICM setup, which is composed of a piezoelectric actuator controlling the vertical movement of the nanopipette, a horizontal dish-holding nanopositioner, a modular piezo controller, a patch-clamp current amplifier, an FGPA-based SICM controller and a computer installed with a programmable user interface.

The parameters are set by the same computer interface for piezo positioning, and the signal subsequently arrives back at the servo. Finally, offset-adjustable command signals amplified by the amplifier module, ranging from –30 to 130 V, for the movement of actuator and stage are delivered to drive the actuator and stage.

In fluorescence-imaging experiments, a dye-labelled specimen is excited by a laser of wavelength 480 nm or 550 nm, and its fluorescence is guided through a beam splitter (DV2, MAG Biosystems) and collected by a high-sensitivity electron-multiplying charge-coupled device (EMCCD) (Ixon+, Andor). EMCCD made on a silicon wafer has the advantages of high sensitivity ($<1e^-$ with EM Gain) and faster speed operation (>10 MHz) compared to a conventional CCD [146]. The electron-hole pairs generated by the illumination of photons are multiplied by high-voltage-induced impact ionisation before output amplification;

therefore, readout noise is no longer a constraint for achieving low light imaging and single-molecule detection. Furthermore, the EMCCD detector is loaded in a cryostat to reach a low temperature of –95 °C for the reduction of dark current noise [146].

2.7 Operating modes of SICM

Topographical scanning in a conventional scanning probe microscopy (SPM) is often operated in a raster fashion, which is the same for SICM. In Figure 2.9 (a1), when direct current (DC) mode is used, the nanopipette tip moves continuously in a single direction and the ion current is measured until it reaches the preset scanning boundary, and the tip will be moved each time to another parallel but reversed probing direction. Under the tip there is an effective spherical volume where a constrained ion current flows through the tip. The total amount of ion current piercing this volume will be reduced when it approaches the substrate. Thus, it can be used as the vertical distance feedback, and a preset current reduction (a so-called setpoint) should be maintained in order to keep a constant distance between the tip and the substrate. All the displacements of piezoelectric actuators are recorded and converted into the height at all probing points. Although DC mode is fast and sensitive to the substrate, as it can sense a slope, it is still not appropriate for soft biological samples with high surface roughness, because the nanopipette may not be able to respond in time to a steeply topographical change before it has made contact with the edge of the object. As shown in Figure 2.9 (a2), the ion current decreases abruptly when the tip approaches the sample surface in DC mode. If any unexpected current drift occurs, the nanopipette is likely to go out of control or even crash.

The alternating current (AC) mode shown in Figure 2.9 (b1) has achieved a better performance with relatively convoluted samples than DC mode, by means of applying a modulating electrical component to the original DC current, leading to a modulating amplitude in the nanopipette. This vertical vibration of the nanopipette tip improves feedback sensitivity, especially when the nanopipette is in close proximity to the sample surface, which makes it

less likely to crash. In Figure 2.9 (b2), the AC component of the ion current is increased dramatically when the tip almost touches the substrate, so its vertical sensitivity is much higher than in DC mode. Therefore, in our system, AC mode is utilised for the nanopipette tip to find the surface of the Petri dish bottom before any measurement is performed. However, AC mode scanning does not provide any particular improvement in lateral sensitivity because part of the detection volume may be blocked by a steep slope, so the measured current may not change accordingly, leading to physical contact with the object. As a result, AC mode still fails to scan highly undulated samples.

To solve this problem in scanning, in hopping mode, as shown in Figure 2.9 (c1), the nanopipette is designed to be lifted to a sufficient height above the sample to recalibrate the current value, which is a considerably away from the substrate, before starting each new independent lateral scanning point [147]. This circumvents the possibility of collision, which exists in pure DC and AC modes, and instead provides highly-contoured samples. Although this method of segmented approaches successfully reveals complex features of a sample without crashes, the scanning efficiency is compromised, so more time is spent than in DC and AC modes. It is possible to speed up the acquisition process by automatically adjusting suitable resolutions in sub-scanning-squares according to the surface roughness, which is illustrated in Figure 2.9 (c2). First, a lower resolution is adopted, so the ion current at the four edges of a predefined square is detected, and then an adaptive number of scanning points is chosen based on the current difference at these corners. The quality of the topographic image can usually be improved significantly when SICM is operated using this hopping mode. AC and DC hopping modes can both accomplish the task.

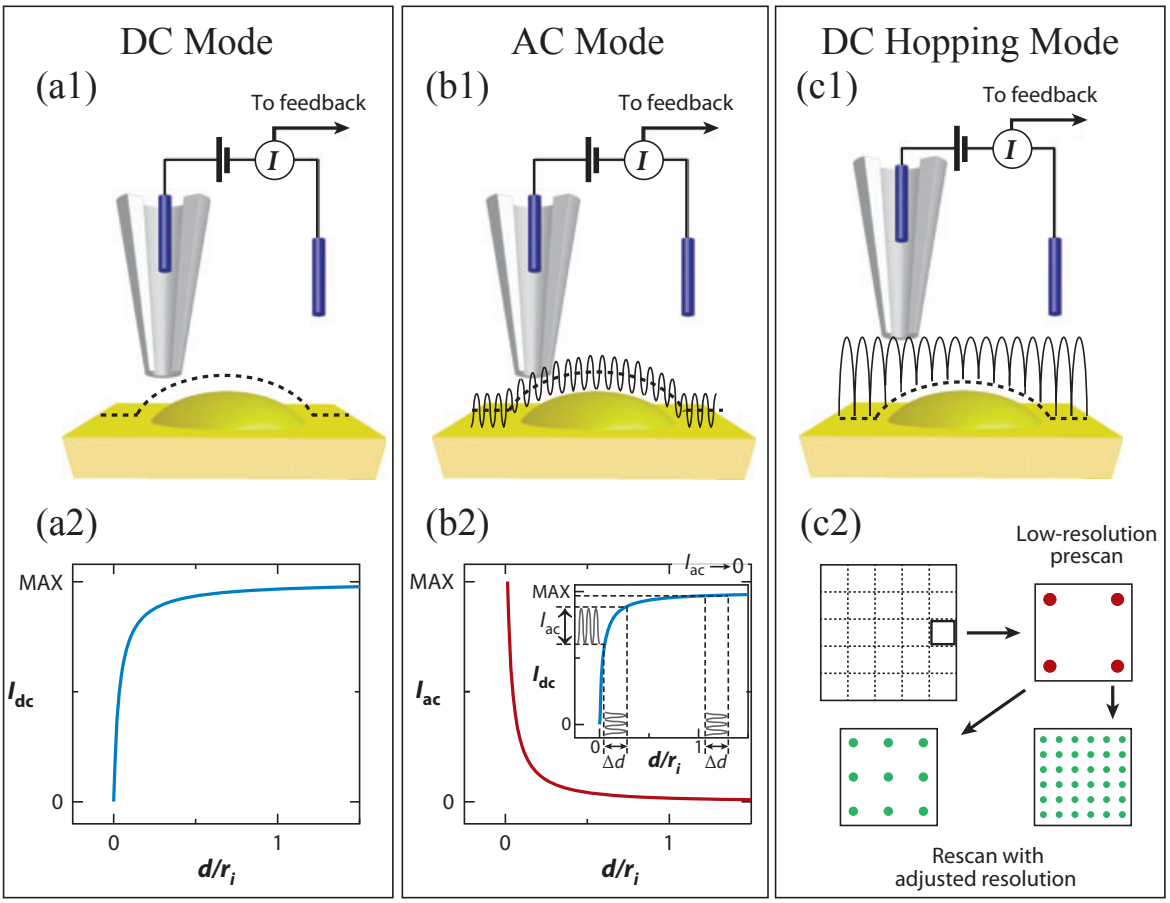

Figure 2.9: Schematic illustration of (a1) DC mode, (b1) AC mode and (c1) DC hopping mode in SICM. The dotted line represents the scanning route of the nanopipette in DC mode, while the solid curves represent the modified trajectories in AC and hopping modes. Approaching curves shown in DC mode (a2) and AC mode (b2) describe the corresponding ion current through the spherical detection volume to the distance between the nanopipette and the substrate, where d/r_i is the nanopipette height normalised to the nanopipette inner radius. The AC part shown in the red curve in (b2) is significant due to modulating actuator movement, as shown in the inset. I_{ac} becomes dramatically larger when the nanopipette height approaches zero. (c2) Adaptive scanning protocols according to the surface roughness in hopping mode. Adjustable scanning resolution correlates to the difference of the measured ion current at four corners of the preliminary scanned square. Figures excerpted from [148].

Chapter 3

Physical models of nanopipette applications

3.1 Physical models of the ion current through a nanopipette

In SICM, the electrical behaviour, i.e. the ion current flowing through the nanoscale aperture of a conical nanopipette driven by the application of the voltage difference between a pair of QRCEs, can be modelled as an effective circuit, as shown in Figure 3.1. It is composed of a series-parallel connection of resistors, capacitors and a voltage source, including the resistance for the bulk of the nanopipette, R_p; the resistance related to the size of the nanopipette tip opening, R_r; the resistance influenced by the height of the nanopipette tip to the substrate underneath, R_h; the resistance for the electrolyte outside the nanopipette, R_e; the capacitance due to the surface charges on the glass wall, C_p; and the unavoidable stray capacitance, C_s, which usually exists between electronic components of instruments in proximity to one another.

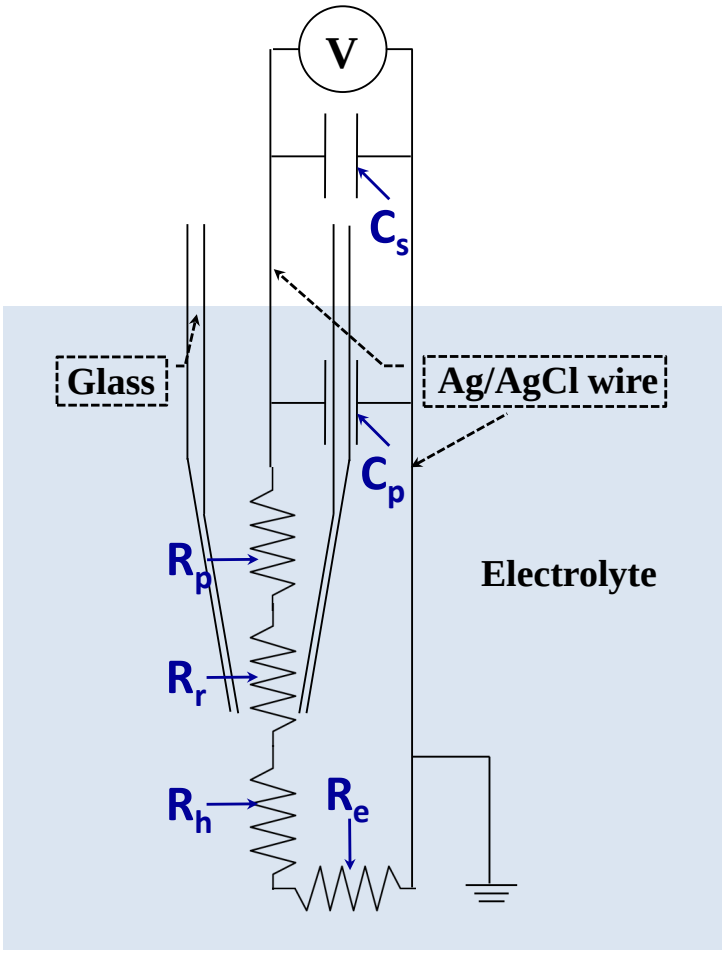

Figure 3.1: The effective circuit for a nanopipette immersed in the electrolyte. R_p, R_r, R_h and R_e represent series-connected resistances related to the bulk of the nanopipette, the tip opening, tip-sample separation and the surrounding electrolyte, respectively. C_p is the capacitance established due to surface charges, and C_s is the stray capacitance, the so-called parasitic capacitance, that is usually formed in electronic circuits. In addition, a connected voltage source, which, in practice is usually a patch–clamp amplifier, provides a fixed voltage difference for this effective circuit.

3.1.1 Analytical modelling of the ion current

The modelling geometry of the nanopipette is depicted in Figure 3.2. In the fully analytical expression developed by Nitz *et al* [149], only the most significant resistances, R_{ptotal}, which comprises R_p and R_r in series, and R_h are considered. Note that R_e is negligible in the

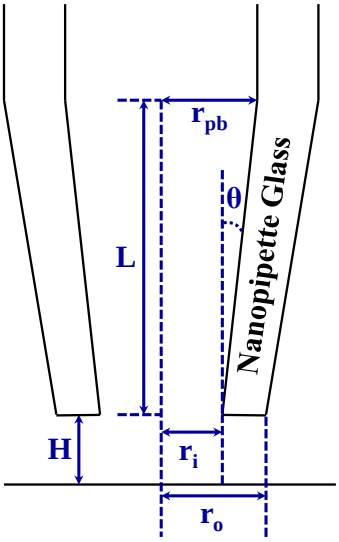

Figure 3.2: The cross-section of a nanopipette, which shows the parameters used in the physical models in this section. r_i, r_o and r_{pb} are the radii measured from the centre at the aperture to the inner glass wall, to the outer glass wall, and to the inner wall of the tip base, respectively. L is the length of the tip, whilst H is the distance between the tip opening and the substrate. θ is the half-cone angle of the nanopipette.

electrolyte. R_{ptotal} can be written as:

$$\begin{aligned} R_{ptotal} &= \frac{1}{\sigma\pi}\int_0^L \frac{dz}{(r_i + z\tan\theta)^2} \\ &= \frac{1}{\sigma\pi\tan\theta}\left(\frac{1}{r_i} - \frac{1}{r_{pb}}\right), \end{aligned} \tag{3.1}$$

where σ is the electrolyte conductivity, L is the length of the nanopipette tip, r_i is the inner radius of the nanopipette tip opening, and r_{pb} is the internal radius of the tip base. If r_i is much smaller than r_{pb}, then

$$R_{ptotal} = \frac{L}{\sigma\pi r_i r_{pb}}, \tag{3.2}$$

where $\tan\theta$ is r_{pb}/L. On the other hand, the height-dependent resistance, R_h, is given by

[150]:

$$R_h = \frac{\frac{3}{2}\ln\left(\frac{r_o}{r_i}\right)}{\sigma\pi H}, \tag{3.3}$$

where r_o is the outer radius of the nanopipette tip opening and H is the distance between the nanopipette tip and the substrate. R_h increases with reduced distance between the nanopipette tip and the sample. Therefore, the overall ion current in the direction of the nanopipette movement (the z–axis), operated at DC mode, $I_{DC}(H)$ can be approximated as:

$$I_{DC}(H) = \frac{V}{R_{ptotal} + R_h} \approx I_{sat}\left(1 + \frac{\frac{3}{2}\ln\left(\frac{r_o}{r_i}\right) r_{pb} r_i}{Hd}\right)^{-1}, \tag{3.4}$$

where V is the applied bias voltage and I_{sat} is the saturated ion current when the nanopipette is still far away from the substrate. I_{sat} is the maximum DC ion current that can be obtained in the measurement and is given by:

$$I_{sat} = \frac{V}{R_{ptotal}}, \tag{3.5}$$

In AC mode, a modulating part of the current is introduced into the DC component. Thus, the AC component, I_{AC}, is given as [151]:

$$I_{AC}(H) = \int_0^T I_{DC}(H + A\sin(\omega t))\sin(\omega t)dt, \tag{3.6}$$

where T is the AC period, A is the voltage amplitude of the AC signal, and ω is the angular AC frequency. With the addition of the AC part, the change of $I_{DC}(H)$ to the nanopipette-to-surface separation becomes very sensitive compared to a typical DC approach curve and therefore more suitable for a contoured sample in the SICM scanning.

3.1.2 Numerical modelling of the ion current

A 2-D comprehensive model for the ion current using the finite element method (FEM) is reported by Edwards and the co-authors. FEM is a form of numerical analysis, in which multiple partial differential equations (PDEs) are coupled for describing the physics in the discretised geographic domain (called meshes or elements). Consequently, calculus of variations is adopted to calculate solutions that have the minimum error functions. Here, a 2-D cylindrically symmetric geometry of the nanopipette, QRCEs and the bath solution is established and resulting approximations are made. Firstly the distributed electric potential is calculated by Poisson's equation, which is given by:

$$\nabla^2 V = \frac{-\rho}{\varepsilon_0}, \tag{3.7}$$

where ρ is the charge density in the domain, and ε_0 is the vacuum permittivity. Assuming there is no space charge inside the nanopipette walls, the right-hand side of Equation 3.7 is zero, resulting in Laplace's equation (in a cylindrical coordinate system):

$$\nabla^2 V = \frac{\partial^2 V}{\partial r^2} + \frac{1}{r}\frac{\partial V}{\partial r} + \frac{\partial^2 V}{\partial z^2} = 0, \tag{3.8}$$

The solved potential, V, can be then fed into the expression for ion current, which is the integration of the current density along the electrode boundary, Ω, written as [150];

$$I = 2\pi\sigma \int_{\Omega} r \nabla V \cdot \widehat{n}, \tag{3.9}$$

where $\widehat{n}$ is the unit vector perpendicular to the surface. Equation 3.9 can be simplified using further approximations, e.g. σ and V may be set to be unity, so that the solutions have free parameters, which can be made to fit numerically with experimental results. This simplified

ion current in a spherical coordinate system is then written as [151]:

$$I = \int_0^{2\pi} \int_0^{\chi} \left(-\frac{\beta}{r_o^2} \right) \sigma r_o^2 \sin\varphi d\varphi d\theta, \tag{3.10}$$

where β=$r_o r_i/(r_i - r_o)$, and χ is the semiangle of the inner nanopipette. Defining appropriate zero-charge boundary conditions ($\nabla V \cdot \widehat{n}$=0), the physical expressions for the electric potential and ion current are coupled, and therefore the associated values are calculated repeatedly during iteration in order to find the final solutions. For a more complicated geography, sometimes a 3-D simulation is necessary. In principle this is feasible if the same zero-charge boundary conditions are defined, and the 3-D Laplace's equation and an analogue expression for the ion current are adopted.

3.1.3 Analytical modelling of the electric field

Ying *et al* propose that under the assumptions of zero surface charge and constant ion current throughout the nanopipette, a small variation in the applied bias voltage at the z–axis, $dV(z)$, may be written as [100]:

$$dV(z) = -IdR_{total} = -\frac{Idz}{\pi\sigma(r_i + z\tan\theta)^2}, \tag{3.11}$$

where z is the distance from the tip opening of the nanopipette. Integration of $dV(z)$, if r_i is much smaller than the length of the nanopipette, L, shows that:

$$\begin{aligned} V(z) &= \frac{r_i}{r_i + z\tan\theta} \frac{I}{\pi\sigma r_i \tan\theta} \\ &= \frac{r_i \Delta V}{r_i + z\tan\theta}, \end{aligned} \tag{3.12}$$

where ΔV=$1/(\pi\sigma r_i \tan\theta)$, and ΔV refers to as the whole difference of the applied voltage across the nanopipette. Therefore, the electric field along the z-axis can be simply derived

by:

$$E(z) = -\nabla V(z) = \frac{\Delta V r_i \tan\theta}{(r_i + z\tan\theta)^2}. \tag{3.13}$$

3.2 The Physics of fluid mechanics in a nanopipette

3.2.1 Effects of electrophoresis, electroosmosis and dielectrophoresis

The nanopipette has the advantage of delivering molecules and ionic particles in a reagent onto the target locally and precisely. However, interactions between the particles and the electric field at the tip of the nanopipette is complex, because multiple mechanisms that are not in thermal equilibrium are involved, which include (1) electrophoresis, (2) electroosmosis and (3) dielectrophoresis.

Electrophoretic flow is widely observed and used as the basic principle in the technique for molecule separation. A uniform external electric field in a solution containing randomly-suspended particles possessing surface charges results in the electrostatic force on these particles generating directional movement along the electric field lines. The motion of a particle with a surface charge is simultaneously impeded by the reverse movement of its own electrical double layer (EDL), in which ions carry an opposite charge of the same amount as the particle itself in order to maintain the electrical neutrality. The electrophoretic velocity, $\vec{v}_{ep}$, is simply written as [108]:

$$\vec{v}_{ep} = \mu_{ep}\vec{E}, \tag{3.14}$$

where $\vec{v}_{ep}$ is the electrophotetic mobility. This can be obtained by a special form of the

Einstein relation [108]:

$$\mu_{ep} = \frac{qD}{k_B T}, \tag{3.15}$$

where D is the diffusivity of the particles, k_B is the Boltzmann factor and T is the temperature in Kelvin.

The electroosmotic flow is the influence of the electric field on the EDL at the interface between the liquid solution and the inner wall of the nanopipette. The nanopipette is made of glass, whose SiOH group carries intrinsic negative charges and therefore naturally forms positive charges in the other half of the EDL in the electrolyte. When the diffuse layer in the EDL on the nanopipette wall is pushed forwards or backwards by the Coulomb force, the electrolyte solution will be dragged with it in the same direction, forming a plug-like flow. The moving velocity of this electroosmotic flow is given by [108]:

$$\vec{v}_{eo} = \mu_{eo}\vec{E}, \tag{3.16}$$

where μ_{eo} is the electroosmotic mobility. This can be calculated by [108]:

$$\mu_{eo} = -\frac{\varepsilon_0 \varepsilon_r \zeta}{\eta}, \tag{3.17}$$

where ε_r is the relative permittivity of the electrolyte solution, ζ is the zeta potential due to the EDL on the nanopipette wall, and η is the solution viscosity.

The third mechanism is dielectrophoresis, which occurs in every dielectric particle in the presence of a non-uniformly-distributed electric field. The dielectric particle is polarised in the non-uniform electric field, generating an induced dipole moment. In the tapered tip of the nanopipette, the electric field nonlinearly achieves its maximum value at the opening, and therefore dielectrophoretic flow certainly exists, although it is not necessarily a dominating mechanism in the fluid. The magnitude and direction of the dielectrophoretic force, $\vec{F}_{dep}$ is

determined by the intrinsic electric properties of the particle itself. Assuming the particle is spherical with low Reynolds numbers, it is written as [100]:

$$\vec{F}_{dep} = 2\pi R^3 \varepsilon_m \mathrm{Re}(CM) \nabla |E_{rms}|^2, \tag{3.18}$$

where R is the particle radius, E_{rms} is the root mean square of the applied electric field, ε_m is the permittivity of the bulk medium and $\mathrm{Re}(CM)$ is the real part of the complex Clausius-Mossotti factor. The direction of $\vec{F}_{dep}$ can be either along the electric field lines or against them, and this is decided by the polarisability relation between the particle and the medium surrounding it, and indicated by the Clausius-Mossotti factor. When the particle has polarisability higher than the medium, $\vec{F}_{dep}$ exerted on the particle makes it move towards the region with lower electric potential, and it is termed positive DEP; when the converse is the case, it is called negative DEP. Dielectrophoresis has been widely applied in cell separation in microfluidics. The velocity of the particle due to $\vec{F}_{dep}$ is given by [100]:

$$\begin{aligned} \vec{v}_{dep} &= \frac{\vec{F}_{dep}}{f} \\ &= \mu_{dep} \nabla |E_{rms}|^2, \end{aligned} \tag{3.19}$$

where f is the frictional parameter of the particle, and μ_{dep} is $2\pi R^3 \varepsilon_m \mathrm{Re}(CM)/f$.

3.2.2 Approximation of the concentration of localised nanodosing

Approximation of the current density, $\vec{J}$, can be made to estimate the amount of molecules being dosed locally on the substrate. The flux of ions driven by the electric field, applied pressure and molecular concentration gradient is written as:

$$\vec{J} = -D\nabla c + (\vec{v}_p + \vec{v}_{ep} + \vec{v}_{eo})c, \tag{3.20}$$

where c is the chemical concentration, and $\vec{v}_p$ is the velocity of molecules induced by applied

pressure. Note that the impact of dielectrophoresis is negligible because the molecular polarizability is small, and the motion of the fluid itself is also ignored here. On the assumption that c is only a function of the radius of a sphere, R, centred at the nanopipette tip, and $c(R)$ can be approximated as [108]:

$$c(R) = c_0 \left[1 - \exp(\frac{-Q_{total}}{4\pi DR})\right], \tag{3.21}$$

where c_0 is the molecule concentration inside the nanopipette further away from the tip, Q_{total} is the total volumetric flow rate of molecules. If the nanopipette is at a distance of H above to a substrate, the distribution of dosing molecules will be different from that shown in Equation 3.21. Therefore, the mathematical treatment of $c(R)$ needs to be changed to [108]:

$$\begin{aligned} c(r) &= c_0 \left(1 - \exp\frac{-Q}{4\pi D\sqrt{r^2 + (H-z)^2}}\right) + c_0 \left(1 - \exp\frac{-Q}{4\pi D\sqrt{r^2 + (H+z)^2}}\right) \\ &= c_0 \left(2 - \exp\left(\frac{-Q}{4\pi D\sqrt{r^2 + (H-z)^2}}\right) - \exp\left(\frac{-Q}{4\pi D\sqrt{r^2 + (H+z)^2}}\right)\right) \end{aligned} \tag{3.22}$$

where r is the radial position in the geometric domain shown in Figure 3.3. $c(r = 0, z = 0)$ indicates the dosing concentration vertically below the nanopipette on the surface, which usually has a value much lower than c_0. It is given by:

$$c(0) = 2c_0 \left(1 - \exp\frac{-Q}{4\pi DH}\right), \tag{3.23}$$

According to the Hagen–Poiseuille law, the flow rate in the nanopipette due only to the pressure drop across the nanopipette is given by [92]:

$$Q_{\Delta P} = \frac{3\pi r_i^3 \tan\theta}{8\eta}\Delta P. \tag{3.24}$$

Therefore, when ΔV and applied pressure difference, ΔP, are considered simultaneously in

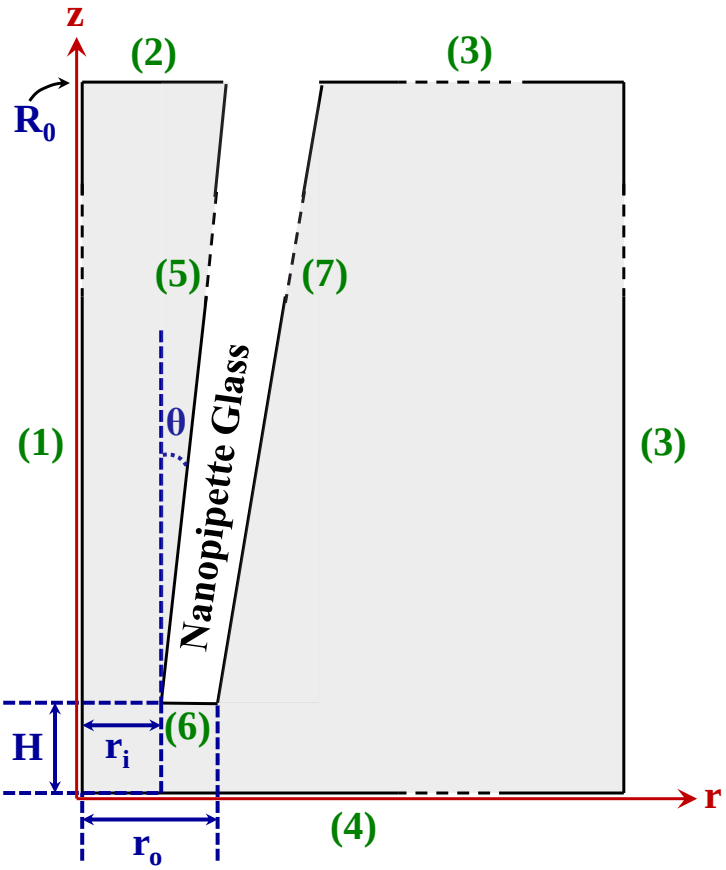

Figure 3.3: The schematic explanation of boundary conditions, numbered from (1) to (7), used in the 2-D geometry of various physical models for a nanopipette. r_i and r_o are the inner and outer radius of the tip opening, respectively. H is tip–sample separation; θ is the half-cone angle of the nanopipette; R_0 is located at the top-left corner of the geometry. r and z axes are situated on the surface of the substrate and the conical centreline of the nanopipette.

the system, and combined with 3.13 and 3.24, Q_{total} can be rewritten as:

$$\begin{aligned} Q_{total} &= Q_{\Delta V} + Q_{\Delta P} \\ &= (\mu_{ep} + \mu_{eo})\pi(r_i + z\tan\theta)^2 \frac{r_i \tan\theta \Delta V}{(r_i + z\tan\theta)^2} + \frac{3\pi r_i^3 \tan\theta}{8\eta}\Delta P \\ &= (\mu_{ep} + \mu_{eo})\pi r_i \tan\theta \Delta V + \frac{3\pi r_i^3 \tan\theta}{8\eta}\Delta P \\ &= \left(\frac{qD}{k_B T} + \frac{-\varepsilon_0 \varepsilon_r \zeta}{\eta}\right)\pi r_i \tan\theta \Delta V + \frac{3\pi r_i^3 \tan\theta}{8\eta}\Delta P. \end{aligned} \tag{3.25}$$

where $Q_{\Delta V}$ and $Q_{\Delta P}$ are the flow rates contributed only by the application of the bias voltage and pressure via a syringe, respectively.

3.2.3 Physical models for the hydrodynamic flow

In this section, Navier–Stokes equations governing the flow of a viscous fluid in the presence of an external electric field and/or with the application of pressure are introduced, which are coupling nonlinear PDEs assuming the conservations of mass, momentum and energy. For the purpose of simplification, firstly, approximations are made: the fluid in the nanopipette is assumed to be an incompressible Newtonian fluid with a low Reynolds number (Re$\approx \rho\vec{v}r_i/\eta \ll 1$), which means that it is a viscous laminar flow (there is no turbulence in the nanopipette) of constant density throughout and its shear stress, τ, follows the formula given by [152, 153]:

$$\tau = \eta \frac{d\vec{v}}{dz}\bigg|_{z=0}, \tag{3.26}$$

where $d\vec{v}/dz$ is the strain rate. In incompressible Navier-Stokes equations, the equation for the conservation of momentum, which can be considered as derived from Newton's Second Law of Motion, is written as [108, 152, 154]:

$$\frac{\partial \vec{v}}{\partial t} + (\vec{v}\cdot\nabla)\vec{v} = -\frac{\nabla P}{\rho} + \frac{\eta\nabla^2\vec{v}}{\rho} + F, \tag{3.27}$$

where F is the applied external force per unit mass. The continuity equation, which is the result of the conservation of mass, is given as [108, 152, 154]:

$$\begin{aligned} &\frac{\partial \rho}{\partial t} + \rho\nabla\cdot\vec{v} = 0 \\ \Rightarrow &\nabla\cdot\vec{v} = 0 \end{aligned} \tag{3.28}$$

where $\partial\rho/\partial \mathrm{t} = 0$ for incompressible fluids. Finally, the equation representing the conservation of energy is actually decoupled from the incompressible Navier-Stokes equations, as there are no energy-related terms entering into the continuity (Equation 3.28) and momentum equations (Equation 3.27). The nanopipette geometry can be depicted as shown in

Table 3.1: A table listing the physical equations for modelling the electrostatic, charge-transport and hydrodynamic behaviours and their corresponding boundary conditions. These numbered boundaries are noted in Figure 3.3.

Physical Models and Corresponding Boundary Conditions	
Laplace Equation	
Boundary	*Physical Description*
(1)	Axial symmetry
(2)	$\vec{E_z}(R_0) = (\Delta V - V_{R_0})\,\frac{\tan\theta}{R_0}$
(3)	V=0
(4)	n·∇V=0, zero charge
(5)	n·∇V=0, zero charge
(6)	n·∇V=0, zero charge
(7)	n·∇V=0, zero charge
Navier–Stokes Equations	
Boundary	*Physical Description*
(1)	Axial symmetry
(2)	$\vec{v} = -\left(\frac{2(R_0^2 - r^2)Q_{\Delta P}}{\pi R_0^4} + \mu_{eo}(\Delta V - V_{R_0})\,\frac{\tan\theta}{R_0}\right)\hat{z}$
(3)	P=0; no viscous stress
(4)	no-slip
(5)	$\vec{v} = -\mu_{eo}\Delta V$
(6)	$\vec{v} = -\mu_{eo}\Delta V$
(7)	no-slip
Nernst–Planck Equation	
Boundary	*Physical Description*
(1)	Axial symmetry
(2)	$c = c_0$
(3)	$c = c_0\left(2 - \exp\left(\frac{-Q}{4\pi D\sqrt{r^2 + (H-z)^2}}\right) - \exp\left(\frac{-Q}{4\pi D\sqrt{r^2 + (H+z)^2}}\right)\right)$
(4)	no flux
(5)	no flux
(6)	no flux
(7)	no flux

Figure 3.3, and the corresponding boundary conditions for various physical models are listed in Table 3.1 [108].

3.3 Analytical modelling of the Faradaic current on a nanoelectrode

The internal space of the nanopipette can be filled with a conducting material, e.g. carbon or platinum, to form a nanoelectrode, as illustrated in Figure 3.4. This electrode is wired to a voltage source, and electrochemical measurement can be performed in the bulk solution with a conjugate redox pair. The Faradaic current in the electrolyte solution underneath the disc-shaped conducting surface at the opening of the tip is diffusion-limited, if the redox reaction at the surface achieves saturation. Cyclic voltammetry of this kind of nanoelectrode demonstrates a sigmoid-shaped curve, and the saturated Faradaic current, I_s, can be approximated as [155]:

$$I_s = \frac{nFC_{tot}}{R_t}, \tag{3.29}$$

where n is the number of electrons involved in the electron transfer, F is Faraday's constant, C_{tot} is the total concentration of redox species in the electrolyte, and R_t is the resistance of mass transfer. For the ideal disc-like tip opening of a nanoelectrode, R_t is written as $1/4D'r_{ne}$, where D' is the diffusion coefficient of the redox mediator, and r_{ne} is the radius of the nanoelectrode. Thus, I_s is written as [72]:

$$I_s = 4.64nFC_{tot}D'r_{ne}. \tag{3.30}$$

By Equation 3.30, the radius of a disc-shaped nanoelectrode can be estimated.

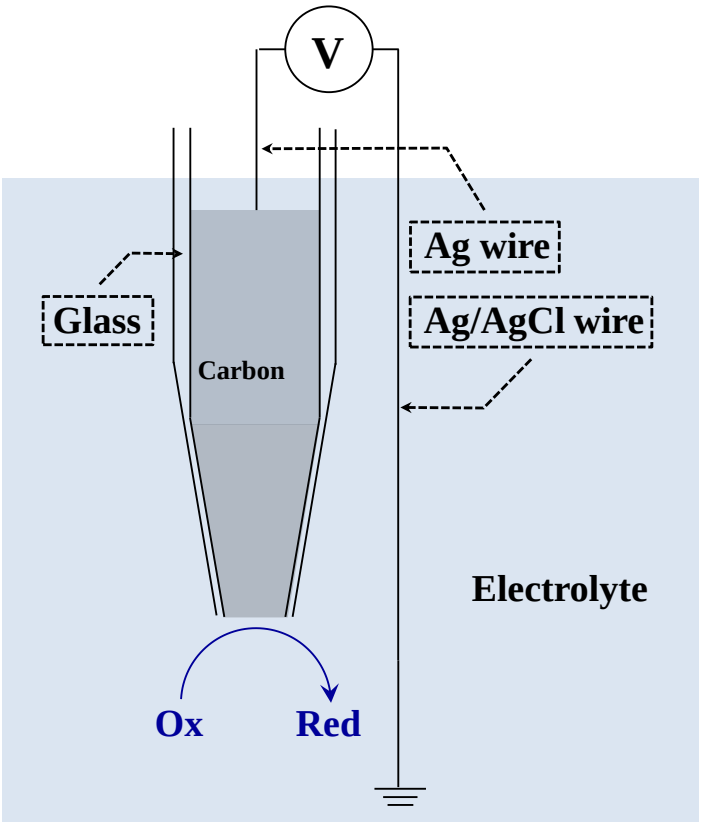

Figure 3.4: A schematic representation of a carbon-filled nanopipette, which is termed a nanoelectrode, performing electrochemical measurement in the electrolyte containing an appropriate redox pair. The oxidised species diffusing to the surface of the nanoelectrode is reduced in the presence of a bias voltage provided via a connected voltage source.

Chapter 4

Nanodosing and detection to probe Alzheimer's disease

4.1 Introduction to Alzheimer's Disease

Dementia is a collective name for a group of diseases that are more common in ageing populations, involving symptoms affecting the daily lives of patients, especially problems concerned with memory, language and perception. Among these, Alzheimer's Disease (AD) is responsible for 60–80% of dementia cases, symptoms of which include short- to long-term memory loss, difficulty acquiring new knowledge, motor coordination problems, disorientation, and even death due to infection [156]. AD is a neurodegenerative disease, which means the loss of neuronal cells develops progressively in the human brain, particularly in the hippocampus and the cerebral neocortex [157]. Thus, certain brain functions are permanently influenced or even completely lost. The cause of AD is still poorly understood, due to the fact that the brain itself is very complex, and currently there is a lack of proper tools to investigate the initial stages of the development of the disease, but extracellular plaques and intracellular tangles are hallmarks of the disease [156].

The role of transmembrane amyloid precursor protein (APP) in the human brain is still unclear. APP is assumed to be proteolytically cleaved by α-secretase and γ-secretase in order

to recycle the used molecules. However, if this cleavage function is activated mistakenly by β-secretase and γ-secretase, a soluble amyloid beta (Abeta) monomer is generated outside the neuron [158]. Multiple monomers self-assemble to form oligomers, fibrils, and then ultimately develop into insoluble Abeta plaques. Various hypotheses concerning the stage at which Abeta aggregates are actually toxic to the neurons have been proposed, but the latest evidence demonstrates it is the small soluble oligomers that cause damage to individual neurons rather than the insoluble form of fibrils or plagues [159].

AD can be classified into two groups, of which the sporadic group accounts for an overwhelming majority and the familial one accounts for the rest. The onset of sporadic AD usually occurs later and is presumably caused by a combination of genetic and environmental factors; however, the real reason is still not confirmed [160]. The risk of onset rises significantly with age, but it is worth noting that AD is not a normal form of ageing. In terms of genetics, it has been discovered that e4 allele of apolopoprotein E gene (APOE-e4) is probably linked to the onset of AD. Its ability to remove Abeta aggregates is weaker than that of its normal form, APOE-e2 allele [161]. The other familial group is closely related to gene mutations, and these crucial gene mutations cause the early onset of AD, e.g. PSEN-1 and PSEN-2 on chromosomes 14 and 1, respectively [162].

It is currently very difficult to identify AD, since brain biopsy is now the only definitive way, although various non-invasive tests, like memory tests and brain-imaging methods are utilised to evaluate a patient's symptoms [163]. Due to the difficulty in diagnosis, the patient is probably unable to notice early symptoms. It is often too late when those symptoms have become significant and are identified in a hospital, because AD gradually progresses over time and the loss of neurons is irreversible. Unfortunately, AD has no current cure, and progression cannot be stopped, since the actual cause of the onset has not been revealed; however, treatments for alleviating or delaying the worsening of symptoms are available. For example, there is medication (acetylcholinesterase inhibitors) to increase the neurotransmitter flow for the remaining neurons [164].

Therefore, the most crucial problem in AD research is to reveal the mechanism by which

a small number of these toxic Abeta oligomers adapt to damage neuronal cells, which is possibly the result of Abeta oligomers binding to specific receptors and/or causing disruptions and forming pores in the cell membrane [165, 166]. Due to the lack of suitable tools to address this nanoscale biological problem, there have not been discoveries showing decisive evidence of how AD initiates its earliest stage, despite decades of research being performed on Abeta. In addition, previous studies focusing on the interactions between Abeta oligomers and neuronal cells have used a concentration of toxic oligomers much higher than in physiological condition; e.g. only roughly 0.5 pM is present in AD-diagnosed cerebrospinal fluid (CSF) [167, 168]. CSF, of which there is approximately 125-150 mL in the whole body, is a transparent body fluid produced in the brain and it is isolated from blood, which circulates in the ventricular system in the brain and spinal cord and efficiently refreshed 4-5 times a day [169]. CSF contains very few (0.3%) proteins and is similar to blood plasma, providing mechanical protection for the brain and buffering abrupt pH changes in the cerebral blood flow [170–172]. Previous studies have shown that Abeta oligomers in CSF induce long-term potentiation (LTP), but this can be prevented by the application of Abeta antibodies *in vivo* [173]. The toxicity of naturally-secreted Abeta oligomers is preserved in CSF [174], so CSF from AD-diagnosed patients without additional preparation will be appropriate for direct use with experimental samples.

The nanodosing biophysical method based on the SICM technique is a powerful way to investigate the response of individual cells under localised dosing. Therefore, in this chapter, how calcium homeostasis is influenced by extracellular artificially-synthesised and naturally-secreted Abeta42 peptides was investigated. In addition, effects of the application of antibodies and/or nanobodies, which are specifically designed in order to bind various termini or epitope segments of toxic oligomers to reduce or eliminate their toxicity, are also discussed in detail in the following sections. It should be noted that the work present in this chapter was performed and analysed in collaboration with Dr Anna Drews.

4.2 Materials and Method

4.2.1 Protocol for the localised nanodosing of neuronal cells

The technique of localised dosing of reagents loaded in a nanopipette, which is one of the applications of SICM, can be adopted for the investigation of the initial mechanism by which toxic aggregates act on neuronal cells. SICM is capable of contactless topographic scanning, and during the process, the dynamic separation between the nanoipette tip and the substrate is precisely controlled by the system monitoring the ion current flowing through the nanopipette aperture to the bath electrode [11]. Therefore, by taking advantage of this property of SICM, the automated nanopipette can be utilised to estimate the distance between the nanopipette tip and the glass substrate or the cell surface, and simultaneously deliver the studied oligomers via the application of biased voltage and/or pressure onto the target [109]. The nanodosing protocol for maintaining the nanopipette at a certain height is shown in Figure 4.1, and explained as follows:

(1) Firstly the nanopipette is made to approach any location on the glass substrate in proximity to the target cell by the vertically-aligned stepper motor, while the piezoelectric actuator, which is installed upside-down as described in Chapter 2, is also turned on with a suitable setpoint to avoid a tip crash. The piezoelectric actuator is adjusted to move roughly 1 μm above the glass, by the piezoelectric actuator, in order to guarantee it will fall an observable and maximised working distance. Note that the working distance of the piezoelectric actuator is 25 μm, and the full range of applied voltage is 10 V. Therefore, the voltage shown by the PC oscilloscope will fall from 10 V to 9.6 V, to demonstrate a movement of $0.4 \times 2.5 = 1\,\mu$m.

(2) Subsequently, the nanopipette is lifted an additional 24 μm up (the working distance of the piezoelectric actuator is 25 μm; thus, 24 μm is left after it has been raised 1 μm).

(3) The nanopipette is moved directly above the targeted cell by a manual adjustment of the bidirectional micromanipulators on the homemade microscope stage.

(4) The nanopipette then comes down to the surface of the target cell at a piezo-controlled

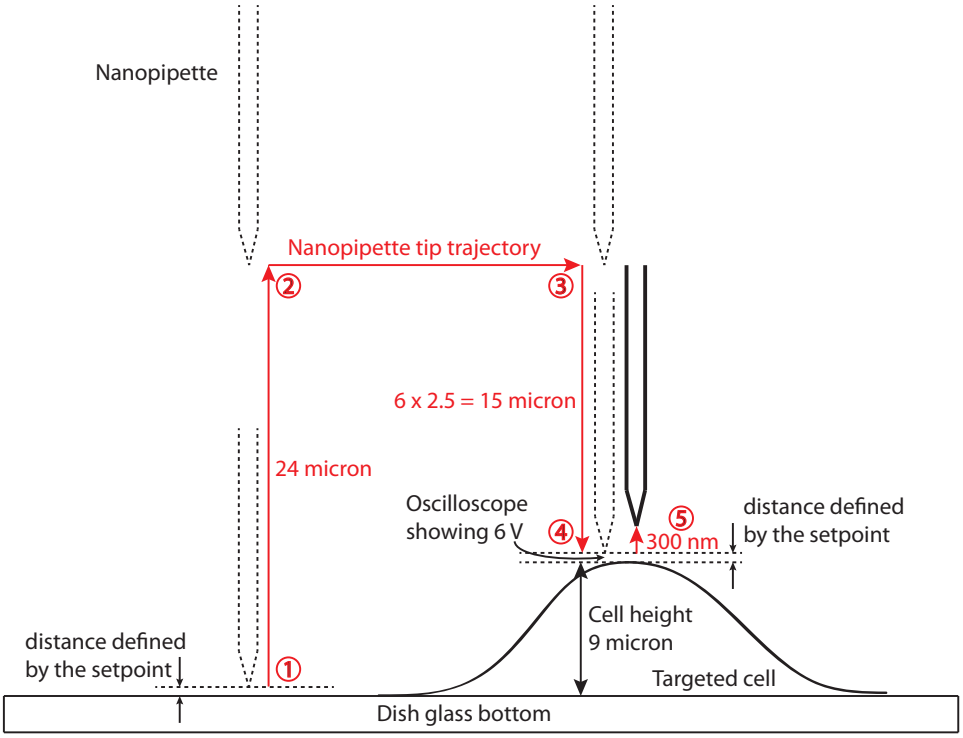

Figure 4.1: Schematic explanation of the protocol of the nanodosing method. Red arrows and lines noted with numbers describe the trajectories of the tip of the nanopipette. Firstly the nanopipette tip approaches via the stepper motor the glass dish bottom to sit at a working distance on the z-axis piezoelectric actuator, where 1 μm out of 25 μm is approximately spent. Afterwards, the nanopipette is lifted 24 μm up and then moved above the targeted cell. Subsequently, the computer-controlled z-piezo actuator is used to approach the surface of the cell automatically within the predefined setpoint. For example, if the cell has a height of 9 μm, the nanopipette tip would fall by 15 μm, and the relative difference in the applied bias voltage would be 6 V. Consequently, the nanopipette tip is further raised by 300 nm and stays there for the next stage of reagent dosing conducted by the additional application of appropriate bias voltage and pressure on the nanopipette.

distance defined by the setpoint. For example, if the cell height is 9 μm, the PC oscilloscope will show that the actuator is now applied at 6 V, which means the tip has moved 6 $\times$ 2.5 = 15 μm from 24 μm above the cell.

(5) Consequently, the height of the cell relative to the glass bottom has become a known quantity, and an extra 300 nm is added to the separation between the tip and the cell top, so that the molecules in the studied reagent are able to reach the cell surface by diffusion, reducing the opportunity for any mechanical ion channels to be triggered due to hydrostatic force/pressure applied from the nanopipette. It is worth mentioning that this nanopipette

dosing method is superior to the bath application, because the much higher local flux of molecules from the nanopipette results in an application of a very low concentration of the reagent onto an individual cell.

The benefit of this nanodosing method is that one can perform quantitative delivery of oligomers via the nanopipette onto the targeted cell. An estimation of the number of oligomers being dosed per unit of time, N_{total}, can be calculated using the mathematical model of the flow rate, Q_{total}, introduced in Chapter 3:

$$N_{total} = c_0 Q_{total} = (\mu_{ep} + \mu_{eo}) c_0 \pi r_i \tan\theta \Delta V + \frac{3\pi c_0 r_i^3 \tan\theta}{8\eta} \Delta P, \tag{4.1}$$

where c_0 is the concentration of the reagent in the nanopipette, which is Abeta42 oligomer plus Abeta42 monomer in the experiment. Assuming a borosilicate glass nanopipette is used and immersed in the buffer solution containing 150 mM sodium ions, μ_{eo} is estimated to be $1.4\times10^{-8}\,\mathrm{m^2 V^{-1} s^{-1}}$. The μ_{ep} is strongly influenced by the ingredients of the buffer solution and differs depending on whether it is fluorescently-labelled or not. For unlabelled Abeta42 oligomer plus monomer dissolved in 10 mM tris(hydroxymethyl)aminomethane (Tris) solution, μ_{ep} is roughly $-2\times10^{-8}\,\mathrm{m^2 V^{-1} s^{-1}}$ for oligomers. Therefore, N_{total} is estimated as follows for a nanopipette with r_i of 100 nm, θ of 3°, ΔP of 15 KPa, η of 1 mPa·s and ΔV of –200 mV:

$$\begin{aligned} N_{total} &= c_0(-2\times10^{-8} + 1.4\times10^{-8})100\pi \times 10^{-9}\tan(3^\circ) + c_0 \frac{3\pi(100\times10^{-9})^3 \tan(3^\circ) 15\times10^3}{8\times10^{-3}} \\ &= 9.38\times10^{-16} c_0. \end{aligned} \tag{4.2}$$

This also provides a good approximation of the number of oligomers dosed on the cell during the experiment. For example, around 280 per second for a nanopipette with r_i of 100 nm and 500 pM oligomers and 2 per second with r_i of 50 nm and 30 pM oligomers. Thus, careful control of the aperture size of the nanopipette allows individual Abeta42 oligomers to be delivered onto the target each second, realising a true single-molecule experiment. Ow-

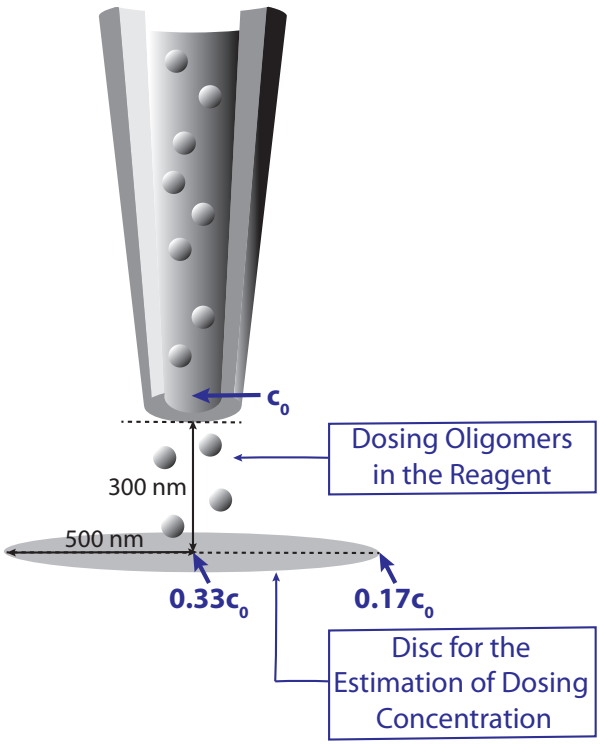

Figure 4.2: Schematic of the distribution of dosed oligomers. C_0 is the concentration of reagent loaded in a nanopipette. After leaving the nanopipette tip, C_0 quickly drops to 0.33 C_0 within 300 nm. presumably it is possible to imagine a dosing disc with a radius of 500 nm, and the diffused oligomers at the rim of this disk would be decreased to a concentration 0.17 C_0. Theoretical models for estimating these concentrations at various locations are discussed in Chapter 2.

ing to the fact that those oligomers are diffused away when leaving the nanopipette tip, their concentration quickly drops. Assuming the diffusivity of Abeta42 is approximately $1.7 \times 10^{-6}\, cm^2 s^{-1}$, and Q_{total} is $-1.16 \times 10^{-16}\, m^3 s^{-1}$, in the case of a nanopipette tip placed 300 nm above the target, according to Equation 3.23, the oligomer concentration on the cell surface right under the tip is calculated to be $0.33c_0$. Similarly, on the periphery of an imaginary disc 500 nm away from this point, the concentration is $0.18c_0$ according to Equation 3.22, which is roughly half of the concentration at its centre point right under the tip, as shown in Figure 4.2. If the aperture radius of the nanopipette and the concentration of reagent are carefully controlled, e.g. 50 nm and 30 pM, a rate of two individual units of Abeta42 encountering the dosed cell per second can be realised.

4.2.2 Cell preparation

Astrocytes used in the experiment were selected by the nanopipette from a mixed glial preparation from P3–P4 rat, which was cultured for 2 weeks in 75 cm^2 cell culture flasks (Corning) with Dulbecco's Modified Eagle's medium (DMEM, Invitrogen) supplemented with 10% fetal bovine serum (FBS), 1% Penicillin and Streptomycin and 1% L-Glutamine (Life Technologies) in an incubator kept at 37°C, where 5%CO_2 was maintained through a delivery tube in a humidified atmosphere.

Once 90% confluence of glial cells was achieved, cells were split and kept in a suitable environment for a long-term culture. According to the schedule of performing experiments, neuronal cells were transported in order to reach a 40–70% confluence, in 35 mm dishes with No. 1 coverslip of 14 mm glass dismeter at the bottom (P35G-1.0-14-C, MatTek). Plated dishes were used for experiments within 1–5 days, and it was possible for their confluence to increase to a level not feasible for single cell measurements afterwards.

Before the measurements, glial in the cultured dishes were immersed in L-15 containing 1.26 mM of calcium ions and 300 μM 2-Methyl-6-(phenylethynyl)pyridine (MPEP) (Sigma Aldrich), which is a highly selective metabotropic glutamate receptor 5 (mGluR5) antagonist and is capable of reducing calcium oscillations owing to communication between astrocytes. The nanopipette was filled with the required concentrations of Abeta42 oligomers or CSF in the presence of antibodies and/or nanobodies in L-15 with a total volume of 1.5 mL. 2 μM ionomycin (Sigma Aldrich) was added to L-15 as a positive control group.

4.2.3 Fluorescent Calcium Indicator: Fluo-4 AM

Once the stimulation of the targeted cell, i.e. toxic oligomers delivered from the nanopipette, can be reproducibly generated, the response of the dosed cell can be measured via a biosensor or monitored by recording the behaviour of a pre-loaded fluorescent dye. In the study in this chapter, a green fluorescent indicator for calcium influx into the cell was used, as shown in Figure 4.3, and its fluorescent intensity was examined via an inverted Plan Apo VC water

immersion 60× objective lens (MRD07601, Nikon).

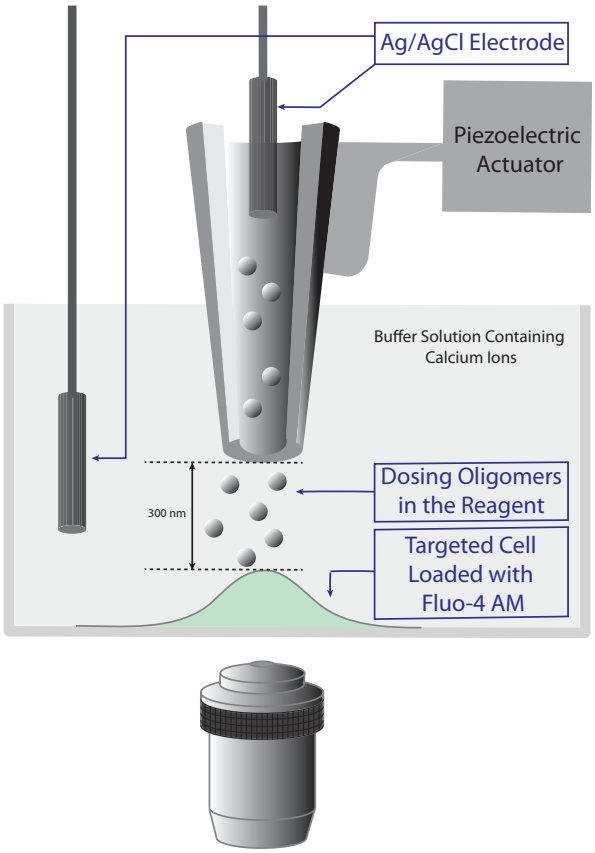

Figure 4.3: Illustration of the simplified setup for performing nanodosing, with a piezoelectric actuator-controlled nanopipette responsible for the delivery of toxic oligomers (e,g, Abeta42 oligomers) onto a targeted cell 300 nm above the cell, which has been loaded with Fluo-4 AM for monitoring the intracellular transient calcium behaviour collected by a suitable objective lens. It should be noted that calcium ions are present in the buffer solution to observe whether calcium influx occurs.

Fluo-4 (λ_{ex} 494 nm; λ_{em} 506 nm, Life Technologies) is a calcium indicator, which is utilised for live-cell labelling and demonstrates roughly more than a 100-fold increase of fluorescence intensity in response to the binding of calcium ions, with a negligible spectral shift, upon excitation by a 488 nm blue diode laser. Fluo-4 is an upgraded version of Fluo-3 with intrinsically higher fluorescence intensity, and it therefore shows a better signal-to-noise ratio. It is usually used for observation of the spatial and temporal distribution of calcium ions in micro-environments, especially flow cytometry, fluorescence live-cell imaging and confocal microscopy. Its acetoxymethyl (AM) ester derivative turns Fluo-4 AM into an uncharged and cell-permeate molecule, so it is capable of passing through the cell membrane easily. As

soon as Fluo-4 AM is inside the cell, it is cleaved by esterases in the cell to become charged. In addition, hydrolysis is required for the esterified groups to bind calcium ions, and its K_d in buffer is approximately 335 nM, providing a useful affinity.

In terms of preparation, Fluo-4 AM is reconstituted in dimethylsulfoxide (DMSO) as suggested by the instructions. 10 μL of solution is added into a vial of Fluo-4 AM and then aliquoted, stored in a -20° freezer. Immediately before the experiment, 1 μL of the aliquot is mixed with 1.5 mL of cell-culture medium (L-15, Life Technologies) to make 2.3 μM Fluo-4 AM solution and added to an L-15-washed cell-loaded glass-bottom dish for labelling. After 10–15 minutes, it is washed twice again with L-15 and then the dish should be ready for measurements.

4.2.4 Abeta42 preparation

Abeta monomer, Hilyte Fluor 647 ABeta42 (Cambridge Bioscience LDT), was kept on ice and subsequently purified using a BioSep gel filtration (SEC-s2000, Phenomenex) in buffer solution, SSPE (0.01 M Na_2HPO_4, 0.15 M NaCl, 1 mM EDTA, pH 7.4). Afterwards, the filtered product was flash frozen and stored in a –80°C freezer. Peptides were always prepared fresh right before the cell-dosing measurements. The purified Abeta42 was diluted to 500 nM in PBS and left shaking at 37°C, at 200 rpm for 5 hours in an incubator. Consequently, it was centrifuged at 1450 ×g for 10 minutes and then diluted to the required concentrations in L-15 cell culture medium. The concentration of oligomers have been confirmed by a single-molecule counting method using confocal two-color coincidence detection (cTCCD). This protocol gave approximately of 3 nM Abeta42 oligomers developed from 500 nM of Abeta42 monomers [175]. Human cerebrospinal fluid (CSF) was used as received without further preparation steps.

4.2.5 Antibodies and nanobodies

The preparation of the bivalent Abeta42 antibody against the N-terminus, Bapineuzumab (Bapi), is described in US patent US 7179892 B2 by Medimmune. It is stored in 25 mM of Histidine, 7% Sucrose, 0.02% Polysorbate 80, pH 6.0 at 48 mg/mL with endotoxin levels lower than 0.005. On the other hand, the Asyn antibodies by Medimmune, asyn0004, aslo0071 and aslo0252, bind to NAC domain, N terminus and C terminus of Asyn with K_D of 70.0, 49.7 and 25.4 nM, respectively.

Nb3 is an Abeta nanobody targeting both Abeta40 and Abeta42 at epitopes 17–28 with K_D of 150 nM, whilst Asyn nanobody Nbsyn87 binds to Asyn residues 118–130 with K_D of 42 nM. They were isolated from a llama (Lama glama) using the immunisation of Abeta40 and human Asyn, respectively, followed by the selection of a phage display and processes of amplification, recloning, expression in the *Escherichia coli* (*E. coli*) and purification, according to protocols that have been published [109].

4.3 Experimental results and discussion

4.3.1 Nanodosing of Abeta42 incubated with antibodies on astrocytes

It is important to investigate physiological concentrations of oligomeric Abeta42 initially inducing toxic effects in astrocytes, which may ultimately trigger the onset of AD. The experiments began with the local nanodosing of oligomeric Abeta42 with a relatively high concentration using a nanopipette onto single astrocytes, whilst their calcium homeostasis was monitored by Fluo-4 AM fluorescence. In the cell preparation, MPEP, an mGluR5 blocker, was added to the cell dish in order to prevent calcium oscillations resulting from interactions between astrocytes, so the experimental cell model was simplified and constrained in a single astrocyte. As shown in Figure 4.4, fluorescence inside a single astrocyte was integrated to demonstrate the total fluorescence at each time point of recording. Firstly,

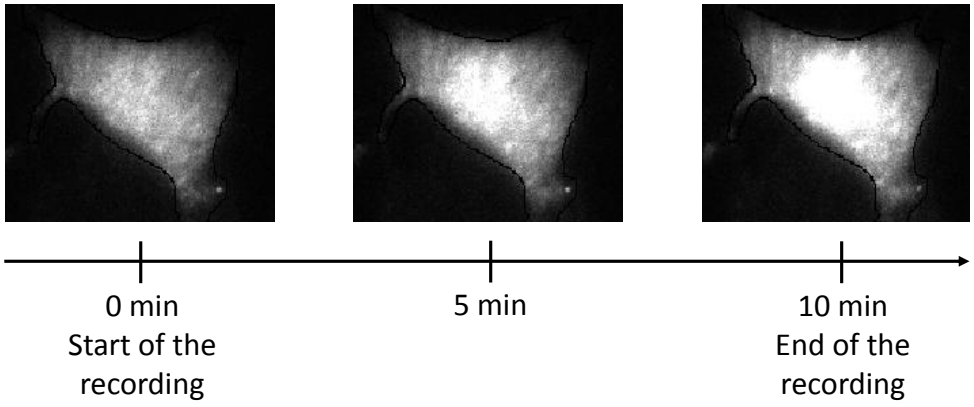

Figure 4.4: Three frames taken at the start, during the middle and at the end of the recording of fluorescence in a single astrocyte being locally nanodosed by 500 pM Abeta oligomers from a nanopipette located 300 nm above. The intensity of the fluorescence increased continuously owing to more and more calcium-sensitive dyes preloaded in the astrocyte being activated over time. The black peripheral around the astrocyte was drawn for the integral of fluorescence inside the area at a specific time point of recording. Note that each pixel in the CCD camera did not reach saturation during the recording.

the nanopipette filled with L-15 only was used to perform a negative control (NC), whilst 2 μM of ionomycin in L-15 was used as a positive control (PC). Ionomycin is an ionophore of calcium ions, i.e. a lipid-soluble calcium importer located across the cell membrane, used to raise the intracellular calcium levels significantly, which is presumably much more efficient than Abeta42 oligomers [176]. However, the amount of Fluo-4 AM taken into each astrocyte, and the calcium flow, is also highly variable in each case. So, it is only meaningful when comparisons are based upon the fluorescence transient (I_f(t)) being normalised in each astrocyte by the calcium influx or efflux measured relative to t=0 (I_{f_0}) during the 10 minutes of fluorescence acquisition, i.e. (I_f(t)-I_{f_0})/I_{f_0}. Even so, the distribution of the normalised fluorescence curves in individual astrocytes was still variable, as shown in Figure 4.5(a), Figure 4.5(b) and Figure 4.5(c). Thus, those curves were further averaged, i.e. only averaged behaviours of astrocytes were adopted for the investigation, in various experimental conditions, and they were arranged together in Figure 4.5(d). Here 500 pM of Abeta42 oligomers were loaded in a nanopipette, as shown in Figure 4.5 (c), and its values fell between L-15 NC and ionomycin PC, which suggests Abeta42 oligomers could induce calcium influx into astrocytes but the efficiency was not as good as that in ionomycin. It is easier for compari-

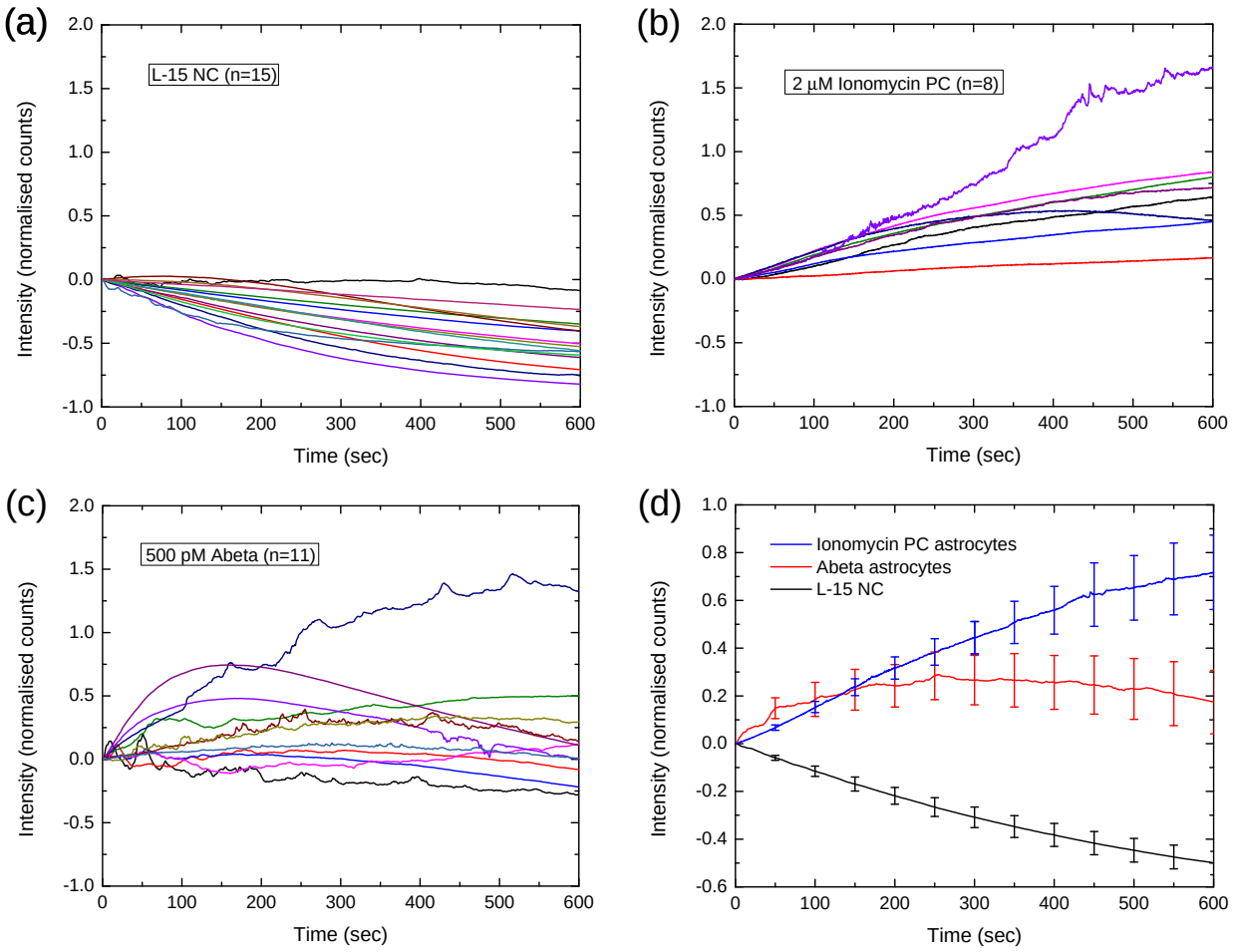

Figure 4.5: Normalised fluorescent transients of individual astrocytes loaded with Fluo-4 AM recorded within 10 min of (a) cell culture medium L-15 as a negative control (NC); (b) 2 μM ionomycin as a positive control (PC); (c) 500 pM Abeta42 loaded into a nanopipette to perform the nanodosing experiment maintained at 300 nm above the targeted astrocyte incubated with MPEP. (d) Averaged fluorescent behaviour in timecourse of L-15, 2 μM ionomycin and 500 pM Abeta42. Error bars are standard error of mean (SEM), shown every 50 seconds.

son between different results to integrate the normalised fluorescent transients within the 10 min measurement, as shown in Figure 4.6, which clearly demonstrates the behaviours of the calcium net flow in different conditions. Note that in the case of NC, where there was only L-15 in a nanopipette, a curve was generated with a negative slope. This was not because calcium ions flowed out of astrocytes; but possibly due to photobleaching of the dye and/or the loss of dye from inside an astrocyte. Therefore, in the following figures, all histograms had been corrected using this L-15 NC.

In Figure 4.5 and Figure 4.6, the nanodosing methodology had proven to be working,

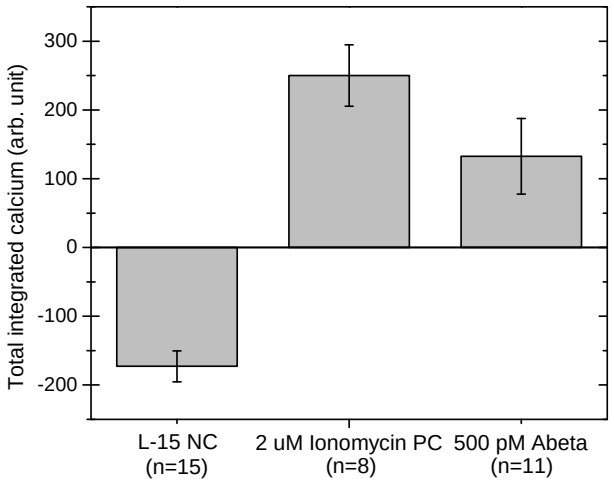

Figure 4.6: Histogram of averaged total integrated calcium flowing into astrocytes versus L-15 as NC, 2 μM ionomycin as PC and 500 pM Abeta42 oligomers. Abeta in the figure denotes Abeta42. Error bars are SEM, and n is the measured number of cells.

so Abeta42 oligomers locally dosed onto astrocytes would induce calcium influx. PC and NC set the upper and lower boundaries of fluorescence transients caused by calcium flow, respectively. Therefore, the next stage would be an investigation of how this abnormal calcium influx can be reduced or blocked by specific antibodies and nanobodies binding to various parts of those toxic Abeta42 oligomers. Therefore, various antibodies and nanobodies which are capable of binding different termini or epitopes of Abeta42 and Asyn were selected. A humanised monoclonal antibody, Bapineuzumab (BAPI), which bivalently binds to the N-terminus of Abeta42, and Nb3, which has a monovalent nanobody designed to be able to bind to epitopes 17-28 of Abeta42, with K_d of 13 nM for Abeta42 monomers both specific binding to Abeta42, were chosen in the blocking experiments [109, 177]. Note that a nanobody is even smaller than a heavy-chain only antibody but without decreasing binding capacity, so this antibody fragment naturally has a volume of approximately $\leq 1/4$ of a typical antibody [178]. On the other hand, alpha-synuclein (Asyn), whose aggregates are responsible for Parkinson's Disease (PD), is plentiful in the human brain, especially in the presynapse of neurons and it is believed to function as a supportive agent relevant to neurotransmitters [179, 180]. In the past, Asyn was not considered an intracellular protein, but researchers have found that a small portion of Asyn monomers made by the SNCA gene can be secreted out of the cell via exocytosis [181]. There is also evidence showing that Abeta and Asyn

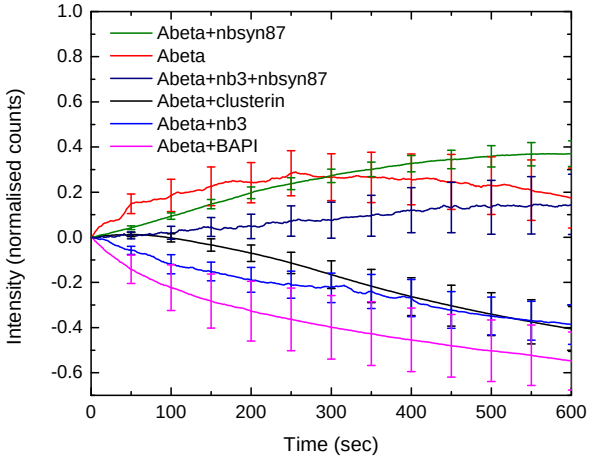

Figure 4.7: Average of normalised fluorescent transients of astrocytes loaded with Fluo-4 AM recorded within 10 min with various experimental conditions. Reagents filled in a nanopipette to perform nanodosing experiments maintained at 300 nm above the targeted astrocytes incubated with MPEP are 500 pM of pure Abeta42 and its mixture with 2 μg/mL clusterin, 150 nM Nb3, 150 nM Nbsyn87, 150 nM Nb+ plus Nbsyn87 and 150 nM Abeta42-specific antibody Bapineuzumab (Bapi). Abeta in the figure denotes Abeta42. Error bars (SEM) are shown every 50 sec.

could co-interact *in vitro* [182, 183] and form co-oligomers using the molecular simulation [184, 185], which might also play a role in the cell toxicity, in addition to Abeta and Asyn oligomers. Therefore, it is also worth trying antibodies and nanobodies against Asyn. An Asyn nanobody, Nbsyn87, binding to Asyn epitope residues 118–130 with K_D of 42 nM, was adopted for testing. Moreover, here, clusterin was also examined, as it is an extracellular molecular chaperone in humans, which binds misfolded protein oligomers and aggregates at a physiological concentration [174].

After a homogeneous mixture of 150 nM of various antibodies and nanobodies, or 2μg/mL clusterin in L-15 containing 500 pM Abeta42 was incubated within 10-15 min at room temperature, those reagents were added to a nanopipette separately, so that the nanodosing experiments could be performed. As shown in Figure 4.7, obviously, two groups, one with increasing fluorescence intensity and the other with decreasing fluorescence intensity over the course of time, were observed in these 6 samples, where the red line denoted there was only 500 pM of Abeta in L-15 so was represented as a PC here.

The fluorescence transient within 10 minutes of video recording was integrated and shown

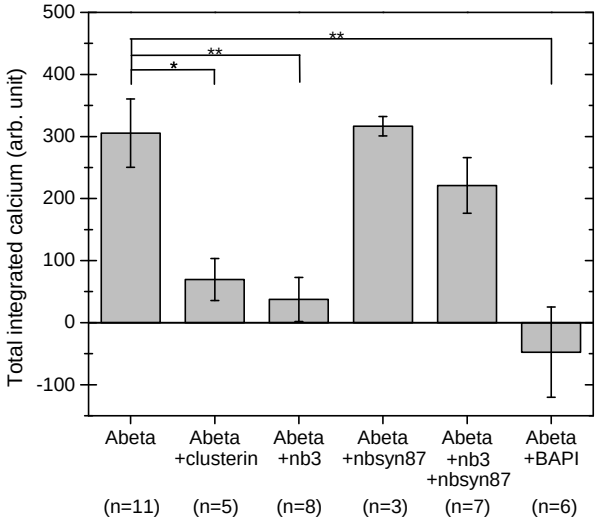

Figure 4.8: Histogram of averaged total integrated calcium influx of astrocytes loaded with Fluo-4 AM recorded within 10 min with various experimental conditions. Reagents filled in a nanopipette to perform nanodosing experiments maintained at 300 nm above the targeted astrocyte incubated with MPEP are 500 pM of pure Abeta42 and its mixture with 2 μg/mL clusterin, 150 nM Nb3, 150 nM Nbsyn87, 150 nM Nb3 plus Nbsyn87 and 150 nM Abeta42-specific antibody Bapineuzumab (Bapi). Abeta denotes Abeta42, whilst n is the sample size. Error bars are SEM, and n is the measured number of cells.

in the histogram in Figure 4.8. The addition of 2 μg/mL of clusterin and 150 nM of Nb3 and 150 nM of Bapi demonstrated statistically different results compared to the Abeta42-only control group. 500 pM of Abeta42 oligomers is more than approximately 1000 times higher than the physiological condition, but 2 μg/mL of clusterin was still able to bind effectively to them, as a previous study showed that clusterin has a high affinity for synthetic Abeta42 oligomers [109]. This confirmed that the removal of those toxic oligomers of Abeta42 could reduce or prevent the abnormal calcium influx into astrocytes, which is responsible for altered calcium homeostasis. Nb3 and Bapi also exhibited statistically-significant outcomes for effective blocking of Abeta42 oligomers from entering astrocytes. This is reasonable because these two antibodies and nanobodies were designed to bind specifically to Abeta42, and this result has therefore made them both candidates for alleviating the toxicity of oligomers in CSF. It is also not surprising that Nbsyn87, which was specifically designed against Asyn, was not observed to be working on binding Abeta42 oligomers. However, it is very surprising that the mixture of Nbsyn87 and Nb3 in the reagent containing Abeta42 oligomers greatly degraded the blocking efficiency of Nb3.

From the results above, the nanodosing methodology has been successfully utilised as a platform for examining the effectiveness of antibodies and nanobodies in reagents containing Abeta42 oligomers with a relatively high concentration (500 pM). It is more critical in solving biological problems if a subtle change of calcium influx caused by Abeta42 oligomers at a physiological concentration (∼pM) is detectable in the nanodosing system. Much lower concentrations of Abeta42 oligomers, from 2.5 nM down to the physiological 500 fM, were tested using the same protocol here by A. Drews *et al.* [109]. This result clearly showed that even at as low as 500 fM, the nanodosing system was still sensitive enough to reveal this tiny amount of excess calcium influx induced by Abeta42 oligomers, demonstrating a statistical significance in the calcium influx compared to the NC.

4.3.2 Nanodosing of CSF incubated with antibodies and nanobodies on astrocytes

It is clinically essential to apply this nanodosing methodology on CSF of AD-diagnosed patients, in order to understand if antibodies and nanobodies function effectively *in vitro*. Although successful blocking of oligomers by specific antibodies and nanobodies examined using the nanodosing method does not guarantee they will work in precisely the same way in the brain, there is certainly a higher chance to treat AD patients successfully if antibodies and nanobodies are able to act against those complex toxic oligomers in CSF. In other words, this should constitute the stage before expensive clinical trials are conducted.

The CSF samples were obtained from both male and female AD patients between the ages of 62 and 82, and there were also control samples taken from healthy individuals, both males and females between the ages 45 and 71. The details for AD CSF are listed in Table 4.1. The integrated calcium influxes of AD patients and healthy subjects measured for astrocytes using the nanodosing method are shown in Figure 4.9(a) and Figure 4.9(b), respectively. The calcium influx for each person was variable, no matter whether the subject was an AD patient or not, but the statistics, which give averages for all individuals, show that CSF in AD patients and healthy controls had indistinguishable outcomes for CSF

Table 4.1: List of AD CSF used in the experiments and its corresponding characteristics including volume (Vol), gender (M for male and F for female) and age.

AD CSF	734c	720c	554b	784c	390d	757c	708c	872c	722c	725c	557b	715c
Vol (mL)	0.5	0.5	0.4	0.5	0.5	0.5	0.5	0.3	0.5	0.5	0.9	0.2
Gender	M	F	F	F	M	F	F	F	M	F	F	M
Age	75	75	80	62	77	63	71	85	77	69	82	72

influx. This result suggests there may exist a comparable amount of toxic oligomers in each person's CSF, no matter whether one is healthy or diagnosed with AD, which is consistent with the enzyme-linked immunosorbent assay (ELISA) measurements, showing no statistical difference between AD patients and healthy controls [167, 168].

Reducing calcium influx induced by Abeta42 oligomers is a potential method for treating AD or delaying the onset of AD. Therefore, 2 μg/mL of clusterin was first tested on AD CSF to find out whether the altered calcium influx was induced by misfolded protein aggregates or by other toxic species in CSF. Due to the fact that each AD CSF gave a wide distribution of the averaged value of the total integrated calcium as shown in Figure 4.10(a), it is easier to discuss the relative calcium reduction, which means the percentage of reduced calcium influx caused by antibodies or nanobodies, which is normalised to the original calcium amount induced by oligomers in the same AD CSF sample, as shown in Figure 4.10(b). Two of the four AD CSF samples (734c and 784c) worked very well with clusterin, whilst the others (720c and 554b) showed no significant difference. The overall outcome is shown in Figure 4.10(c) and suggests 2 μg/mL of clusterin could remove a certain level of oligomeric aggregates in AD CSF, which is similar to the effect of clusterin on synthetic Abeta42 oligomers shown in the previous section. This therefore indicates that at least one kind of misfolded protein aggregate is responsible for the calcium influx observed in astrocytes. Two objectives, finding out which toxic oligomers were responsible for the altered homeostasis and which antibodies and nanobodies could effectively block this abnormal early-stage calcium influx into astrocytes, were set and it is hoped that they were achieved in the following experiments.

Recombinantly produced nanobodies, Nb3 and Nbsyn87, which were designed specifically for Abeta42 and Asyn, respectively, were used in the CSF nanodosing experiments. In

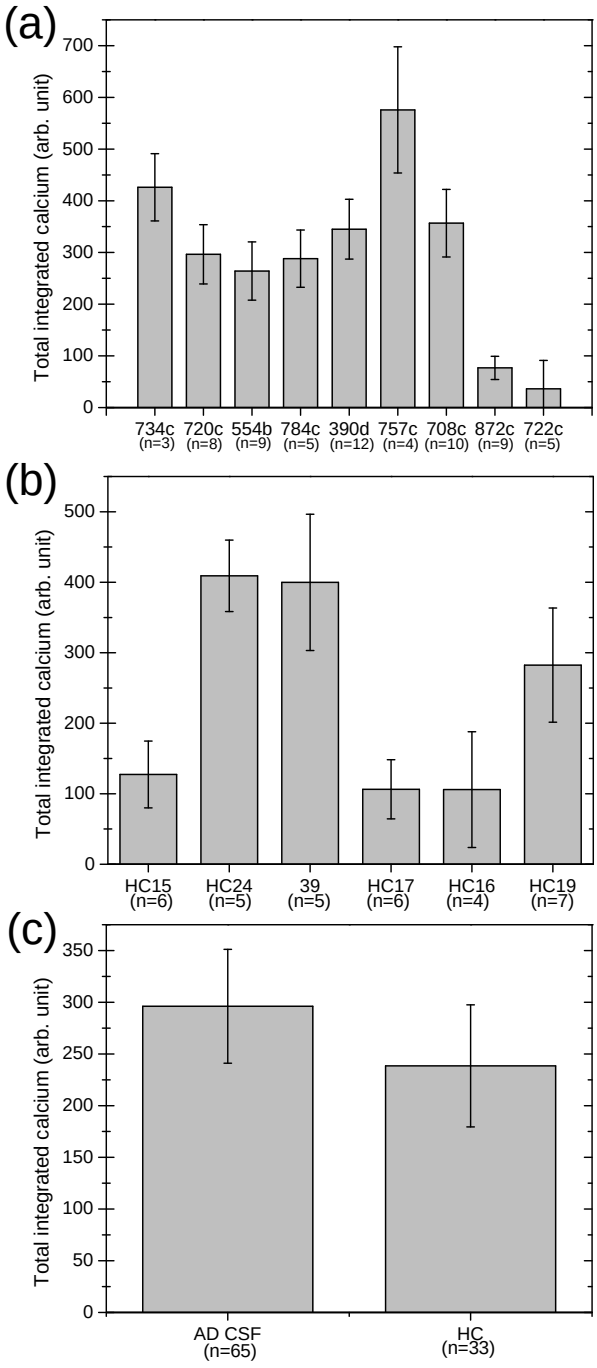

Figure 4.9: Histogram of the total integrated calcium in averaged fluorescent transients of single astrocytes locally dosed by a nanopipette filled with (a) individual clinically-diagnosed AD CSF, 734c, 720c, 554b, 784c, 390d, 757c, 708c, 872c and 722c, (b) individual healthy control (HC), HC15, HC24, 39, HC17, HC16 and HC19, and (c) their corresponding integral behaviour for AD CSF and HC. Error bars are SEM, and n is the measured cell number.

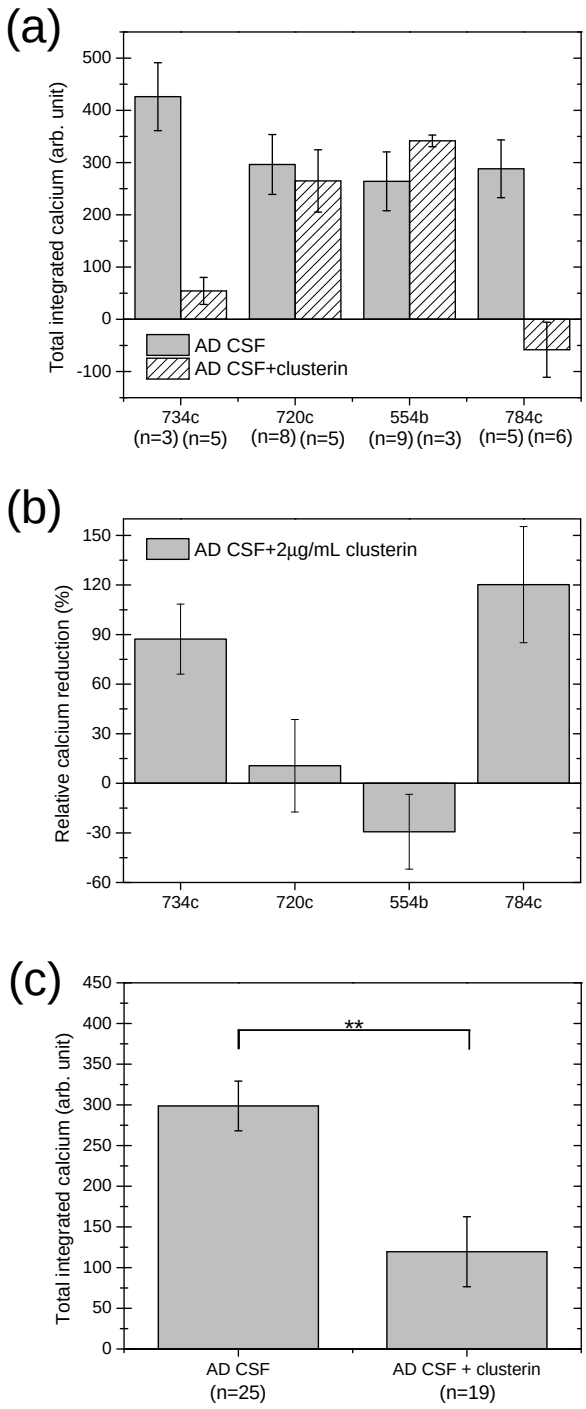

Figure 4.10: Histogram of the total integrated calcium in averaged fluorescent transients recorded within 10 min of single astrocytes being locally dosed by a nanopipette filled with (a) individual AD CSF, 734c, 720c, 554b, and 784c and the homogeneous mixture incubated with $2\,\mu$g/mL clusterin. (b) Relative calcium reduction in percentage after the addition of $2\,\mu$g/mL clusterin in individual AD CSF described in (a). (c) Overall behaviour of the integrated calcium of AD CSF listed in (a) and this AD CSF plus $2\,\mu$g/mL clusterin, which displays a statistical significance between these two conditions. Error bars are SEM, and n is the measured number of cells.

the results for the blocking of Abeta42-induced calcium influx in astrocytes in the previous section, it was demonstrated that Nb3 could bind Abeta42 oligomers effectively, and Nbsyn87 could not. The outcomes for AD CSF incubated with Nb3 and Nbsyn87 are shown in Figure 4.11 and Figure 4.12, respectively. Values for those abnormal calcium influxes in different AD CSF samples and with the addition of Nb3 (Figure 4.11(a)) and Nbsyn87 (Figure 4.11(b)) were still highly variable, but their relative calcium reductions (Figure 4.11(b) and Figure 4.12(b)) both clearly displayed successful calcium blocking of respective AD CSF samples, with Nb3 showing a superior blocking effect for oligomers. This suggests that AD CSF contains more than one kind of toxic oligomer leading to an abnormal calcium influx, with co-oligomers formed by Abeta42 and Asyn or Asyn oligomers alone being able to play a role in producing this calcium influx. Notably Nb3 worked in both AD CSF and HC samples, which suggests AD CSF and HC samples both contain oligomers composed, at the very minimum, of Abeta42 oligomers and this confirmed once again that healthy and AD-diagnosed individuals may both have oligomers in CSF that are toxic to cells. Overall behaviours of Nb3 (Figure 4.11(c)) and Nbsyn87 (Figure 4.12(c)) could both be statistically significant in reducing excess calcium influx when they were pre-incubated for 10–15 min with CSF. On the other hand, the outcome of the combination of these two nanobodies, Nb3 and Nbsyn87, which worked separately in AD CSF, was intriguing, because it resulted in a noneffective blocking effect in AD CSF 390d, so very little reduction of toxic oligomer-induced extra calcium influx was observed. This result is consistent with the experiment, in which a mixture of Nb3 and Nbsyn87 was incubated together with synthetic Abeta42 oligomers, although in this case the only possible source of Asyn is the cell itself.

Next, the Abeta42 antibody, Bapi, which was the most effective in blocking abnormal calcium influx induced by synthetic Abeta42 in the previous section, was tested on the CSF of different AD patients. The results were shown in Figure 4.13(a). Surprisingly, even though it largely deceased the amount of excess calcium flowing into astrocytes by blocking a large portion of the 500 pM synthetic Abeta42 oligomers, the 150 nM of Bapi with AD CSF demonstrated much less reduction or even no effect at all, which is clearly shown in the relative calcium reduction in Figure 4.13(b). Overall the behaviour of Bapi in different

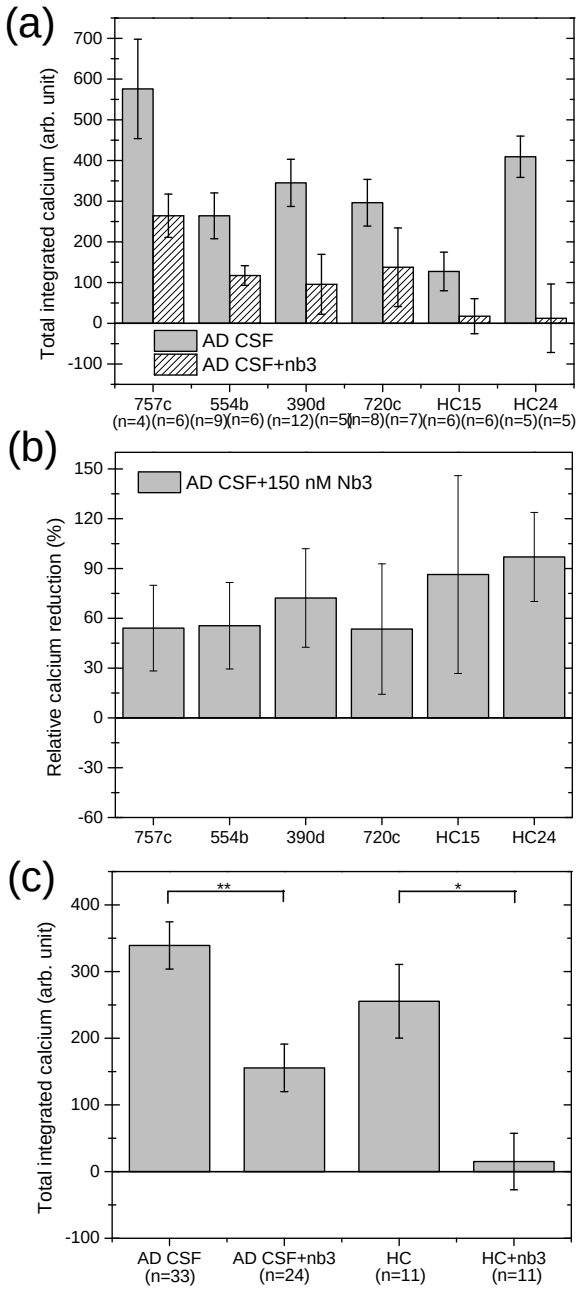

Figure 4.11: Histogram of the total integrated calcium of averaged fluorescent transients recorded within 10 min of single astrocytes being locally dosed by a nanopipette filled with (a) individual AD CSF, 757c, 554b, 390d and 720c, and HC, HC15 and HC24, with their corresponding mixture with 150 nM Nb3. (b) Relative calcium reduction in percentage after the addition of 150 nM Nb3 in individual AD CSF described in (a). (c) Integral behaviour of the integrated calcium of AD CSF and HC listed in (a) and these samples plus 150 nM Nb3, where there is a statistical significance between AD CSF and AD CSF plus Nb3; this is also the case HC and HC plus Nb3. Error bars are SEM, and n is the measured number of cells.

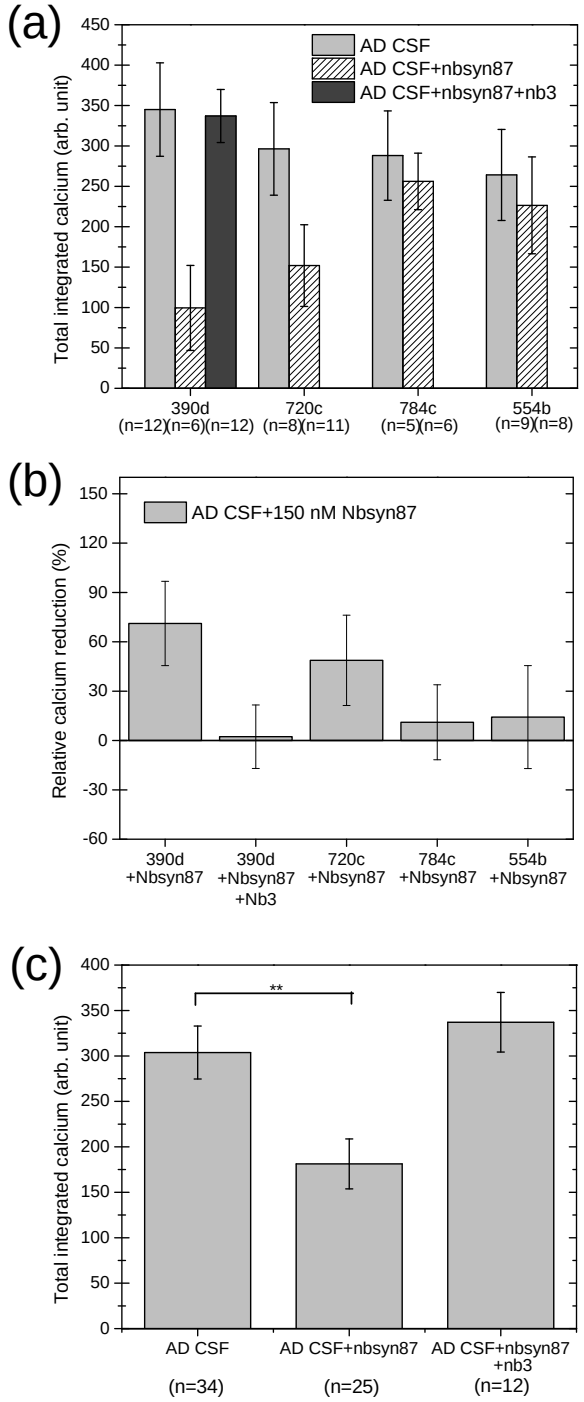

Figure 4.12: Histogram of the total integrated calcium of averaged fluorescent transients recorded within 10 min of single astrocytes being locally dosed by a nanopipette filled with (a) individual AD CSF, 390d, 720c, 784c and 554b, with their corresponding mixture with 150 nM Nbsyn87. There is a bar showing a special case of 390d incubated with 150 nM Nb3 and 150 nM Nbsyn87. (b) Relative calcium reduction in percentage after the addition of 150 nM Nbsyn87 in individual AD CSF described in (a), in which the second bar is the result of 390d incubated with 150 nM Nb3 and 150 nM Nbsyn87. (c) Integral behaviour of the integrated calcium of AD CSF listed in (a) and these samples plus 150 nM Nbsyn87, and a special condition, AD CSF (390d only) plus 150 nM Nb3 and 150 nM Nbsyn87. Results demonstrated that there is a statistical significance between AD CSF and AD CSF plus Nbsyn87. Error bars are SEM, and n is the measured number of cells.

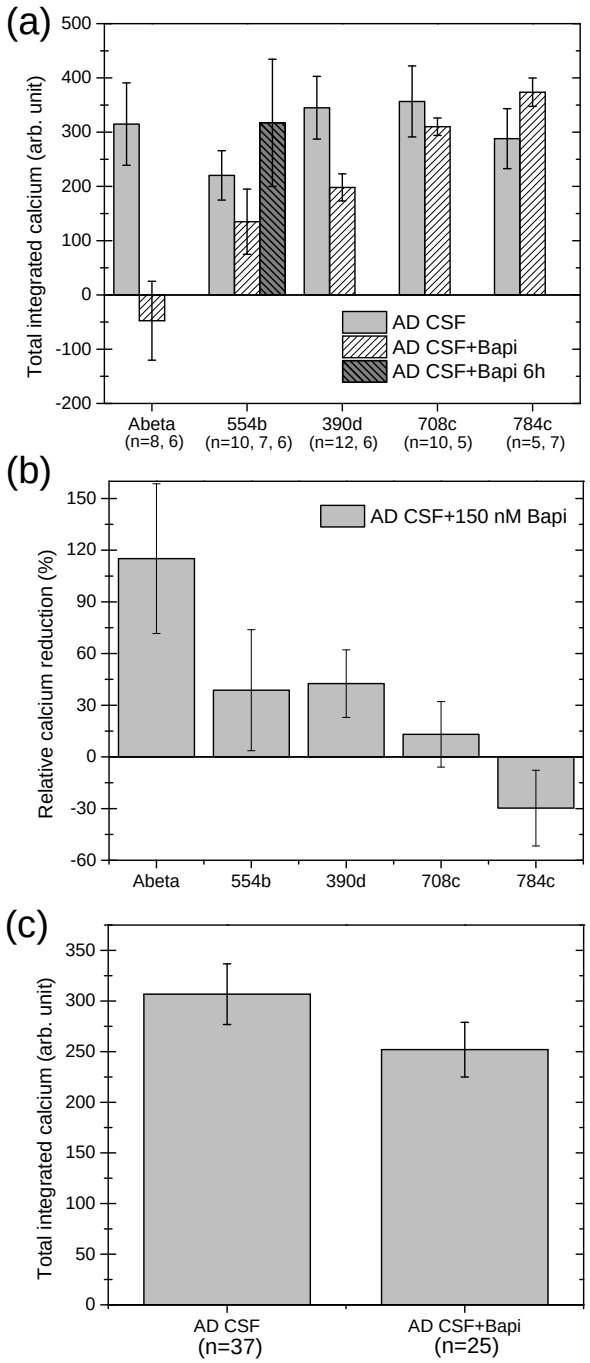

Figure 4.13: Histogram of the total integrated calcium of averaged fluorescent transients recorded within 10 min of single astrocytes being locally dosed by a nanopipette filled with (a) 500 pM Abeta42 oligomers, individual AD CSF, 554b, 390d, 708c and 784c, with the results of corresponding mixtures with 150 nM of Abeta42 antibody Bapi. A special condition, with 554b being incubated with 150 nM of Bapi for 6 hours is also shown here. (b) Relative calcium reduction in percentage after the addition of 150 nM of Bapi in 500 pM of Abeta42 oligomers and individual AD CSF described in (a). (c) Integral behaviour of the integrated calcium of AD CSF listed in (a) and these samples plus 150 nM of Bapi. AD CSF and AD CSF plus 150 nM of Bapi exhibited no statistical difference. Error bars are SEM; n is the measured number of cells.

samples of CSF shown in Figure 4.13(c) further confirmed 150 nM of Bapi was not capable of binding toxic oligomers in AD CSF effectively as it was with only synthetic Abeta42 oligomers. In addition, assuming that CSF circulates 4 times in a day, the incubation time with 150 nM Bapi was increased by up to 6 hours in order to observe if the blocking effect between 150 nM Bapi and AD CSF oligomers was improved or altered accordingly. As shown in Figure 4.13(a), still no improvement was observed by this long time incubation in the CSF of an individual with AD (patient 554b).

Another hypothesis to explain why 150 nM of Bapi does not work properly in AD CSF was that its concentration may not be high enough to bind a major portion of the toxic oligomers in AD CSF. Thus, a higher concentration of Bapi (1 μM) was incubated with five different AD CSF samples (390d, 784c, 725c, 557b and 715c), in an attempt to diminish the abnormal calcium influx in astrocytes, as shown in Figure 4.14(a). However, even though the concentration of Bapi was higher, it demonstrates neither a relative calcium reduction in individual samples of AD CSF nor a statistical significance in the integral behaviour, as shown in Figure 4.14(b) and Figure 4.14(c), respectively.

Although the Abeta antibody, Bapi, did not work effectively enough to stop the excess calcium from flowing into astrocytes, it is also worth examining antibodies designed specifically against Asyn, because Nbsyn87 could decrease calcium influx by binding Asyn oligomers or co-oligomers containing Asyn in AD CSF. Asyn antibodies provided by Medimmune included NJP228, asyn0004, aslo0071, aslo0252 and aslo0071, in which NJP228 is an isotype control IgG antibody presumably having no affinity to Asyn. In Figure 4.15(a1) and Figure 4.15(a2), the mixture of AD CSF 390d and NJP228 clearly showed that NJP228 worked ineffectively, as a negative control, whilst NJP228 plus Nb3 demonstrated a very impressive calcium reduction in abnormal calcium influx, showing a similar result in that for Abeta42 oligomers plus Nb3 and AD CSF plus Nb3. Due to the limited volume of CSF samples ($\leq$1 mL per person), unfortunately not all the antibodies and various corresponding experimental conditions, e.g. various kinds of mixtures and incubation times, could be conducted on a single AD CSF. Therefore, AD CSF samples causing higher abnormal calcium

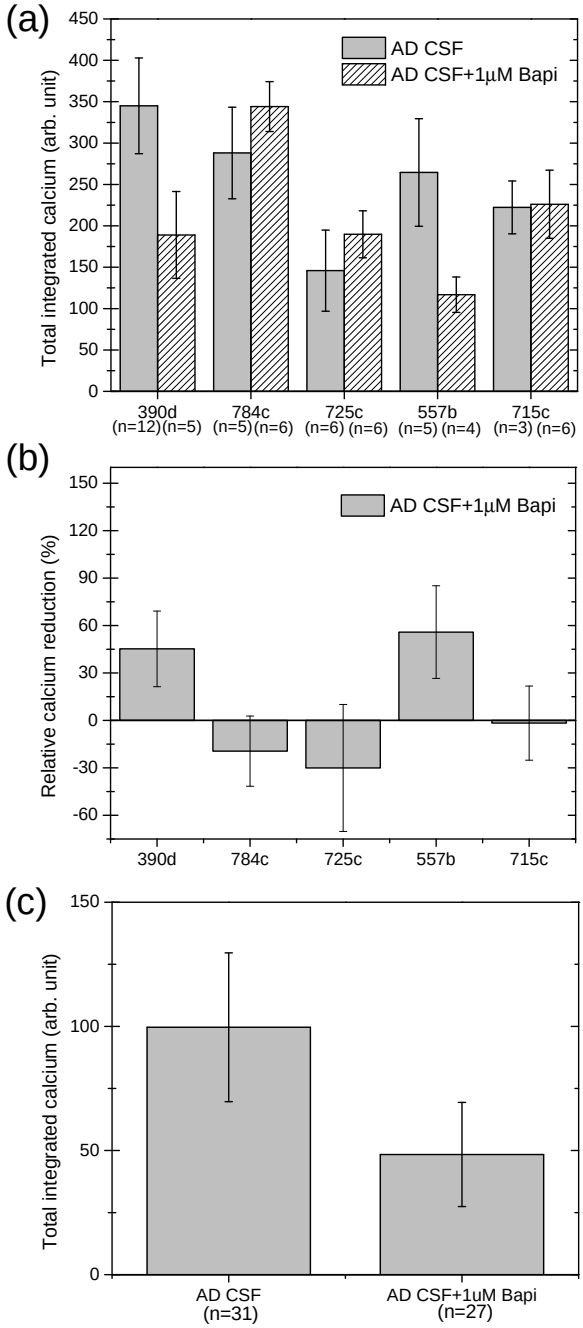

Figure 4.14: Histogram of the total integrated calcium of averaged fluorescent transients recorded within 10 min of single astrocytes being locally dosed by a nanopipette filled with (a) individual AD CSF, 390d, 784c, 725c, 557b and 715c, with their corresponding mixture with 1 μM Abeta42 antibody Bapi. (b) Relative calcium reduction in percentage after the addition of 1 μM Bapi in individual AD CSF described in (a). (c) Integral behaviour of the integrated calcium of AD CSF listed in (a) and these samples plus 1 μM Bapi. AD CSF and AD CSF plus 1 μM Bapi exhibited no statistical difference between each other. Error bars are SEM, and n is the measured number of cells.

influx were firstly used in the blocking experiments.

In a series of experiments using AD CSF 390d, asyn0004 and aslo0071 were also tested. aslo0071 caused a statistically significant reduction in calcium influx into astrocytes, as shown in Figure 4.15(a1) and Figure 4.15(a2). Another set of experiments was performed using AD CSF 708c, with aslo0252 examined in various conditions, i.e. aslo0252 only, aslo0252 incubated for 6 hours and aslo0252 plus Nb3. As shown in Figure 4.15(b1) and Figure 4.15(b2), of these, aslo0252 and aslo0252 plus Nb3 effectively decreased the abnormal calcium influx (with a statistically significant difference), suggesting successful binding with the toxic oligomers in AD CSF . When AD CSF 720c was utilised, control antibody NJP228 and a longer period of incubation (6 hours) were mainly tested. Neither control NJP228 nor asyn0004 6h and aslo0071 6h reduce the calcium influx, as shown in Figure 4.15(c1) and Figure 4.15(c2). These results were consistent with aslo0252 6h and Bapi 6h incubated with AD CSF, as shown in Figure 4.15(b1) and Figure 4.13(a), respectively, indicating that an additional 6 hours of incubation for the mixture of antibody and CSF may not lead to a better binding. Of course, it would be necessary to increase the statistical sample size by repeating those experiments, especially with asyn0071 and aslo0252, when a new AD CSF, which causes a relatively large amount of abnormal calcium influx into astrocytes, is available.

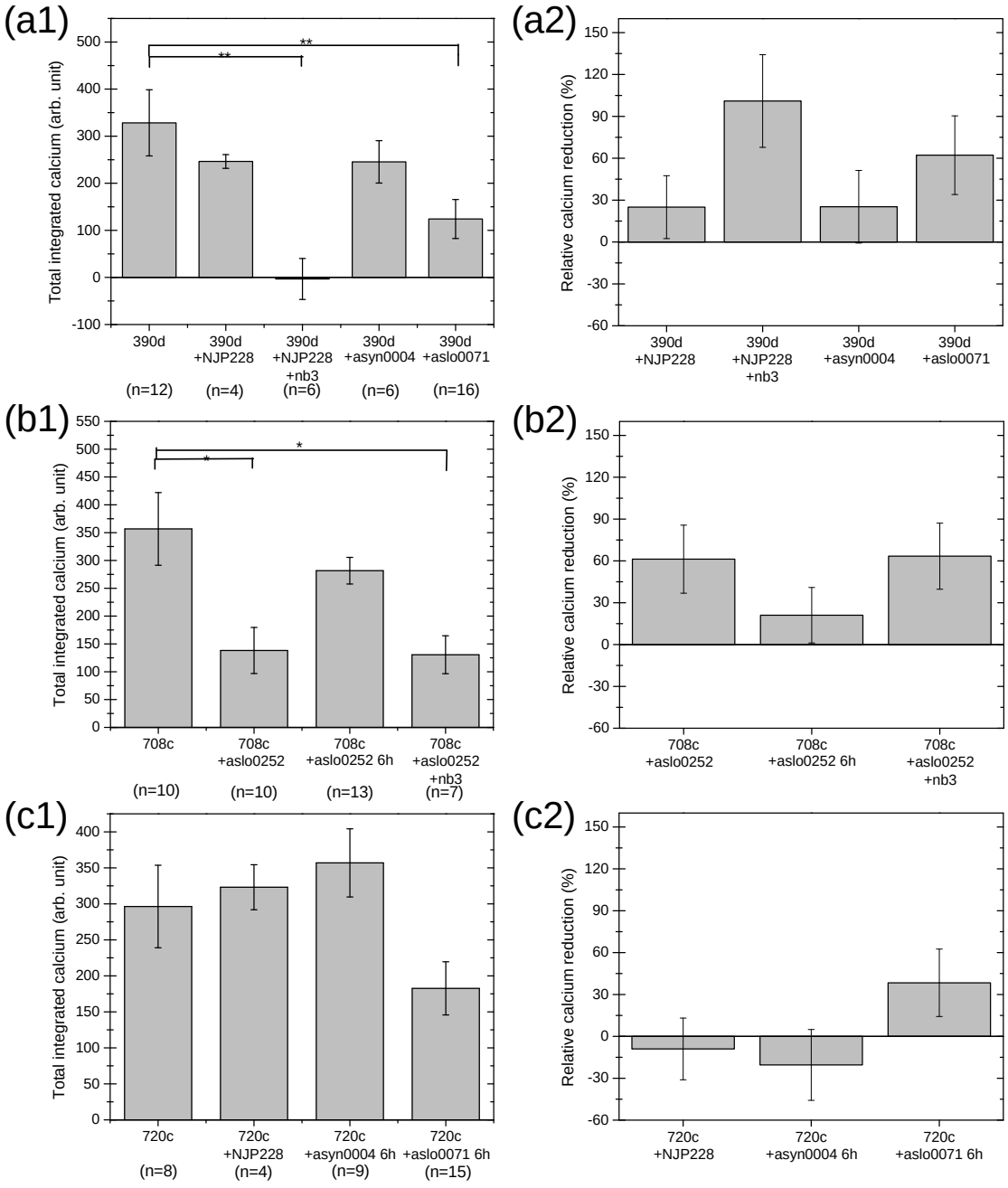

Figure 4.15: Histogram of the total integrated calcium of averaged fluorescent transients recorded within 10 min of single astrocytes being locally dosed by a nanopipette filled with AD CSF and AD CSF plus 150 nM antibody and/or 150 nM nanobody. (a1) AD CSF 390d and its mixture with control antibody NJP228, NJP228 plus Nb3, Asyn antibody asyn0004 and Asyn antibody aslo0071; (b1) AD CSF 708c and its mixture with various conditions of Asyn antibody asyn0252, i.e. aslo0252 only, aslo0252 incubated for 6 hours and aslo0252 plus Nb3; (c1) AD CSF 720c and its mixture with NJP228, Asyn antibody asyn0004 incubated for 6 hours and Asyn antibody aslo0071 incubated for 6 hours. (a2), (b2) and (c2) Corresponding relative calcium reductions in percentages for (a1), (b1) and (c1), respectively. Statistical differences only appear in (a1) between: 1. 390d and 390d plus NJP228 and Nb3; 2. 390d plus aslo0071, and in (b1) between: 1. 708c and 708c plus aslo0252; 2. 390d plus aslo0252 and Nb3. Error bars are SEM, and n is the measured number of cells.

4.4 Discussion

4.4.1 Nanodosing methodology for examining the effectiveness of antibodies and nanobodies in physiological conditions

The intracellular concentration of calcium ions is critical for cells. The adjustment of the calcium concentration by conducting calcium influx and efflux via the activation of specific ion channels is able to regulate enzyme and protein functions and enable signal transduction further. Imbalanced calcium homeostasis in neuronal cells could result in cell damage as a result of activated apoptosis, and consequently trigger the onset of neurodegenerative diseases [186]. Investigation of the interaction between toxic oligomers in AD patients finds abnormal calcium influx in neuronal cells probably via the pore-forming process in the cell membrane [165, 166, 187]. Abnormal calcium influx in neuronal cells induced by oligomers naturally formed in the brain is likely to be an important feature in the early stage of neurodegenerative diseases.

The local nanodosing method using an oligomer-filled nanopipette onto a fluorescent calcium indicator (Fluo-4 AM)-loaded single neuronal cell immersed in calcium-rich buffer solution is based on SICM technique. The resulting calcium flow into the cell is monitored over time by observing its fluorescent transients. This has created an appropriate platform for testing the effectiveness of antibodies and nanobodies targeting toxic oligomers *in vitro*. The dosing number of oligomers can be precisely controlled by setting specific system parameters, i.e. values of applied bias voltage and pressure, so quantitative analysis is possible. For example, two oligomers per second are delivered onto the targeted cell 300 nm beneath the nanopipette with a 50 nm inner radius and filled with 30 pM of reagent, which is applied by 200 mV and 15 KPa. Antibodies and nanobodies are expected to bind the toxic oligomers effectively and therefore reduce the abnormal calcium influx into cells in this nanodosing system, which is probably the result of temporary pores in the cell membrane formed by those oligomers. However, absolute values of the fluorescent transients are less meaningful than the extracted amount of calcium influx normalised at t=0, because the response of each

measured cell is actually highly variable. This indicates that the sample size is important if the distribution of fluorescent transients is broad.

The work carried out by Narayan *et al.* showed that synthetic oligomers, with a main population smaller than 10mers, of Abeta40 and Abeta42, triggered calcium oscillations of astrocytes when they were added in the bath solution [188]. The concentrations in this paper were reduced to 200 pM, although in the physiological microenvironment in CSF, there are oligomers of roughly 0.5 pM, which is 100 times lower than in the experimental conditions. The calcium oscillations caused by abnormal calcium influx induced by Abeta oligomers could result in reactive oxidative species (ROS) production, which is thought to be one of the factors leading to the death of neurons and could then be followed by cascade reactions causing cell damage and subequently activation of caspase 3. Notably, this phenomenon was mainly observed in astrocytes, suggesting that astrocytes may be the cell type that is damaged in the early stages by the toxicity of Abeta oligomers, which is consistent with previous studies. Thus, astrocytes were adopted as model cells in the nanodosing experiments. It is estimated there is approximately 0.5 pM of soluble oligomers in human CSF of diagnosed AD patients. With the extremely low concentration of oligomers in the bath application, it is difficult to generate an observable cell response due to the depletion of oligomers on the cell surface.

This issue is overcome using two strategies: 1. MPEP, which prevents calcium oscillation between astrocytes, was adopted in order to eliminate the unwanted background fluorescence resulting from the influence from neighbouring astrocytes; 2. a much higher dosing flux of oligomers encountering the cell is achieved by the forced delivery via a nanopipette located closely (300 nm) above the cell. These two important factors make possible the detection of the very subtle oligomer-induced calcium influx changes at the initial stage (within 10 minutes) of cell damage. This increased encounter rate of dosed oligomers also mimics the fact that neuronal cells are densely packed with roughly 10–20 nm gaps in the brain [189]. Although the phenomenon of calcium oscillation between astrocytes was eliminated in the experiments, it naturally exists as a second messenger in the brain and may affect neighbouring astrocytes or even distant ones, because any altered homeostasis due to Abeta42

oligomers could be spread from where a single Abeta42-damaged astrocyte is located by communication between neighbouring cells. Approximately 0.2% of the population of Abeta42 oligomers are able to cause these abnormal calcium oscillations, because large oligomers may cause larger calcium influx initiating oscillations [188].

Although the nanodosing method used to test the effectiveness of antibodies and nanobodies has been verified by utilising the synthetic Abeta42 oligomers, this methodology is not able to reveal the physical mechanisms by which Abeta42 oligomers enter astrocytes. Those Abeta42 oligomers presumably temporarily penetrate across the lipid bilayer in the cell membrane without the need for Abeta42 oligomers to bind to any receptors [109, 165, 166, 187]. These pores, which are not permanent, could disappear once oligomers pass through and calcium influx is then reduced. In addition, the dosing concentration is low, and dosing area is small ($\sim 1\,\mu m^2$), so the involvement of any receptor interactions is not specific.

4.4.2 The antibody and nanobody against Abeta42 oligomers and the possible existence of co-oligomers

In experiments into the effectiveness of antibodies and nanobodies, it must be kept in mind that only a statistical difference between the two sets of data is able to prove the effectiveness of an antibody. A difference in value between any two pieces of data in terms of total integrated calcium that does not have statistical significance is not entirely meaningless, if the sample size (the measured number of cells in the Abeta42 nanodosing experiments) can be increased. In this chapter, the statistical model of one-way analysis of variance (ANOVA) was adopted to determine whether there exists a statistically significant difference between the means of two or more groups of data sets, which are independent of one another.

In the Abeta42 nanodosing experiments, shown in Figure 4.8, it is clearly demonstrated that $2\,\mu g/mL$ of clusterin, 150 nM of Nb3 and 150 nM of Abeta42-specific antibody Bapi are capable of effectively reducing the calcium influx into targeted astrocytes. The entry of extracellular calcium is suppressed by the antibodies and/or nanobodies tested due to

the binding to Abeta42 oligomers, so the probability of interaction being made with the cell membrane to generate transient pores or, less likely, trigger any calcium-regulating receptors is greatly lowered. The failure of Nbsyn87 to prevent calcium influx is predictable, since Nbsyn87 is designed to bind to Asyn epitope residues. However, in the experiments dosing a mixture of 150 nM Nb3 plus 150 nM Nbsyn87, which was expected to work as well as the experiments dosing 150 Nb3 only, surprisingly showed an interference between Nb3 and Nbsyn87. This may be Nb3 losing its capacity to bind Abeta42 or there may be other pore-forming species preserved, i.e. co-oligomers, which are formed and dosed onto the astrocyte. The assumption that the interaction between Nb3 and Nbsyn87 interferes with Nb3 binding was proven to be false by the same application of 150 nM Nb3 plus 150 nM Nbsyn87 on a vesicle assay (its concept is shown in Figure 4.16), in which similar blocking effect was observed, for 150 nM of Nb3 only or 150 nM of Nb3 plus 150 nM of Nbsyn87 (results not shown). However, transient interactions between Nb3 and Nbsyn87 might occur, which might generate a hybrid complex that is able to influence the pore-forming properties of Abeta42 oligomers that had already bound with Nb3, leading to triggered calcium influx, whilst in the vesicle assay this calcium influx was not observed probably because its artificial membrane composition was different from that of an astrocyte. In addition, there might be other species like co-oligomers that lead to the entry of calcium ions through the cell membrane, even though a large proportion of Abeta42 oligomers in the nanopipette should have been bound by Nb3. In fact, a small proportion of Asyn produced by the SNCA gene is present intracellularlly, and Asyn monomers are secreted from astrocytes via exocytosis [181]. In addition, there has been evidence for a co-interaction between Abeta and Asyn *in vitro* [182, 183, 190], and simulations have also shown the formation of co-oligomers of Abeta and Asyn is indeed feasible [184, 185]. Therefore, it is assumed that Nbsyn87 in the nanopipette and Asyn secreted above the cell surface from the targeted astrocyte may interact together with Abeta42 during the experiment, which takes about 15 minutes, to generate pore-forming oligomers, which might not be completely blocked by Nb3 and Nbsyn87. These co-oligomers might be composed of Abeta42, Asyn and bond Nb3 and/or Nbsyn87. Nbsyn87 bound onto Asyn demonstrated an influence on the structure of Asyn aggregates, so presumably co-

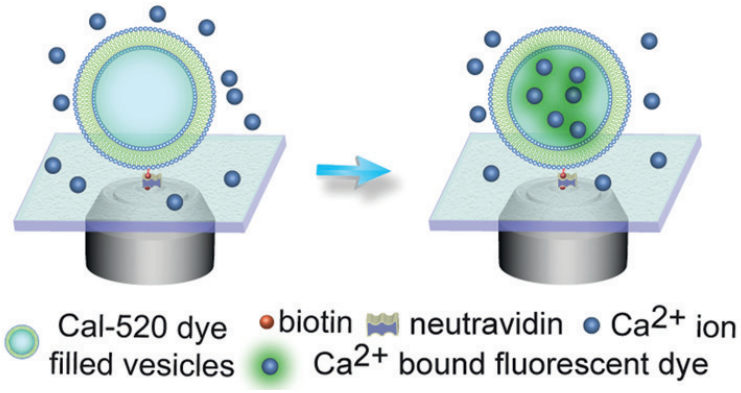

Figure 4.16: Schematic diagram of a Cal-520 filled 1-palmitoyl-2-oleoylsn-glycero-3-phosphocholine (POPC) vesicle assay, with biotinylated lipids fixed with neutravidins on the PLL–PEG surface. Figure excerpted from [192]

oligomers containing nanobodies may have a different structure from co-oligomers in which nanobodies are absent, and they may still remain toxic [182, 183, 191] and form co-oligomers using molecular simulation [184, 185].

4.4.3 Tests on antibodies and nanobodies targeting Abeta and Asyn oligomers and their likely co-oligomers in AD CSF

The nanodosing experiments to test the effectiveness of antibodies and nanobodies on AD CSF will be valuable for pharmaceutical companies, as those results will provide critical information about antibodies and nanobodies in real physiological conditions before the commencement of the next stage, involving very expensive clinical trials. The CSF samples, including AD CSF and HC, gave highly variant results with abnormal calcium influxes. This may be attributed to the fact that the progression of AD cannot be quantitatively characterised currently, so the differences in the progression of the disease between patients and therefore each patient's pathology may be different, implying the amount of toxic oligomers in the brain may also vary. Hence, AD CSF samples that gave rise to a higher abnormal calcium influx were used for the antibody and nanobody blocking experiments. In addition, to confirm if an antibody or nanobody works in reducing abnormal calcium influx, usually at least 4 to 5 AD CSF samples are needed to give statistically convincing outcomes, which

is time-consuming.

Surprisingly, the overall behaviours of AD CSF and HC samples used in this chapter showed similar total amounts of integrated calcium, which is consistent with the enzyme-linked immunosorbent assay (ELISA) measurements, which also showed no statistical difference between AD patients and healthy controls [167, 168]. This suggests there might exist an equally comparable amount of toxic oligomers in each person, no matter whether healthy or AD diagnosed, and relative conditions triggering the onset of AD may occur on a case-by-case basis in each person, rather than simply being dependent the absolute amount of those toxic oligomers in the brain. Alternatively, the number of toxic oligomers might be raised regionally in the brain according to the progression of AD, before being released into CSF for circulation.

The results demonstrated that Nb3 and Nbsyn87 can both reduce the oligomer-induced calcium influx, which suggests the toxic oligomers in AD CSF samples contain at least Abeta oligomers, Asyn oligomers and most likely, co-oligomers composed of Abeta and Asyn. Note that the co-oligomers in CSF are not necessarily in the same form as those appearing in the Abeta42 nanodosing experiments, because co-oligomers in CSF, if they exist, may be complex and contain isoforms of different proteins.

In the case of the antibody Bapi, the results indicate that it does not effectively bind a large portion of oligomers in AD CSF to reduce the abnormal calcium influx. This result is sensible if there are other toxic species like Asyn oligomers and co-oligomers, to which Bapi might not be able to bind, in the AD CSF. In fact, the usage of Bapi in clinical trials unfortunately failed in 2012, and the concentration was 10^6 times lower than the $1\,\mu$M used here. This failure might have been avoided if the Bapi nanodosing experiments that showed Bapi cannot effectively prevent AD CSF oligomers from entering astrocytes were conducted before the clinical trials [193, 193, 194].

On the other hand, Asyn antibodies, aslo0252 and aslo0071, which were designed specifically to bind C- and N-termini of Asyn, respectively, were capable of decreasing the excess calcium flow into astrocytes. All the results of working nanobodies and antibodies, i.e. Nb3,

Nbsyn87, aslo0071 and aslo0252, suggest that toxic oligomers in AD CSF may include Abeta oligomers, Asyn oligomers and co-oligomers containing Abeta and Asyn. In addition, this co-oligomer might involve more exposed N- and C-termini of Asyn with Abeta components more hidden inside the oligomeric structure, and the steric effect might play a role in the fact that Bapi was less effective at binding, whilst aslo0071 and aslo0252 worked properly, although 2 or 3 more AD CSF samples are needed to confirm that aslo0071 and aslo0252 have a prevalent blocking effect for abnormal calcium influx among different AD CSF samples.

4.5 Conclusions

It has been proved that the localised nanodosing technique based on SICM, in which a nanopipette is loaded with reagents, may be successfully applied in an investigation observing the instantaneous response of an individual targeted cell upon regional stimulation under physiological conditions. This methodology provides an appropriate platform for determining the effectiveness of antibodies and nanobodies against AD, which is specifically designed to bind Abeta42 oligomers in order to reduce or eliminate their toxicity to astrocytes, by means of blocking those oligomers from crossing the cell membrane. This physical phenomenon of oligomers entering astrosytes is monitored via the change of fluorescent transient in calcium indicator (Fluo-4 AM)-loaded astrosytes within 10 minutes of video recording, with the fluorescent indicator being reactive to calcium ions coming from the extracellular buffer solution into the cell cytosol. In fact, antibodies and nanobodies specifically-designed for Asyn were also examined in the experiments, because Asyn is abundant in the brain, and its misfolded soluble form is probably the cause of Parkinson's Disease (PD). It is also likely to form co-oligomers with Abeta.

The results have demonstrated that the Abeta42 nanobody, Nb3, works well in the reduction of the excess calcium influx induced by both artificially-synthesised and naturally-secreted Abeta42 oligomers in astrocytes; however, Bapi only effectively decreases the abnormal calcium influx due to synthesised Abeta42 oligomers, even though a concentration

approximately seven times higher of Bapi has also been tested. This may be atributed to the fact that some other species in AD-diagnosed CSF also competitively bind to Bapi, which weakens the ability of Bapi to block Abeta42 from entry; or co-oligomers that have formed between Abeta42 and Asyn may have changed their conformations, so that Bapi could not bind to their N-terminus as well as with synthetic Abeta42. Intriguingly, Nb3 and Nbsyn87 binding to Abeta residues 17–28 and Asyn residues 118–130, respectively, both largely diminished the calcium influx when incubated in AD CSF. This suggests that the intrinsically smaller volume of nanobodies is able to reach and bind to the correct epitopes more effectively in co-oligomers formed by Abeta42 and Asyn, when free access to this binding domain may be hindered for other large antibodies owing to a steric effect. On the other hand, among Asyn antibodies, only aslo0071 and aslo0252 showed statistical significance in AD CSF, suggesting that N- and C-termini may be exposed more to the environmental solution in the co-oligomers formed in AD CSF, although a larger sample size is recommended to confirm this result further. Therefore, according to the convincing nanodosing methodology, altered homeostasis in astrocytes induced by co-oligomers formed by at least Abeta42 and Asyn in AD CSF can be alleviated or eliminated by Nb3 and Nbsyn87, which suggests those small-size nanobodies may provide higher binding efficiency compared with typical antibodies, and they should be considered candidates to be utilised in future clinical trials for the treatment of AD.

Chapter 5

Establishment of the SICM with an Angularly-aligned Micromanipulated Sensor Holder

In Chapter 4, it has been proved that Abeta42 oligomers delivered via a nanopipette onto astrocytes can induce a transient calcium ion influx, which suggests that temporary disruption in the cell membrane may occur, and calcium ions may enter at the same time, as Abeta42 oligomers attempt to pass through. However, although this methodology provides a suitable platform for examining the effectiveness of antibodies and nanobodies designed specifically againt Alzheimer's Disease, it can neither determine the physical mechanism of Abeta42 oligomers interferencing neuronal cells, mainly astrocytes, nor exclude the possibility of the involvement of certain receptors in regulating the inward flow of calcium ions. If transient oligomer-induced pores in the cell membrane exist as hypothesised, there may be leakage of intracellular molecules at the same time, and these might be detectable using a nanoscale sensor located on the target cell.

SICM can be utilised for localised delivery of molecules onto a simple cell, by taking advantage of its precise control of nanopipette–sample separation. This has been successfully verified in Chapter 4, in which stimulation was applied to the targeted cell by a nanopipette

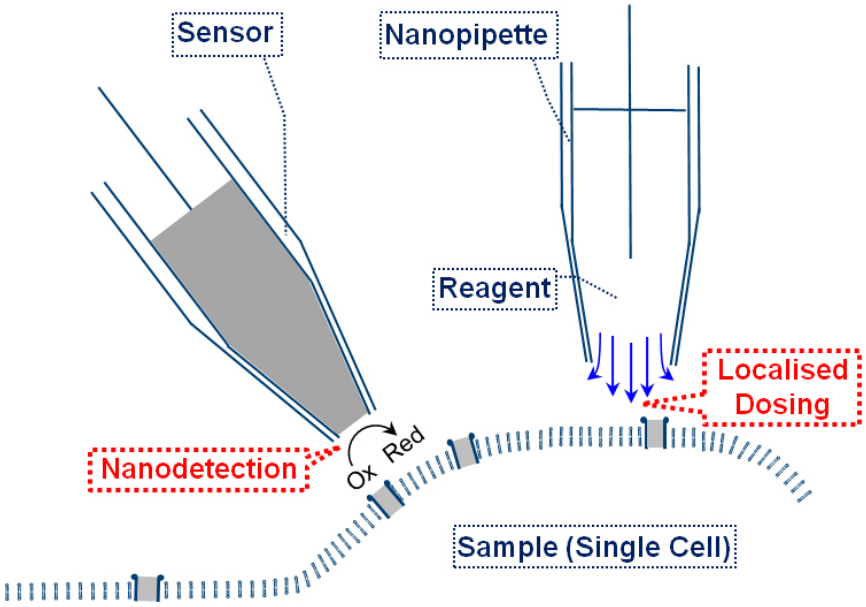

Figure 5.1: Graphical representation of the function of the new setup based on SICM, with one nanopipette responsible for localised dosing of reagents onto an individual cell, and the other nanopipette-modified sensor enabling the detection of a specific response, e.g. electrochemical reactions, in the same cell.

sending Abeta42 oligomers, and the transient response of the cell was fluorescently recorded by a camera. By the same token, considering a nanopipette as the source of the stimulation sent to the object, the detection can be carried out by a nanoscale sensor, which converts the reaction to electronic signals. It is feasible to transform a nanopipette chemically into a sensor to perform specific measurements, so that its holder can be designed in the same manner as the nanopipette itself. This concept is depicted in Figure 5.1, in which a typical nanopipette and a carbon-filled nanopipette for performing electrochemical sensing, for example, is used for localised dosing and detection, respectively. Therefore, a modified SICM setup must be adopted for this new measurement method; i.e. an extra holder is needed for the sensor, which is micromanipulated and angled, so that both tips may approach each other on the target cell. This new SICM is shown in Figure 5.2. In the following sections all the important parts for building it will be introduced in detail.

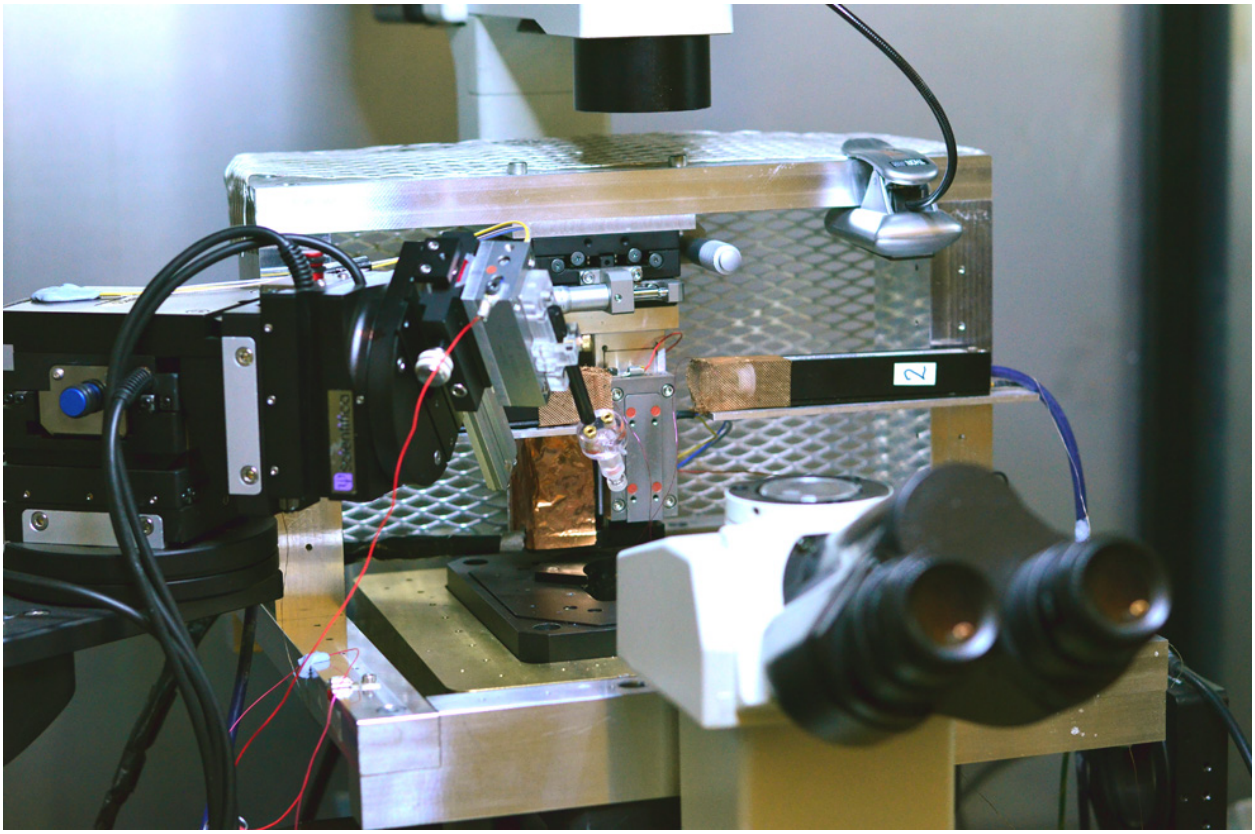

Figure 5.2: The modified new SICM setup installed on an inverted microscope, with a micromanipulated and angled extra holder for the nanoscale transister-based sensor. Both the sensor and SICM tips may approach each other on the same target cell.

5.1 Active vibration isolation system

The sources of static and dynamic acoustic noise (4–100 Hz) in a building come from the environment and motorised instruments placed near the experimental setup [195]. To avoid the influence from ambient vibration on measurements, which is usually transferred through the supportive columns of the optical table placed on the floor, a specially designed vibration isolation system must be used as the platform for the new system to sit on. This optical table has a well-damped structure with a hexagonal honeycomb made of clay in between a pair of metal plates. It has the properties of high stiffness, low mass and great thickness in order to shift the resonant frequency of the optical table further up, much higher than 100 Hz, to decrease the influence on the compliance characteristics brought in from ambiance via the supportive legs [195]. Thus, it can be decoupled from its supports that are in contact with the ground.

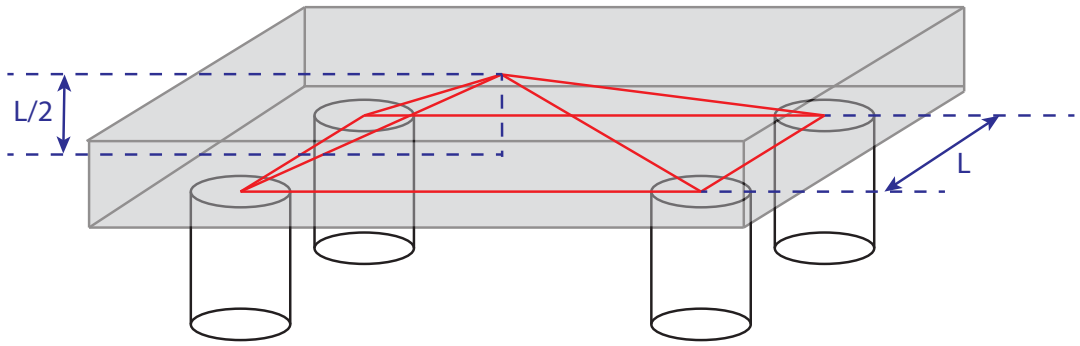

Figure 5.3: Illustration of an optical table with four active vibration isolation columns. The centre of gravity of the whole system (including the optical table itself) should be located in the pyramidal space with side length L and height L/2, where L is the separation between centres of two columns at the short side.

A well-designed optical table may not be enough to guarantee the table-top is free from vibration. Unlike the supports for the other SICM setup, in which a passive isolation system including an air reservoir is adopted for damping; here, an active vibration control is chosen for the optical table supports. This is a combination of vertical and horizontal dampers. The table is seismically mounted on these supports, and has a very low resonant frequency (with transmissibility of 0.3 to be at less than 2 Hz), so that the surface of the table can be mostly decoupled from the ambient noise [195]. The active support contains a horizontal vibration absorbing damper, a pair of air chambers for vertical damping mechanism and for the self-levelling system as well, which needs pressurised nitrogen.

However, compromise between isolation and stability must be made. Any effect on the table-top that causes the centre of gravity of the whole system, including the table itself, to move away from its original central location may form a torque and the table will incline. Any active method that works against this unwanted disturbance might instead lead to the oscillation of the table from side to side. This is a general method to improve the stability of the system empirically by making the centre of gravity sit in the pyramid, which is shown in Figure 5.3. The length of the side of the pyramid is defined as the distance between the centre of two closer supports, L, whilst its height is roughly $L/2$ [195]. In addition, the nitrogen flow must not be large to induce dynamic oscillation in the table due to an excessively quick response from the self-levelling device.

5.2 Reduction of electrical disturbance and noise

When establishing a new setup to conduct single-cell–level measurements, reduction of the electrical noise from various kinds of sources is critical. Such disturbances could lead to a misreading of the ion current and ultimately to the breaking of the nanopipette tip, leading to the sensitivity of the system being degraded. In addition, if the new setup is used to perform the patch–clamp technique, noise reduction is even more crucial, because the nanopipette will need to be in firm contact with the targeted cell and any movement of the automated system component induced by the noise could result in failure in the experiment, e.g. damage to the cell or complete loss of the patch (robust contact between the cell membrane and the nanopipette tip opening).

The sources of electrical interference are diverse but can be roughly categorised into radiated pickup and conducted pickup. Radiated pickup may come through the air from radio frequency (RF) interference, but it comes mainly from the power supply (mains hum), forming line-frequency noise at 50 Hz and its harmonics in the UK. The AC electromagnetic induction may cause unwanted current in the circuitry if the setup is placed near power supplies or transformers. On the other hand, conducted noise may come directly from power cables, ground loops created unintentionally or even metal components picking up radiated noise at a distance.

The process of reducing electrical noise is almost empirical, because it must be dealt with on a case by case basis in different laboratories. However, there still exist principles to follow: ensuring the grounding is carefully applied at necessary parts of the setup. There are various kinds of grounds: (1) signal ground; (2) shield ground; (3) earth ground. A single ground point is first chosen on the optical table, on which microscope, homemade SICM metal stage, manipulators, the chassis of the computer and controllers and piezo actuators are carefully connected separately to form a star-like network and avoid ground loops, and ultimately an individual wire is linked to the plug, referred to as "signal ground" at the rear panel of the two patch–clamp amplifiers. It should be noted that the earth ground, which is installed in power supplies and literally connected to the "earth", is only for preventing the

occurrence of electric shock, whilst the signal ground presents the common reference zero point for the circuitry and does not necessarily need to be connected to the earth ground (and is usually not). In addition, a Faraday cage is usually used to cover the microscope and the stage carrying the sample, which will ideally eliminate most of the radiated noise in the air, and this is also connected to the ground point which finally enters the amplifier. In our case, due to limitations in space and in order to preserve the area for the movement of the micromanipulator, a large Faraday cage without doors plus smaller handmade metal shields sitting on the SICM stage are used.

Although a metal shield might block the transmitted noise from the component behind the shield, there is also a probability that it will nevertheless pick up random noise. Thus, it is necessary to be careful when introducing a metal shield and it must always be linked to the point for the signal ground. The conducted noise can usually be largely reduced by putting a ferrite bead, which converts RF noise into unnoticeable heat, onto power supply cables. Most of the length of the two headstage cables of the amplifiers is kept inside the Faraday cage and gently twisted when they return to the rear panels of the amplifiers to neutralise electromagnetic interference. However, the headstages themselves should stay separated. Signally-grounded shielding is introduced to each of their heads. In general, it is recommended that a coaxial Bayonet Neill-Concelman (BNC) connector, which has a built-in shield, be used; however, one must be aware that the metal layers potentially result in ground loops, as each BNC cable returns to a separate signal ground from each instrument, rather than to that from the amplifier. This issue might be solved by breaking off the metal shield. Finally, electrical isolation is sometimes the answer to the problem, i.e. it would be best to keep the main sources of noise (e.g. monitors and computers) away from the amplifiers if possible. It is also a good idea to adopt an independent power line for computers and monitors.

5.3 Homemade modular frame and angled micromanipulator

The new SICM frame is designed to be modular, with threads created at a regular distance in between, as shown in Figure 5.4. Therefore, extensibility for future improvements or new applications is preserved, and it can be built on the same frame. The rack is stabilised with screws on a phase-contrast inverted microscope (Eclipse TE200, Nikon), and an upside-down aluminium XY-axis stage (LD–5047–S1, Chuo Precision Industrial Co. LTD, as depicted in Figure 5.5), a piezoelectric actuator (P-753.2CD, PI, the same as that used in Figure 2.5) and a stepper motor (M–111.1DG, PI, as represented in Figure 5.6) with travel range of 15 mm are fixed via adaptors at the top of the crossbeam, as shown in the middle of the bottom row of Figure 5.4. In addition, a heavy brass stabiliser for a horizontal piezoelectric nanopositioning stage of travel distance 100 μm (P–517.2CL, PI, as demonstrated in Figure 5.7), with a homemade dish holder installed at its centre is settled on the original microscope stage in order to reduce the inevitable vibration caused by SICM scanning.

A nanopipette holder is then fixed to the piezoactuator with its tip pointing perpendicularly to the dish bottom and loaded with the sample. During measurement, firstly the coarse approach is conducted by operating the stepper motor progressively downwards, and simultaneously the XY-axis stage is adjusted carefully to move the tip into the field of view, so that the nanopipette tip can be observed via the ocular lens on the microscope. Note that a likely cause of a broken tip is excessive speed of movement in the stepper motor, which provides no distance feedback and which can only be monitored visually. Secondly, a fine approach to the sample surface or the dish bottom is carried out with a distance-feedback system by the piezoelectric actuator, and consequently hopping mode topographical scanning can be performed with proper physical settings, as described in Chapter 2.

A second nanopipette/electrode is connected to the micromanipulator (PatchStar, Scientifica) via a homemade holder, a piezoelectric actuator and its adaptor. PatchStar is a motorised micromanipulator with high accuracy (20 mm of travel distance in each axis with

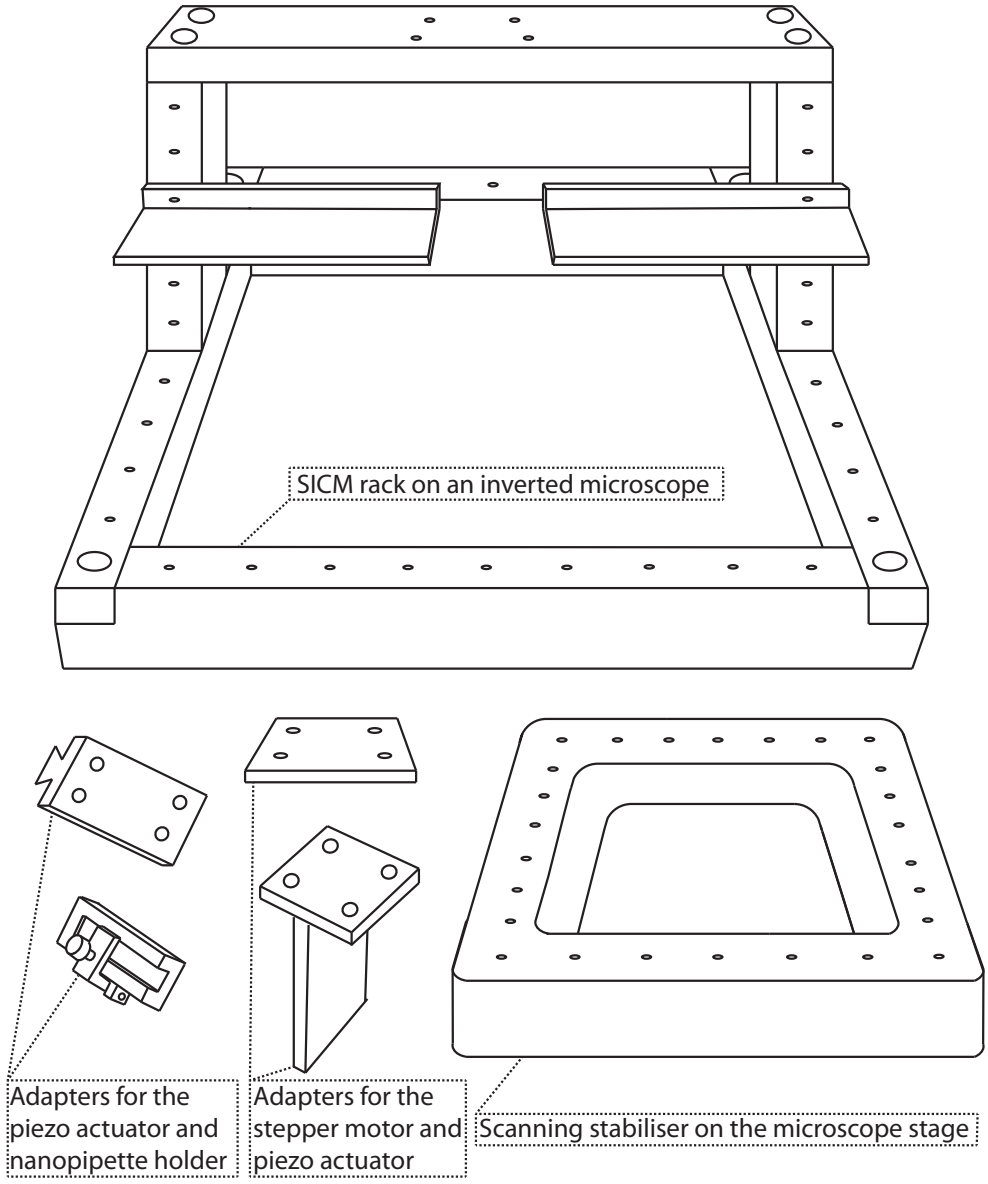

Figure 5.4: Illustrations of a homemade modular SICM frame, a brass stabiliser for the nanopositioner, and adapters for piezoelectric actuators and the stepper motor. (upper) The rack for immobilising components used in the new SICM setup. This is composed of aluminium bricks with modular thread designs for future functional expansion. Two extrusive racks fixed separately on the columns provide support for the headstages of the amplifiers. (lower left) Adapters are designed for the stage that performs horizontal (X- and Y-axes) movement of the nanopipette, for the vertically-aligned stepper motor for coarse approaching of the nanopipette, and for the piezoactuator in order to perform fine adjustment of the height of the nanopipette tip. (lower right) A heavy brass block with threads fixed to the microscope stage along with the XY nanopositioner is designed to reduce the acoustic noise generated during the scanning.

20 nm resolution) and stability, which can be treated as X-, Y-, and Z-axis low-noise stepper motors integrated in one system [199]. In addition, the optional movement mode along the

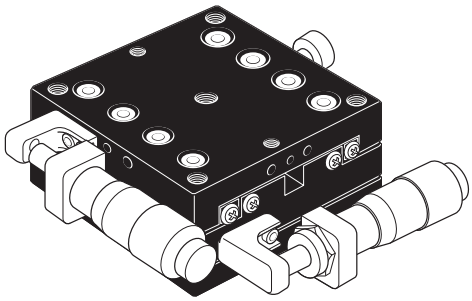

Figure 5.5: Schematic diagram of the XY stage installed on the homemade SICM frame, on which a vertically-aligned stepper motor and an electric piezoactuator are connected via adapters. The horizontal motion of the nanopipette is controlled precisely by a pair of micromanipulators for X and Y directions separately (0.5 mm per turn). Figure excerpted from [196].

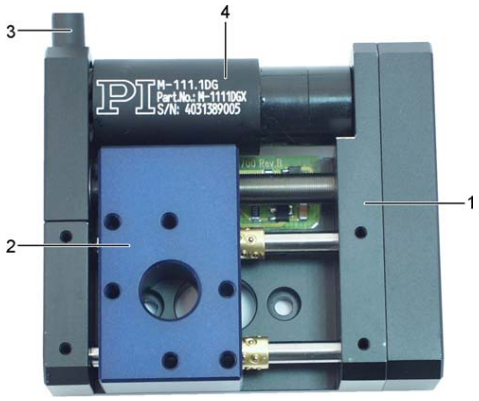

Figure 5.6: Photograph of a micro-translation stage designed using a stepper motor. 1 denotes the metal base; 2 the moving stage with a travel range of 15 mm with threaded holes; 3 the servo motor cable; 4 the stepper motor. Note that the motor is covered by a piece of copper foil to reduce electromagnetic interference generated during its operation. Figure excerpted from [197].

nanopipette/electrode axis makes this very convenient, and it is possible to perform an angled approach to the side of the sample. It is designed to be modular so that the nanopipette can be loaded and approached from various angles and directions. Additionally, the switch-controlled extensible arm holds the nanopipette, and the magnetically-stabilised rotary base simplifies the procedure of nanopipette replacement. In our setup, the PatchStar is held on a column in order to align it with the SICM stage and is set to lie at a low profile by an L-shaped bracket (PS-7800), as shown in Figure 5.8, so that the movable holder together with the nanopipette can approach the sample without hitting any other parts installed on

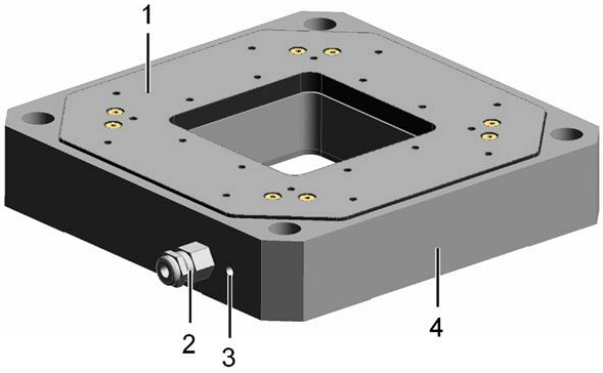

Figure 5.7: The nanopositionor used in SICM is illustrated, where 1 is the moving platform with a Petri dish holder fixed in its rectangular cavity; 2 is the cable outlet; 3 is the protective earth connection; 4 is the metal base. This positioner is positioned on the brass stabiliser on the microscope stage with maximum closed-loop travel of 100 μm $\times$ 100 μm. Figure excerpted from [198].

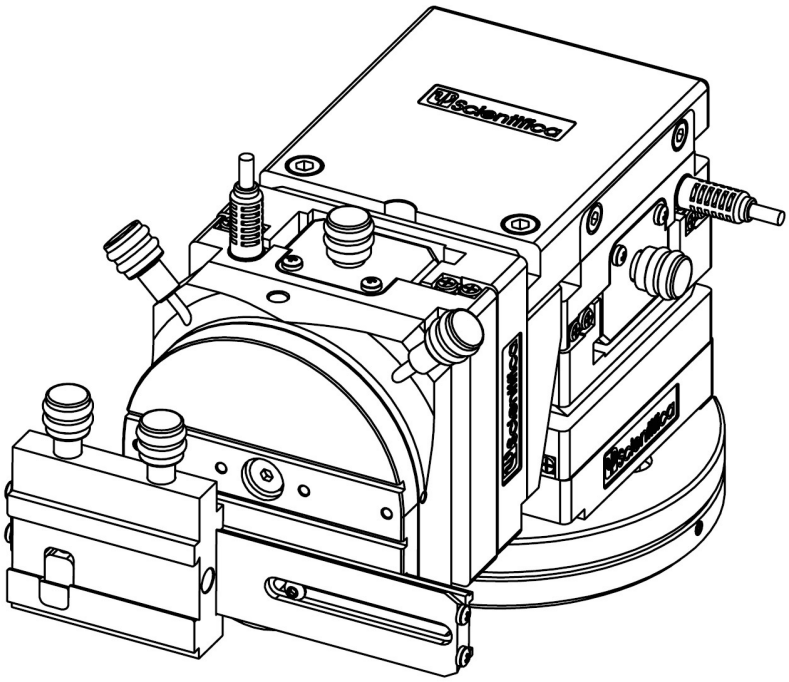

Figure 5.8: Schematic diagram of the low profile PatchStar micromanipulator with an L-shaped bracket. Three modules responsible for the movement individually of X-, Y- and Z-axis are shown, and the travel distance is 20 mm on each axis and the step size is 100 nm. The movement of the modules can be controlled by a wheeled control cube or by a Windows-based program termed LinLab, which allows four optional approach speeds to be set along various axes, with a virtual approach axis along the nanopipette. In addition, the design of a carriage sitting on a slide rail attached to a rotary with magnetic locks makes it convenient for nanopipette/sensor replacement. Figure excerpted from [199]

the stage and the microscope. Precise control of the motor movement at various axes and the speed of approach can be fulfilled by either a wheeled control cube or by computer software termed "LinLab," in which current positions are recorded and shown.

5.4 Perfusion system

An optional perfusion system is built for a consistant supply of fresh buffer medium for the cells. The buffer medium is kept at 37° in a water bath (SUB Aqua 2 Plus, Grant), with fluid being delivered by a peristaltic pump (Peristaltic Pump P-1, Pharmacia) into the target Petri dish containing live cells; at the same time, excessive medium above the desired liquid level is removed by a fixed needle tip that is connected to a suction pump (Medical Suction, SAM 12) via tubing. The medium can first be pumped into a syringe without a plunger at a higher place than the dish, if this direct delivery of medium into the dish using the peristaltic pump induces physical interference to the measurement, e.g. resulting in noisy topographic imaging, so that the fluid is then drew into the dish more smoothly by gravity. Alternatively, if the volume of the buffer medium used for the experiment is not as much as one litre, a syringe pump (PHD 2000, Havard Apparatus) can also accomplish the task.

5.5 Light sources for the setup and camera

When the vertical nanopipette holder is used, the usual upright light source (without a condenser) from the 12 V, 100 W illumination pillar powered by TE–PS100 will inevitably be nullified, because the light path is partially blocked by the holder itself. In this case, one or multiple portable clip-on LED lamps (PSX501, Thorlabs) are used merely to illuminate the sample.

The light source for performing the fluorescence experiments is provided by a molecular LED system (OptoLED, Cairn Research). A triple coupling, carrying three LED heads (each with a two-by-two LED array) of wavelengths 365, 470 and 530 nm, connected to the

microscope by arranging its tube through the space under the illumination pillar enables direct band-pass filtered (470, 505 and 540 nm) LED illumination of the sample area. LED technology has been developed to cover wavelengths ranging from infrared to near ultraviolet, and the intensity of LEDs has increased progressively. Thus, these properties have made LEDs one of various options for light sources, as well as e.g. laser, arc lamps and incandescent lamps. Although laser has been widely adopted in single–molecule experiments due to its high intensity, monochromaticity and collimation, the LED system has the particular advantage of being much less costly and its comparable properties can fulfil experiments with lower requirements.

The OptoLED is a constant-current power supply (0–10 V), which is able to drive two LED heads, with a current ranging from 0 to 5 amps. The output of the LED is approximately proportional to the applied voltage; however, it is in fact influenced especially by temperature, i.e. heat dissipation along with illumination decreases the light intensity by more than 10 % [200]. The solution provided by OptoLED is to overdrive the LEDs according to the feedback signal from a photodiode in order to maintain a constant optical efficiency. The advantage of driving the LEDs according to the detection results from a photodiode is that the optical output can be more linear, but its disadvantage is a longer response time for the application, with a requirement to be switched on and off periodically or for pulse waves to reduce possible phototoxicity. Note that the original switching times for OptoLEDs can be less than 100 ns.

A digital 14-bit CCD camera (pco.pixelfly usb, PCO) is installed in the side port of the microscope. When acquiring experimental data, adjusting the changeover lever of the optical path allows 20 % of light to be directed to the camera, whilst the remaining 80 % goes to the eyepiece tube port. The camera has relatively low noise, a resolution of 1.4 megapixels, and a high pick quantum efficiency of 62 % [201].

5.6 Examples of topographic imaging using SICM

In order to perform quantitative localised dosing of a reagent via the vertically-aligned nanopipette, it is crucial that the tip of the nanopipette can be maintained at a constant height from the substrate that is preset via a user interface. The most effective way to examine this feedback-controlled movement of the nanopipette is to conduct topographic imaging of samples, although the function of topographic scanning possessed by the new SICM setup is not utilised in this thesis. In figure 5.9, three 3-D topographic images of primary rat glial cultures using SICM in the setup are exhibited. The scannings were completed in hopping mode with a setpoint at 1% and a falling rate of 500 nm/ms. The maximum scanning area is 30×30 μm^2, which is defined by the nanopositioner holding the cell dish, but only around 10×10 μm^2 was scanned in the examples shown in Figure 5.9 to save time. Figure 5.9(a), (b) and (c) have resolutions of 469, 166 and 59 nm, and they took approximately 5, 20 and 60 minutes, respectively. In fact, it was possible for the coarse scanning shown in Figure 5.9(a) to reveal the intercellular network between astrocytes, so the user can choose a suitable scanning resolution according to the specific experimental conditions.

5.7 Function of patch–clamp recording

Patch–clamp technique is an important electrophysiological tool, which can resolve conductance under the tip of a nanopipette with a high temporal resolution. The opening of a small set or a group of ionic channels distributed on an individual cell owing to external stimulation influences significantly the amount of ion flow through the nanopipette aperture. It was developed by Sakmann and Neher in the late 1970s [42], and is mainly used for the investigation of networks of excitable cells, for example neurons and cardiomyocyte cells. The ion current of the cell responding to the applied stimulation through the electrically-isolated patch is at the level of tens to hundreds of picoamperes and can be recorded using a specialised electronic amplifier. The configuration of a tight contact, so-called patch, between the nanopipette tip and the cell membrane (a giga-ohm seal should be now observed)

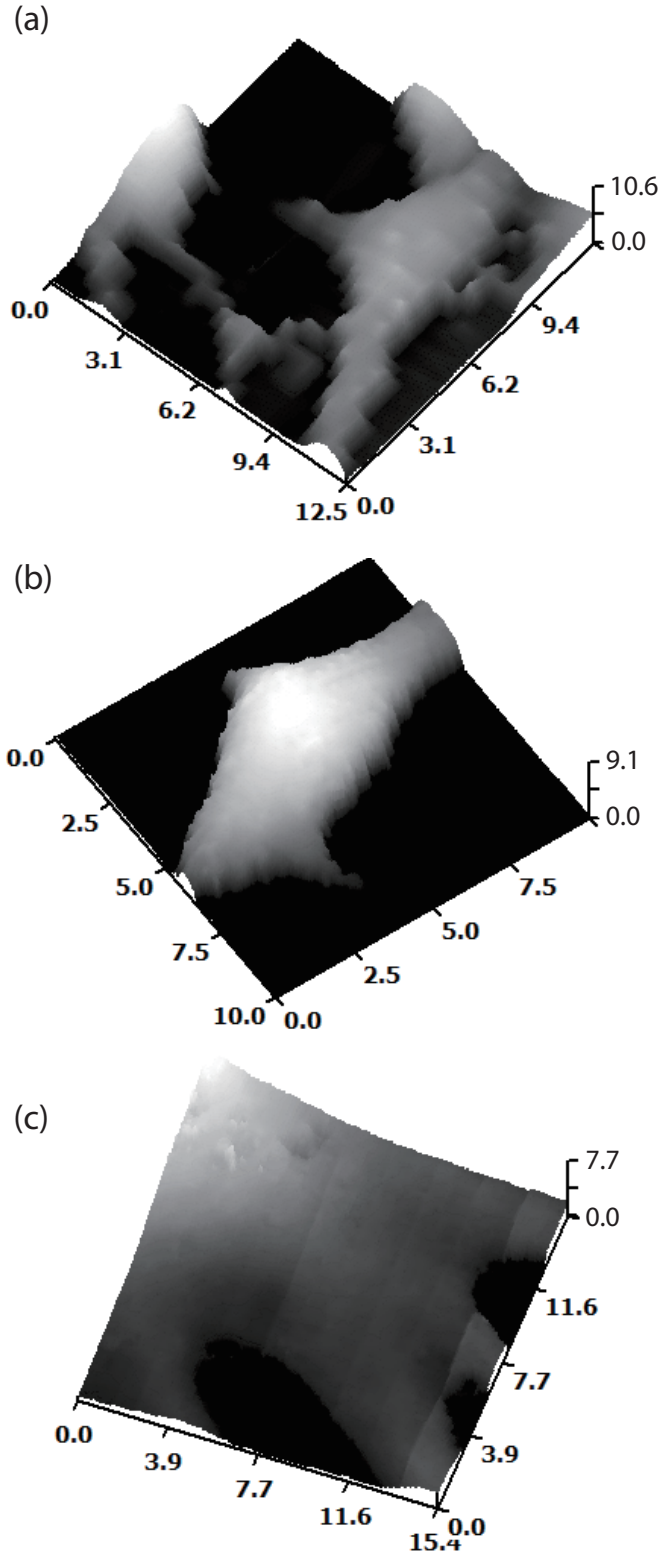

Figure 5.9: Topographic images of astrocytes using SICM in a resolution of (a) 469, (b) 166 and (c) 59 nm. They were performed in the hopping mode, with a setpoint of 1% and the tip falling rate of 500 nm/ms. Note that the X-. Y- and Z-axis are in a unit of μm.

is termed cell-attached recording, as shown in Figure 5.10(a), so only intracellular ions can flow through the nanopipette aperture. If strong suction is applied once again to rupture the membrane patch, leading to a continuous connection between the pipette's inner surface and the cell cytoplasm, it is called whole-cell recording (Figure 5.10(c)) and is frequently used for studying electrical signals from the entire cell. The other two operation modes are inside-out (Figure 5.10(b)) and outside-out recordings (Figure 5.10(d)), which are utilised to examine the characteristics of single-channel currents in different intracellular and extracellular chemical environments, respectively.

This patch–clamping function can be realised on the same setup. The borosilicate glass capillary (O.D. 1.0 mm, I.D. 0.58 mm) is used and the pulling program for a microscale pipette is: Heat:465, Filament:3, Velocity:45, Delay:130, Pull:105. The schematics of a whole–cell patch–clamp technique are depicted in Figure 5.10. When a nanopipette which is loaded with intracellular solution approaches the cell surface, positive pressure is firstly applied using a 1 mL syringe to prevent the adsoprtion of any unwanted objects near the nanopipette aperture. The pipette is controlled carefully by the angled micromanipulator as shown in Figure 5.8. Subsequently when the tapered part of the nanopipette touches the target cell (when a slight distortion of the cell membrane should be observed), the pressure is released and an Ω-shaped protrusion in the cell membrane with angstrom level glass–membrane separation is formed with the application of negative pressure (which traditionally was usually applied by the mouth via the syringe connected to the pipette holder) [42]. A giga-ohm seal between the nanopipette and the cell patch area is achieved immediately or within several seconds. This tight seal dramatically increases the signal-to-noise ratio of the measurements, because it electrically isolates the cell membrane and minimises the current leakage from the rim of the patch into the nanopipette. Under this condition, the potential of the membrane patch may be controlled via external voltage application. Therefore, charged ions flowing through a small set of single channels at the membrane patch are collected by the electrode immersed in the nanopipette, and then this current is amplified. For recording the ion current of the entire cell due to voltage clamping, as shown in Figure 5.10, zero-current cell-resting potential (it is usually –70 mV for neurons) is applied and subsequently additional suction

(or small voltage jumps) needs to be undertaken to rupture the membrane patch without impairing the giga-seal. The pipette interior and the cell cytoplasm are now contiguous, and therefore the ion current in the whole cell is successfully recorded. Under these conditions, the resistance of the nanopipette drops to less than 20 MΩ [202]. The whole-cell recording mode offers reproducible measurements of physiological ion events under voltage clamping, especially on excitable cells and voltage-controlled receptors.

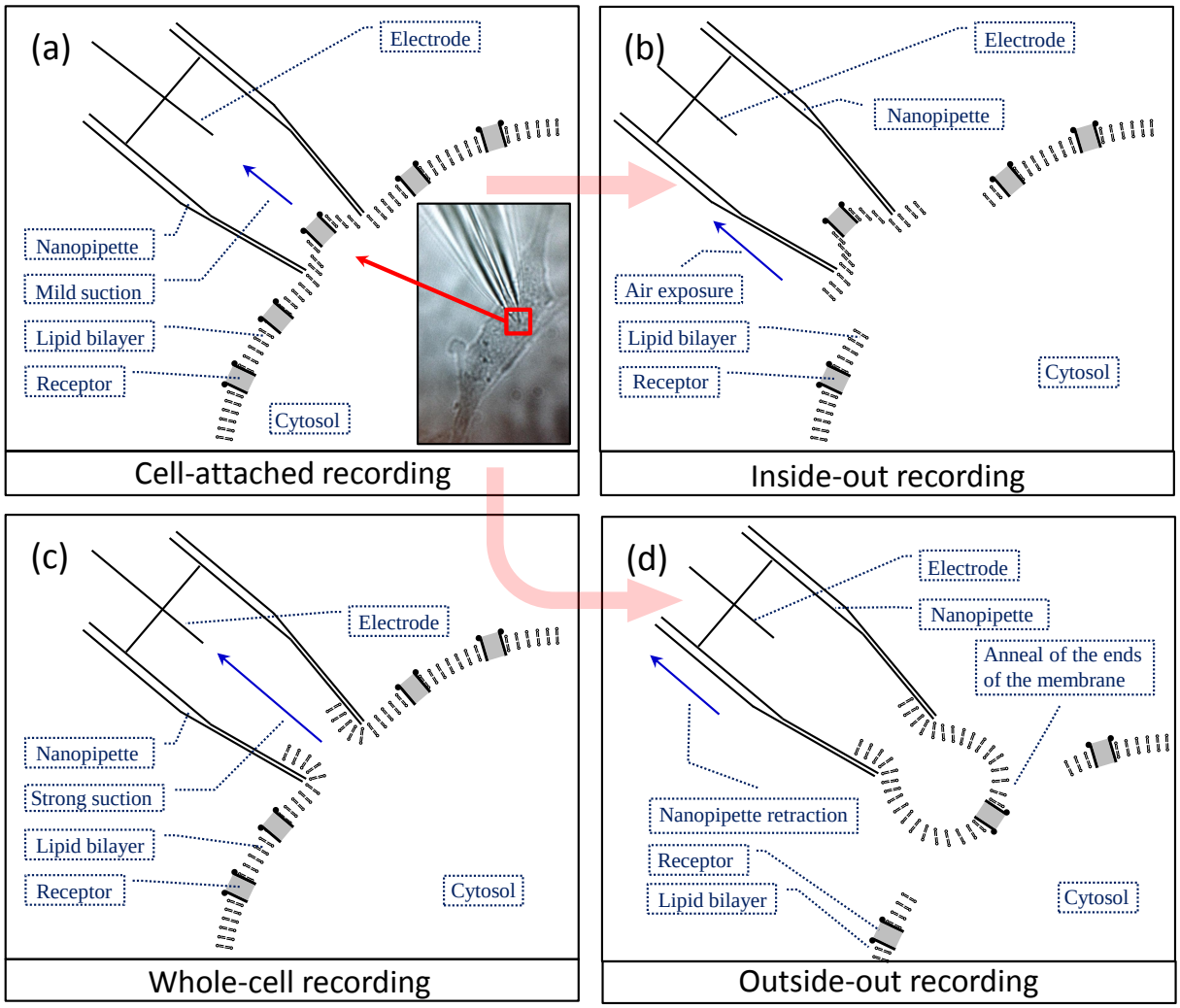

Figure 5.10: Schematic diagrams of four basic recording modes of the patch–clamp technique. (a) The nanopipette firstly has positive pressure applied to drive away unwanted particles in the buffer solution when it approaches the target cell, and subsequently pressure is changed to be negative by mild suction after the nanopipette tip is firmly attached (with a giga-seal) on the cell membrane. A single ion channel or a small number of ion channels is now captured in the inner space of the nanopipette tip and cell attachment may feasibly be conducted. In the inlet, a nanopipette patching a cell viewed using a 40× objective (Nikon, CFI Plain Flour oil immersion ×40) is demonstrated. (b) When the giga-seal is established, the nanopipette is retracted upwards so that exposure to the air can remove the cell patch, enabling inside-out recording. (c) Alternatively, when the giga-seal is formed, a pulse of stronger suction can be applied to rupture the cell membrane, where the intracellular cytoplasm is contiguous with the nanopipette interior. Therefore, the ion current flowing through every ion channel is collected simultaneously via the patched pipette under appropriate voltage bias, which constitute whole-cell recording. (d) Retraction of the nanopipette after the membrane is ruptured, i.e. in the mode of whole-cell recording, further breaking of the cytoplasmic bridge and annealing of the end of the membrane realise the outside-out recording. Notably (a), (b) and (d) are so-called single-channel recordings.

Three physical parameters obtained from whole-cell recording:

1. Direct current (DC)
2. Series resistance (R_s)
3. Membrane resistance (R_m)

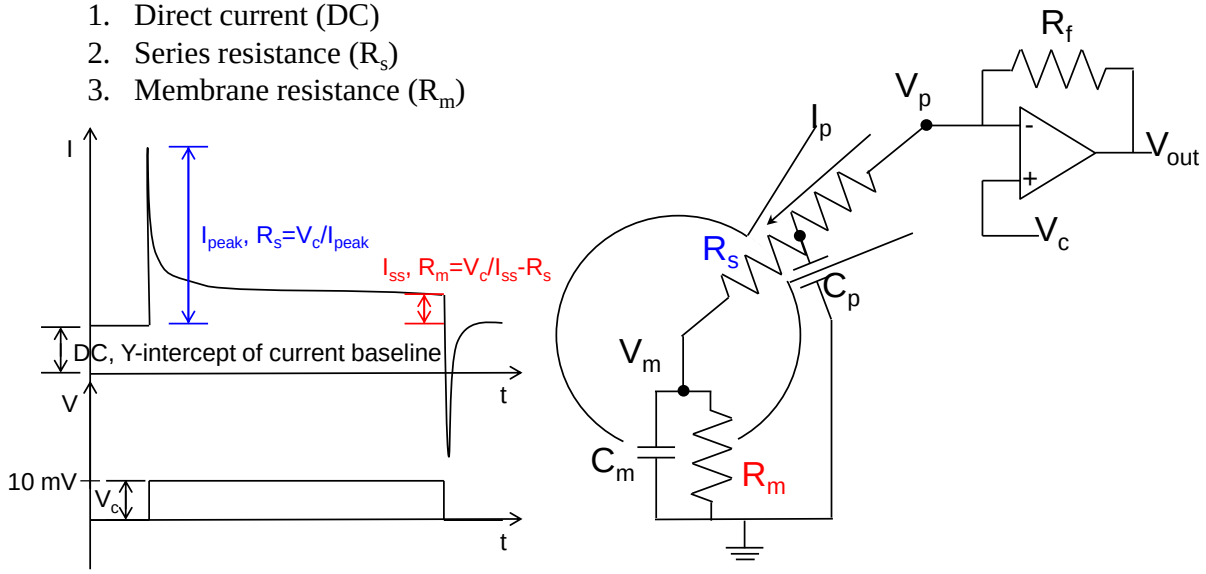

Figure 5.11: (right) A simplified equivalent circuit for modelling electronic characteristics in patch–clamp recording in the whole-cell mode, in which I_p is the nanopipette current; R_s, R_m and R_f are series resistance, membrane resistance and resistance in the amplifier, respectively; C_p, C_m are nanopipette and membrane capacitances, respectively; V_p, V_m, V_c and V_{out} are nanopipette, membrane, input and output voltages, respectively. Note that V_p is equal to V_c. (left) A capacitive current through the cell membrane under the stimulation of a periodic square wave of 10 mV. Three parameters, including DC offset, R_s and R_m, can be read and calculated simply from this current curve, where I_{ss} is the steady-state current.

5.7.1 Angled whole-cell patch–clamp

After a cell is firmly attached by a nanopipette with a suitable size of opening, its cell membrane can then be ruptured by the careful application of negative pressure so that its cytosol becomes contiguous with the intracellular solution pre-loaded in the nanopipette. Electronic properties of this whole system, including the cell, the nanopipette and the current amplifier, can be modelled as a simplified equivalent circuit, as shown in Figure 5.11 [202]. This model is composed of several resistances representing various objects in series, two capacitances indicating the nature of accumulation of charges on opposite sides of a dielectric material, and an operational amplifier. In general, a stimulation of a periodic square wave is applied via the nanopipette, so that a featured capacitive current through the cell membrane can be utilised to extract important parameters, especially series resistance (R_s), which is

sometimes referred to as input resistance, and membrane resistance (R_m). The diagram in Figure 5.11 illustrates these electronic characteristics.

An example of the procedure for performing whole-cell recording is shown in Figure 5.12(a) and (b). The tip of the nanopipette was tightly pressed onto a target neuron, with R_s, achieving 32 Gohm under a periodic square wave of 10 mV. A circle around the tip of the nanopipette due to its pressing the cell was observed. Subsequently, a light suction was applied, so that the cell was recorded in whole-cell mode. It is difficult to determine a status change from optical observation, but an effective membrane rupture is confirmed if a capacitive current appears. On the other hand, from diffusion into the cell of a fluorescent dye that was pre-loaded in the patching nanopipette, it is evident that whole-cell mode was successful, as shown in the inset of Figure 5.12(b). At the same time, electronic parameters, including the DC offset, R_s and R_m, can be monitored over time. Another example of these parameters is demonstrated in Figure 5.13, in which they are shown stabilised at roughly 400 seconds, although an initial sudden jump of R_s, probably due to a subtle movement of the tip was observed. Therefore, it was shown that whole-cell patch–clamp mode was successfully achieved and the system was ready for the experiments in the next stage, e.g. the application of electrical stimulation or reagent dosing in order to record the collective behaviour of one or more specific ion channels.

5.7.2 Smart patch–clamp

The disadvantage of the patch–clamp technique is that it lacks the ability to determine where the patch is located in subcellular structures, if the probing region is smaller than the optical resolution of microscopic objectives. Therefore, the combination of SICM and patch–clamp analysis provides precise positioning of the recorded channels, which is termed the scanning patch–clamp or smart patch–clamp method. The experimental protocol developed by Novak *et al* is as follows: (1) a nanoscale resolution of surface topography is first obtained by SICM with a small opening nanopipette; (2) the nanopipette is widened carefully on the same setup for the cell-attached analysis, which utilises the predefined three-dimensional

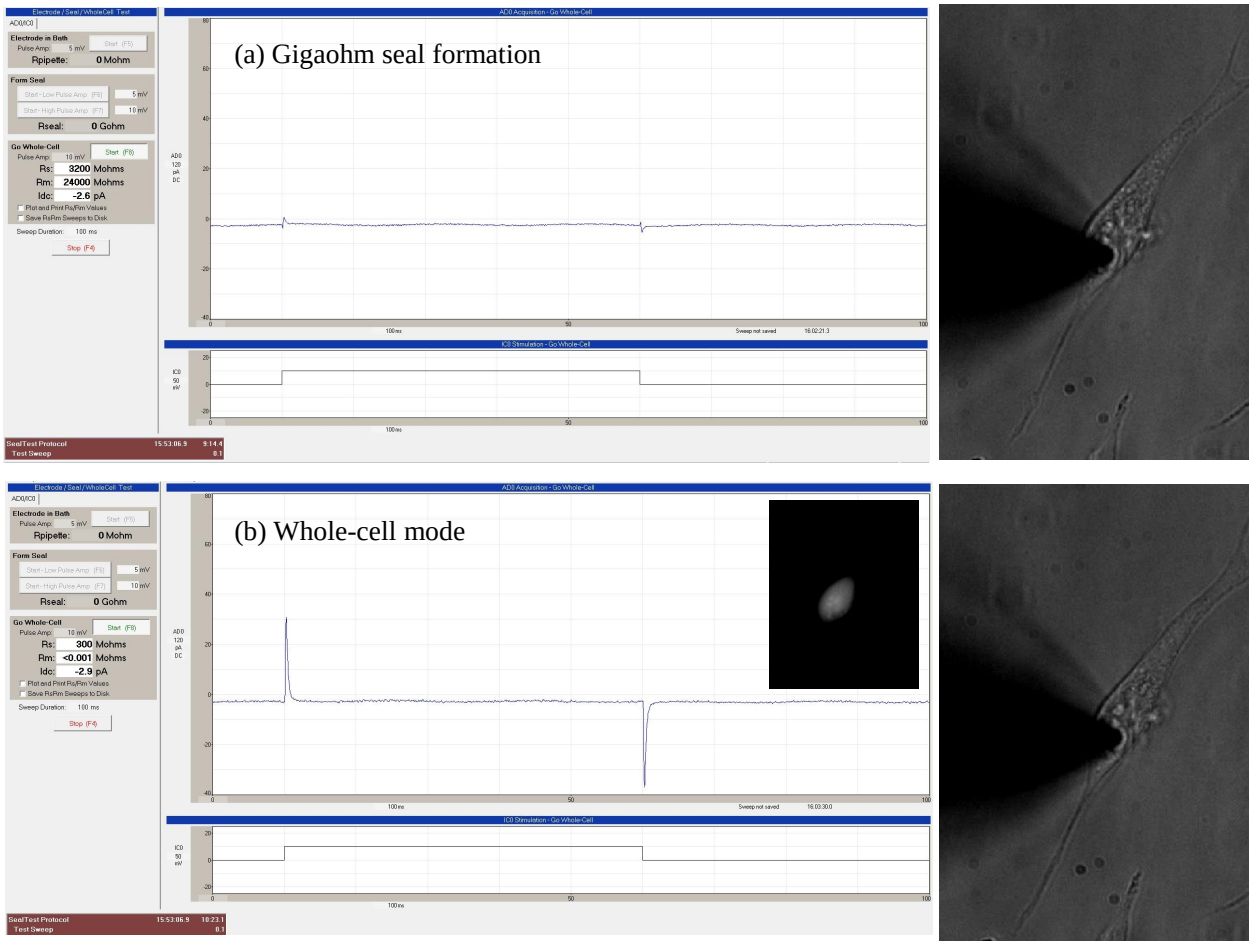

Figure 5.12: The featured capacitive current and an optical image of the nanopipette and target neuron during (a) gigaohm seal formation and (b) whole-cell recording. Note that the real-time electronic properties were acquired by WinLTP. The inset in (b) indicates a successful rupture of the cell membrane for whole-cell mode, with a pre-loaded fluorescent dye, 2.9 μM of Alexa AF488, diffusing into the neuron, and this dye was excited by an LED of 470 nm powered at 500 mW.

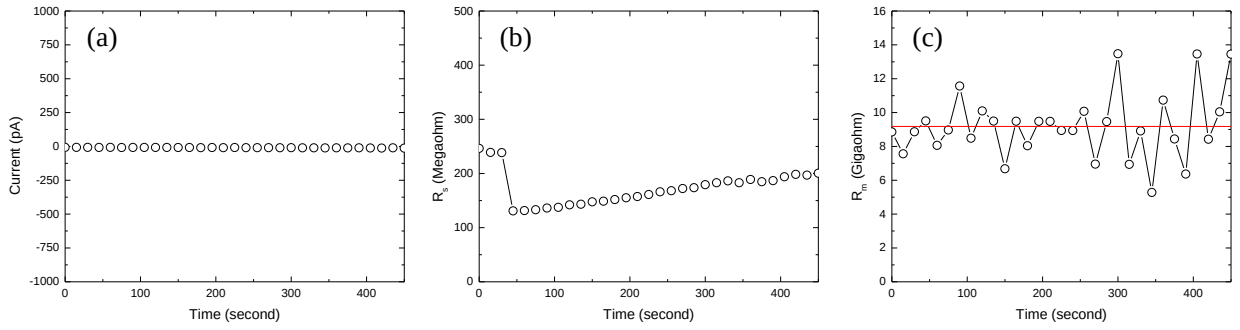

Figure 5.13: Real-time monitoring of (a) DC offset, (b) R_s and (c) R_m. Red line in (c) indicates an averaged value of R_m within the observation window of 450 seconds.

coordinates used in SICM [49]. The new setup introduced in this chapter should be able to carry out this smart patch–clamp technique, as the widening of the tip using the suggested method in their paper has been tested successfully, although further optimisation to obtain a tip opening with a desired size, and more practice of vertically-aligned whole-cell recording are needed.

5.8 Conclusions

In this Chapter, a new setup that is capable of conducting localised reagent dosing via a nanopipette and nanodetection using a sensor fixed to an angularly-aligned micromanipulator, in which application of stimulation on a single cell and the time-course monitoring of its response can be used to model a biological system of interest at a single-cell level. Therefore, using this rig to reveal the mechanism of the onset of a disease that has not been fully understood may shed light on possible treatments. This multifunctional setup is equipped with an LED lightsource and a CCD camera, and it has been optimised electronically; thus, it has the potential to allow experiments to be carried out that are not even covered in this thesis; e.g. smart patch–clamp and intracellular ROS recording over time via a fluorescent indicator. Examples of topographic imaging using SICM, and whole-cell recording have been demonstrated here, which proves this new rig based on SICM is very useful for experiments at the single-cell level.

Chapter 6

Single-cell ATP probing by nanoscale theta-nanopipette-based EGOFET

6.1 Introduction to nanoscale biosensors

If transient pores in the cell membrane are formed simultaneously when Abeta42 oligomers enter, there should be other kinds of intracellular molecules leaking out of the cell, e.g. free cytosolic adenosine triphosphate (ATP), and these might be detectable using a nanoscale sensor with a sufficient sensitivity situated right above the dosed cell. ATP is a critical molecule in the human body, because one of its derivatives, cyclic adenosine monophosphate (cAMP), is a second messenger in the intracellular system that triggers important physiological functions, e.g. proliferation, differentiation and apoptosis, and ATP itself can be released to regulate intercellular signalling [203]. The release pathways of ATP through cell membranes are usually via exocytosis of secretory vesicles, or ATP transporters or the physical rupturing of cell membranes [204, 205]. In healthy neuronal cells, released ATP can be used to mediate the propagation of calcium waves in astrocytes [206, 207]. Previous studies have also found that aggregates of Abeta42 peptides can induce the production of reactive oxygen species (ROS) in microglial cells [208] and enhance the intensity, velocity and distance of calcium signalling in astrocytes [209]. All of this evidence indicates Abeta42 does indeed

play a role in modifying homeostasis. In addition, intracellular ATP is of approximately millimolar, which is a relatively high concentration [210–212], and there has been evidence demonstrating oligomer-induced ATP leakage [213]. Therefore, it is likely that ATP leakage induced by Abeta42 oligomer of a physiological concentration will be detected above a resting neuronal cell by an ATP biosensor with a millimolar sensitivity.

Modified nanopipettes in SICM have been recently adopted for the development of sensors. Scanning electrochemical microscopy (SECM) is realised by replacing the nanopipette in SICM with a nanoelectrode, which is capable of revealing the specific chemical properties of a scanned area [214, 215]. The tip of the nanoelectrode can be designed as a highly-sensitive detector for specific molecules, with a diffusion-limited Faradaic current characterised by charges, redox species and a concentration of electrolyte [216]. A benefit of having nanoelectrodes with a tip diameter of several nanometers is that they can minimise the invasion and damage of a targeted object, which is especially critical when measurements are performed in live cells.

Various biological applications have been conducted using nanoelectrodes. Wang *et al.* were the first to measure intracellular oxidative bursts in murine macrophages using a nanoelectrode with a diameter of about 150 nm functionalised with platinum black [217]. Actis *et al.* have produced platinum-coated nanoelectrodes, whose tip opening of approximately 5–200 nm can be precisely altered to detect intracellular and extracellular oxygen consumption in a brain slice [218]. It is notable that this kind of nanoelectrode with a disc-shaped opening was manufactured using a simple and fast method by filling pyrolytically deposited carbon into a nanopipette. However, this platinum-coated nanoelectrode must be operated at a high applied bias voltage of 800 mV versus Ag/AgCl reference electrode may measure not only targeted species but also unwanted ones in live cells. In this case all kinds of activated species will contribute to the Faradaic current. Clausmeyer *et al.* deposited Prussian Blue into a nanocavity etched on the tip surface of a nanoelectrode, which is a redox mediator for hydrogen peroxide [219]. As a result, the operated DC voltage was applied at –50 mV, which is reasonably low, and this sensor had a detection limit of 10 μM hydrogen perox-

ide. Intracellular ROS and reactive nitrogen species (RNS) can potentially be detected by a nanoelectrode inserted in cells under constant-voltage recording mode, which means that signal distortion can be avoided by proper electrical isolation from the cell membrane.

For intracellular measurements, a sensor is usually designed so that its detection limit will be able to reach as low as submicromolar concentrations; however, it is not easy to achieve this with nanoelectrodes, because a compromise between two contradictory conditions, i.e. a sufficiently low impedance and minimal rupture of cell membranes, must be achieved. In other words, the dimension of the nanoelectrode opening cannot be made to be too small; otherwise, the signal-to-noise ratio will be too low for proper data collection to be carried out. Therefore, many nanoscale sensors with a high surface-area-to-volume ratio have been designed in order to achieve high sensitivity at a single-molecule level. Among these, a sensor built on a nanoscale field-effect transistor (nanoFET) is one of the most promising candidates for intracellular applications [220]. This kind of sensor is able to circumvent the problem related to impedance, because there is no direct current flowing into the tip of a nanoFET sensor. The transconductance of a nanoFET sensor is defined by $\Delta I_{out}/\Delta V_{in}$, which is usually inversely proportional to its own size of the active area [221]. Therefore, in general, nanoFET sensors have higher sensitivity and higher spatial resolution than nanoelectrodes.

For a nanoFET sensor, either organic or inorganic semiconductors can be used as the active material. Although an inorganic semiconductor manufacturing process has been fully developed, and inorganic semiconductors with a higher carrier mobility are suitable for high-speed applications, organic conducting polymers have the advantages of low-cost processing, high sensitivity and high tunability, especially in the fields of chemical and biological sensing [222]. Among the various kinds of conducting polymers that are fabricated for electronic devices, polypyrrole (Ppy) has the characteristics of low redox potential and good biological compatibility [223, 224]. The conductivity of Ppy can be effectively increased by electrochemical doping, in which Ppy under the application of a voltage will be swollen and dopant ions in a solution are allowed to diffuse to fill in available vacancies to achieve electric neutrality. Previous studies had shown that nanoFET sensors made of Ppy are capable of detecting

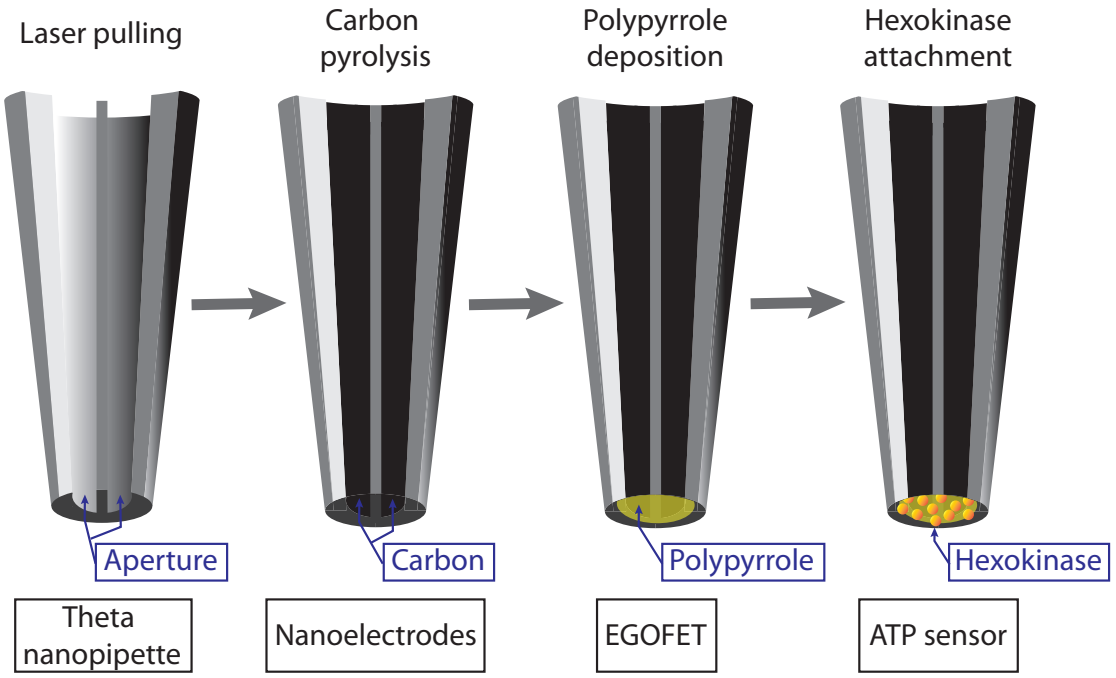

Figure 6.1: Schematic cross-section of different stages of a theta nanopipette during the manufacturing process for producing an ATP sensor. First, the nanopipette experienced pyrolytic carbon filling in the pair of vacant barrels (nanoelectrodes). Subsequently, a Ppy layer was deposited to connect individual semilunar carbon fillings (EGOFET). Finally, hexokinase was attached to the Ppy layer to establish ATP sensitivity (ATP sensor).

changes in pH in a solution, in which protonation and deprotonation may increase and decrease the conductivity of the Ppy layer, respectively [225]. In addition, different chemical species could be detected by modifying a Ppy-nanoFET-based sensor with specific reactors [226, 227].

In this chapter, a low-cost manufacturing process without the need for a conventional cleanroom, with a newly developed theta-nanopipette-based ATP sensor is introduced. This process was operated using an angular-aligned micromanipulated holder in the new SICM setup described in the previous chapter, and the sensor produced could continue to carry out ATP measurements (without being withdrawn from the holder) directly at room temperature if needed. As shown in Figure 6.1, the fabrication process has four main steps: (1) producing a theta nanopipette with two suitable sizes of semilunar openings; (2) pyrolytical filling of carbon into these two channels; (3) individual Ppy deposition on both of the carbon-filled channels until a Ppy connecting bridge is established; and (4) successful constraining of

appropriate units of hexokinases, which enable catalysis of phosphorylation of the substrate (ATP acts as the phosphate donor), near the active channel of an electrolyte-gated organic FETs (EGOFET). Finally, electronic characteristics of EGOFETs and EGOFET-converted ATP sensors in a solution were discussed in detail, and experimental results on cells were reported, too.

6.2 Materials and methods

6.2.1 Cell preparation

Astrocytes used in the experiment were selected by the nanopipette from a mixed glial preparation from P3–P4 rat, which was cultured for 2 weeks in 75 cm^2 cell culture flasks (Corning) with Dulbecco's Modified Eagle's medium (DMEM, Invitrogen) supplemented with 10% fetal bovine serum (FBS), 1% Penicillin and Streptomycin and 1% L-Glutamine (Life Technologies) in an incubator kept at 37°C, where 5% CO_2 was maintained through a delivery tube in a humidified atmosphere.

Once 90% confluence of glial cells was achieved, cells were split and kept in a suitable environment for a long-term culture. According to the schedule of performing experiments, neuronal cells were transported in order to reach a 40–70% confluence, in 35 mm dishes with No. 1 coverslip of 14 mm glass diameter at the bottom (P35G-1.0-14-C, MatTek). Plated dishes were used for experiments within 1–5 days, and it was possible for their confluence to increase to a level not feasible for single–cell measurements afterwards.

6.2.2 Abeta42 preparation

Abeta monomer, Hilyte Fluor 647 ABeta42 (Cambridge Bioscience LDT), was kept on ice and subsequently purified using a BioSep gel filtration (SEC-s2000, Phenomenex) in buffer solution, SSPE (0.01 M Na_2HPO_4, 0.15 M NaCl, 1 mM EDTA, pH 7.4). Afterwards, the filtered product was flash frozen and stored in a –80°C freezer. Peptides were always prepared

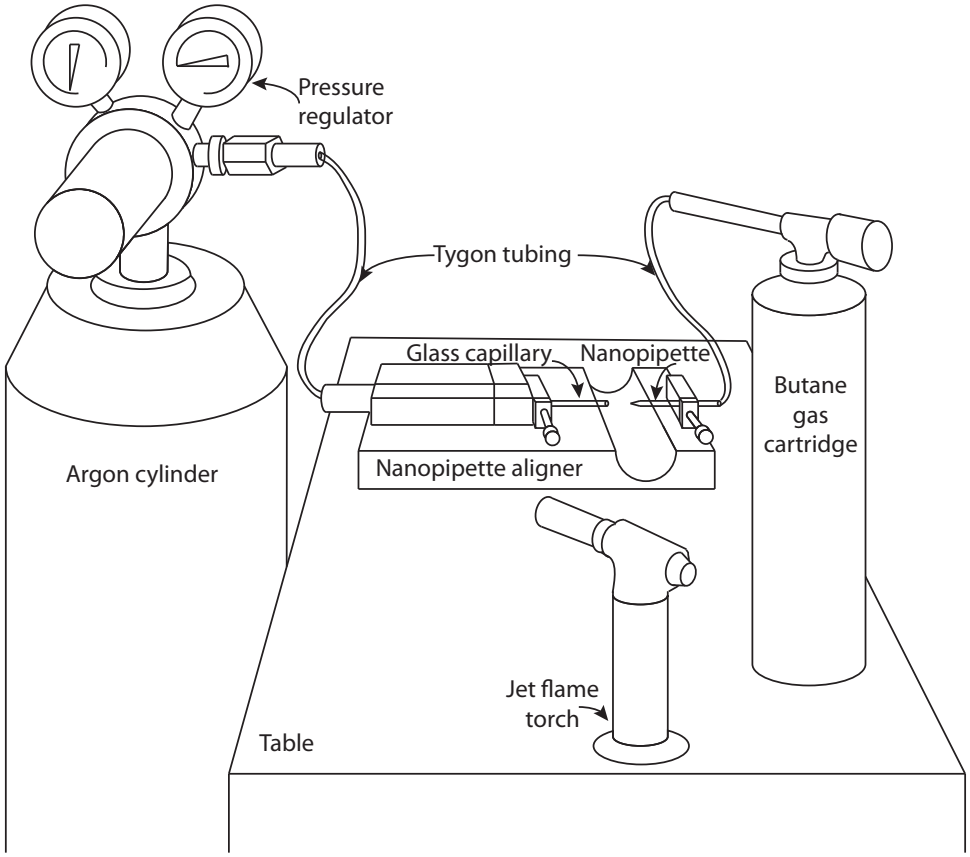

Figure 6.2: Schematic illustration of the setup for fabricating theta-nanopipette-transformed nanoelectrodes. A butane-filled theta nanopipette is fixed to one end of the nanopipette aligner, whilst pressure-regulated argon is transferred via tygon tubing connected to a glass capillary, which is fixed to a slidable metal block set, in order to allow controllable flow onto the sheathed nanopipette tip. Combustion via a jet flame torch is applied to provide pyrolytic carbon deposition inside two vacant channels at the nanopipette tip.

fresh right before the cell-dosing measurements. The purified Abeta42 was diluted to 500 nM in PBS and left shaking at 37°C, at 200 rpm for 5 hours in an incubator. Consequently, it was centrifuged at 1450 ×g for 10 minutes and then diluted to the required concentrations in L-15 cell culture medium. The concentration of oligomers have confirmed by a single-molecule counting method using confocal two-color coincidence detection (cTCCD). This protocol gave approximately of 3 nM Abeta42 oligomers plus 500 nM of Abeta42 monomers [175].

6.2.3 Fabrication of theta-nanopipette-based ATP sensors

Each length of quartz theta tubing with septum thickness of 0.15 mm (QT120-90-7.5, Sutter Instrument) was fixed and processed using a CO_2 laser puller (P-2000, Sutter Instrument) with parameters: HEAT:670, FIL:3, VEL:45, DEL:130, PUL=95 to generate a pair of theta nanopipettes, with an inner radius of roughly 100 nm and a septum thickness smaller than 50 nm separating two vacant channels with a similar semilunar shape and size. Afterwards, as shown in Figure 6.2, a theta nanopipette was fixed on a screw-tightened metal square at one end of a homemade nanopipette aligner, on which a tygon tubing connected glass capillary (Q120-90-10, Sutter Instrument) was fixed on a set of slidable metal blocks on the other end. This tygon tubing was used to transfer Argon from a pressure-regulated cylinder out of this glass capillary; the end of the nanopipette was also connected to a butane gas cartridge via tygon tubing of the same size. Therefore, the butane-filled tip of the nanopipette was covered by the argon-flowing glass capillary, which produced a locally oxygen-deficient environment at the tip, and then it was heated up by a butane-filled jet flame torch for around 10 seconds in order to deposit enough carbon pyrolytically into the two vacant channels extended to the tip.

After electrochemical characterisation in a solution with 1 mM FcMeOH (335061, Sigma Aldrich) and 100 mM KCl, suitable carbon-filled theta nanopipettes were selected to be immersed in a solution containing 0.5 M pyrrole (131709, Sigma Aldrich), 0.2 M $LiClO_4$ and 0.1 M $HClO_4$, in order to form Ppy deposition bridging carbon-fillings at both channels via oxidative polymerisation with consecutive dimerisation of two radical cation pyrrole monomers.

As shown in Figure 6.3, carbon nanoelectrodes termed drain and source in an EGOFET were connected to the application of bias voltages (V_G and V_{DS}), whilst the gate electrode was immersed in the pyrrole solution. The growth of Ppy separately on the two carbon electrodes via cyclic voltammetry of V_G=–0.3 to 0.65 V and simultaneously (V_{DS}=0.5 V) was monitored by an increase of Faradaic current at two electrodes during repeated scan cycles. This Ppy-growing process would be stopped when separate Ppy layers made contact

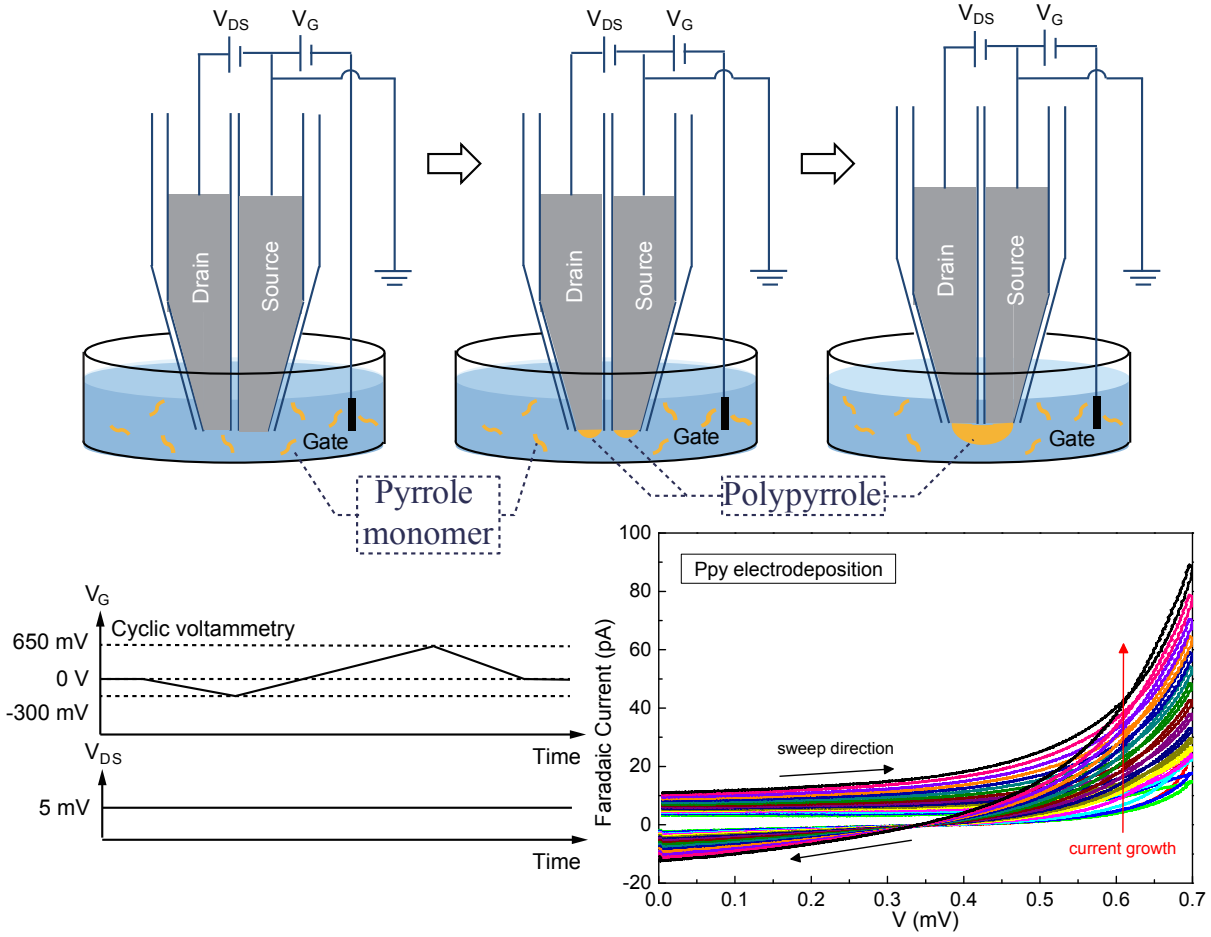

Figure 6.3: Illustrations of the fabrication process of Ppy deposition on two semilunar surfaces of carbon nanoelectrodes. (Upper) A pair of carbon-deposited nanoelectrodes is immersed in a solution containing 0.5 M filtered pyrrole monomers, 0.2 M $LiClO_4$ and 0.1 M $HClO_4$. Ppy starts to grow, cycle by cycle, during the application of cyclic voltammetry of V_G=–300 to 650 mV, whilst V_{DS} is maintained at 5 mV, as depicted in the (lower left). Ppy grown separately on nanoelectrodes will consequently make contact after a few scan cycles. (Lower right) Ppy growth at one side of the carbon nanoelectrode demonstrated by a cyclical increase of Faradaic current during cyclic voltammetry from 0 to 0.7 V.

with each other, which could be acknowledged by observing a pair of symmetrical waveforms at the two channels. In this way, a nanoscale EGOFET with a thin Ppy layer used as the active material was fabricated.

Owing to the fact that an EGOFET-converted ATP sensor reacts with protons generated from phosphorylation involving ATP, an unbuffered solution, which contains 120 mM NaCl, 5 mM KCl, 5 mM $MgCl_2$ and 20 mM D-glucose, and is adjusted to pH 7.5 to 8, is necessary for the experiments. Ppy-based EGOFET was consequently processed and con-

verted into an ATP sensor by linking enough units of hexokinase onto the Ppy layer via glutaraldehyde molecules. An EGOFET was immersed firstly in lightly-mixed (with a 5 μL pipette tip) 25% glutaraldehyde in water (G5882, Sigma Aldrich) and then 500 U/mL Hexokinase and Glucose-6-phosphate Dehydrogenase from baker's yeast (S. cerevisiae, H8629, Sigma Aldrich), each for at least 30 minutes, whilst cyclic voltammetry was still conducted. Finally a successful ATP sensor was rinsed carefully three times using unbuffered solution to wash away hexokinase that was not firmly attached. A new ATP sensor was fabricated and kept in the unbuffered solution with adjusted pH before any measurements were taken. ATP disodium salt hydrate (A2383, Sigma Aldrich) was used for ATP sensor calibration.

6.3 Experimental results

6.3.1 Characterisation of carbon nanoelectrodes and the EGOFET

Characterisation of how carbon were deposited in the pair of semilunar channels in a theta-nanopipette was done by performing cyclic voltammetry (0 to 0.5 V) with the nanoelectrode tip being immersed in solution containing 1 mM of FcMeOH. The Faradaic current at each surface of the carbon fillings was monitored over time during repeated scan cycles in order to estimate the surface shape created by combustion. An example of the characterisation of paired carbon fillings is shown in Figure 6.4(a), with a saturated Faradaic current of 50$\pm$10 pA and V_G at 0.5 V demonstrating that its surface was likely to be relatively flat, so that its charge flow is not limited by a planar diffusive influx of redox mediators, FcMeOH. It is important for the pair of carbon fillings to have similar surface areas in order to provide a better platform for the next-stage of the sensor fabrication. Ppy itself is pH-sensitive due to protonation or deprotonation occurring when the surrounding pH has changed. Thus, when the tip of a nanoFET, i.e. EGOFET in this case, was soaked in various reagents, the magnitude of I_{DS} would change according to the solution pH under cyclic voltammetry of V_G=–0.6 to 0.2 V and simultaneously V_{DS} biased at 10 mV, as shown in Figure 6.4(b), where pH of calibration solutions is widely distributed from 0.8 to 10. Here the off-state

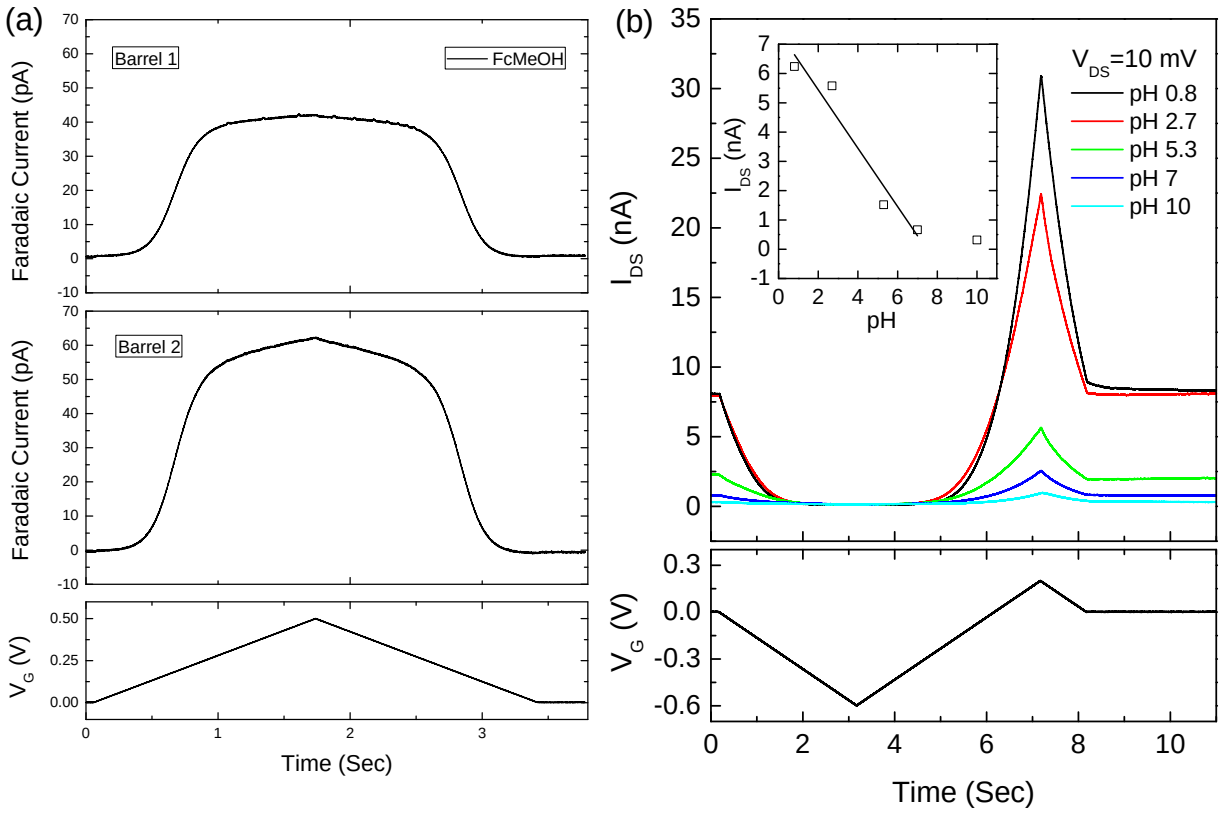

Figure 6.4: Diagrams of (a) Faradaic current of two carbon nanoelectrodes and (b) equilibrated I_{DS} in different pH solutions (0.8, 2.7, 5.3,7 and 10) during the application of cyclic voltammetry of V_G=–0.6 to 0.3 V. The inset in (b) demonstrates I_{DS} averaged in a complete scan cycle according to tests on solutions of varying pH. The black line is a guide for the eye.

of the EGOFET was observed when V_G was lower than –0.5 V. The inset in Figure 6.4 is an example showing a relationship between I_{DS}, which was extracted by averaging an equilibrated waveform during a complete scan cycle, and pH ranging from 1 to 10 for this specific Ppy EGOFET.

In the previous example, EGOFET was biased at V_{DS}=10 mV. As shown in Figure 6.5, the inset demonstrated a linear relationship between averaged I_{DS} and V_{DS}, when an EGOFET was conducted, with cyclic voltammetry of V_G=–0.6 to 0.2 V in PBS of pH 7.0. Therefore, in theory, I_{DS} can be greatly amplified by increasing V_{DS} to reach a satisfactory signal-to-noise ratio, if the stability of an EGOFET can be maintained. Note that the new EGOFET was designed for any kind of experimental measurement.

In the case demonstrated in Figure 6.4(b), the EGOFET was turned off when V_G was

lower than an estimated –0.5 V. However, when the current axis was plotted on a logarithmic scale, as shown in Figure 6.6, a massive leakage current of more than 0.1 nA was observed at V_G=–600 mV in various pH conditions. It is apparent this EGOFET could not be considered a good electronic switch, and presumably the leakage current could not be reduced any further even if a V_G was applied at less than –1 V, because I_{DS} had reached a plateau at –600 mV, as shown in Figure 6.6. Note that in a well-fabricated traditional FET, I_{DS} versus V_G would have a relatively steep slope with V_G applied in the negative region. The same situation occurred for other EGOFETs but they are not displayed here, and a highly negative V_G is also not recommended, because it may damage the device itself. Nevertheless, this drawback did not matter, since the ultimate target of producing a nanopipette-based EGOFET is to amplify I_{DS} greatly, in order to obtain a high signal-to-noise ratio, and at the same time to keep its physical size as small as possible to minimise invasion of cells during intracellular measurements.

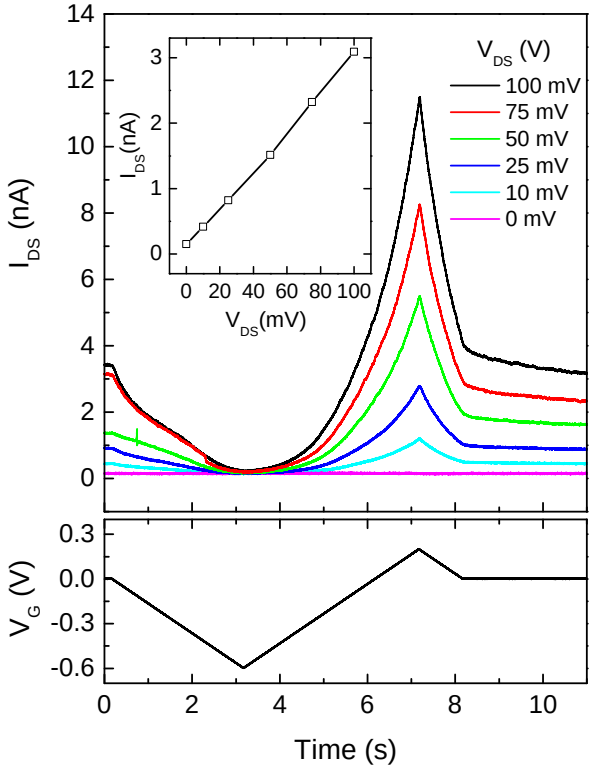

Figure 6.5: A diagram of equilibrated I_{DS} with different applications of V_{DS} (0, 10, 25, 50, 75 and 100 mV) in pH 7.0 PBS during cyclic voltammetry. The inset demonstrates the equilibrated I_{DS} obtained from averaging a complete scan cycle at different V_{DS}. A linear relationship between I_{DS} and V_{DS} can be seen.

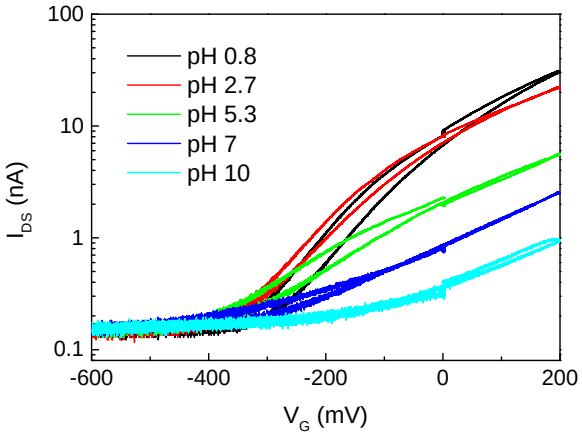

Figure 6.6: A graph of logarithmic scale of I_{DS} versus V_G in solutions of varying pH.

6.3.2 Measurements using an EGOFET

The scan range of cyclic voltammetry was subsequently modified without approaching radical voltages during pH measurements, and a theta nanopipette with smaller openings was

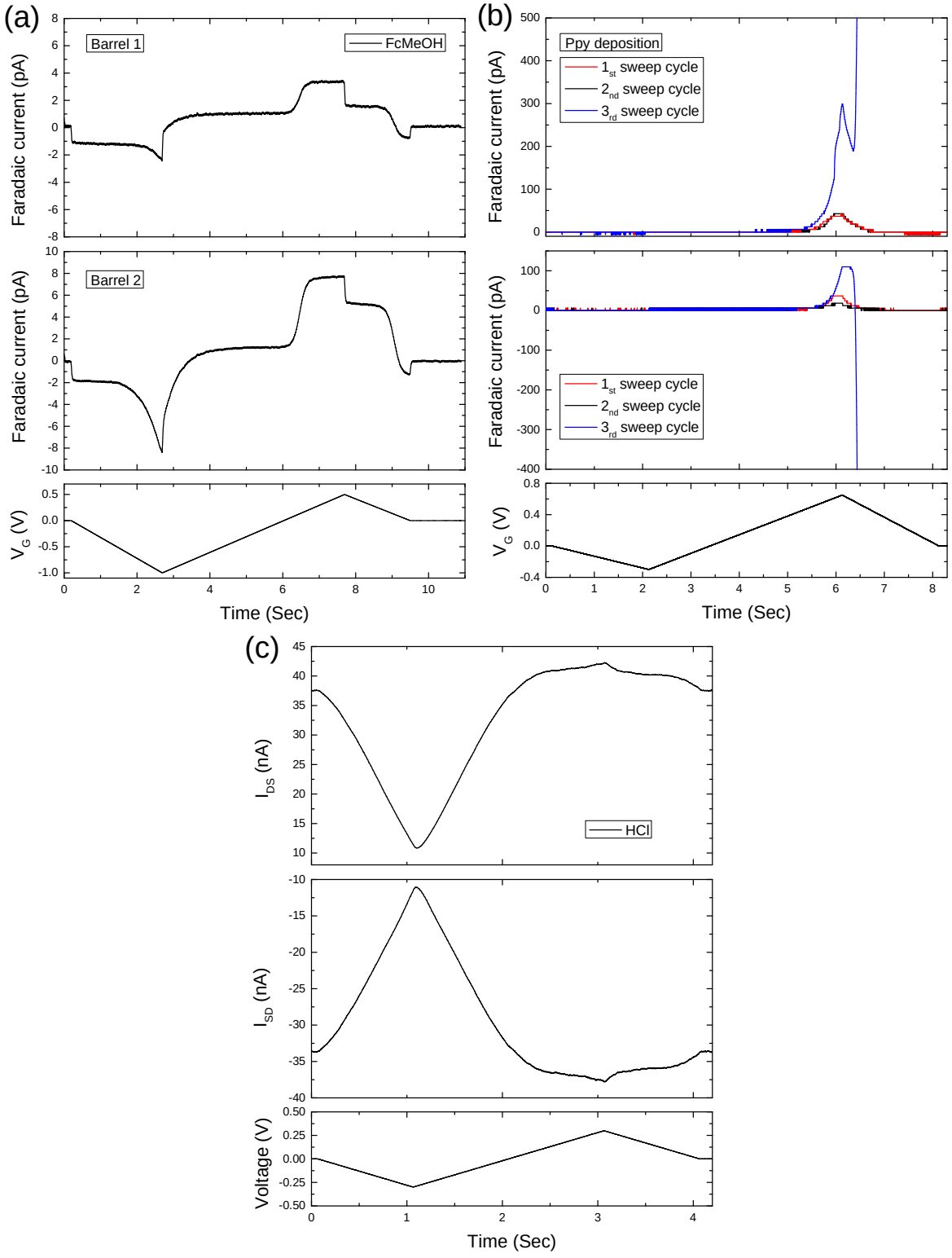

Figure 6.7: Individual waveforms over time measured at two channels in a theta nanopipette with respect to defined voltage scans during (a) characterisation of carbon-deposited nanoelectrodes, (b) Ppy growth on the pair of carbon fillings and (c) equilibrated Ppy EGOFET in 100 mM HCl solution.

selected to make a smaller FET. The manufacturing process was therefore updated and shown in Figure 6.7. For the purpose of obtaining small openings in carbon electrodes, Faradaic current smaller than 50 pA at V_G during 0 to 0.5 V was adopted. An example is shown in Figure 6.7(a). Note that an obvious capacitive effect at V_G=0.5 V suggested the double layer charging current made a comparable contribution to that of the mass transport due to the relatively small and flat carbon surfaces of nanoelectrodes. Figure 6.7(b) demonstrates gradual Ppy growth on the flat carbon surfaces of a nanoelectrode when each scan cycle reached nearly 0.65 V, which was similar to the lower right graph in Figure 6.3. Furthermore, the contact with individual Ppy growth was successfully made in the third cycle, since an abrupt increase in I_{DS} in the opposite direction at each nanoelectrode was observed, which indicated that they now represented I_{DS} and I_{SD}. These symmetric waveforms were clear in Figure 6.7(c), when a successfully-made EGOFET was operated in 100 mM HCl. Empirical evidence suggests a freshly-fabricated EGOFET should be immersed in this 100 mM HCl for an hour with cyclic voltammetry of V_G=–0.3 to 0.3 V before the next stage should be conducted. Note that the waveform of I_{DS} in Figure 6.7(c) appeared upside down, with left and right reversed when compared to Figure 6.5, owing to an exchange of anode and cathode in voltage sources in the system. This did not actually matter because the cyclic voltammetry was always symmetrically swept, i.e. V_G=–0.3 to 0.3 V, during measurements of pH or ATP concentration.

The pH-sensing results using cyclic voltammetry of V_G=–0.3 to 0.3 V are displayed in Figure 6.8(a), with I_{DS} equilibrated after the protonation and deprotonation of the Ppy layer at the tip of EGOFET. In this case no off-state current was observed due to the scan voltage not covering a very negative range, but this had no influence on the pH-sensing results of EGOFETs. Averaged I_{DS} at each complete cycle in time-course is shown in Figure 6.8(b), which demonstrates how I_{DS} varies accordingly in different pH solutions. It took roughly 100 seconds to achieve physical equilibrium for an EGOFET that had begun to be dipped in a new reagent with a relatively small pH difference (≤ 2). In order to remove any nonlinear effects on I_{DS}, normalisation of saturated and averaged I_{DS}, was taken, as shown in the inset of Figure 6.8(b). In figure 6.9(a), pH calibrations of 17 different EGOFETs were put

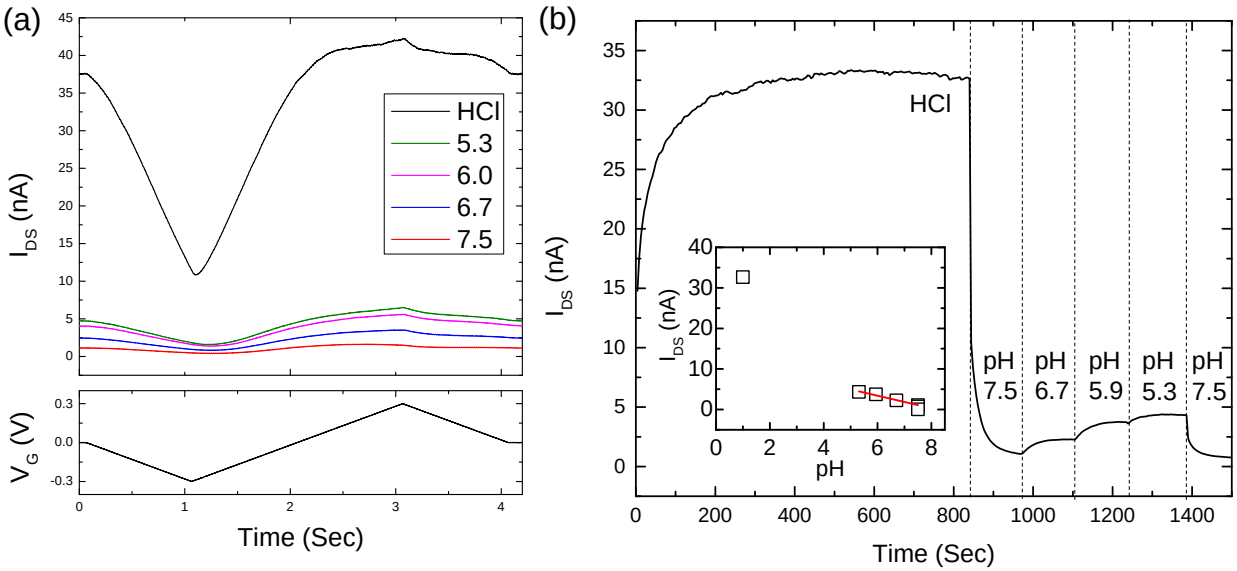

Figure 6.8: Diagrams of (a) equilibrated I_{DS} and (b) averaged I_{DS} in time-course at different pH (1, 5.3, 6.0, 6.7 and 7.5) under the application of cyclic voltammetry of V_G=–0.3 to 0.3 V. The inset in (b) demonstrates I_{DS}, which showed a linear response versus pH ranging from 5.3 to 7.5.

together. These curves were highly divergent due to that fact that the surface area of the Ppy layer of each EGOFET could not be finely tuned, and this is accompanied by other nonlinear effects probably also caused also by each nonideal EGOFET structure. Hence, it was more reasonable to plot an averaged current normalised at pH 7.2, and this gave rise to a predictable relationship between pH 4.5 to 8, which is suitable for biological applications, since physiological pH approximately falls between approximately pH 6 to 8.

6.3.3 Three approaches to EGOFET-converted ATP sensors

The next stage in gaining sensitivity to ATP would be to take advantage of an enzyme that is capable of performing phosphorylation involving ATP of a substrate molecule, and simultaneously a proton is produced for detection. The phosphorylation involving ATP by hexokinase is written as: D-glucose + ATP = D-glucose 6-phosphate + ADP + proton, where D-glucose is the substrate for hexokinase [203]. One of the products, protons, should be detectable with the pH-sensing EGOFET described in the previous sections, before it is dissipated in the bath solution. Therefore, three approaches were adopted for the purpose

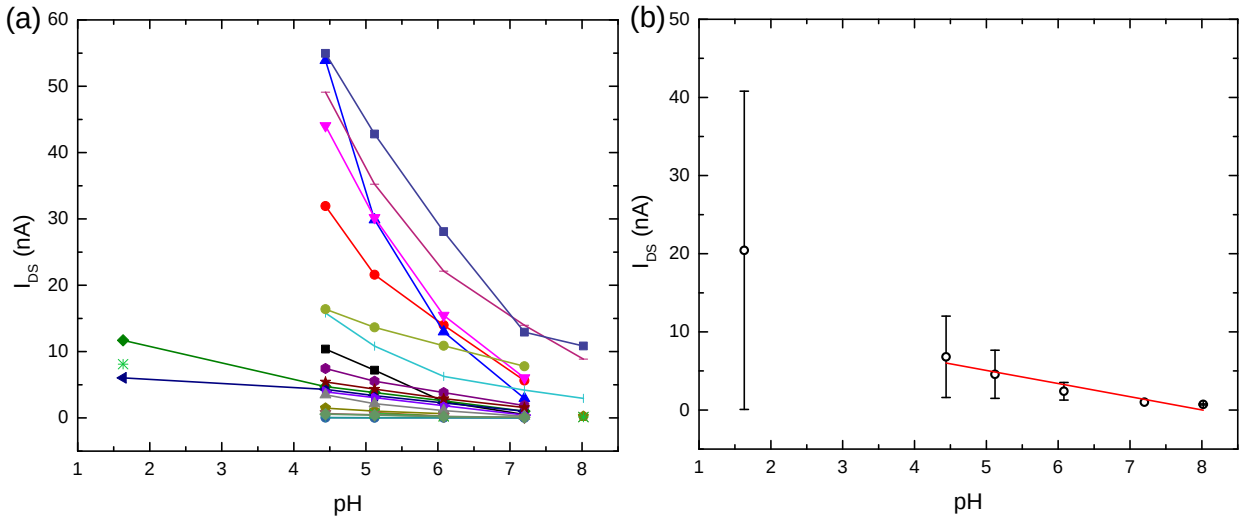

Figure 6.9: Diagrams of (a) raw data of averaged I_{DS} versus pH in 17 different Ppy EGOFETs and (b) I_{DS} normalised at pH=7, exhibiting a roughly linear response at pH ranging from 4.5 to 8.

of detecting Abeta42 oligomer-induced ATP leakage: (1) hexokinase and Abeta42 oligomers were both applied in the bath solution, in which protons generated by phosphorylation involving Abeta42 oligomer-induced ATP leakage would be detected by an EGOFET situated above a targeted astrocyte; (2) hexokinase was loaded in a nanopipette with its tip arranged next to an EGOFET above a targeted astrocyte, so that local pH change due to Abeta42 oligomer-induced ATP leakage in this microenvironment could be sensed; (3) hexokinase was attached onto the Ppy active layer on an EGOFET via a linker molecule, glutaraldehyde, and Abeta42 oligomer-induced ATP leakage at the cell membrane could be transduced to an electronic signal at the EGOFET. Schematic illustrations of these three approaches are depicted in Figure 6.10.

The application of 12.2 U/mL hexokinase into the bath solution containing 100 μM of ATP indicated that a pH change in the solution due to phosphorylation involving ATP leads to an obvious and immediate increase of I_{DS} from 106.7 to 327.7 pA, as shown in Figure 6.11(b), whilst the addition of the same volume of pure water as a negative control into 100 μM of ATP solution produced no response at all, and so no observable proton production in the solution. The pH in different solutions after experiments were performed was also determined by a commercial pH meter, which showed pH 7.61 and 6.21 for the

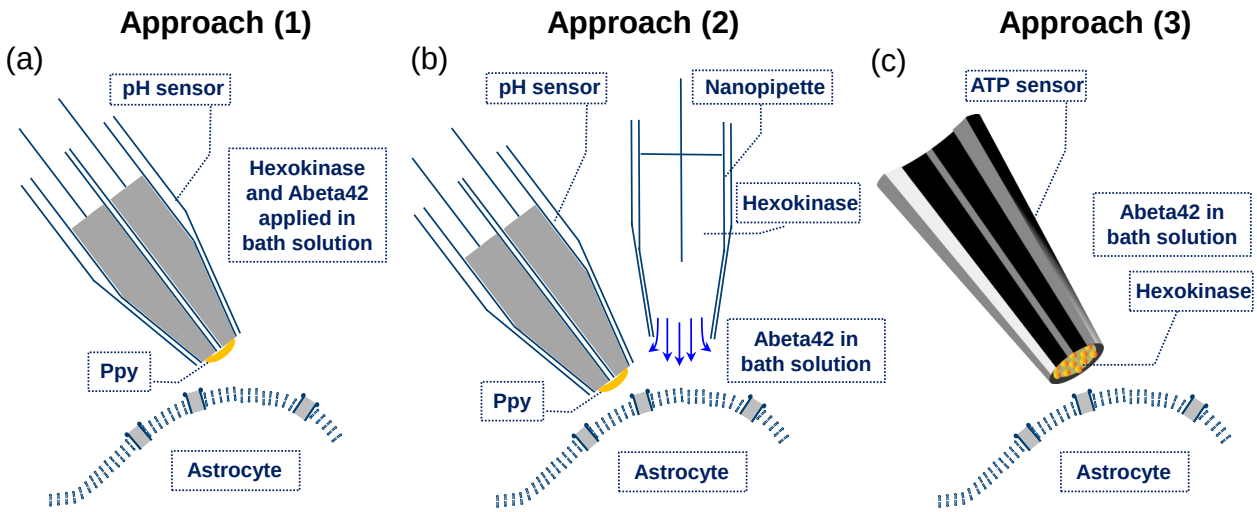

Figure 6.10: Schematic illustrations of three approaches using an EGOFET-based ATP sensor in cell experiments. (a) approach (1): Abeta42 oligomer-induced ATP release from the cell membrane would be involved in phosphorylation by hexokinase in the bath solution, and protons may be detected by an EGOFET above the targeted astrocyte. (b) approach (2): Abeta42 oligomer-induced ATP release from the cell membrane would be involved in phosphorylation by hexokinase delivered via a nanopipette, and protons can be detected using an EGOFET above the targeted astrocyte. (c) approach (3): Abeta42 oligomer-induced ATP release from the cell membrane would be involved in phosphorylation by hexokinase attached to the Ppy layer via glutaraldehyde on an EGOFET, with protons generated at the tip that could be detected directly above the targeted astrocyte.

100 μM of ATP solution and the same solution with 12.2 U/mL hexokinase, respectively (Figure 6.11(c)). A pH that was lower by 1.4 indicated that a substantial amount of protons was generated owing to phosphorylation involving ATP in the bath solution.

6.3.4 Experimental results under approach (1)

Experiments on astrocytes using approach (1), which is guaranteed to be able to sense at least 100 μM of ATP or higher, were carried out. In Figure 6.12(a) and figure 6.12(b), 100 U/mL hexokinase were applied in the bath solution, before Abeta42 oligomers were added. However, the results did not demonstrate that the pH sensors were able to detect any change in pH, if there was ATP leaking out of the targeted astrocyte due to Abeta42 oligomer invasion. In figure 6.12(b), around 500 seconds after the measurement, 10 μM of ATP was pipetted into the bath solution, and it was proved that this EGOFET was sensitive to proton

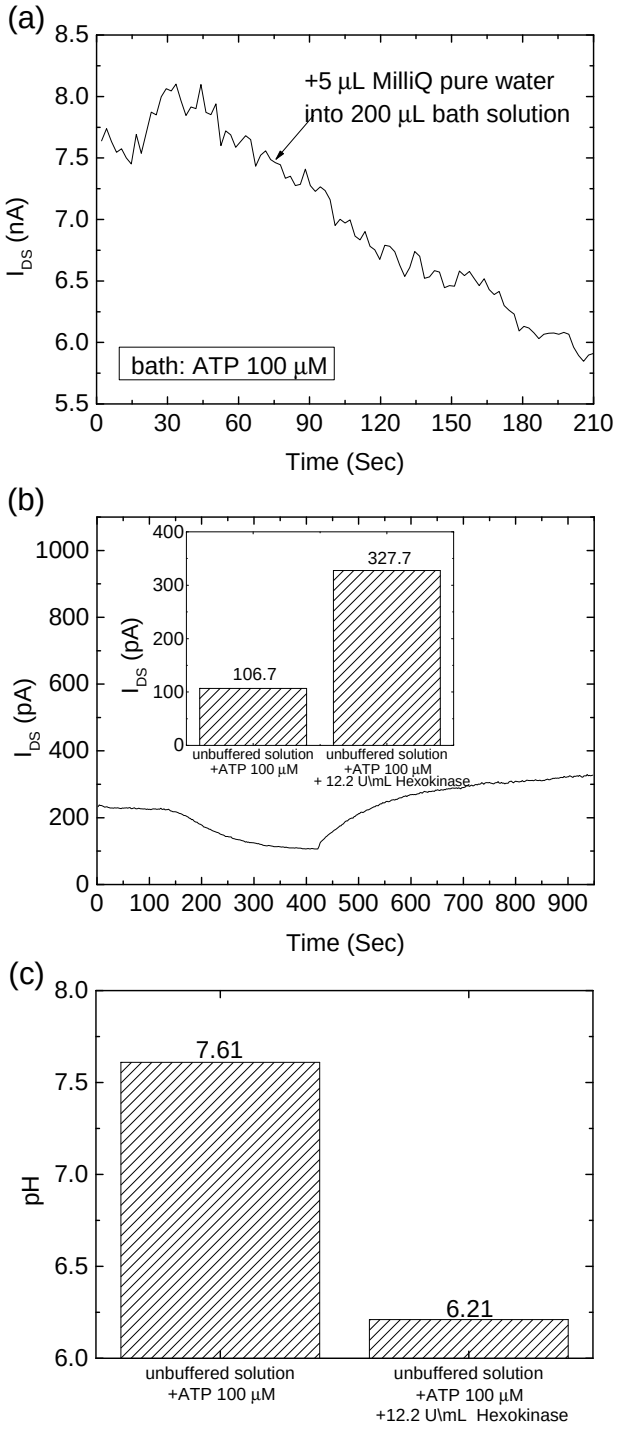

Figure 6.11: Control experiments under approach (1). (a) 5 μL of MilliQ pure water was added into a 200 μL bath solution containing 100 μM of ATP as a negative control. (b) 12.2 U/mL of hexokinase was added into the bath solution containing 100 μM of ATP as a positive control. The inset showed the equilibrated I_{DS} before and after the addition of 12.2 U/mL hexokinase. (c) The pH of the solutions used in the negative and positive controls was measured with a commercial pH meter.

generation due to the 10 μM of ATP involved in phosphorylation. Considering that the timing of the addition of hexokinase and Abeta42 oligomers might be one of the parameters influencing proton generation, although reagents had in all cases been mixed well in the cell dish, 40.8 U/mL hexokinase and 1 μM of Abeta42 oligomers were mixed homogeneously beforehand in a 2 mL Eppendorf Tube and carefully added to the bath solution after the readout of I_{DS} had achieved equilibrium. This was comparable to the previous results that showed only a decline in I_{DS}; i.e. there was no detectable pH change recorded, as shown in Figure 6.12(c) and Figure 6.12(d). Similarly, one of the EGOFETs was responsive to the addition of 1 mM of ATP to the solution, as expected. The next experiment was designed to have hexokinase added into the bath solution after the Abeta42 oligomers. Thus, firstly 1.1 μM of Abeta42 oligomers were injected into the cell dish, and then 40.8 U/mL hexokinase was pipetted in and mixed. As shown in Figure 6.12(e), I_{DS} stayed at the same level, and this EGOFET was shown to be able to sense the addition of 1 μM of ATP in the solution, although I_{DS} dramatically dropped instead, with the subsequent addition of 50 μM of ATP. Approach (1) might not be capable of providing enough sensitivity to Abeta42 oligomer-induced ATP release in an astrocyte.

6.3.5 Experimental results under approach (2)

Experiments under approach (2) were subsequently tried. 500 U/mL hexokinase, which was much higher than the concentrations that could be achieved in previous experiments, was loaded into a nanopipette with inner radius of roughly 100 nm, which was held vertically on the newly-built SICM, whilst an EGOFET was held on an angularly-aligned micromanipulator. In Figure 6.13(a), it seemed that the EGOFET was highly responsive to 1 μM of ATP in the bath solution involved in phosphorylation by hexokinase. I_{DS} was increased and then declined when the EGOFET approached and was then withdrawn from the nanopipette tip delivering hexokinase. However, this change could merely be due to the slight difference in pH between the bath solution and hexokinase-carrying solutions in the nanopipette, although the unbuffered solution for the nanopipette and the cell dish were from the same

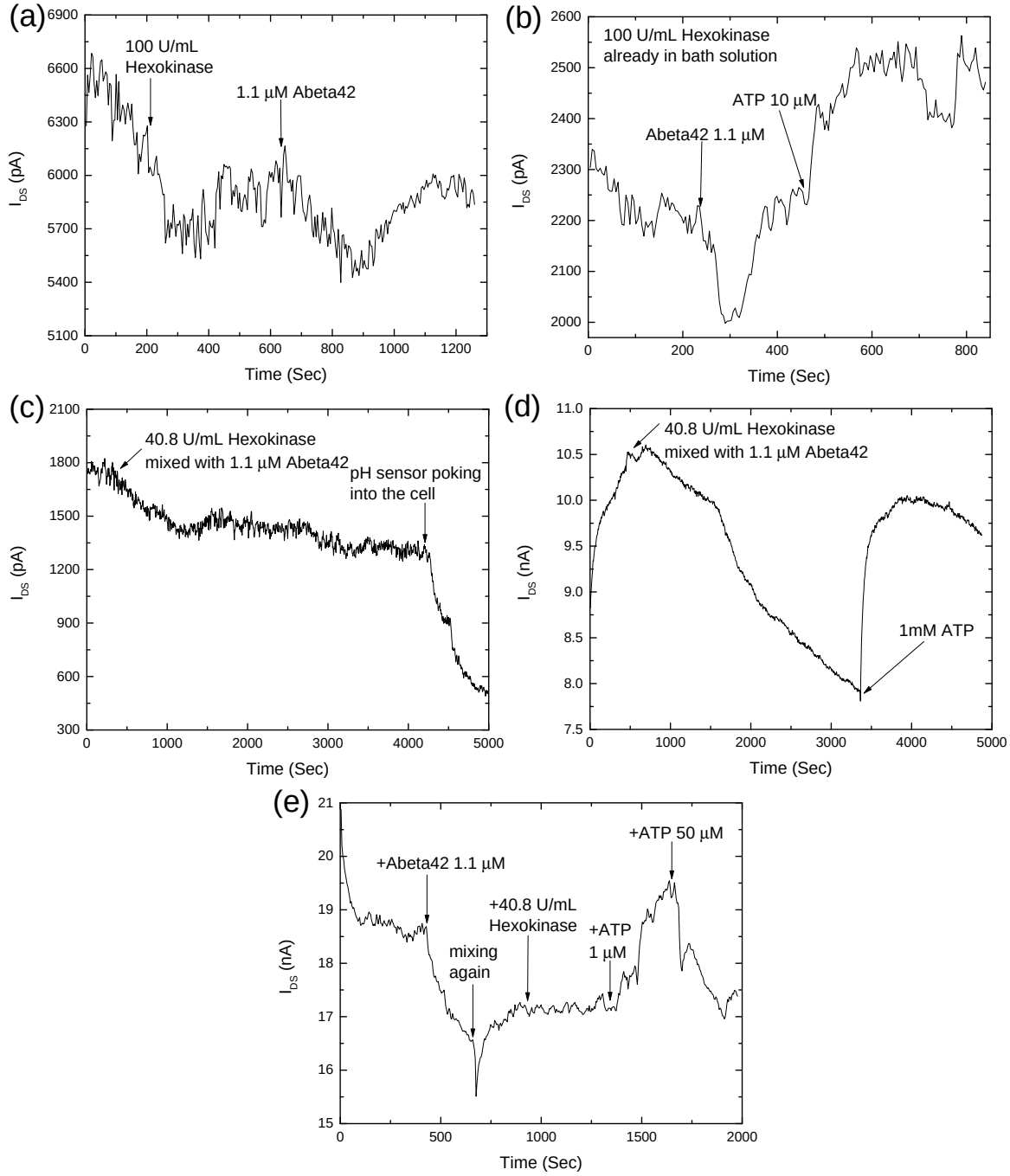

Figure 6.12: Five representative experiments on astrocytes under approach (1), in which hexokinase and Abeta42 oligomers were added to the bath solution. Tests of ATP sensitivity of the EGOFET may be performed by directly adding ATP solution into the cell dish after the cell measurements.

preparation with adjusted pH right before the measurements. A minute deviation in pH in the two solutions may have developed because a similar response, as seen in Figure 6.13(a), was still observed, even when the same unbuffered solution was loaded in the nanopipette

and in the bath separately, as shown in Figure 6.13(b). As expected, when buffer solution, Tris of pH 5.31, was filled in both the nanopipette and the dish, no variation of I_{DS} could be observed, no matter how an EGOFET was moved around the nanopipette tip, as shown in Figure 6.13(c). Of course, using the buffer solution in these conditions was not beneficial to the theta-nanopipette-based ATP sensing, because protons generated may react with the conjugate acid-base pairs, before an EGOFET can detect it.

6.3.6 Experimental results under approach (3)

Finally the approach (3) was conducted, i.e. attaching hexokinase onto the ppy layer of an EGOFET via glutaraldehyde. It should be noted that the pure unbuffered solution and the unbuffered solution containing 1 mM of ATP were always prepared fresh immediately before the experiments, and their pH was adjusted in order to produce as much unbuffered solution containing 1 mM of ATP as pure unbuffered solution itself, so that any detected current increase would have removed the contribution of an intrinsically lower solution pH and therefore could be attributed to phosphorylation involving ATP at the sensor tip. EGOFET was immersed in 25% glutaraldehyde solution for more than 30 minutes and then in 500 U/mL of hexokinase solution, once again for more than 30 minutes. ATP sensors were firstly stabilised in the unbuffered solution, and were then taken out so that measurements could be performed in separate homemade containers (200 μL) with, respectively 1 μM, 10 μM, 100 μM and 1 mM of premade ATP solution for calibration.

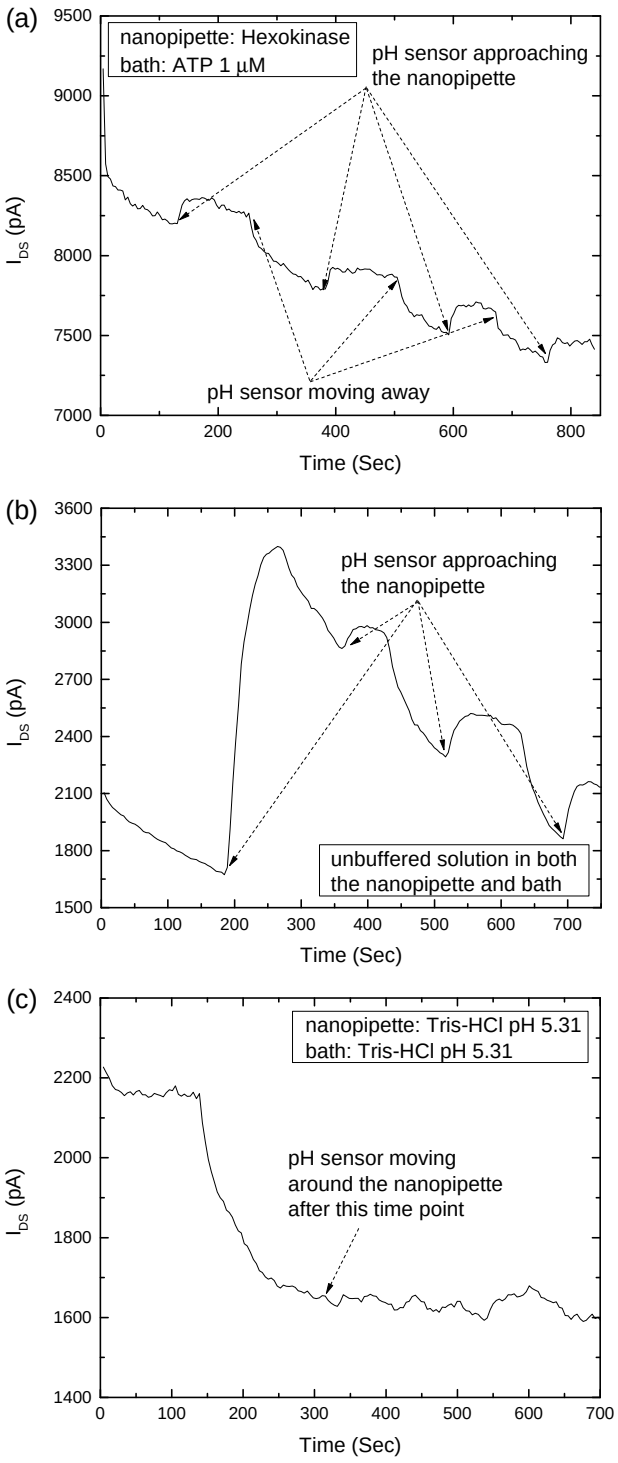

Figure 6.13: Control experiments under approach (2) conducted by repeatedly allowing an EGOFET to approach a nanopipette and then withdrawing it. (a) 1 μM of ATP in the bath solution and 500 U/mL hexokinase in the nanopipette. (b) the same unbuffered solution of pH 8.0 in both the bath solution and the nanopipette. (c) the same buffer solution (Tris, pH 5.31) in both of the bath solution and the nanopipette.

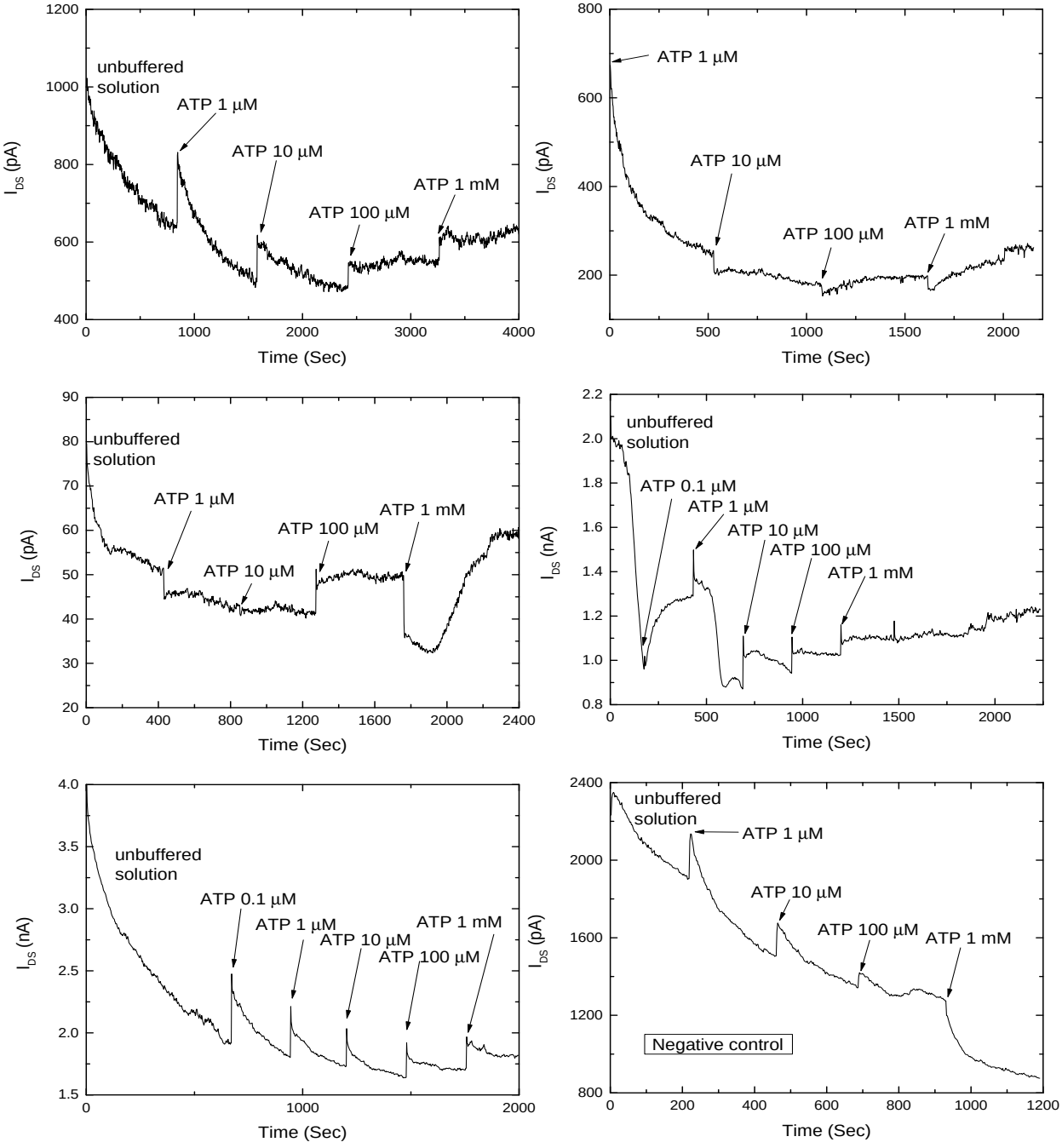

Figure 6.14: Examples of ATP calibrations of different ATP sensors under approach (3), where ATP sensors were dipped in separated dishes holding various concentrations of ATP solutions. The lower right one is a representative negative control.

Examples of ATP calibrations between working ATP sensors and a corresponding negative control are shown in Figure 6.14. It has been observed that I_{DS} showed a massive jump (and sometimes even a drop), every time an ATP sensor was lifted up into the air from the solution and then immersed in another solution with a different ATP concentration. This

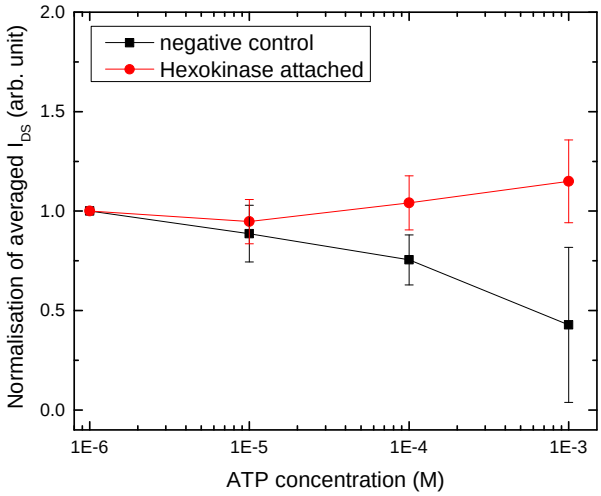

Figure 6.15: Normalisation and averaging of equilibrated I_{DS} calibrations of ATP sensors under approach (3) using separate dishes holding various concentrations of ATP solutions. Error bars are standard deviation.

might also suggest a longer time may be taken to achieve a new equilibrium state, which could be different from that in the previous solution. These current jumps also occurred in negative control groups, in which only pH sensing EGOFETs were used. The saturated I_{DS} at various ATP concentrations was extracted, averaged and normalised at 1 μM of ATP, as shown in Figure 6.15. This suggests that the sensitivity of the ATP sensors was roughly 10 μM ATP and higher, although the sensors basically suffered from a decline in I_{DS} during the measurement. Even so, two distinct trends in averaged I_{DS} in the successful ATP sensors and the control group indicated clearly that approach (3) would enable ATP detection higher than 10 μM.

In fact, conducting the calibrations by dipping an ATP sensor into reagents of different ATP concentrations might cause damage to the sensor itself, with a nanoscale active Ppy layer possibly being dried in the air and moistened in the solution repeatedly. Therefore, a new method of performing calibrations was to immerse an ATP sensor in the 200 μL unbuffered solution until the I_{DS} had reached equilibrium, and a varying number of 1 mM doses of ATP solution were subsequently added in order to achieve various intended ATP concentrations. Some examples of working ATP sensors and a negative control are shown in Figure 6.16, and these displayed a much less abrupt current jump compared with the former

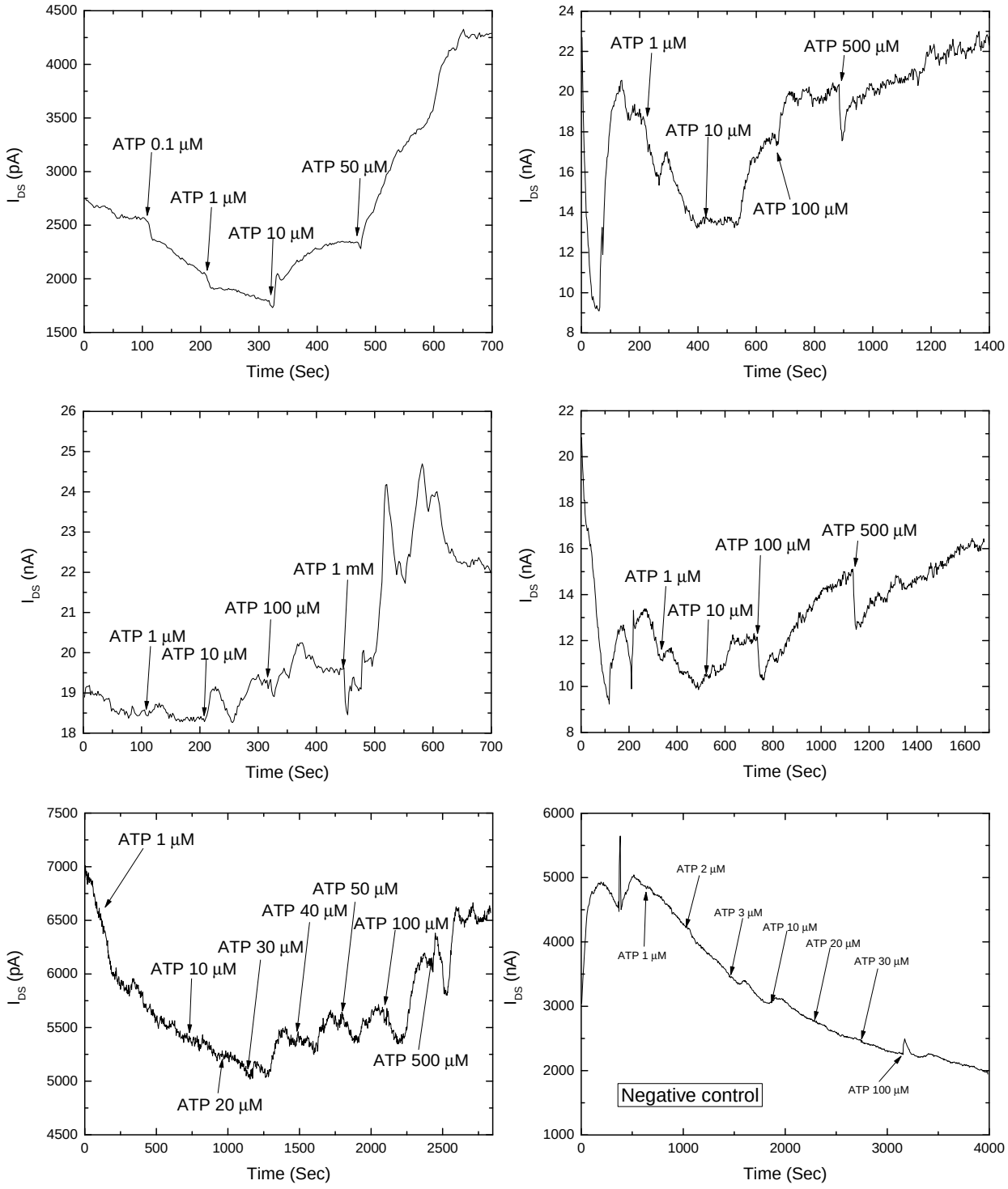

Figure 6.16: Examples of ATP calibrations with different ATP sensors under approach (3), with ATP sensors kept in a dish containing only the unbuffered solution at first, and then ATP solution was added in fixed concentrations until the target concentration was reached. The lower right calibration is a representative negative control.

calibration method shown in Figure

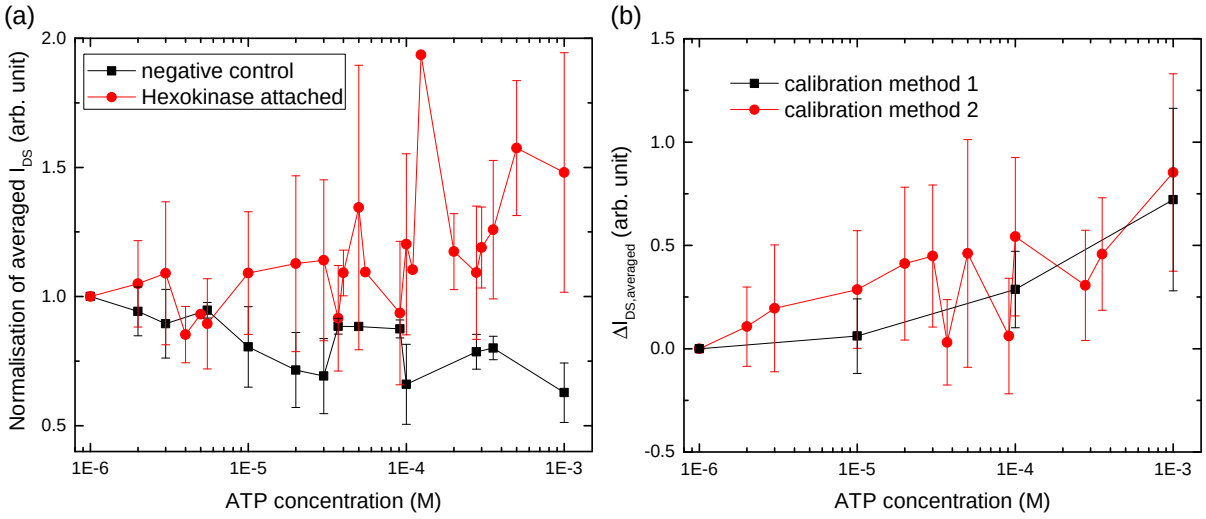

Figure 6.17: (a) Normalisation and averaging of equilibrated I_{DS} calibrations of ATP sensors under approach (3) using a single dish in the presence of various concentrations of ATP solution one by one. Error bars are standard deviations. (b) Comparison of the net increase in I_{DS} between ATP-sensing and negative control groups using two calibration methods, i.e. dipping the ATP sensor in different dishes containing the ATP solution or keeping the sensor in one dish, initially with unbuffered solution, and subsequently raising its ATP concentration by the addition of ATP reagents.

Again, equilibrated I_{DS} in ATP-responsive curves and negative controls was taken, averaged and normalised at 1 μM of ATP for the calibration analysis, as shown in Figure 6.17(a). Data points of the ATP calibrations and control groups demonstrated two clear individual trends, as shown in Figure 6.15. The comparison of calibrations between ATP sensors kept immersed in the same bath solution and dipped into separate ATP solutions are shown in Figure 6.17(b), and this actually suggests no detectable improvement using this updated calibration method.

Successful ATP sensors under approach (3) were carried on for the cell measurements, where Abeta42 oligomers were added directly into the bath solution, and possible Abeta42 oligomer-induced ATP leakage from the cell membrane could be transduced into electronic signals at the sensor tip. A positive control was tried in the first set of experiments, in which no Abeta42 oligomers were applied; instead, the other nanopipette held vertically was used to squeeze and break the targeted astrocyte under an ATP sensor. As shown in Figure 6.18(a), no ATP release due to the cell being squeezed was seen, even if there is

presumably sub-millimolar level of ATP in a cell. In addition, not surprisingly, I_{DS} dropped dramatically when the sensor came into contact with the astrocyte until I_{DS} reached zero. In Figure 6.18(b), 1.1 μM Abeta42 oligomers was added to the bath solution, but no response was detected within 2 minutes. Interestingly, this time I_{DS} increased greatly when the ATP sensor itself squeezed an astrocyte, and this phenomenon was reproducible twice. I_{DS} then decreased to zero when the sensor was totally destroyed by being crushed on the glass bottom through the astrocyte. In Figure 6.18(c) and Figure 6.18(d), encouragingly, I_{DS} showed a clear increase for approximately 500 seconds, and then declined back to the baseline or even lower. Unfortunately, the current did not recover even though the bath solution was remixed and the sensor was moved around to search for possible regions of higher ATP concentration, or was made to approach the cell surface. Again, in Figure 6.18(c), I_{DS} was temporarily raised when the ATP sensor was moved closer to the astrocyte surface and likely to squeeze it; of course, the sensor lost its function after this.

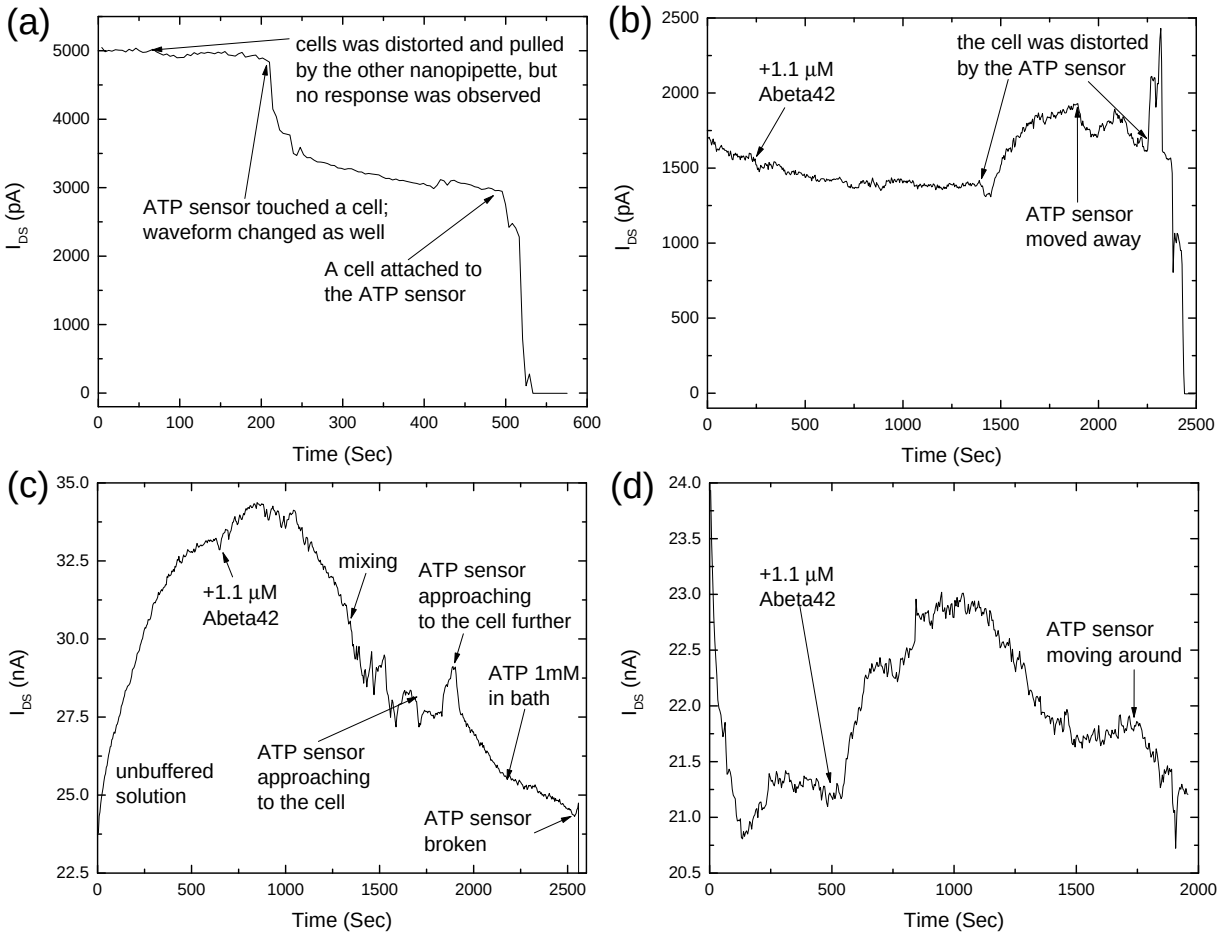

Figure 6.18: Representative experiments on astrocytes under approach (3). Note that (a) was supposed to be a positive control. Tests of ATP sensitivity of the ATP sensors and cell squeezing may be performed by directly adding ATP solution into the cell dish and by approaching the sensor onto a cell, respectively, after the cell measurements.

6.4 Discussion

A nanoscale transistor was fabricated electrochemically on a theta nanopipette with surface modification to facilitate the detection of local ATP distribution above a single cell. A transistor is an active device; one of its basic functions is as an electronic switch, and it plays a critical role in forming logic gates and has been comprehensively utilised to establish complex digital and analogue circuits in chips in the modern electronic industries. In addition, another important function is that it can be used to amplify electrical input signals by modulating its output impedance, which nonlinearly depends on the applied bias voltages [228]. It is fabricated using either inorganic or organic semiconductors as its active material, depending on specific applications, in which techniques for producing transistors based on inorganic semiconductors, especially silicon, are now highly developed, whilst organic semiconductors can be more suitable for biologically-relevant applications [229, 230]. Transistors can be classified into bipolar transistors (BJTs) and field-effect transistors (FETs). Although the transconductance of BJTs is higher than that of FETs, the development in FETs has been dramatically advanced over that of BJTs due to its lower power consumption and significant progress in current manufacturing processes [228].

6.4.1 Comparison of nanopipette-based EGOFETs to conventional inversed FETs

The structure of an EGOFET fabricated on a theta nanopipette tip is comparable to a traditional inverted FET [231]. An FET is usually composed of a semiconducting active layer, on which drain and source electrodes are symmetrically located at the two ends, and a gate electrode is situated separately with dielectric material. The region of the semiconductor directly opposite the gate is where it is capable of forming a more conductive channel between drain and source electrodes under the electric field generated from the gate. Thus, an FET is defined as turned on if appropriate bias voltages are applied from gate and drain versus source, which allows electrical carriers to move relatively freely in the channel temporarily

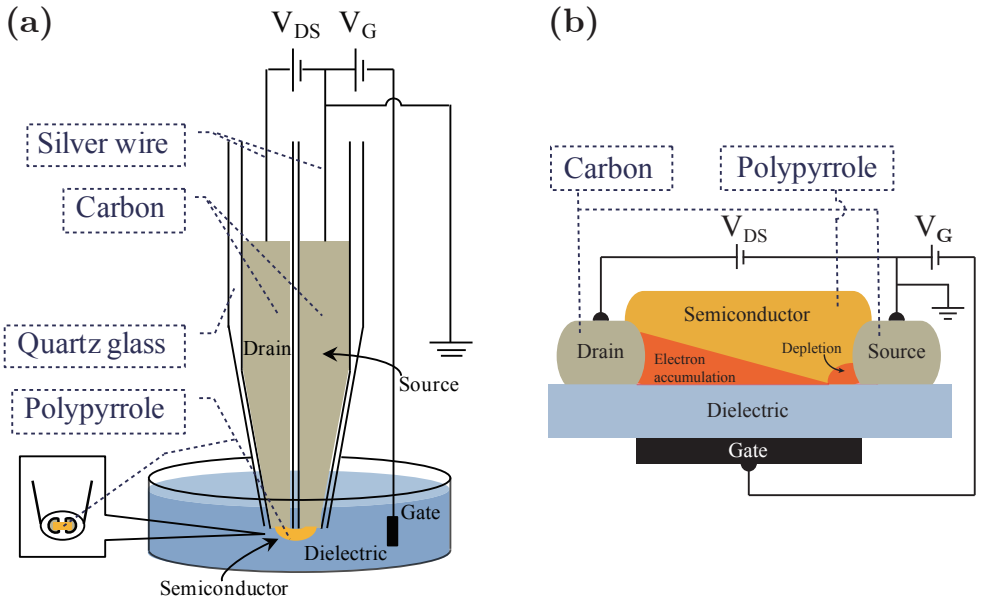

Figure 6.19: Schematic comparison of the configuration of drain, source and gate electrodes, dielectric material and semiconductor in (a) a Ppy EGOFET and (b) a conventional inverted FET.

formed.

The comparison of drain, source, gate, dielectric material and semiconductor in a nanopipette-based EGOFET with the same components in an inverted FET is depicted in Figure 6.19. The structure of a conventional FET is shaped by the design of a photo–mask followed by chemical etching and deposition in the manufacturing process; however, in the case of a nanopipette-based nanoFET, its physical geometry is controlled predominantly by the laser-pulling process. The septum thickness of a theta nanopipette was altered by a laser puller so that there was approximately 50 nm separating each semilunar-shaped channel. Therefore, this septum roughly defines the channel length between drain and source electrodes. After these two semilunar vacant channels are filled with conductive carbon particles, and a layer of Ppy is made to bridge these two separated carbon domains, it will function like an FET when the gate and its tip are immersed in the bath solution under proper application of bias voltages. It should be noted that this nanopipette-based nanoscale FET is electrolyte-gated, so its electrical characteristics may vary, when the location of the gate placed in the solution has been changed and/or the electrolyte composition has been modified.

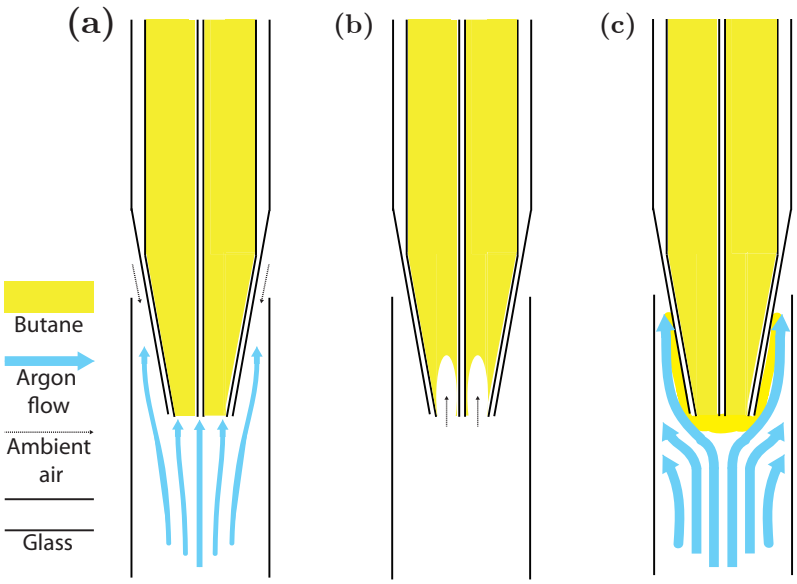

Figure 6.20: Illustration of the butane-filled nanopipette influenced by (a) suitable (b) zero and (c) excessive flow rates of argon delivered via a glass capillary sheathing the tip.

6.4.2 Nanoelectrodes made of a carbon filled theta-nanopipette

The method to convert two vacant glass channels into conductive drain and source electrodes involved pyrolytically depositing carbon onto the interior wall of the two channels and completely filling the tip openings. When there is sufficient oxygen in the air, flame-heated butane will form carbon dioxide and water ($2C_4H_{10}+13O_2 \rightarrow 8CO_2+10H_2O$); when oxygen is limited, incomplete combustion of butane produces by-products of CO and very fine carbon particles (soot) [232]. Therefore, in order to fulfil this chemical condition with the required geometry, on one hand, butane provided from a commercial camping gas cartridge was transferred into the theta nanopipette via tygon tubing connected at its end. The valve installed on the cartridge was closed right after opening by a half–turn in order to limit the amount of butane injected, which unfortunately did not allow a precise control. On the other hand, low-rate argon flow was supplied to the nanopipette tip sheathed by a glass capillary via another length of tygon tubing in order to create an appropriate interface between abundant butane (limited oxygen) and ambient air at the tip. Therefore, a balance between the pressure of butane and ambient air/argon coming from opposite directions can be empirically made by adjusting the volumetric flow rate of the argon, so that a plane carbon surface is

produced during combustion by a jet flame torch, as shown in Figure 6.20(a). When there is no argon being delivered to the nanopipette tip, a cavity in the carbon deposition may be created, because the ambient air with a higher pressure (1 atm) than the butane naturally flows into the tip as shown in Figure 6.20(b); whilst strong argon flows along the tapered tip caused carbon depositions which was supposed to be separated at two sides to make contact, because butane may leak out of the tip and be entrained in the argon flow due to a lower pressure zone built up outside the tip, as shown in Figure 6.20(c).

6.4.3 Characterisation of carbon nanoelectrodes

Pyrolytic carbon deposited in the two channels of a theta nanopipette is highly dependent on the gas flow in the system. Electrochemical characterisation of a pair of carbon electrodes was carried out with redox reactions of FcMeOH and $FcMeOH^+$ in the solution occurring at the carbon surface. A positive interval of 0 to 0.5 V in the cyclic voltammetry allows the monitoring of the redox pair to migrate towards the carbon surface, and FcMeOH and $FcMeOH^+$ were oxidised and reduced, respectively, generating Faradaic current. Faradaic current over time is usually diffusion-limited and highly influenced by the electrode shape under cyclic voltammetry [233, 234]. When the carbon plane is of nanoscale and flat, convergent diffusion of the redox mediators from the solution to its edge is significant, and this provides a sufficient amount of species for the redox reactions, so a sigmoidal profile is observed, as shown in Figure 6.21(a). On the other hand, when there is an open and narrow cavity formed inside the carbon fillings, the influx of redox mediators will be limited by the planar diffusion into the cavity, so peaks will be observed in the voltammetric profile, as shown in Figure 6.21(b). In addition, the magnitude of the Faradaic current also provides a good estimation of the opening size of the carbon nanoelectrodes, which replaces complicated procedures using scanning electron microscopy (SEM). Faradaic current around 10 pA indicates an approximated semilunar aperture with a radius of about 48.65 nm, which is calculated using Equation 3.30. Examples of Ppy deposited FET are shown in Figures 6.22(a), 6.22(b) and 6.22(c), which had Faradaic current around 20 pA and 50 pA and larger

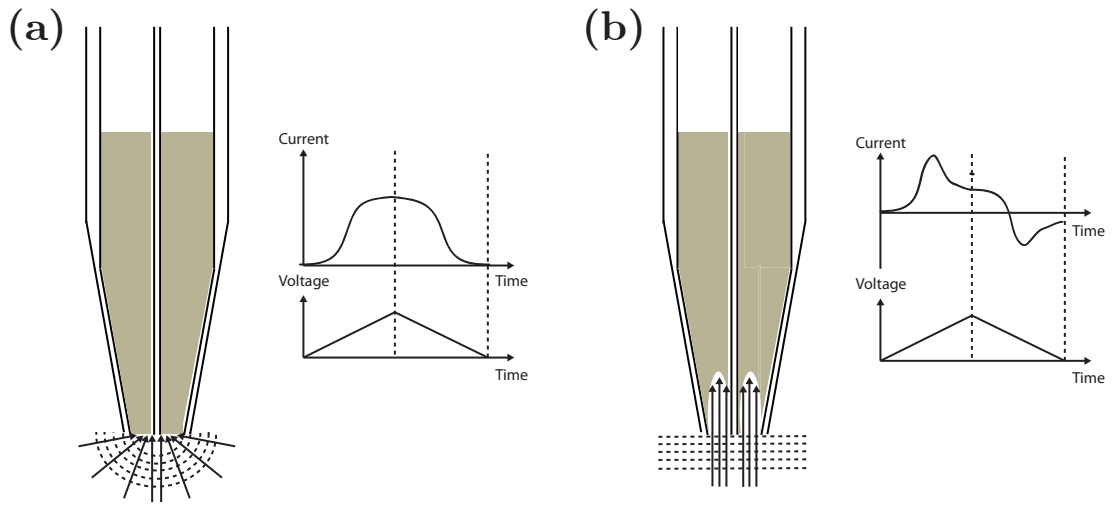

Figure 6.21: Schematic illustrations of voltammetric patterns influenced by the shape of carbon deposition formed in two of the nanopipette channels, where the mass transport of the redox mediators, FcMeOH and $FcMeOH^+$, to the carbon surfaces is generally limited by diffusion.

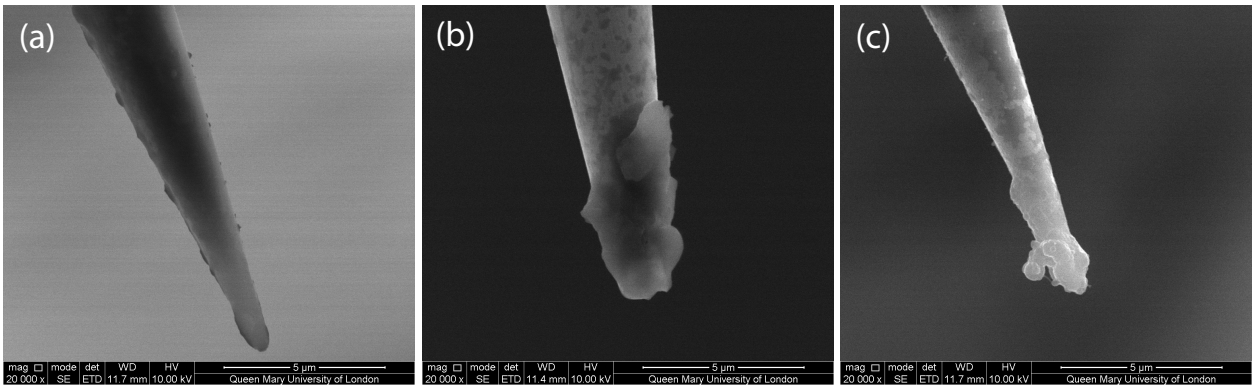

Figure 6.22: Images of the tip of a Ppy EGOFET by SEM, when the characteristic Faradaic currents at two carbon barrels were each around (a) 20 pA, (b) 50 pA and (c) higher than 50 pA.

than 50 pA, respectively. Although a very thin Ppy layer could provide probably the best platform for producing an ATP sensor, the size of semilunar openings was almost impossible to fine–tune, as the same set of parameters in a laser puller with a manual combustion process gave Faradaic current ranging from 2 to 100 pA.

6.4.4 Fabrication of an EGOFET using Ppy as the active semiconductive layer

After carbon nanoelectrodes with an appropriate exposed surface were obtained, electrodeposition of Ppy was carried out in 0.5 M of pyrrole, 0.2 M of $LiCO_4$ and 0.1 M of $HClO_4$ dissolved in distilled water with cyclic voltammetry of V_G=–300 to 650 mV on both carbon electrodes for the purpose of forming a thin Ppy layer across each side. Ppy was selected to make an EGOFET due to its biocompatibility and high conductivity under doping ($\geq$500 S/cm) [235]. Firstly, pyrrole monomers in the solution were oxidised to form dimers, and this mechanism was performed consecutively and polymerised to develop Ppy, with ClO_4^- ions diffused into vacant spaces in the oxidised Ppy to maintain the charge neutrality [236, 237]. Therefore, Ppy began to grow on each carbon surface of the nanoelectrodes when each scan cycle approached 0.65 V, which was monitored by the increase of Faradaic current cycle by cycle. In fact, the optimal voltage for Ppy polymerisation is usually at 0.8 V or above, but it was intentionally lowered to 0.65 V in order to reduce of thickness of the crossed Ppy layer. It is easy to form a contact between two-flank Ppy growth layers with a high polymerisation voltage, e.g. higher than 0.8 V [238], but an over-thickened Ppy bridge may not beneficial for the properties of the next-stage ATP sensor, as the location of hexokinases was designed so that it would, ideally stay as close to the active Ppy domain as possible, so that generated protons, could be detected by the EGOFET itself. Hence, as shown in Figure 6.7(b), the Ppy contact was designed to occur within 2 to 3 scan cycles to form an effective Ppy layer as thin as possible. However, precisely when the Ppy bridge is formed, and its thickness, cannot be controlled, which may be attributed to the unpredictable distribution of the electric field resulting from a random topography of carbon nanoelectrode surfaces established during combustion.

The theory that Ppy is semiconductive is the same as for other conjugated polymers, with valence electrons on the backbone with alternating single and double carbon–carbon bonds delocalised on the extended π–system [236, 237]. Removing a small portion of these electrons in an insulated Ppy forms radical cations on the Ppy chain, i.e. holes. Holes

together with quantised lattice vibration are termed (bi)polaron, and they can move along the chain, making a contribution to increase its conductivity. When Ppy is electrochemically grown, it is also simultaneously oxidatively p-type doped, and counterions in the solution will diffuse into the vacancy in its interlaced polymerised structure to reach electrical neutrality, which increases its volume. With the doping, a pair of additional impurity energy states (polarons) will appear in between the valence and conduction bands of Ppy, and these may approach each other as the doping level increases (bipolarons), or even be extended to form impurity bands with a much higher doping (bipolaron bands).

As discussed above, during the polymerisation and oxidative doping of Ppy, counterions ClO_4^- are diffused to fill the vacancies in the Ppy chain; however, when the Ppy EGOFET was immersed and voltage scanned in 0.1 M of HCl for around one hour, it was likely that the counterions would achieve a rebalanced state, so the ClO_4^- that was temporarily trapped might be released and replaced by Cl^-. It is because Cl^- and ClO_4^- are smaller anions and so easier to exchange with species similar in size in a solution, that it may also take longer to achieve equilibrium in contrast to other larger anions that have already been firmly trapped [239, 240]. The sensitivity of the Ppy EGOFET to the solution pH was high. The Ppy layer experienced deprotonation with pH$\leq$ 7, which may repel Cl^- and revert Ppy into an undoped insulator. At the same time, due to the cyclic voltammetry of V_G=–0.3 to 0.3 V, the Ppy layer attempted to swell and shrink according to the scan voltage, which may help this process involving counterion diffusion to speed up the attainment of equilibrium. In a lower pH solution, protonation may play a role to improve the conductivity of the Ppy layer, although it may not be increased dramatically [241].

6.4.5 Experiments under approach (1)

The advantage of using approach (1) for ATP detection is that it is the simplest of any of the three approaches. In approach (1), in order to transduce the ATP concentration to electronic signals at an EGOFET, hexokinase was directly added to the bath solution without additional tip processing. Although the increase of glucose phosphorylation-induced

I_{DS} proved its sensitivity to ATP, it only reached as low as 100 μM, which may be attributed to the hexokinase being highly diluted in the large volume of bath solution, and generated protons not appearing directly under the ATP sensor so they could not be collected efficiently.

6.4.6 Experiments under approach (2)

Approach (2) is an updated version of approach (1), which delivers the hexokinase just next to an EGOFET via another nanopipette, in an attempt to solve the problem of low hexokinase concentration, when it is applied in the bath solution. The calibration results exhibited a very good sensitivity to local pH change; however, convoluted pH variations, caused by inhomogeneous proton distribution at the hexokinase delivery interface and protons generated by hexokinase catalysis are not distinguishable. The evidence is that even though the same preparation of unbuffered solution was loaded in the nanopipette and bath solution, the sensor can still reveal minute pH differences, which might have been established after the unbuffered solution was dispensed and exposed to the air. Unfortunately, using a buffer solution cannot solve this issue, because it is necessary for the EGOFET to work in an unbuffered solution, in which generated protons would not be removed by pre-existing conjugate acid-base pairs, which are present in the buffered solution.

In addition, there has been another issue, of making appropriate adjustments to allow a suitable efflux rate of hexokinase through the nanopipette, which could potentially be achieved by applying pressure on the nanopipette or with an electric field induced from an electrode immersed inside the nanopipette. The optimal condition has not been found, since the size of the nanopipette aperture and the volumetric flow rate set by the syringe pump were both critical parameters. An excessive efflux would apparently induce unwanted flow or even generate a vortex around the targeted astrocyte. It is worth noting that I_{DS} on an EGOFET, no matter whether or not hexokinase has been fixed on its Ppy layer, will be greatly increased when the Ppy layer is physically squeezed by a cell, or when a strong flow is applied near the Ppy layer. This might be attributed to the pressure the Ppy layer experienced [242, 243].

6.4.7 Experiments under approach (3)

Alternatively, approach (3) provides local fixation of hexokinase onto the Ppy layer of an EGOFET. Here, glutaraldehyde was used as an irrevocable crosslinker with identical reactive groups, which realise intermolecular linkages. It has therefore been adopted widely for high quality ultrastructural preservation for electron microscopy. Glutaraldehyde has a tendency to polymerise to form cyclic or long-chain compounds at a more alkaline pH, so it was used at around pH 3.5 to stay as monomeric as possible during experiments with a high concentration of 25% wt. in H_2O at room temperature. As the tip of an EGOFET was dipped in glutaraldehyde solution for more than 30 minutes, complex reactions involving the formation of Schiff bases will be processed between the aldehyde groups in glutaraldehyde and the amine groups of Ppy via nucleophilic attack, and therefore methylene bridges will connect amine groups at Ppy, and a portion of single and oligomeric glutaraldehyde molecules with only one side fixed on the Ppy and the other side left unbound will also exist [244, 245]. Subsequently, this modified EGOFET was transferred immediately and its tip immersed in 500 U/mL of hexokinase solution for more than 30 minutes in order to link the ϵ-amino groups of lysine residues in hexokinase using the unbound ends of the methylene bridges. After a couple of careful rinses of the tip, the ATP sensor was ready for experiments to be carried out. The solution adopted for calibration and measurement should always contain D-glucose, which is the substrate for hexokinase to conduct glycolysis, and magnesium ions are also necessary to serve as the reaction activators for hexokinase.

Discouragingly, the success rate for producing a functional ATP sensor was lower than 10%, although the protocol for hexokinase attachment onto the Ppy layer of an EGOFET is simple. This may be attributable to inefficient crosslinkages between Ppy and hexokinase, because this process was conducted in two separated steps, i.e. firstly in a dish containing glutaraldehyde solution and then in another one with hexokinase solution, although this protocol was suggested in the work present by Zhang *et al.* [246]. A conventional way to perform crosslinkages is to mix an appropriate weight of a desired enzyme into buffer solution containing glutaraldehyde, usually of 1–5 wt.%, and to pour this well-mixed solution onto

a target material until the solvent naturally evaporates [247]. However, these functional molecules in a tiny volume of mixed solution, as small as a droplet, will only be able to stay on a relatively large flat surface; whilst a needle-like sensor cannot hold a droplet. Although various concentrations of glutaraldehyde and hexokinase in a mixture had been tested, it was very difficult to find an optimised recipe, because these theta-nanopipette-based ATP sensors were not yet highly sensitive and did not respond effectively to altered conditions. Alternatively, a portion of hexokinase might lose its function during the crosslinkages; for example, the dimeric units in a hexokinase might acquire an altered morphology due to strain resulting from glutaraldehyde stretching.

On the other hand, the morphology and thickness of the Ppy layer in an EGOFET may also have influence on the sensitivity of the ATP sensors under approach (3). Of the SEM images, Figure 6.22(a) probably demonstrates the more ideal Ppy deposition, in that it has a thinner Ppy layer, on which hexokinases may have an opportunity to be attached more closely to the active region for (bi)polaron transport, and therefore protons generated by hexokinases may be more likely to diffuse inwards and were therefore able to increase the conductivity of the Ppy active channel. In contrast, EGOFETs in Figure 6.22(b) and Figure 6.22(c) may possess a higher I_{DS} and more hexokinases could be fixed to the overgrown Ppy layer, but there may be a much greater distance between hexokinases and the active Ppy region, and many of the generated protons may directly dissipate into the bath solution without being collected. Unfortunately, in general, the Ppy deposition is expected to be more like that in Figure 6.22(b), because how Ppy grows and when it forms a Ppy bridge are not finely controllable. This high variance of Ppy growth also greatly increases the difficulty of ascertaining optimised conditions for the protocol. The advantages and disadvantages of these three approaches are compiled in Table 6.1.

For the experiment on single astrocytes, which was designed to reveal the mechanism of Abeta42 oligomers interferencing with the cell membrane, unfortunately approach (1) did not seem to have enough ATP sensitivity; whilst approach (3) provided a very low success rate ($\leq$10%) in producing a working ATP sensor. A couple of experiments on astrocytes

Table 6.1: Advantage and disadvantage of three approaches for ATP detection.

	Advantage	Disadvantage
Approach (1)	Simplest method	Sensitivity is relatively low (100 μM)
Approach (2)	High sensitivity to local pH change	(a) unbuffered carrier solution for hexokinase also contributes to the convoluted detection ATP signal (b) conditions of delivery of hexokinase via the nanopipette have not been optimised
Approach (3)	Local fixation of hexokinase at the Ppy layer of an EGOFET provides sensitivity of 10 μM	Very low yield (lower than 10%) in producing a functional ATP sensor

were encouraging in that they demonstrated an initial increase in I_{DS} right after Abeta42 oligomers were added to the bath solution, and this then dropped down to base level or lower. However, the number of samples was not enough to verify or contradict this hypothesised invasion mechanism. The fact that the yield of theta nanopipette-based ATP sensors was very low has made it very difficult to obtain statistically significant results. It is suggested that the design of a theta nanopipette-based ATP sensor be radically updated, which will be discussed in the chapter on future work.

6.5 Conclusions

pH sensing EGOFETs have been successfully fabricated on theta-nanopipettes, which are processed firstly with channels filled with pyrolytically-deposited graphite and then with a Ppy layer, grown electrochemically, across these two electrode openings. Three approaches, taking advantage of hexokinases in order to generate protons during the catalysis of ATP, have been examined to turn the pH sensor into an ATP sensor. In approach (3), crosslinking of hexokinases and the Ppy layer is realised via glutaraldehyde, and the sensitivity of ATP reaches 10 μM. This has the highest ATP sensitivity of any of the three approaches; however, the success rate for producing this type of ATP sensor is less than 10%. Therefore, it is very difficult to ascertain optimal conditions for this ATP sensor, and it is not possible to reach a higher sensitivity.

Unfortunately, no statistically significant results for Abeta42 oligomer-induced ATP leakage were observed above the cell membrane. This may be attributed to: (1) the number of samples not being sufficient due to an extremely low yield from the sensors; (2) the sensitivity of the ATP sensor not being high enough to detect released ATP that is greatly diluted once it goes into the bath solution; (3) the possibility that the hypothesised mechanism for Abeta42 oligomers forming temporary pores in the cell membrane is not correct, although this is less likely as the evidence in the previous chapter supported this hypothesis; the experimental results in this chapter, however, were not able to verify or contradict it. In fact, an updated version of the ATP sensor using the concept in approach (2) may be able to achieve a much better sensitivity to ATP than 10 μM, as long as it has been optimised to minimise significantly the influence of the unbuffered carrier solution for the delivery of hexokinases. Thus, a better ATP sensor still has the potential to verify the hypothesised pore-forming mechanism induced by Abeta42 oligomers.

Chapter 7

Conclusions and Future Work

7.1 Conclusions

SICM is a technique that is capable of realising topographic imaging in a bath solution without physical contact between the probe and the substrate. Although hydrostatic pressure and hydrodynamic force still exist during the scanning and may be applied on a soft sample, such external stimulation can be significantly reduced by careful adjustment, or even become negligible if a modified scanning method is used. Compared with AFM, which has an atomic-level resolution but may unavoidably touch the sample, SICM can produce reproducible topographic images after repeated scanning is performed in the same area. The best resolution that SICM can achieve at present is approximately 5 nm, using a nanopipette as its probe with a diameter of 12.5 nm, which should be sufficient to characterise many complex biological systems. The fabrication of a nanopipette is relatively easy–a glass capillary processed by a laser puller with suitable parameters will produce a pair of nanopipettes with the desired size of opening. The application of a bias voltage between an Ag/AgCl electrode inserted into the nanopipette pre-loaded with a buffer solution, and the other Ag/AgCl electrode immersed in a dish containing a bath solution results in an ion current flowing through the aperture of the nanopipette. Any object appearing in the spherical detection volume under the tip will hinder this current flow and therefore cause a reduced current

value. In order to maintain the nanopipette at a constant height on the substrate during the scanning, this current is fed back in real-time to an automated piezoelectric actuator in the z-axis, which will move the nanopipette upwards when the current is decreased to a pre-defined level to avoid any possible contact with the tip. Subsequently, non-contact topographic imaging is achieved using the appropriate scanning mode, corresponding to the roughness of the sample. The rig for performing SICM has been developed over two decades, so the technique has matured and there are commercialised products available; however, in order to gain hybrid functions via combination with other optical or electrical techniques, a homemade setup based on SICM is usually adopted in a laboratory.

Basic applications of SICM can be performed on static topographic comparison between the same samples developed in different environments and conditions, or on dynamic observation of changes in a subcellular structure over time. It should be noted that due to the limitation in its scanning speed, the mechanism intended for observation needs to fall inside a window of tens of seconds, since the fastest hopping-mode imaging available currently is 18 seconds with a resolution of 64×64 pixels for an area of $10\times10\,\mu m^2$ [248]. Nevertheless, the most attractive characteristics of SICM are that it can be used to deliver a reagent locally at the same time as the scanning, and it can be integrated into other powerful techniques. The possibility of a subcellular resolution for topographic imaging allows subsequent patch–clamp recording, also at a subcellular level, in which the same nanopipette can be processed to conduct both experiments. Simultaneous recording of fluorescent behaviour in pre-loaded dyes in cells during the application of external stimulations via a nanopipette further increase the variety of the cutting-edge investigation topics. On the other hand, the tip of the single-barrel nanopipette can be simply modified to become sensitive to specific molecules; usage of a double- or quadruple-barrel nanopipette not only links SECM to SICM but has also inspired numerous new applications.

In this thesis, the application based on SICM is utilised to investigate Alzheimer's Disease, which is a neurodegenerative disease involving brain-shrinkage in patients and extracellular Abeta plaques in the brain. Evidence has shown that it is likely that Abeta oligomers are

involved in the onset of the disease. Thus, in the experiment, a nanopipette loaded with synthetic Abeta42 oligomers or CSF in AD patients is used to dose these toxic oligomers on astrocytes locally and quantitatively, and these are hypothesised to be one of the primary targets of these oligomers. In the experimental system, cells were pre-incubated with an mGluR5 blocker and a calcium indicator, so that oligomer-induced calcium influx in single cells could be monitored in real time using a CCD camera, and abnormal calcium homeostasis indicated malfunctioning cells. It was first proved that synthetic Abeta42 oligomers of 100 pM can be effectively deactivated using 150 nM of clusterin, as well as Nb3 (a nanobody against Abeta) and Bapi (an antibody against Abeta), and such a calcium influx can still have statistical significance in a physiological concentration as low as 500 fM of Abeta42 oligomers, which is a critical prerequisite for the following experiments using CSF in AD patients. As with results using synthetic Abeta42 oligomers, the mixture of AD CSF and clusterin or Nb3 worked effectively to reduce calcium influx; however, interestingly, Nbsyn87 (a nanobody against Asyn), aslo0071 (an antibody against Asyn), aslo0252 (an antibody against Asyn), or Bapi with a high concentration of 1 μM successfully decreased the amount of calcium influx. Asyn is also a misfolded oligomer like Abeta, and it is presumed to be the cause of the onset of Parkinson's Disease. Therefore, the ineffectiveness of low concentrations of Bapi and the effectiveness of Nbsyn87, aslo0071 and aslo0252 may suggest that these toxic species that result in abnormal calcium influx may actually be in the form of co-oligomers composed of both Abeta and Asyn. In addition, in the case of Nb3 and Nbsyn87, the successful blocking of partial calcium influx may also suggest that nanobodies that have an intrinsically smaller volume than conventional antibodies are able to reach the target epitopes easier, whilst movement of large antibodies towards target termini may be hindered by the complex structure of co-oligomers. More experiments are needed for further determination of the structure of these co-oligomers; e.g. they might tend to expose their N- and C-termini of Asyn to the surroundings. The hypothesis that co-oligomers are likely to be the cause of the onset of AD might provide a new direction to treatments for AD or even possibly for PD.

The formation of transient pores due to the interference in the cell membrane by physical

contact with misfolded oligomers is hypothesised as a cause of abnormal calcium influx. In order to confirm this hypothesis, a new setup based on SICM with a second nanopipette/sensor holder fixed on an angularly-aligned micromanipulator was established. In this setup, the vertically-aligned nanopipette is responsible for the delivery of oligomers at a constant height above the target cell, as described previously, whilst a sensor is placed close to the delivery spot for the detection of the immediate response of the cell. Producing a sensor with a sensitivity to ATP is the aim of the experiment, because ATP is not only involved in multiple pathways in cellular communication, but it is also expected to have a high intracellular concentration of several millimolars. Thus, it is likely to to possible to probe an ATP release if there are oligomer-induced transient pores formed in the cell membrane. The ATP sensor is fabricated on the tip of a double-barrel nanopipette, with a relatively simple manufacturing process, involving firstly filling pyrolytical graphite in the pair of vacant channels, followed by electrochemical deposition of Ppy to link these two carbon-filled electrodes, and then the placement of hexokinase near the Ppy layer. This ATP sensor operates as a hexokinase-cofunctioned electrolyte-gated organic field-effect-transistor to transduce the amount of catalysed ATP to an electronic signal, using pH-sensitive Ppy as its biocompatible active material, with protonation and deprotonation increasing and decreasing the conductivity of Ppy, respectively. Three different approaches that attempt to maintain hexokinases near the Ppy layer were adopted. An approach using the addition of hexokinase in the bath solution had the lowest sensitivity to ATP ($\sim$100 μM), whilst attaching hexokinase on the Ppy layer via crosslinking molecules had a higher sensitivity to ATP ($\sim$10 μM). The latter approach has the possibility of achieving a higher sensitivity down to nanomolar level, according to a previous study [246]; however, it was difficult to optimise the sensor further using this approach due to the low success rate ($\leq$10%) in fabricating it. It should be noted that an approach involving using a second nanopipette for the delivery of hexokinase to the Ppy layer was actually very sensitive to changes in pH that most likely came not only from the hexokinase carrier solution but also from catalysed ATP. Therefore, as long as these two sources of protons can be deconvoluted, it may be possible to achieve the highest sensitivity to ATP of these three approaches. So far, no oligomer-induced ATP release has been detected

using either of these three sensing approaches, which may be attributed to the possibility that the extracellular ATP concentration is greatly diluted, so an ATP sensor with a much higher sensitivity is probably required; it is also possible, although much less likely, that the hypothesis that oligomer-induced transient pores are formed might be incorrect, although this hypothesis is supported indirectly by previous studies [165, 166, 187].

7.2 Future work

7.2.1 Determination of the effectiveness of antibodies and/or nanobodies on PD CSF samples

The methodology based on SICM utilised to examine the effectiveness of antibodies and/or nanobodies designed specifically against AD/PD has been proved successful. By taking advantage of the same concept, it is likely that antibodies and/or nanobodies that bind Abeta are also able to reduce significantly the cellular calcium influx induced by toxic co-oligomers composed of Abeta and Asyn in CSF from PD patients. If this hypothesis is true, it would suggest that the oligomers that cause PD may not just be a single type of Asyn peptide; instead, co-oligomers formed by Abeta and Asyn may play a role in PD. Therefore, a new strategy for the treatments of both AD and PD, or even for other neurodegenerative diseases, might need to be considered. Firstly, it is suggested that a higher concentration, of $1\,\mu$M of various antibodies and nanobodies against AD and PD, be tested on PD CSF samples. Subsequently, the concentration of those antibodies and/or nanobodies that work over a physiological range should be decreased, and the number of samples should be increased to obtain statistically significant results between the tested antibodies and/or nanobodies and control groups.

7.2.2 High-throughput antibody and/or nanobody screening on a microfluidic droplet platform

This method is time-consuming due to the fact that only the fluorescent response of a single cell is recorded each time, when a nanopipette is located on the target cell. A high-throughput screening of antibodies and/or nanobodies can be carried out on a microfluidic droplet platform. As shown in Figure 7.1, separate trypsinised cells that were pre-incubated with Fluo-4 AM in L15 (containing calcium) are loaded into the device from one inlet; whilst AD/PD CSF with antibodies and/or nanobodies is loaded from another. CSF, antibodies and/or nanobodies, and L15 containing floating single cells are well-mixed and are then encapsulated in hydrophilic droplets that are naturally formed by injecting hydrophobic solution. A large number of droplets is collected, so the calcium influx in individual cells is monitored simultaneously by recording the fluorescence behaviours over time under illumination from a 488 nm laser. Note that the concentration of CSF is reduced only by approximately half due to mixing with L15, and the normalisation of calcium influx is the same as in the SICM-based method.

7.2.3 A new quadruple-barrel based ATP sensor

The yield from an ATP sensor with hexokinases interconnected with a Ppy layer by glutaraldehyde is low, which might be attributed to the inefficiency of the fixation of hexokinases. In fact, the sensing method that uses one nanopipette for delivering hexokinase near an EGOFET pH sensor, i.e. approach (2), has the potential to work in single-cell experiments, because it is very sensitive to pH changes in the microenvironment, although protons produced by the catalysis of ATP, and those introduced by the hexokinase carrier solution are highly convoluted. A quadruple-barrel may solve this issue and give the high sensitivity to ATP. As shown in Figure 7.2, pyrolytic carbon is deposited to fill a pair of neighbouring channels or opposite channels, on which a Ppy layer is deposited electrochemically to interlink these carbon electrodes, functioning as an EGOFET. Abeta42 oligomers and hex-

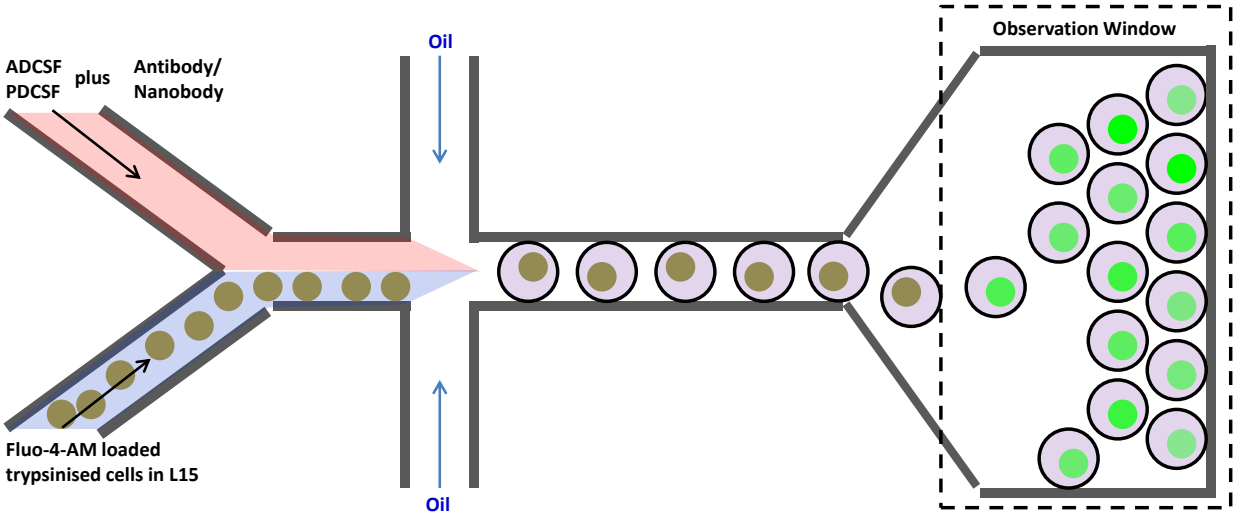

Figure 7.1: Schematic illustration of a microfluidic device, in which single live cells and toxic oligomers and/or antibodies are encapsulated in single droplets. Fluo-4 AM preloaded separated cells in L15 and CSF from patients, with or without antibodies or nanobodies, are loaded from two inlets that converge to one channel. Subsequently, the mixed solutions with cells and molecules of interest are encapsulated in single droplets that are phase separated due to the injection of oil from two sides. These droplets are gathered in a pool and then illuminated by a laser of 488 nm, with their fluorescence over time being recorded using a camera with high a sensitivity.

okinases can then be delivered individually via the other vacant channels. The advantages of using this quadruple-barrel nanopipette are that: (1) the EGOFET and the reagent deliveries are all located in the same place; (2) the influence of pH changes introduced by the hexokinase carrier solution would be deconvoluted, because it should already have led to a new equilibrium value in the drain-to-source current before measurements are carried out on single cells. Therefore, it may become a highly-sensitive ATP sensor, as long as a set of pulling parameters that give rise to suitable openings has been found, and the delivery rate of reagents can be optimised. It is worth noting that it may become a glucose sensor if hexokinase is replaced by glucose oxidase.

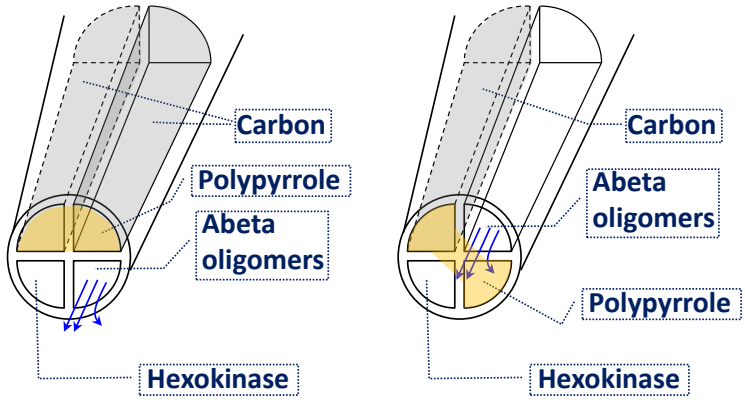

Figure 7.2: A design illustrating an ATP sensor based on a quadruple-barrel nanopipette. Neighbouring or opposite channels, on which a Ppy layer that bridges the two is electrochemically deposited, are filled with pyrolytic carbon. Abeta42 oligomer (or other toxic species to be tested) and hexokinases are delivered via the other two vacant channels.

7.2.4 Observation of the time-resolved pore-forming process using whole-cell recording

There may be alternative ways to investigate the pore-forming mechanism induced by Abeta42 oligomers. When a cell is recorded in whole-cell mode using the patch–clamp technique, its R_s, R_m and the DC offset can be monitored over time. When one or multiple Abeta42 oligomers pass through the cell membrane, it is likely that temporary pores are formed. This may be reflected in changes in R_m, i.e. a decrease in R_m with more or larger pores formed.

7.2.5 Potassium ion sensor

In addition, this pore-forming mechanism may be confirmed using a potassium ion sensor fabricated on a double-barrel nanopipette, as shown in Figure 7.4. As in the previous cases, one channel is used for the delivery of Abeta42 oligomers, whilst the tip of the other channel is filled with an organic ion exchanger resin, which, it is suggested by Happel *et al* [249] should use 3 mg of potassium tetrakis(4 chlorophenyl)borate in 100 μL 2-Nitrophenyl octyl ether. This resin can work as a liquid membrane that can selectively allow potassium ions to pass

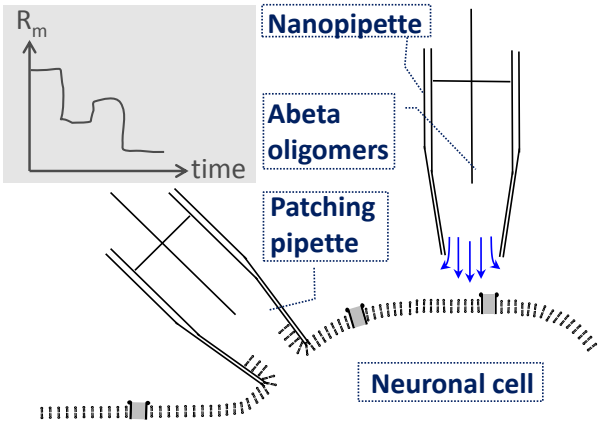

Figure 7.3: Schematic illustration of a cell under whole-cell recording, with Abeta42 oligomers being delivered locally via another nanopipette that is located above the same cell. The inset indicates that the membrane resistance (R_m) of the patched cell is monitored over time.

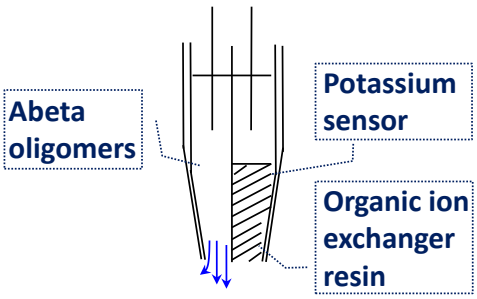

Figure 7.4: Schematic diagram of a double-barrel nanopipette, with one channel for delivery of Abeta42 oligimers and the other acting as a potassium sensor. In the potassium sensing channel, the tip is filled with organic ion exchanger resin in order to allow potassium ions under the tip to pass selectively through to the electrode side.

through. There are about 140 mM of potassium ions in neurons, so temporary pores induced by Abeta42 oligomers may result in a high potassium efflux, and they can be collected on the other side of the resin. The amount of potassium that passes may be quantified by recording the fluorescence emitted by a potassium indicator on the other side of the resin, such as APG-1, APG-2 or PBFI, if a well-aligned laser is focused in the nanopipette near the edge of the resin. Otherwise, changes in the potential induced by potassium ions, which is linear to the potassium concentration, can be adopted as a potassium concentration-relevant parameter.

Bibliography

[1] S. Weiss, "Fluorescence spectroscopy of single biomolecules," *Science*, vol. 283, no. 5408, pp. 1676–1683, 1999.

[2] W. E. Moerner, "New directions in single-molecule imaging and analysis," *Proceedings of the National Academy of Sciences*, vol. 104, no. 31, pp. 12596–12602, 2007.

[3] G. Binnig, H. Rohrer, C. Gerber, and E. Weibel, "Surface studies by scanning tunneling microscopy," *Phys. Rev. Lett.*, vol. 49, pp. 57–61, 1982.

[4] G. Binnig, C. F. Quate, and C. Gerber, "Atomic force microscope," *Phys. Rev. Lett.*, vol. 56, pp. 930–933, 1986.

[5] J. Rheinlaender, N. A. Geisse, R. Proksch, and T. E. Schaffer, "Comparison of scanning ion conductance microscopy with atomic force microscopy for cell imaging," *Langmuir*, vol. 27, no. 2, pp. 697–704, 2011.

[6] P. K. Hansma, B. Drake, O. Marti, S. A. Gould, and C. B. Prater, "The scanning ion-conductance microscope.," *Science*, vol. 243, no. 4891, pp. 641–643, 1989.

[7] A. I. Shevchuk, G. I. Frolenkov, D. Snchez, P. S. James, N. Freedman, M. J. Lab, R. Jones, D. Klenerman, and Y. E. Korchev, "Imaging proteins in membranes of living cells by high-resolution scanning ion conductance microscopy," *Angewandte Chemie International Edition*, vol. 45, no. 14, pp. 2212–2216, 2006.

[8] J. Rheinlaender and T. E. Schffer, "Image formation, resolution, and height measurement in scanning ion conductance microscopy," *Journal of Applied Physics*, vol. 105, no. 9, p. 094905, 2009.

[9] J. Rheinlaender and T. E. Schaffer, "Lateral resolution and image formation in scanning ion conductance microscopy," *Analytical chemistry*, vol. 87, no. 14, pp. 7117–7124, 2015.

[10] F. Anariba, J. H. Anh, G.-E. Jung, N.-J. Cho, and S.-J. Cho, "Biophysical applications of scanning ion conductance microscopy (sicm)," *Modern Physics Letters B*, vol. 26, no. 05, p. 1130003, 2012.

[11] A. I. Shevchuk, J. Gorelik, S. E. Harding, M. J. Lab, D. Klenerman, and Y. E. Korchev, "Simultaneous measurement of ca 2+ and cellular dynamics: combined scanning ion conductance and optical microscopy to study contracting cardiac myocytes," *Biophysical Journal*, vol. 81, no. 3, pp. 1759–1764, 2001.

[12] D. Pastré, H. Iwamoto, J. Liu, G. Szabo, and Z. Shao, "Characterization of ac mode scanning ion-conductance microscopy," *Ultramicroscopy*, vol. 90, no. 1, pp. 13–19, 2001.

[13] C.-C. Chen and L. A. Baker, "Effects of pipette modulation and imaging distances on ion currents measured with scanning ion conductance microscopy (sicm)," *Analyst*, vol. 136, no. 1, pp. 90–97, 2011.

[14] P. Novak, C. Li, A. I. Shevchuk, R. Stepanyan, M. Caldwell, S. Hughes, T. G. Smart, J. Gorelik, V. P. Ostanin, G. W. Moss, *et al.*, "Nanoscale live-cell imaging using hopping probe ion conductance microscopy," *Nature methods*, vol. 6, no. 4, pp. 279–281, 2009.

[15] Y. Takahashi, Y. Murakami, K. Nagamine, H. Shiku, S. Aoyagi, T. Yasukawa, M. Kanzaki, and T. Matsue, "Topographic imaging of convoluted surface of live cells by scanning ion conductance microscopy in a standing approach mode," *Physical Chemistry Chemical Physics*, vol. 12, no. 34, pp. 10012–10017, 2010.

[16] S. Mann, G. Hoffmann, A. Hengstenberg, W. Schuhmann, and I. Dietzel, "Pulse-mode scanning ion conductance microscopya method to investigate cultured hippocampal cells," *Journal of neuroscience methods*, vol. 116, no. 2, pp. 113–117, 2002.

[17] A. Zhukov, O. Richards, V. Ostanin, Y. Korchev, and D. Klenerman, "A hybrid scanning mode for fast scanning ion conductance microscopy (sicm) imaging," *Ultramicroscopy*, vol. 121, pp. 1–7, 2012.

[18] J. Rheinlaender, N. A. Geisse, R. Proksch, and T. E. Schaffer, "Comparison of scanning ion conductance microscopy with atomic force microscopy for cell imaging," *Langmuir*, vol. 27, no. 2, pp. 697–704, 2010.

[19] P. Happel, G. Hoffmann, S. Mann, and I. Dietzel, "Monitoring cell movements and volume changes with pulse-mode scanning ion conductance microscopy," *Journal of microscopy*, vol. 212, no. 2, pp. 144–151, 2003.

[20] Y. E. Korchev, J. Gorelik, M. J. Lab, E. V. Sviderskaya, C. L. Johnston, C. R. Coombes, I. Vodyanoy, and C. R. Edwards, "Cell volume measurement using scanning ion conductance microscopy," *Biophysical journal*, vol. 78, no. 1, pp. 451–457, 2000.

[21] A. Shevchuk, S. Tokar, S. Gopal, J. L. Sanchez-Alonso, A. I. Tarasov, A. C. Vélez-Ortega, C. Chiappini, P. Rorsman, M. M. Stevens, J. Gorelik, *et al.*, "Angular approach scanning ion conductance microscopy," *Biophysical journal*, vol. 110, no. 10, pp. 2252–2265, 2016.

[22] X. Liu, X. Yang, B. Zhang, X. Zhang, H. Lu, J. Zhang, and Y. Zhang, "High-resolution morphological identification and characterization of living neuroblastoma sk-n-sh cells by hopping probe ion conductance microscopy," *Brain research*, vol. 1386, pp. 35–40, 2011.

[23] J. Gorelik, L. Q. Yang, Y. Zhang, M. Lab, Y. Korchev, and S. E. Harding, "A novel z-groove index characterizing myocardial surface structure," *Cardiovascular research*, vol. 72, no. 3, pp. 422–429, 2006.

[24] A. R. Lyon, K. T. MacLeod, Y. Zhang, E. Garcia, G. K. Kanda, Y. E. Korchev, S. E. Harding, J. Gorelik, *et al.*, "Loss of t-tubules and other changes to surface topography in ventricular myocytes from failing human and rat heart," *Proceedings of the National Academy of Sciences*, vol. 106, no. 16, pp. 6854–6859, 2009.

[25] T. Sun, P. S. Donoghue, J. R. Higginson, N. Gadegaard, S. C. Barnett, and M. O. Riehle, "The interactions of astrocytes and fibroblasts with defined pore structures in static and perfusion cultures," *Biomaterials*, vol. 32, no. 8, pp. 2021–2031, 2011.

[26] M. Miragoli, A. Moshkov, P. Novak, A. Shevchuk, V. O. Nikolaev, I. El-Hamamsy, C. M. Potter, P. Wright, S. S. A. Kadir, A. R. Lyon, *et al.*, "Scanning ion conductance microscopy: a convergent high-resolution technology for multi-parametric analysis of living cardiovascular cells," *Journal of The Royal Society Interface*, vol. 8, no. 60, pp. 913–925, 2011.

[27] P. Happel, F. Wehner, and I. D. Dietzel, "Scanning ion conductance microscopy-a tool to investigate electrolyte-nonconductor interfaces," in *Modern Research and Educational Topics in Microscopy, Vol. 2*, pp. 968–975, Formatex, 2007.

[28] Y. Zhang, J. Gorelik, D. Sanchez, A. Shevchuk, M. Lab, I. Vodyanoy, D. Klenerman, C. Edwards, and Y. Korchev, "Scanning ion conductance microscopy reveals how a functional renal epithelial monolayer maintains its integrity," *Kidney international*, vol. 68, no. 3, pp. 1071–1077, 2005.

[29] P. Happel, K. Möller, R. Kunz, and I. D. Dietzel, "A boundary delimitation algorithm to approximate cell soma volumes of bipolar cells from topographical data obtained by scanning probe microscopy," *BMC bioinformatics*, vol. 11, no. 1, p. 323, 2010.

[30] J. Gorelik, Y. Zhang, A. I. Shevchuk, G. I. Frolenkov, D. Sánchez, M. J. Lab, I. Vodyanoy, C. R. Edwards, D. Klenerman, and Y. E. Korchev, "The use of scanning ion conductance microscopy to image a6 cells," *Molecular and cellular endocrinology*, vol. 217, no. 1, pp. 101–108, 2004.

[31] A. I. Shevchuk, G. I. Frolenkov, D. Sánchez, P. S. James, N. Freedman, M. J. Lab, R. Jones, D. Klenerman, and Y. E. Korchev, "Imaging proteins in membranes of living cells by high-resolution scanning ion conductance microscopy," *Angewandte Chemie*, vol. 118, no. 14, pp. 2270–2274, 2006.

[32] S. A. Mann, B. Versmold, R. Marx, S. Stahlhofen, I. D. Dietzel, R. Heumann, and R. Berger, "Corticosteroids reverse cytokine-induced block of survival and differentiation of oligodendrocyte progenitor cells from rats," *Journal of neuroinflammation*, vol. 5, no. 1, p. 39, 2008.

[33] X. Yang, X. Liu, X. Zhang, H. Lu, J. Zhang, and Y. Zhang, "Investigation of morphological and functional changes during neuronal differentiation of pc12 cells by combined hopping probe ion conductance microscopy and patch-clamp technique," *Ultramicroscopy*, vol. 111, no. 8, pp. 1417–1422, 2011.

[34] W. Shin and K. D. Gillis, "Measurement of changes in membrane surface morphology associated with exocytosis using scanning ion conductance microscopy," *Biophysical journal*, vol. 91, no. 6, pp. L63–L65, 2006.

[35] X. Yang, X. Liu, H. Lu, X. Zhang, L. Ma, R. Gao, and Y. Zhang, "Real-time investigation of acute toxicity of zno nanoparticles on human lung epithelia with hopping probe ion conductance microscopy," *Chemical research in toxicology*, vol. 25, no. 2, pp. 297–304, 2012.

[36] P. Ruenraroengsak, P. Novak, D. Berhanu, A. J. Thorley, E. Valsami-Jones, J. Gorelik, Y. E. Korchev, and T. D. Tetley, "Respiratory epithelial cytotoxicity and membrane damage (holes) caused by amine-modified nanoparticles," *Nanotoxicology*, vol. 6, no. 1, pp. 94–108, 2012.

[37] Y. Zhang, D. Sanchez, J. Gorelik, D. Klenerman, C. Edwards, Y. Korchev, *et al.*, "Basolateral p2x 4-like receptors regulate the extracellular atp-stimulated epithelial na+ channel activity in renal epithelia," *American Journal of Physiology-Renal Physiology*, vol. 292, no. 6, pp. F1734–F1740, 2007.

[38] M. Ibrahim, M. Navaratnarajah, U. Siedlecka, C. Rao, P. Dias, A. V. Moshkov, J. Gorelik, M. H. Yacoub, and C. M. Terracciano, "Mechanical unloading reverses transverse tubule remodelling and normalizes local ca2+-induced ca2+ release in a rodent model of heart failure," *European journal of heart failure*, vol. 14, no. 6, pp. 571–580, 2012.

[39] M. Ibrahim, A. Al Masri, M. Navaratnarajah, U. Siedlecka, G. K. Soppa, A. Moshkov, S. A. Al-Saud, J. Gorelik, M. H. Yacoub, and C. M. Terracciano, "Prolonged mechanical unloading affects cardiomyocyte excitation-contraction coupling, transverse-tubule structure, and the cell surface," *The FASEB Journal*, vol. 24, no. 9, pp. 3321–3329, 2010.

[40] C. M. Potter, M. H. Lundberg, L. S. Harrington, C. M. Warboys, T. D. Warner, R. E. Berson, A. V. Moshkov, J. Gorelik, P. D. Weinberg, and J. A. Mitchell, "Role of shear stress in endothelial cell morphology and expression of cyclooxygenase isoforms," *Arteriosclerosis, thrombosis, and vascular biology*, vol. 31, no. 2, pp. 384–391, 2011.

[41] C. M. Potter, S. Schobesberger, M. H. Lundberg, P. D. Weinberg, J. A. Mitchell, and J. Gorelik, "Shape and compliance of endothelial cells after shear stress in vitro or from different aortic regions: scanning ion conductance microscopy study," *PloS one*, vol. 7, no. 2, p. e31228, 2012.

[42] O. Hamill, A. Marty, E. Neher, B. Sakmann, and F. Sigworth, "Improved patch-clamp techniques for high-resolution current recording from cells and cell-free membrane patches," *Pflgers Archiv*, vol. 391, no. 2, pp. 85–100, 1981.

[43] Y. E. Korchev, Y. A. Negulyaev, C. R. Edwards, I. Vodyanoy, *et al.*, "Functional localization of single active ion channels on the surface of a living cell," *Nature cell biology*, vol. 2, no. 9, p. 616, 2000.

[44] Y. Gu, J. Gorelik, H. A. Spohr, A. Shevchuk, S. E. Harding, I. Vodyanoy, D. Klenerman, Y. E. Korchev, *et al.*, "High-resolution scanning patch-clamp: new insights into cell function," *The FASEB Journal*, vol. 16, no. 7, pp. 748–750, 2002.

[45] J. Gorelik, Y. Gu, H. A. Spohr, A. I. Shevchuk, M. J. Lab, S. E. Harding, C. R. Edwards, M. Whitaker, G. W. Moss, D. C. Benton, *et al.*, "Ion channels in small cells and subcellular structures can be studied with a smart patch-clamp system," *Biophysical Journal*, vol. 83, no. 6, pp. 3296–3303, 2002.

[46] H. Duclohier, "Neuronal sodium channels in ventricular heart cells are localized near t-tubules openings," *Biochemical and biophysical research communications*, vol. 334, no. 4, pp. 1135–1140, 2005.

[47] A. K. Dutta, Y. E. Korchev, A. I. Shevchuk, S. Hayashi, Y. Okada, and R. Z. Sabirov, "Spatial distribution of maxi-anion channel on cardiomyocytes detected by smart-patch technique," *Biophysical journal*, vol. 94, no. 5, pp. 1646–1655, 2008.

[48] A. F. James, R. Z. Sabirov, and Y. Okada, "Clustering of protein kinase a-dependent cftr chloride channels in the sarcolemma of guinea-pig ventricular myocytes," *Biochemical and biophysical research communications*, vol. 391, no. 1, pp. 841–845, 2010.

[49] P. Novak, J. Gorelik, U. Vivekananda, A. I. Shevchuk, Y. S. Ermolyuk, R. J. Bailey, A. J. Bushby, G. W. Moss, D. A. Rusakov, D. Klenerman, *et al.*, "Nanoscale-targeted patch-clamp recordings of functional presynaptic ion channels," *Neuron*, vol. 79, no. 6, pp. 1067–1077, 2013.

[50] E. Betzig and R. J. Chichester, "Single molecules observed by near-field scanning optical microscopy," *Science*, vol. 262, pp. 1422–1422, 1993.

[51] M. Snyder, D. Vlachos, and V. Nikolakis, "Quantitative analysis of membrane morphology, microstructure, and polycrystallinity via laser scanning confocal microscopy: application to nax zeolite membranes," *Journal of membrane science*, vol. 290, no. 1, pp. 1–18, 2007.

[52] E. Betzig, G. H. Patterson, R. Sougrat, O. W. Lindwasser, S. Olenych, J. S. Bonifacino, M. W. Davidson, J. Lippincott-Schwartz, and H. F. Hess, "Imaging intracellular fluorescent proteins at nanometer resolution," *Science*, vol. 313, no. 5793, pp. 1642–1645, 2006.

[53] V. O. Nikolaev, A. Moshkov, A. R. Lyon, M. Miragoli, P. Novak, H. Paur, M. J. Lohse, Y. E. Korchev, S. E. Harding, and J. Gorelik, "β2-adrenergic receptor redistribution in heart failure changes camp compartmentation," *Science*, vol. 327, no. 5973, pp. 1653–1657, 2010.

[54] A. Bruckbauer, P. James, D. Zhou, J. W. Yoon, D. Excell, Y. Korchev, R. Jones, and D. Klenerman, "Nanopipette delivery of individual molecules to cellular compartments for single-molecule fluorescence tracking," *Biophysical journal*, vol. 93, no. 9, pp. 3120–3131, 2007.

[55] A. Shevchuk, P. Novak, M. Velazquez, T. Fleming, and Y. Korchev, "Combined ion conductance and fluorescence confocal microscopy for biological cell membrane transport studies," *Journal of Optics*, vol. 15, no. 9, p. 094005, 2013.

[56] J. Gorelik, A. Shevchuk, M. Ramalho, M. Elliott, C. Lei, C. Higgins, D. Klenerman, N. Krauzewicz, Y. Korchev, *et al.*, "Scanning surface confocal microscopy for simultaneous topographical and fluorescence imaging: application to single virus-like particle entry into a cell," *Proceedings of the National Academy of Sciences*, vol. 99, no. 25, pp. 16018–16023, 2002.

[57] A. I. Shevchuk, P. Hobson, M. J. Lab, D. Klenerman, N. Krauzewicz, and Y. E. Korchev, "Imaging single virus particles on the surface of cell membranes by high-resolution scanning surface confocal microscopy," *Biophysical journal*, vol. 94, no. 10, pp. 4089–4094, 2008.

[58] A. I. Shevchuk, P. Novak, M. Taylor, I. A. Diakonov, A. Ziyadeh-Isleem, M. Bitoun, P. Guicheney, J. Gorelik, C. J. Merrifield, D. Klenerman, *et al.*, "An alternative mechanism of clathrin-coated pit closure revealed by ion conductance microscopy," *J Cell Biol*, vol. 197, no. 4, pp. 499–508, 2012.

[59] R. W. Clarke, A. Drews, H. Browne, and D. Klenerman, "A single gd glycoprotein can mediate infection by herpes simplex virus," *Journal of the American Chemical Society*, vol. 135, no. 30, pp. 11175–11180, 2013.

[60] Y. E. Korchev, M. Raval, M. J. Lab, J. Gorelik, C. R. Edwards, T. Rayment, and D. Klenerman, "Hybrid scanning ion conductance and scanning near-field optical microscopy for the study of living cells," *Biophysical journal*, vol. 78, no. 5, pp. 2675–2679, 2000.

[61] A. Rothery, J. Gorelik, A. Bruckbauer, W. Yu, Y. Korchev, and D. Klenerman, "A novel light source for sicm–snom of living cells," *Journal of microscopy*, vol. 209, no. 2, pp. 94–101, 2003.

[62] Y. Takahashi, A. Kumatani, H. Shiku, and T. Matsue, "Scanning probe microscopy for nanoscale electrochemical imaging," *Analytical chemistry*, vol. 89, no. 1, pp. 342–357, 2016.

[63] J. Rodriguez-Lopez, M. A. Alpuche-Avilés, and A. J. Bard, "Interrogation of surfaces for the quantification of adsorbed species on electrodes: oxygen on gold and platinum in neutral media," *Journal of the American Chemical Society*, vol. 130, no. 50, pp. 16985–16995, 2008.

[64] M. S. Li, F. P. Filice, J. D. Henderson, and Z. Ding, "Probing cd2+-stressed live cell membrane permeability with various redox mediators in scanning electrochemical microscopy," *The Journal of Physical Chemistry C*, vol. 120, no. 11, pp. 6094–6103, 2016.

[65] E. Lee, J. Sung, T. An, H. Shin, H. G. Nam, and G. Lim, "Simultaneous imaging of the topography and electrochemical activity of a 2d carbon nanotube network using a dual functional l-shaped nanoprobe," *Analyst*, vol. 140, no. 9, pp. 3150–3156, 2015.

[66] Y. Takahashi, A. I. Shevchuk, P. Novak, Y. Murakami, H. Shiku, Y. E. Korchev, and T. Matsue, "Simultaneous noncontact topography and electrochemical imaging by secm/sicm featuring ion current feedback regulation," *Journal of the American Chemical Society*, vol. 132, no. 29, pp. 10118–10126, 2010.

[67] D. J. Comstock, J. W. Elam, M. J. Pellin, and M. C. Hersam, "Integrated ultramicroelectrode- nanopipet probe for concurrent scanning electrochemical microscopy and scanning ion conductance microscopy," *Analytical chemistry*, vol. 82, no. 4, pp. 1270–1276, 2010.

[68] D. A. Walsh, J. L. Fernandez, J. Mauzeroll, and A. J. Bard, "Scanning electrochemical microscopy. 55. fabrication and characterization of micropipet probes," *Analytical chemistry*, vol. 77, no. 16, pp. 5182–5188, 2005.

[69] W. Shi and L. A. Baker, "Imaging heterogeneity and transport of degraded nafion membranes," *Rsc Advances*, vol. 5, no. 120, pp. 99284–99290, 2015.

[70] C. A. Morris, C.-C. Chen, and L. A. Baker, "Transport of redox probes through single pores measured by scanning electrochemical-scanning ion conductance microscopy (secm-sicm)," *Analyst*, vol. 137, no. 13, pp. 2933–2938, 2012.

[71] C. A. Morris, C.-C. Chen, T. Ito, and L. A. Baker, "Local ph measurement with scanning ion conductance microscopy," *Journal of The Electrochemical Society*, vol. 160, no. 8, pp. H430–H435, 2013.

[72] Y. Takahashi, A. I. Shevchuk, P. Novak, B. Babakinejad, J. Macpherson, P. R. Unwin, H. Shiku, J. Gorelik, D. Klenerman, Y. E. Korchev, *et al.*, "Topographical and electrochemical nanoscale imaging of living cells using voltage-switching mode scanning electrochemical microscopy," *Proceedings of the National Academy of Sciences*, vol. 109, no. 29, pp. 11540–11545, 2012.

[73] Y. Takahashi, A. I. Shevchuk, P. Novak, Y. Zhang, N. Ebejer, J. V. Macpherson, P. R. Unwin, A. J. Pollard, D. Roy, C. A. Clifford, *et al.*, "Multifunctional nanoprobes for nanoscale chemical imaging and localized chemical delivery at surfaces and interfaces," *Angewandte Chemie International Edition*, vol. 50, no. 41, pp. 9638–9642, 2011.

[74] M. Sen, Y. Takahashi, Y. Matsumae, Y. Horiguchi, A. Kumatani, K. Ino, H. Shiku, and T. Matsue, "Improving the electrochemical imaging sensitivity of scanning electrochemical microscopy-scanning ion conductance microscopy by using electrochemical pt deposition," *Analytical chemistry*, vol. 87, no. 6, pp. 3484–3489, 2015.

[75] M. A. OConnell and A. J. Wain, "Mapping electroactivity at individual catalytic nanostructures using high-resolution scanning electrochemical–scanning ion conductance microcopy," *Analytical chemistry*, vol. 86, no. 24, pp. 12100–12107, 2014.

[76] M. A. O'Connell, J. R. Lewis, and A. J. Wain, "Electrochemical imaging of hydrogen peroxide generation at individual gold nanoparticles," *Chemical Communications*, vol. 51, no. 51, pp. 10314–10317, 2015.

[77] B. P. Nadappuram, K. McKelvey, R. Al Botros, A. W. Colburn, and P. R. Unwin, "Fabrication and characterization of dual function nanoscale ph-scanning ion conductance microscopy (sicm) probes for high resolution ph mapping," *Analytical chemistry*, vol. 85, no. 17, pp. 8070–8074, 2013.

[78] A. Page, M. Kang, A. Armitstead, D. Perry, and P. R. Unwin, "Quantitative visualization of molecular delivery and uptake at living cells with self-referencing scanning ion conductance microscopy-scanning electrochemical microscopy," *Analytical Chemistry*, vol. 89, no. 5, pp. 3021–3028, 2017.

[79] K. McKelvey, B. P. Nadappuram, P. Actis, Y. Takahashi, Y. E. Korchev, T. Matsue, C. Robinson, and P. R. Unwin, "Fabrication, characterization, and functionalization of dual carbon electrodes as probes for scanning electrochemical microscopy (secm)," *Analytical chemistry*, vol. 85, no. 15, pp. 7519–7526, 2013.

[80] Y. Zhou, C.-C. Chen, A. E. Weber, L. Zhou, and L. A. Baker, "Potentiometric-scanning ion conductance microscopy," *Langmuir*, vol. 30, no. 19, pp. 5669–5675, 2014.

[81] C.-C. Chen, Y. Zhou, C. A. Morris, J. Hou, and L. A. Baker, "Scanning ion conductance microscopy measurement of paracellular channel conductance in tight junctions," *Analytical chemistry*, vol. 85, no. 7, pp. 3621–3628, 2013.

[82] Y. Zhou, C.-C. Chen, A. E. Weber, L. Zhou, L. A. Baker, and J. Hou, "Potentiometric-scanning ion conductance microscopy for measurement at tight junctions," *Tissue barriers*, vol. 1, no. 4, p. e25585, 2013.

[83] N. Ebejer, M. Schnippering, A. W. Colburn, M. A. Edwards, and P. R. Unwin, "Localized high resolution electrochemistry and multifunctional imaging: Scanning

electrochemical cell microscopy," *Analytical chemistry*, vol. 82, no. 22, pp. 9141–9145, 2010.

[84] N. Ebejer, A. G. Güell, S. C. Lai, K. McKelvey, M. E. Snowden, and P. R. Unwin, "Scanning electrochemical cell microscopy: a versatile technique for nanoscale electrochemistry and functional imaging," *Annual Review of Analytical Chemistry*, vol. 6, pp. 329–351, 2013.

[85] M. Kang, D. Momotenko, A. Page, D. Perry, and P. R. Unwin, "Frontiers in nanoscale electrochemical imaging: faster, multifunctional, and ultrasensitive," *Langmuir*, vol. 32, no. 32, pp. 7993–8008, 2016.

[86] C. G. Williams, M. A. Edwards, A. L. Colley, J. V. Macpherson, and P. R. Unwin, "Scanning micropipet contact method for high-resolution imaging of electrode surface redox activity," *Analytical chemistry*, vol. 81, no. 7, pp. 2486–2495, 2009.

[87] Y. Takahashi, A. Kumatani, H. Munakata, H. Inomata, K. Ito, K. Ino, H. Shiku, P. R. Unwin, Y. E. Korchev, K. Kanamura, *et al.*, "Nanoscale visualization of redox activity at lithium-ion battery cathodes," *Nature communications*, vol. 5, p. 5450, 2014.

[88] B. Paulose Nadappuram, K. McKelvey, J. C. Byers, A. G. Guell, A. W. Colburn, R. A. Lazenby, and P. R. Unwin, "Quad-barrel multifunctional electrochemical and ion conductance probe for voltammetric analysis and imaging," *Analytical chemistry*, vol. 87, no. 7, pp. 3566–3573, 2015.

[89] D. Momotenko, J. C. Byers, K. McKelvey, M. Kang, and P. R. Unwin, "High-speed electrochemical imaging," *ACS nano*, vol. 9, no. 9, pp. 8942–8952, 2015.

[90] D. Momotenko, K. McKelvey, M. Kang, G. N. Meloni, and P. R. Unwin, "Simultaneous interfacial reactivity and topography mapping with scanning ion conductance microscopy," *Analytical chemistry*, vol. 88, no. 5, pp. 2838–2846, 2016.

[91] D. Sánchez, U. Anand, J. Gorelik, C. D. Benham, C. Bountra, M. Lab, D. Klenerman, R. Birch, P. Anand, and Y. Korchev, "Localized and non-contact mechanical stimulation of dorsal root ganglion sensory neurons using scanning ion conductance microscopy," *Journal of neuroscience methods*, vol. 159, no. 1, pp. 26–34, 2007.

[92] D. Sánchez, N. Johnson, C. Li, P. Novak, J. Rheinlaender, Y. Zhang, U. Anand, P. Anand, J. Gorelik, G. I. Frolenkov, *et al.*, "Noncontact measurement of the local mechanical properties of living cells using pressure applied via a pipette," *Biophysical Journal*, vol. 95, no. 6, pp. 3017–3027, 2008.

[93] M. Pellegrino, M. Pellegrini, P. Orsini, E. Tognoni, C. Ascoli, P. Baschieri, and F. Dinelli, "Measuring the elastic properties of living cells through the analysis of current–displacement curves in scanning ion conductance microscopy," *Pflügers Archiv-European Journal of Physiology*, vol. 464, no. 3, pp. 307–316, 2012.

[94] M. Miragoli, J. L. Sanchez-Alonso, A. Bhargava, P. T. Wright, M. Sikkel, S. Schobesberger, I. Diakonov, P. Novak, A. Castaldi, P. Cattaneo, *et al.*, "Microtubule-dependent mitochondria alignment regulates calcium release in response to nanomechanical stimulus in heart myocytes," *Cell reports*, vol. 14, no. 1, pp. 140–151, 2016.

[95] R. W. Clarke, A. Zhukov, O. Richards, N. Johnson, V. Ostanin, and D. Klenerman, "Pipette–surface interaction: current enhancement and intrinsic force," *Journal of the American Chemical Society*, vol. 135, no. 1, pp. 322–329, 2012.

[96] R. W. Clarke, P. Novak, A. Zhukov, E. J. Tyler, M. Cano-Jaimez, A. Drews, O. Richards, K. Volynski, C. Bishop, and D. Klenerman, "Low stress ion conductance microscopy of sub-cellular stiffness," *Soft matter*, vol. 12, no. 38, pp. 7953–7958, 2016.

[97] M. Pellegrino, P. Orsini, and F. De Gregorio, "Use of scanning ion conductance microscopy to guide and redirect neuronal growth cones," *Neuroscience research*, vol. 64, no. 3, pp. 290–296, 2009.

[98] M. Pellegrino, P. Orsini, M. Pellegrini, P. Baschieri, F. Dinelli, D. Petracchi, E. Tognoni, and C. Ascoli, "Weak hydrostatic forces in far-scanning ion conductance microscopy used to guide neuronal growth cones," *Neuroscience research*, vol. 69, no. 3, pp. 234–240, 2011.

[99] L. Ying, A. Bruckbauer, A. M. Rothery, Y. E. Korchev, and D. Klenerman, "Programmable delivery of dna through a nanopipet," *Analytical Chemistry*, vol. 74, no. 6, pp. 1380–1385, 2002.

[100] L. Ying, S. S. White, A. Bruckbauer, L. Meadows, Y. E. Korchev, and D. Klenerman, "Frequency and voltage dependence of the dielectrophoretic trapping of short lengths of dna and dctp in a nanopipette," *Biophysical journal*, vol. 86, no. 2, pp. 1018–1027, 2004.

[101] L. Ying, A. Bruckbauer, A. M. Rothery, Y. E. Korchev, and D. Klenerman, "Programmable delivery of dna through a nanopipet," *Analytical chemistry*, vol. 74, no. 6, pp. 1380–1385, 2002.

[102] A. Bruckbauer, D. Zhou, L. Ying, Y. E. Korchev, C. Abell, and D. Klenerman, "Multicomponent submicron features of biomolecules created by voltage controlled deposition from a nanopipet," *Journal of the American Chemical Society*, vol. 125, no. 32, pp. 9834–9839, 2003.

[103] L. Ying, S. S. White, A. Bruckbauer, L. Meadows, Y. E. Korchev, and D. Klenerman, "Frequency and voltage dependence of the dielectrophoretic trapping of short lengths of dna and dctp in a nanopipette," *Biophysical journal*, vol. 86, no. 2, pp. 1018–1027, 2004.

[104] J. D. Piper, C. Li, C.-J. Lo, R. Berry, Y. Korchev, L. Ying, and D. Klenerman, "Characterization and application of controllable local chemical changes produced by

reagent delivery from a nanopipet," *Journal of the American Chemical Society*, vol. 130, no. 31, pp. 10386–10393, 2008.

[105] A. López-Córdoba, P. Jönsson, B. Babakinejad, P. Actis, P. Novak, T. Yasufumi, A. Shevchuck, U. Anand, P. Anand, A. Drews, *et al.*, "Sicm-based nanodelivery system for local trpv1 stimulation," *Biophysical Journal*, vol. 108, no. 2, p. 332a, 2015.

[106] A. Bruckbauer, P. James, D. Zhou, J. W. Yoon, D. Excell, Y. Korchev, R. Jones, and D. Klenerman, "Nanopipette delivery of individual molecules to cellular compartments for single-molecule fluorescence tracking," *Biophysical journal*, vol. 93, no. 9, pp. 3120–3131, 2007.

[107] A. Bruckbauer, D. Zhou, L. Ying, C. Abell, and D. Klenerman, "A simple voltage controlled enzymatic nanoreactor produced in the tip of a nanopipet," *Nano Letters*, vol. 4, no. 10, pp. 1859–1862, 2004.

[108] B. Babakinejad, P. Jonsson, A. Lopez Cordoba, P. Actis, P. Novak, Y. Takahashi, A. Shevchuk, U. Anand, P. Anand, A. Drews, *et al.*, "Local delivery of molecules from a nanopipette for quantitative receptor mapping on live cells," *Analytical chemistry*, vol. 85, no. 19, pp. 9333–9342, 2013.

[109] A. Drews, J. Flint, N. Shivji, P. Jönsson, D. Wirthensohn, E. De Genst, C. Vincke, S. Muyldermans, C. Dobson, and D. Klenerman, "Individual aggregates of amyloid beta induce temporary calcium influx through the cell membrane of neuronal cells," *Scientific reports*, vol. 6, 2016.

[110] F. O. Laforge, J. Carpino, S. A. Rotenberg, and M. V. Mirkin, "Electrochemical attosyringe," *Proceedings of the National Academy of Sciences*, vol. 104, no. 29, pp. 11895–11900, 2007.

[111] P. Actis, M. M. Maalouf, H. J. Kim, A. Lohith, B. Vilozny, R. A. Seger, and N. Pourmand, "Compartmental genomics in living cells revealed by single-cell nanobiopsy," *ACS nano*, vol. 8, no. 1, pp. 546–553, 2013.

[112] Y. Nashimoto, Y. Takahashi, Y. Zhou, H. Ito, H. Ida, K. Ino, T. Matsue, and H. Shiku, "Evaluation of mrna localization using double barrel scanning ion conductance microscopy," *ACS nano*, vol. 10, no. 7, pp. 6915–6922, 2016.

[113] K. T. Rodolfa, A. Bruckbauer, D. Zhou, A. I. Schevchuk, Y. E. Korchev, and D. Klenerman, "Nanoscale pipetting for controlled chemistry in small arrayed water droplets using a double-barrel pipet," *Nano letters*, vol. 6, no. 2, pp. 252–257, 2006.

[114] B. D. Aaronson, J. Garoz-Ruiz, J. C. Byers, A. Colina, and P. R. Unwin, "Electrodeposition and screening of photoelectrochemical activity in conjugated polymers using scanning electrochemical cell microscopy," *Langmuir*, vol. 31, no. 46, pp. 12814–12822, 2015.

[115] K. T. Rodolfa, A. Bruckbauer, D. Zhou, Y. E. Korchev, and D. Klenerman, "Two-component graded deposition of biomolecules with a double-barreled nanopipette," *Angewandte Chemie*, vol. 117, no. 42, pp. 7014–7019, 2005.

[116] K. McKelvey, M. A. O'Connell, and P. R. Unwin, "Meniscus confined fabrication of multidimensional conducting polymer nanostructures with scanning electrochemical cell microscopy (seccm)," *Chemical Communications*, vol. 49, no. 29, pp. 2986–2988, 2013.

[117] A. N. Patel, K. McKelvey, and P. R. Unwin, "Nanoscale electrochemical patterning reveals the active sites for catechol oxidation at graphite surfaces," *Journal of the American Chemical Society*, vol. 134, no. 50, pp. 20246–20249, 2012.

[118] E. E. Oseland, Z. J. Ayres, A. Basile, D. M. Haddleton, P. Wilson, and P. R. Unwin, "Surface patterning of polyacrylamide gel using scanning electrochemical cell microscopy (seccm)," *Chemical Communications*, vol. 52, no. 64, pp. 9929–9932, 2016.

[119] D. Momotenko, A. Page, M. Adobes-Vidal, and P. R. Unwin, "Write–read 3d patterning with a dual-channel nanopipette," *ACS nano*, vol. 10, no. 9, pp. 8871–8878, 2016.

[120] S. K. Seol, D. Kim, S. Lee, J. H. Kim, W. S. Chang, and J. T. Kim, "Electrodeposition-based 3d printing of metallic microarchitectures with controlled internal structures," *Small*, vol. 11, no. 32, pp. 3896–3902, 2015.

[121] L. K. Bright, C. A. Baker, M. T. Agasid, L. Ma, and C. A. Aspinwall, "Decreased aperture surface energy enhances electrical, mechanical, and temporal stability of suspended lipid membranes," *ACS applied materials & interfaces*, vol. 5, no. 22, pp. 11918–11926, 2013.

[122] Y. Zhou, L. K. Bright, W. Shi, C. A. Aspinwall, and L. A. Baker, "Ion channel probes for scanning ion conductance microscopy," *Langmuir*, vol. 30, no. 50, pp. 15351–15355, 2014.

[123] F. C. Macazo and R. J. White, "Bioinspired protein channel-based scanning ion conductance microscopy (bio-sicm) for simultaneous conductance and specific molecular imaging," *Journal of the American Chemical Society*, vol. 138, no. 8, pp. 2793–2801, 2016.

[124] S. Umehara, N. Pourmand, C. D. Webb, R. W. Davis, K. Yasuda, and M. Karhanek, "Current rectification with poly-l-lysine-coated quartz nanopipettes," *Nano letters*, vol. 6, no. 11, pp. 2486–2492, 2006.

[125] S. Umehara, M. Karhanek, R. W. Davis, and N. Pourmand, "Label-free biosensing with functionalized nanopipette probes," *Proceedings of the National Academy of Sciences*, vol. 106, no. 12, pp. 4611–4616, 2009.

[126] B. Vilozny, P. Actis, R. A. Seger, Q. Vallmajo-Martin, and N. Pourmand, "Reversible cation response with a protein-modified nanopipette," *Analytical chemistry*, vol. 83, no. 16, pp. 6121–6126, 2011.

[127] P. Actis, A. Rogers, J. Nivala, B. Vilozny, R. A. Seger, O. Jejelowo, and N. Pourmand, "Reversible thrombin detection by aptamer functionalized sting sensors," *Biosensors and Bioelectronics*, vol. 26, no. 11, pp. 4503–4507, 2011.

[128] P. Actis, B. Vilozny, R. A. Seger, X. Li, O. Jejelowo, M. Rinaudo, and N. Pourmand, "Voltage-controlled metal binding on polyelectrolyte-functionalized nanopores," *Langmuir*, vol. 27, no. 10, pp. 6528–6533, 2011.

[129] P. Actis, O. Jejelowo, and N. Pourmand, "Ultrasensitive mycotoxin detection by sting sensors," *Biosensors and Bioelectronics*, vol. 26, no. 2, pp. 333–337, 2010.

[130] R. A. Nascimento, R. E. Ozel, W. H. Mak, M. Mulato, B. Singaram, and N. Pourmand, "Single cell glucose nanosensor verifies elevated glucose levels in individual cancer cells," *Nano letters*, vol. 16, no. 2, pp. 1194–1200, 2016.

[131] N. Sa and L. A. Baker, "Rectification of nanopores at surfaces," *Journal of the American Chemical Society*, vol. 133, no. 27, pp. 10398–10401, 2011.

[132] N. Sa, W.-J. Lan, W. Shi, and L. A. Baker, "Rectification of ion current in nanopipettes by external substrates," *ACS nano*, vol. 7, no. 12, pp. 11272–11282, 2013.

[133] D. Perry, B. P. Nadappuram, D. Momotenko, P. D. Voyias, A. Page, G. Tripathi, B. G. Frenguelli, and P. R. Unwin, "Surface charge visualization at viable living cells," *J. Am. Chem. Soc*, vol. 138, no. 9, pp. 3152–3160, 2016.

[134] D. Perry, R. Al Botros, D. Momotenko, S. L. Kinnear, and P. R. Unwin, "Simultaneous nanoscale surface charge and topographical mapping," *ACS nano*, vol. 9, no. 7, pp. 7266–7276, 2015.

[135] Minus k Technology, "Bm-1 bench top vibration isolation platform, product description." http://www.minusk.com/products/bm1-bench-top-vibration-isolation-platforms.html.

[136] Sutter Instrument, *P-2000 Laser Based Micropipette Puller System, Operation Manual*.

[137] R. D. Purves, "The mechanics of pulling a glass micropipette," *Biophysical Journal*, vol. 29, no. 3, pp. 523–529, 1980.

[138] J. J. Nicholas, *Developing Scanning Ion Conductance Microscopy (SICM) for Nanoscale Force and Topographic Characterisation of Live cells*. PhD thesis, University of Cambridge.

[139] Warner Instruments, *Specialized Tools for Bioresearch, Microelectrode/Micropipette Holders*.

[140] R. Bates and J. Macaskill, "Standard potential of the silver-silver chloride electrode," *Pure Appl. Chem*, vol. 50, pp. 1701–1706, 1978.

[141] C. G. Zoski, *Handbook of electrochemistry*. Elsevier, 2006.

[142] Physik Instrumente, "Piezo technology, product description." https://www.physikinstrumente.co.uk/en/know-how-technology/piezo-technology/.

[143] Physik Instrumente, *P-753 Positioning Systems, PZ254E, User Manual*.

[144] Physik Instrumente, *P-73x Nanopositioners, PZ103E, User Manual*.

[145] Physik Instrumente, *E-500/E-501 Series Modular Piezo Controller, PZ 62E, User Manual*.

[146] Andor, "ixon emccd cameras, product description." http://www.andor.com/cameras/ixon-emccd-camera-series.

[147] P. Novak, C. Li, A. I. Shevchuk, R. Stepanyan, M. Caldwell, S. Hughes, T. G. Smart, J. Gorelik, V. P. Ostanin, M. J. Lab, G. W. J. Moss, G. I. Frolenkov, D. Klenerman, and Y. E. Korchev, "Nanoscale live-cell imaging using hopping probe ion conductance microscopy," *Nat Meth*, vol. 6, no. 4, pp. 279–281, 2009.

[148] C.-C. Chen, Y. Zhou, and L. A. Baker, "Scanning ion conductance microscopy," *Annual Review of Analytical Chemistry*, vol. 5, no. 1, pp. 207–228, 2012.

[149] H. Nitz, J. Kamp, and H. Fuchs, "A combined scanning ion-conductance and shear-force microscope," *Probe microsc*, vol. 1, pp. 187–200, 1998.

[150] M. A. Edwards, C. G. Williams, A. L. Whitworth, and P. R. Unwin, "Scanning ion conductance microscopy: a model for experimentally realistic conditions and image interpretation," *Analytical chemistry*, vol. 81, no. 11, pp. 4482–4492, 2009.

[151] F. Anariba, J. H. Anh, G.-E. Jung, N.-J. Cho, and S.-J. Cho, "Biophysical applications of scanning ion conductance microscopy (sicm)," *Modern Physics Letters B*, vol. 26, no. 05, p. 1130003, 2012.

[152] T. E. Faber, *Fluid dynamics for physicists*. Cambridge University Press, 1995.

[153] P. Jönsson, J. McColl, R. W. Clarke, V. P. Ostanin, B. Jönsson, and D. Klenerman, "Hydrodynamic trapping of molecules in lipid bilayers," *Proceedings of the National Academy of Sciences*, vol. 109, no. 26, pp. 10328–10333, 2012.

[154] N. Calander, "Analyte concentration at the tip of a nanopipette," *Analytical chemistry*, vol. 81, no. 20, pp. 8347–8353, 2009.

[155] A. J. Bard, L. R. Faulkner, J. Leddy, and C. G. Zoski, *Electrochemical methods: fundamentals and applications*, vol. 2. wiley New York, 1980.

[156] A. Association *et al.*, "2017 alzheimer's disease facts and figures," *Alzheimer's & Dementia*, vol. 13, no. 4, pp. 325–373, 2017.

[157] C. L. Masters, R. Bateman, K. Blennow, C. C. Rowe, R. A. Sperling, and J. L. Cummings, "Alzheimer's disease," vol. 1, p. 15056, 2015.

[158] R. J. O'Brien and P. C. Wong, "Amyloid precursor protein processing and alzheimer's disease," *Annual review of neuroscience*, vol. 34, pp. 185–204, 2011.

[159] C. Haass and D. J. Selkoe, "Soluble protein oligomers in neurodegeneration: lessons from the alzheimer's amyloid [beta]-peptide," *Nature reviews. Molecular cell biology*, vol. 8, no. 2, p. 101, 2007.

[160] M. Gatz, C. A. Reynolds, L. Fratiglioni, B. Johansson, J. A. Mortimer, S. Berg, A. Fiske, and N. L. Pedersen, "Role of genes and environments for explaining alzheimer disease," *Archives of general psychiatry*, vol. 63, no. 2, pp. 168–174, 2006.

[161] E. Corder, A. Saunders, W. Strittmatter, D. Schmechel, P. Gaskell, G. a. Small, A. Roses, J. Haines, and M. A. Pericak-Vance, "Gene dose of apolipoprotein e type 4 allele and the risk of alzheimers disease in late onset families," *Science*, vol. 261, no. 5123, pp. 921–923, 1993.

[162] D. Scheuner, C. Eckman, M. Jensen, X. Song, M. Citron, N. Suzuki, T. Bird, J. Hardy, M. Hutton, W. Kukull, *et al.*, "Secreted amyloid β–protein similar to that in the senile plaques of alzheimer's disease is increased in vivo by the presenilin 1 and 2 and app mutations linked to familial alzheimer's disease," *Nature medicine*, vol. 2, no. 8, pp. 864–870, 1996.

[163] G. McKhann, D. Drachman, M. Folstein, R. Katzman, D. Price, and E. M. Stadlan, "Clinical diagnosis of alzheimer's disease report of the nincds-adrda work group* under the auspices of department of health and human services task force on alzheimer's disease," *Neurology*, vol. 34, no. 7, pp. 939–939, 1984.

[164] A. Martorana, Z. Esposito, and G. Koch, "Beyond the cholinergic hypothesis: do current drugs work in alzheimer's disease?," *CNS neuroscience & therapeutics*, vol. 16, no. 4, pp. 235–245, 2010.

[165] R. Kayed and C. A. Lasagna-Reeves, "Molecular mechanisms of amyloid oligomers toxicity," *Journal of Alzheimer's Disease*, vol. 33, no. s1, pp. S67–S78, 2013.

[166] C. L. Masters and D. J. Selkoe, "Biochemistry of amyloid β-protein and amyloid deposits in alzheimer disease," *Cold Spring Harbor perspectives in medicine*, vol. 2, no. 6, p. a006262, 2012.

[167] M. J. Savage, J. Kalinina, A. Wolfe, K. Tugusheva, R. Korn, T. Cash-Mason, J. W. Maxwell, N. G. Hatcher, S. J. Haugabook, G. Wu, *et al.*, "A sensitive aβ oligomer assay discriminates alzheimer's and aged control cerebrospinal fluid," *Journal of Neuroscience*, vol. 34, no. 8, pp. 2884–2897, 2014.

[168] T. Yang, T. T OMalley, D. Kanmert, J. Jerecic, L. R. Zieske, H. Zetterberg, B. T. Hyman, D. M. Walsh, and D. J. Selkoe, "A highly sensitive novel immunoassay specifically detects low levels of soluble aβ oligomers in human cerebrospinal fluid," *Alzheimer's research & therapy*, vol. 7, no. 1, p. 14, 2015.

[169] B. L. Wright, J. T. Lai, and A. J. Sinclair, "Cerebrospinal fluid and lumbar puncture: a practical review," *Journal of neurology*, vol. 259, no. 8, pp. 1530–1545, 2012.

[170] K. Felgenhauer, "Protein size and cerebrospinal fluid composition," *Journal of Molecular Medicine*, vol. 52, no. 24, pp. 1158–1164, 1974.

[171] B. F. Westmoreland, *Medical neuroscience*. Little Brown, 1994.

[172] E. R. Kandel, J. H. Schwartz, T. M. Jessell, S. A. Siegelbaum, A. J. Hudspeth, *et al.*, *Principles of neural science*, vol. 4. McGraw-hill New York, 2000.

[173] D. M. Walsh, I. Klyubin, J. V. Fadeeva, W. K. Cullen, R. Anwyl, M. S. Wolfe, M. J. Rowan, and D. J. Selkoe, "Naturally secreted oligomers of amyloid β protein potently inhibit hippocampal long-term potentiation in vivo," *Nature*, vol. 416, no. 6880, pp. 535–539, 2002.

[174] J. J. Yerbury and M. R. Wilson, "Extracellular chaperones modulate the effects of alzheimers patient cerebrospinal fluid on aβ1-42 toxicity and uptake," *Cell Stress and Chaperones*, vol. 15, no. 1, pp. 115–121, 2010.

[175] P. Narayan, A. Orte, R. W. Clarke, B. Bolognesi, S. Hook, K. A. Ganzinger, S. Meehan, M. R. Wilson, C. M. Dobson, and D. Klenerman, "The extracellular chaperone clusterin sequesters oligomeric forms of the amyloid-β1- 40 peptide," *Nature structural & molecular biology*, vol. 19, no. 1, pp. 79–83, 2012.

[176] Sigma–Aldrich, *Ionomycin calcium salt from Streptomyces conglobatus, product information*.

[177] G. Paraschiv, C. Vincke, P. Czaplewska, M. Manea, S. Muyldermans, and M. Przybylski, "Epitope structure and binding affinity of single chain llama anti-β-amyloid antibodies revealed by proteolytic excision affinity-mass spectrometry," *Journal of Molecular Recognition*, vol. 26, no. 1, pp. 1–9, 2013.

[178] Ablynx, "Understanding nanobodies, product description." http://www.ablynx.com/technology-innovation/understanding-nanobodies/.

[179] M. G. Spillantini, R. A. Crowther, R. Jakes, M. Hasegawa, and M. Goedert, "α-synuclein in filamentous inclusions of lewy bodies from parkinsons disease and dementia with lewy bodies," *Proceedings of the National Academy of Sciences*, vol. 95, no. 11, pp. 6469–6473, 1998.

[180] M. Baba, S. Nakajo, P.-H. Tu, T. Tomita, K. Nakaya, V. Lee, J. Q. Trojanowski, and T. Iwatsubo, "Aggregation of alpha-synuclein in lewy bodies of sporadic parkinson's disease and dementia with lewy bodies.," *The American journal of pathology*, vol. 152, no. 4, p. 879, 1998.

[181] H.-J. Lee, S. Patel, and S.-J. Lee, "Intravesicular localization and exocytosis of α-synuclein and its aggregates," *Journal of Neuroscience*, vol. 25, no. 25, pp. 6016–6024, 2005.

[182] P. K. Mandal, J. W. Pettegrew, E. Masliah, R. L. Hamilton, and R. Mandal, "Interaction between aβ peptide and α synuclein: molecular mechanisms in overlapping pathology of alzheimers and parkinsons in dementia with lewy body disease," *Neurochemical research*, vol. 31, no. 9, pp. 1153–1162, 2006.

[183] K. Ono, R. Takahashi, T. Ikeda, and M. Yamada, "Cross-seeding effects of amyloid β-protein and α-synuclein," *Journal of neurochemistry*, vol. 122, no. 5, pp. 883–890, 2012.

[184] J. C. Jose, P. Chatterjee, and N. Sengupta, "Cross dimerization of amyloid-β and αsynuclein proteins in aqueous environment: A molecular dynamics simulations study," *PloS one*, vol. 9, no. 9, p. e106883, 2014.

[185] I. F. Tsigelny, L. Crews, P. Desplats, G. M. Shaked, Y. Sharikov, H. Mizuno, B. Spencer, E. Rockenstein, M. Trejo, O. Platoshyn, *et al.*, "Mechanisms of hybrid oligomer formation in the pathogenesis of combined alzheimer's and parkinson's diseases," *PloS one*, vol. 3, no. 9, p. e3135, 2008.

[186] R. Mark, K. Hensley, D. Butterfield, and M. Mattson, "Amyloid beta-peptide impairs ion-motive atpase activities: evidence for a role in loss of neuronal ca2+ homeostasis and cell death," *The Journal of Neuroscience*, vol. 15, no. 9, pp. 6239–6249, 1995.

[187] A. Demuro, M. Smith, and I. Parker, "Single-channel ca2+ imaging implicates a142 amyloid pores in alzheimers disease pathology," *The Journal of Cell Biology*, vol. 195, no. 3, pp. 515–524, 2011.

[188] P. Narayan, K. M. Holmstrom, D.-H. Kim, D. J. Whitcomb, M. R. Wilson, P. St. George-Hyslop, N. W. Wood, C. M. Dobson, K. Cho, A. Y. Abramov, *et al.*, "Rare individual amyloid-β oligomers act on astrocytes to initiate neuronal damage," *Biochemistry*, vol. 53, no. 15, pp. 2442–2453, 2014.

[189] E. Syková and C. Nicholson, "Diffusion in brain extracellular space," *Physiological reviews*, vol. 88, no. 4, pp. 1277–1340, 2008.

[190] M. NIljina, *Aggregation of Alpha-synuclein Using Single-molecule Spectroscopy*. PhD thesis, University of Cambridge.

[191] M. Iljina, L. Hong, M. H. Horrocks, M. H. Ludtmann, M. L. Choi, C. D. Hughes, F. S. Ruggeri, T. Guilliams, A. K. Buell, J.-E. Lee, *et al.*, "Nanobodies raised against monomeric -synuclein inhibit fibril formation and destabilize toxic oligomeric species," *BMC biology*, vol. 15, no. 1, p. 57, 2017.

[192] P. Flagmeier, S. De, D. C. Wirthensohn, S. F. Lee, C. Vincke, S. Muyldermans, T. P. Knowles, S. Gandhi, C. M. Dobson, and D. Klenerman, "Ultrasensitive measurement of ca2+ influx into lipid vesicles induced by protein aggregates," *Angewandte Chemie*, 2017.

[193] S. Salloway, R. Sperling, N. C. Fox, K. Blennow, W. Klunk, M. Raskind, M. Sabbagh, L. S. Honig, A. P. Porsteinsson, S. Ferris, *et al.*, "Two phase 3 trials of

bapineuzumab in mild-to-moderate alzheimer's disease," *New England Journal of Medicine*, vol. 370, no. 4, pp. 322–333, 2014.

[194] R. Vandenberghe, J. O. Rinne, M. Boada, S. Katayama, P. Scheltens, B. Vellas, M. Tuchman, A. Gass, J. B. Fiebach, D. Hill, *et al.*, "Bapineuzumab for mild to moderate alzheimers disease in two global, randomized, phase 3 trials," *Alzheimer's research & therapy*, vol. 8, no. 1, p. 18, 2016.

[195] Thor Labs, "Optical tables tutorial, product description." https://www.thorlabs.com/newgrouppage9.cfm?objectgroup_id=8275.

[196] Chuo Precision Industrial Co., LTD, "High-grade aluminum xy-axis stage, product description." http://www.chuo.co.jp/english/contents/hp0045/list.php?CNo=45&ProCon=434.

[197] Physik Instrumente, *M-11x Micro-translation stage, MP41EE, User Manual*.

[198] Physik Instrumente, *P-5x7/P-5x8 Stage, User Manual*.

[199] Scientifica, "Patchstar micromanipulator, product description." http://www.scientifica.uk.com/products/scientifica-patchstar-micromanipulator.

[200] Cairn Research, *Dual OptoLED, Instruction Manual*.

[201] PCO., *pco.pixelfly usb, product data sheet*.

[202] B. Sakmann, *Single-channel recording*. Springer Science & Business Media, 2013.

[203] H. Lodish, A. Berk, S. L. Zipursky, P. Matsudaira, D. Baltimore, J. Darnell, *et al.*, *Molecular cell biology*, vol. 3. Scientific American Books New York, 1995.

[204] S. Coco, F. Calegari, E. Pravettoni, D. Pozzi, E. Taverna, P. Rosa, M. Matteoli, and C. Verderio, "Storage and release of atp from astrocytes in culture," *Journal of Biological Chemistry*, vol. 278, no. 2, pp. 1354–1362, 2003.

[205] K. Tanaka, S. Gilroy, A. M. Jones, and G. Stacey, "Extracellular atp signaling in plants," *Trends in cell biology*, vol. 20, no. 10, pp. 601–608, 2010.

[206] C. E. Stout, J. L. Costantin, C. C. Naus, and A. C. Charles, "Intercellular calcium signaling in astrocytes via atp release through connexin hemichannels," *Journal of Biological Chemistry*, vol. 277, no. 12, pp. 10482–10488, 2002.

[207] P. B. Guthrie, J. Knappenberger, M. Segal, M. V. Bennett, A. C. Charles, and S. B. Kater, "Atp released from astrocytes mediates glial calcium waves," *Journal of Neuroscience*, vol. 19, no. 2, pp. 520–528, 1999.

[208] S. Y. Kim, J. H. Moon, H. G. Lee, S. U. Kim, and Y. B. Lee, "Atp released from [beta]-amyloid-stimulated microglia induces reactive oxygen species production in an autocrine fashion," *Experimental & molecular medicine*, vol. 39, no. 6, p. 820, 2007.

[209] N. J. Haughey and M. P. Mattson, "Alzheimers amyloid β-peptide enhances atp/gap junction-mediated calcium-wave propagation in astrocytes," *Neuromolecular medicine*, vol. 3, no. 3, pp. 173–180, 2003.

[210] H. Imamura, K. P. H. Nhat, H. Togawa, K. Saito, R. Iino, Y. Kato-Yamada, T. Nagai, and H. Noji, "Visualization of atp levels inside single living cells with fluorescence resonance energy transfer-based genetically encoded indicators," *Proceedings of the National Academy of Sciences*, vol. 106, no. 37, pp. 15651–15656, 2009.

[211] G. Marcaida, M.-D. Miñana, S. Grisolıa, and V. Felipo, "Determination of intracellular atp in primary cultures of neurons," *Brain Research Protocols*, vol. 1, no. 1, pp. 75–78, 1997.

[212] U. Winkler, P. Seim, Y. Enzbrenner, S. Köhler, M. Sicker, and J. Hirrlinger, "Activity-dependent modulation of intracellular atp in cultured cortical astrocytes," *Journal of Neuroscience Research*, 2017.

[213] F. Sáez-Orellana, P. Godoy, C. Bastidas, T. Silva-Grecchi, L. Guzmán, L. Aguayo, and J. Fuentealba, "Atp leakage induces p2xr activation and contributes to acute synaptic excitotoxicity induced by soluble oligomers of β-amyloid peptide in hippocampal neurons," *Neuropharmacology*, vol. 100, pp. 116–123, 2016.

[214] A. J. Bard, F. R. F. Fan, J. Kwak, and O. Lev, "Scanning electrochemical microscopy. introduction and principles," *Analytical Chemistry*, vol. 61, no. 2, pp. 132–138, 1989.

[215] S. Amemiya, A. J. Bard, F.-R. F. Fan, M. V. Mirkin, and P. R. Unwin, "Scanning electrochemical microscopy," *Annual Review of Analytical Chemistry*, vol. 1, no. 1, pp. 95–131, 2008.

[216] J. T. Cox and B. Zhang, "Nanoelectrodes: Recent advances and new directions," *Annual Review of Analytical Chemistry*, vol. 5, no. 1, pp. 253–272, 2012.

[217] Y. Wang, J.-M. Nol, J. Velmurugan, W. Nogala, M. V. Mirkin, C. Lu, M. Guille Collignon, F. Lematre, and C. Amatore, "Nanoelectrodes for determination of reactive oxygen and nitrogen species inside murine macrophages," *Proceedings of the National Academy of Sciences*, vol. 109, no. 29, pp. 11534–11539, 2012.

[218] P. Actis, S. Tokar, J. Clausmeyer, B. Babakinejad, S. Mikhaleva, R. Cornut, Y. Takahashi, A. Lpez Crdoba, P. Novak, A. I. Shevchuck, J. A. Dougan, S. G. Kazarian, P. V. Gorelkin, A. S. Erofeev, I. V. Yaminsky, P. R. Unwin, W. Schuhmann, D. Klenerman, D. A. Rusakov, E. V. Sviderskaya, and Y. E. Korchev, "Electrochemical nanoprobes for single-cell analysis," *ACS Nano*, vol. 8, no. 1, pp. 875–884, 2014.

[219] J. Clausmeyer, P. Actis, A. L. Crdoba, Y. Korchev, and W. Schuhmann, "Nanosensors for the detection of hydrogen peroxide," *Electrochemistry Communications*, vol. 40, no. 0, pp. 28 – 30, 2014.

[220] B. Tian and C. M. Lieber, "Synthetic nanoelectronic probes for biological cells and tissues," *Annual Review of Analytical Chemistry*, vol. 6, no. 1, pp. 31–51, 2013.

[221] W. Lu, P. Xie, and C. M. Lieber, "Nanowire transistor performance limits and applications," *Electron Devices, IEEE Transactions on*, vol. 55, pp. 2859–2876, Nov 2008.

[222] H. Yoon, "Current trends in sensors based on conducting polymer nanomaterials," *Nanomaterials*, vol. 3, no. 3, pp. 524–549, 2013.

[223] D. J. Shirale, M. A. Bangar, W. Chen, N. V. Myung, and A. Mulchandani, "Effect of aspect ratio (length:diameter) on a single polypyrrole nanowire fet device," *The Journal of Physical Chemistry C*, vol. 114, no. 31, pp. 13375–13380, 2010.

[224] M. M. Alam, J. Wang, Y. Guo, S. P. Lee, and H.-R. Tseng, "Electrolyte-gated transistors based on conducting polymer nanowire junction arrays," *The Journal of Physical Chemistry B*, vol. 109, no. 26, pp. 12777–12784, 2005.

[225] R. M, S. V. Subramanyam, and S. Chatterjee, "Contribution of polarons and bipolarons to low-temperature conductivity in doped polypyrrole," *Phys. Rev. B*, vol. 43, pp. 4236–4243, Feb 1991.

[226] H. Yoon, S. Ko, and J. Jang, "Field-effect-transistor sensor based on enzyme-functionalized polypyrrole nanotubes for glucose detection," *The Journal of Physical Chemistry B*, vol. 112, no. 32, pp. 9992–9997, 2008.

[227] Q. Chi and S. Dong, "Amperometric biosensors based on the immobilization of oxidases in a prussian blue film by electrochemical codeposition," *Analytica Chimica Acta*, vol. 310, no. 3, pp. 429 – 436, 1995.

[228] D. A. Neamen, *Semiconductor Physics and Devices: Basic Principles*. McGraw-Hill Education, 2012.

[229] K. M. Ziadan, "Conducting polymers application," in *New Polymers for Special Applications*, InTech, 2012.

[230] P. Lin, F. Yan, J. Yu, H. L. Chan, and M. Yang, "The application of organic electrochemical transistors in cell-based biosensors," *Advanced Materials*, vol. 22, no. 33, pp. 3655–3660, 2010.

[231] L. Kergoat, B. Piro, M. Berggren, G. Horowitz, and M.-C. Pham, "Advances in organic transistor-based biosensors: from organic electrochemical transistors to electrolyte-gated organic field-effect transistors," *Analytical and bioanalytical chemistry*, vol. 402, no. 5, pp. 1813–1826, 2012.

[232] D. Hucknall, *Chemistry of hydrocarbon combustion*. Springer Science & Business Media, 2012.

[233] J. Wang, *Analytical electrochemistry*. John Wiley & Sons, 2006.

[234] A. W. Bott, "Mass transport," *simulation*, vol. 47906, p. 1382, 1996.

[235] R. Ansari, "Polypyrrole conducting electroactive polymers: synthesis and stability studies," *Journal of Chemistry*, vol. 3, no. 4, pp. 186–201, 2006.

[236] D. Ateh, H. Navsaria, and P. Vadgama, "Polypyrrole-based conducting polymers and interactions with biological tissues," *Journal of the royal society interface*, vol. 3, no. 11, pp. 741–752, 2006.

[237] P. Camurlu, "Polypyrrole derivatives for electrochromic applications," *RSC Advances*, vol. 4, no. 99, pp. 55832–55845, 2014.

[238] G. D. Sulka, K. Hnida, and A. Brzózka, "ph sensors based on polypyrrole nanowire arrays," *Electrochimica Acta*, vol. 104, pp. 536–541, 2013.

[239] A. Michalska and K. Maksymiuk, "Counter-ion influence on polypyrrole potentiometric ph sensitivity," *Microchimica Acta*, vol. 143, no. 2-3, pp. 163–175, 2003.

[240] A. Gelmi, M. K. Ljunggren, M. Rafat, and E. Jager, "Influence of conductive polymer doping on the viability of cardiac progenitor cells," *Journal of Materials Chemistry B*, vol. 2, no. 24, pp. 3860–3867, 2014.

[241] Q. Pei and R. Qian, "Protonation and deprotonation of polypyrrole chain in aqueous solutions," *Synthetic metals*, vol. 45, no. 1, pp. 35–48, 1991.

[242] D. Maddison, J. Unsworth, and J. Lusk, "Pressure dependence of electrical conductivity in polypyrrole," *Synthetic metals*, vol. 22, no. 3, pp. 257–264, 1988.

[243] B. Lundberg, B. Sundqvist, O. Inganäs, I. Lundström, and W. R. Salaneck, "Pressure dependent electrical conductivity of polypyrrole," *Molecular Crystals and Liquid Crystals*, vol. 118, no. 1, pp. 155–158, 1985.

[244] I. Migneault, C. Dartiguenave, M. J. Bertrand, and K. C. Waldron, "Glutaraldehyde: behavior in aqueous solution, reaction with proteins, and application to enzyme crosslinking," *Biotechniques*, vol. 37, no. 5, pp. 790–806, 2004.

[245] Y. Wine, N. Cohen-Hadar, A. Freeman, and F. Frolow, "Elucidation of the mechanism and end products of glutaraldehyde crosslinking reaction by x-ray structure analysis," *Biotechnology and bioengineering*, vol. 98, no. 3, pp. 711–718, 2007.

[246] Y. Zhang, J. Clausmeyer, B. Babakinejad, A. Lopez Cordoba, T. Ali, A. Shevchuk, Y. Takahashi, P. Novak, C. Edwards, M. Lab, *et al.*, "Spearhead nanometric field-effect transistor sensors for single-cell analysis," *ACS nano*, vol. 10, no. 3, pp. 3214–3221, 2016.

[247] O. Barbosa, C. Ortiz, Á. Berenguer-Murcia, R. Torres, R. C. Rodrigues, and R. Fernandez-Lafuente, "Glutaraldehyde in bio-catalysts design: a useful crosslinker and a versatile tool in enzyme immobilization," *Rsc Advances*, vol. 4, no. 4, pp. 1583–1600, 2014.

[248] H. Ida, Y. Takahashi, A. Kumatani, H. Shiku, and T. Matsue, "High speed scanning ion conductance microscopy for quantitative analysis of nanoscale dynamics of microvilli," *Analytical Chemistry*, vol. 89, no. 11, pp. 6015–6020, 2017.

[249] P. Happel, D. Thatenhorst, and I. D. Dietzel, "Scanning ion conductance microscopy for studying biological samples," *Sensors*, vol. 12, no. 11, pp. 14983–15008, 2012.